FACULTÉ DES ÉTUDES SUPÉRIEURES ET POSTDOCTORALES

uOttawa

L'Université canadienne
Canada's university

FACULTY OF GRADUATE AND POSTDOCTORAL STUDIES

Jesse Scott Smith
AUTEUR DE LA THÈSE / AUTHOR OF THESIS

Ph.D. (Physics)
GRADE / DEGREE

Department of Physics
FACULTÉ, ÉCOLE, DÉPARTEMENT / FACULTY, SCHOOL, DEPARTMENT

A High-Pressure Study of the Heavy Alkaline Earth Hydrides
TITRE DE LA THÈSE / TITLE OF THESIS

S. Desgreniers
DIRECTEUR (DIRECTRICE) DE LA THÈSE / THESIS SUPERVISOR

CO-DIRECTEUR (CO-DIRECTRICE) DE LA THÈSE / THESIS CO-SUPERVISOR

EXAMINATEURS (EXAMINATRICES) DE LA THÈSE / THESIS EXAMINERS

J. Armitage	I. L'Heureux
Y. Song	Z. Stadnik

Gary W. Slater
Le Doyen de la Faculté des études supérieures et postdoctorales / Dean of the Faculty of Graduate and Postdoctoral Studies

A high-pressure study of the heavy alkaline earth hydrides

Jesse S. Smith

Thesis submitted to the
Faculty of Graduate and Postdoctoral Studies
In partial fulfillment of the requirements for the degree of
Doctor of Philosophy in Physics

Department of Physics
Faculty of Science
University of Ottawa

Library and Archives
Canada

Published Heritage
Branch

395 Wellington Street
Ottawa ON K1A 0N4
Canada

Bibliothèque et
Archives Canada

Direction du
Patrimoine de l'édition

395, rue Wellington
Ottawa ON K1A 0N4
Canada

Your file Votre référence
ISBN: 978-0-494-59516-9
Our file Notre référence
ISBN: 978-0-494-59516-9

NOTICE:

The author has granted a non-exclusive license allowing Library and Archives Canada to reproduce, publish, archive, preserve, conserve, communicate to the public by telecommunication or on the Internet, loan, distribute and sell theses worldwide, for commercial or non-commercial purposes, in microform, paper, electronic and/or any other formats.

The author retains copyright ownership and moral rights in this thesis. Neither the thesis nor substantial extracts from it may be printed or otherwise reproduced without the author's permission.

AVIS:

L'auteur a accordé une licence non exclusive permettant à la Bibliothèque et Archives Canada de reproduire, publier, archiver, sauvegarder, conserver, transmettre au public par télécommunication ou par l'Internet, prêter, distribuer et vendre des thèses partout dans le monde, à des fins commerciales ou autres, sur support microforme, papier, électronique et/ou autres formats.

L'auteur conserve la propriété du droit d'auteur et des droits moraux qui protège cette thèse. Ni la thèse ni des extraits substantiels de celle-ci ne doivent être imprimés ou autrement reproduits sans son autorisation.

In compliance with the Canadian Privacy Act some supporting forms may have been removed from this thesis.

While these forms may be included in the document page count, their removal does not represent any loss of content from the thesis.

Conformément à la loi canadienne sur la protection de la vie privée, quelques formulaires secondaires ont été enlevés de cette thèse.

Bien que ces formulaires aient inclus dans la pagination, il n'y aura aucun contenu manquant.

Canada

Abstract

The heavy alkaline earth hydrides consist of the Group II (alkaline earth metal) hydrides, namely CaH_2, SrH_2, and BaH_2, which adopt the cotunnite-type structure at ambient pressure and temperature conditions. There has been much recent research interest in these compounds; in the past decade numerous experimental and theoretical studies exploring the hydrides in both applied and fundamental respects have been added to the literature. The present work constitutes a study of the heavy alkaline earth hydrides subjected to extreme pressure conditions (at ambient temperature). Specifically, pressure-dependent angle-dispersive powder x-ray diffraction and Raman spectroscopy experiments, as well as first-principles calculations, have been carried out to explore the structural stability, compressibility, and optical phonon spectra of the heavy alkaline earth hydrides. To complement the work on the hydrides, a companion study on BaF_2—a structural analogue—is presented, as well as a description of some selected experimental techniques used to carry out the research. The powder x-ray diffraction results reveal that all of the heavy alkaline earth hydrides undergo a pressure-induced, first-order structural phase transition. The proposed Ni_2In structure for the high-pressure phase is based on both the results of first-principles calculations and an isostructural comparison with BaF_2. The transition pressures and the proposed high-pressure structure are corroborated by the results of the Raman spectroscopy measurements. Where applicable, equation of state parameters from both the experimental and theoretical studies are reported, and a comparison of these respective parameters at ultra-high pressures (greater than 50 GPa) suggests that the experimentally observed bulk moduli are overestimated due to the presence of non-hydrostatic pressure conditions.

Statement of originality and collaborative contributions

The author states that, to the best of his knowledge, this body of work constitutes original research in the field of physics. Furthermore, inasmuch as the central portion of this work consists of collaborative publications, the specific contributions of the author are as follows:

> All experimental aspects pertaining to this work (including preparation, design, execution, and analysis) were done either solely by the author or in direct cooperation with the relevant coauthors, *except* the diffraction and Raman experiments on CaH_2 carried out at the National Synchrotron Light Source (USA) and the diffraction experiments carried out on BaF_2 at Super Photon ring-8 (Japan).
>
> All theoretical aspects pertaining to this work were done by Professor John S. Tse and/or Dr. Dennis D. Klug.
>
> All manuscripts (including text, figures, tables, etc.) submitted for publication were prepared by the author *except* the original manuscript (text and selected figures) for CaH_2 was prepared by John S. Tse, and details regarding the methods used for first-principles calculations in relevant works were prepared by John S. Tse and/or Dennis D. Klug.
>
> In accord with the nature of graduate studies, all of the author's work was done under the direct and close supervision of his research supervisor, Professor Serge Desgreniers.

Acknowledgments

I would like to express my thanks to the University of Ottawa, the Faculty of Graduate and Postdoctoral Studies, the Faculty of Science, the Department of Physics, and Professor Serge Desgreniers for generous financial support throughout my graduate studies. This support, provided in the form of scholarships, assistantships, and travel bursaries, significantly reduced the financial burden often associated with student life. The corresponding freedom and security have allowed me to focus on my education and research in a way that would not have been otherwise possible.

I would like to acknowledge three individuals who were particularly influential during my undergraduate studies at Temple University: Professor Chyan Long Lin, Dr. Jason A. Zan, and Professor Charles Dyke. Professor Lin and Dr. Zan enthusiastically introduced me to experimental physics. They trusted me to "do it myself" long before I had earned their trust, and selflessly gave their time and energy as I learned my way around (and broke a few things in) the lab. Professor Dyke was the first one to explain to me that the goal of an educator is to help students become colleagues. Over what must have been for him a long four years, he gave me invaluable help whenever I asked for it, and I still rely heavily on the principles I learned through his example.

I would like to thank a couple of my peers, Dr. Roxana Flacau and Ryan Bolen. While I appreciate the contributions each made to the research presented in this thesis, I am most grateful for their friendship.

I am indebted to Professor John S. Tse and Dr. Dennis D. Klug, who carried out all of the first-principles calculations presented in this work. The have shed much light on my research through many helpful discussions, and their enthusiasm for high-pressure research has been infectious.

I am grateful to Dr. Ning Chen, Dr. Chang-Yong Kim, and Professor De-Tong Jiang for their assistance in carrying out experiments at the Hard X-ray MicroAnalysis beamline at the Canadian Light Source. Dr. Chen, in particular, has suffered through many long nights at the beamline to help my collaborators and me get our results.

I am grateful to have been a member of the *Laboratoire de physique des solides denses*, led by Professor Serge Desgreniers. I have benefited greatly from the equipment, research opportunities, and camaraderie that come with being a member of the group. It has been the ideal environment for me to carry out my research.

I cannot adequately express my gratitude to my research supervisor, Professor Serge Desgreniers. I have benefited beyond measure from his unique combination of knowledge, skill, and patience. He has given me complete freedom to carry out my research in the manner I chose, never telling me what to do but rather showing me how to do it, by way of example. He has been completely selfless, going, I believe, well beyond what would reasonably be expected of a supervisor. In short, he has treated me like a colleague since the beginning, but given me the time and attention a student often needs right up until the end.

I am grateful for the friendship and support of my family. Particularly, I appreciate the effort Tierney Zan put into editing the manuscript.

Finally, I am most grateful for Renée.

Table of contents

List of figures

Chapter 1

Chapter 2

Chapter 3

Chapter 4

Chapter 5

Chapter 7

List of tables

Chapter 1

Chapter 2 and Chapter 3

None

Chapter 4

Chapter 5

Chapter 6

Chapter 7

Chapter 1 Introduction

As an undergraduate I studied under a philosophy professor who would frequently point out that there are two kinds of people in the world, after which he would identify the two kinds and expound on the differences between them. Perhaps it is because dualisms are ubiquitous in philosophy that he managed to employ this method of comparison in a seemingly endless number of combinations. In keeping with this spirit, there are two kinds of physicists, theoretical and experimental, and rather than enumerate the differences between them, let it suffice to point out that the work that follows has been produced by the latter kind.

This work consists of research related to the study of the heavy alkaline earth hydrides submitted to extreme pressure conditions. It is divided into chapters which include this introduction, a collection of related articles published in peer-reviewed scientific journals, and a concluding chapter which brings together some common themes arising from the individual articles and suggests possible future avenues of research. With this in mind, each chapter is presented as an individual work with separate numbering of figures, tables, equations, and references (although there is a continuous numbering of pages).

Inasmuch as the central portion of the work consists of publications which out of necessity omit a wealth of information concerning experimental techniques and data reduction/analysis methods, the primary aim of this introductory chapter is to present a detailed exposition of these topics. The hope is that it will serve both high-pressure specialists and the broader scientific audience alike, providing a useful resource for the former and a reasonable background for the latter. Equations are introduced sparingly, and are used more in the spirit of facilitating discussion than in stating physical laws. A topical selection of works is provided at the end of this chapter for the interested reader who would like to explore specific topics in greater depth.

This introduction is in the style of a continuous narrative. However, topics are divided among numbered sections, with subsections set apart in italics, to assist the reader. After a general exposition of studying materials as a function of pressure, following sections include methods of static pressure generation, pressure measurement, sample preparation (including preparation of the high-pressure diamond anvil cell), and sample loading. With the exception of Chapter 6, each publication includes results from powder x-ray diffraction and Raman spectroscopy experiments as well as first-principles calculations. However, the experimental methods relevant to high-pressure angle-dispersive powder x-ray diffraction using synchrotron radiation will constitute the primary focus of the introduction with respect to experimental methods and data analysis. The introduction concludes with a section describing the initial motivation for studying the heavy alkaline earth hydrides and introducing the articles presented in the following chapters.

1. Studying the structure of materials as a function of pressure

Leaving aside plasmas and decomposition for the sake of discussion, an element or compound may exist as a gas, liquid, or solid, and furthermore, may exhibit various types of ordering in each of these phases (for example, different crystal structures in the case of the solid state). The particular state (and accompanying order) of a system depends on a number of different properties, or state variables, used to describe the system. The state variables salient to this work are T, S, P, and V, for temperature, entropy, pressure, and volume, respectively. State variables can be classified as either extensive or intensive. The appropriate classification of the four state variables mentioned above can be readily distinguished; the extensive variables S and V are such that the total value for the system is the sum of the constituent parts (the total volume of the system is the sum of the volumes occupied by the individual atoms), whereas the intensive variables T and P are such that the total value for the system is the same as the value for the constituent parts (the temperature in one part of the system is the same as the temperature everywhere, provided the system is in thermodynamic equilibrium).

Conjugate properties are extensive and intensive properties whose product has the dimension of energy. From the first law of thermodynamics and the definition of mechanical work, the internal energy of a system can be expressed as an exact differential in terms of these products and their corresponding differentials:

$$dE = TdS - PdV \tag{1}$$

However, from a practical point of view, the experimentalist is not typically varying (directly) the entropy and volume of the system but rather the intensive variables temperature and pressure. Through the process of Legendre transformation, other thermodynamic potentials H, F, and G, representing the enthalpy, Helmholtz free energy, and Gibbs free energy, respectively, can be expressed, with differentials covering the various combinations of the independent state variables:

$$dH = TdS + VdP \tag{2}$$

$$dF = -SdT - PdV \tag{3}$$

$$dG = -SdT + VdP \tag{4}$$

The Gibbs free energy is most appropriate for understanding the study of systems as a function of pressure (and similarly, temperature), as its differential (Equation 4) contains the intensive properties as the independent variables.

Considering how the Gibbs free energy varies with temperature and pressure, it is clear that within the stable temperature and pressure regime of a given phase, it decreases with increasing temperature and increases with increasing pressure. However, in the case of a phase transition, the temperature and pressure of a system remain constant; heat flowing in or out of the system and similarly work done on or by the system change only the entropy and volume. From Equation 4 it is clear that there is no change in the Gibbs free energy across a phase transition because temperature and pressure remain constant.

Inasmuch as all of the experimental results presented in following chapters were obtained at a constant (ambient) temperature, I here consider in more detail the specific case of the variation of the Gibbs free energy at constant temperature, shown in Figure 1.

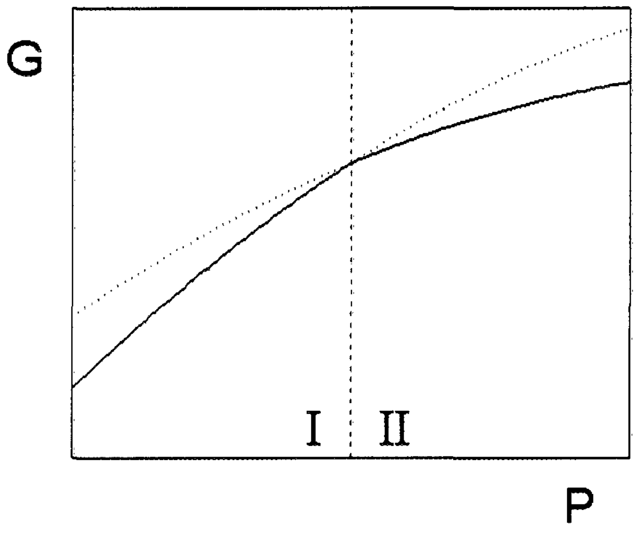

Figure 1: Pressure dependence of the Gibbs free energy at constant temperature. The pressure-induced phase transition occurs at the intersection of the two curves, at which point the energy associated with the high-pressure structure, Phase II, is less than that associated with the low-pressure structure, Phase I. There is no change in the Gibbs free energy across this transition.

A system will always adopt the state with the minimum energy (provided there are no barriers to reaching this ground state). Figure 1 includes the pressure-dependent Gibbs free energy for two separate phases. A transition from Phase I to Phase II occurs at the intersection of these two curves. To reiterate, *dG* vanishes across the pressure-induced phase transition; its first derivative with respect to pressure at constant temperature, however, does not:

$$\left(\frac{\partial G}{\partial P}\right)_T = V \tag{5}$$

It is finite and discontinuous, thus a pressure-induced phase transition is referred to as a *first-order* phase transition. Figure 2 shows the variation of volume as a function of pressure.

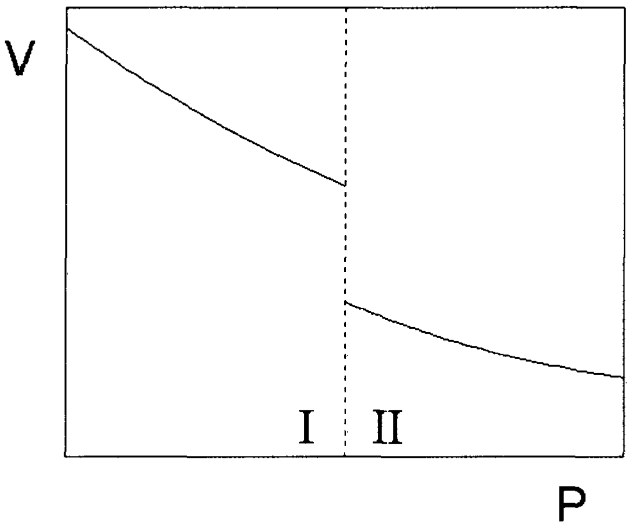

Figure 2: The pressure dependence of the volume at constant temperature. The finite change in volume across the phase transition corresponds to the finite change in the first pressure derivative of the Gibbs free energy (see the subtle "kink" in Figure 1).

There is a finite volume collapse across the phase transition. In the case of a solid-solid phase transition, this volume collapse is brought about by a change in the crystal structure, characterized by a more efficient packing of atoms brought about, for example, by an increase in coordination number (the number of nearest-neighbor atoms) or a change in the nature of the bonding between atoms.

The primary objective of the research presented in the following chapters is to look for first-order pressure-induced structural phase transitions in the heavy alkaline earth hydrides. Although discussed in more detail later, it is worth noting that some general motivations for looking for high-density structures include identifying novel material properties (e.g., super-hard materials) or unusual phase transitions (e.g., insulator-metal transitions), or recovering dense phases at ambient pressure (e.g., efficient, dense packing of hydrogen for hydrogen storage and exchange in commercial applications).

In addition to identifying structural phase transitions and determining the crystal structure of the high-pressure phases, a secondary objective of the work is to study the compressibility of materials, for both ambient-pressure and high-pressure phases. Returning to a more general discussion for the moment, in addition to looking at the variation of thermodynamic potentials (e.g., the Gibbs free energy) with respect to changes among state variables, one can also characterize the properties of a material by observing the change in one state variable with respect to another. These are called constitutive relations. Perhaps the most familiar example is that of Hooke's Law for a mass attached to a stiff spring; the force the spring exerts on the mass depends on the displacement of the mass from the equilibrium position of the spring, and the constitutive relation between the two is the spring constant, k. For small (infinitesimal) displacements, the force varies linearly.

For the purposes of this work, the constitutive relation of interest is between pressure and volume:

$$\left(\frac{\partial P}{\partial V}\right)_T = -\frac{B_T}{V} \tag{6}$$

B_T is called the isothermal bulk modulus (one can think of it as the *in*compressibility of a material); it describes how the pressure in the system changes for a corresponding change in volume. If one induces an infinitesimal strain in a system (e.g., by applying pressure) which reduces the volume, the corresponding increase in pressure is linear, proportional to B_T and $1/V$ (consider the slope of a very small segment of one of the curves in Figure 2). For large compressions, however, the linear relationship no longer holds; the more one compresses a material, the harder it is to compress. Take as an example a foam rubber ball, often used in physical therapy to strengthen the muscles in the hand. Initially it is quite easy to compress, but as the volume of the ball decreases (and the density of the foam rubber increases), it becomes quite difficult to compress.

To characterize the compression of materials over a large change in volume, *viz.*, a finite strain, it is necessary to consider how the bulk modulus varies with pressure. From finite strain theory one can obtain the volume of a material with respect to its volume at zero pressure, V_0, for a given compression f. By expanding the Helmholtz free energy F in powers of f, and going through a lengthy calculation, one can obtain the Birch-Murnaghan equation of state. In his *Introduction to the Physics of the Earth's Interior*,[1] Poirier shows the calculation in detail after expanding F to second-order, after which he states without demonstration the third-order Birch-Murnaghan equation of state:

$$P = \frac{3B_{0T}}{2}\left[\left(\frac{V}{V_0}\right)^{-7/3} - \left(\frac{V}{V_0}\right)^{-5/3}\right]\left\{1 + \frac{3}{4}(B_0' - 4)\left[\left(\frac{V}{V_0}\right)^{-2/3} - 1\right]\right\} \tag{7}$$

Here B_{0T} is the isothermal bulk modulus at zero pressure, B_0' is the first derivative (with respect to pressure, evaluated at zero pressure) of the isothermal bulk modulus (i.e., it quantitatively accounts for materials being more difficult to compress as the pressure is increased), and V_0 is the volume at zero pressure. In practice, zero pressure is assumed to be ambient pressure (1 atm).

Upon obtaining the pressure dependence of the volume for a given phase of a material, B_{0T}, B_0', and V_0 can be obtained by fitting the corresponding data to Equation 7, treating each as a parameter in a χ^2-minimization. To obtain the most reliable values, it is necessary to have a relatively large compression over a correspondingly large pressure range (this is particularly important for B_0'). In practice, this is not always possible. One alternative is to assume a value for B_0'. In the following chapters, the value obtained from first-principles calculations is frequently used. Similarly, one can assume $B_0' = 4$. In this case, the second term in the braces of Equation 7 vanishes and one is left with the second-order Birch-Murnaghan equation of state (it turns out that many materials have a B_0' close to 4).

One final point worth mentioning is that the derivation of the Birch-Murnaghan equation of state assumes hydrostatic pressure conditions (or perhaps more appropriately, isotropic compression). The compression f is itself a function of the trace of the infinitesimal strain tensor. The off-diagonal elements are zero for isotropic compression, but are non-zero for anisotropic compression. As further discussed below, the uniaxial compression stroke of the diamond anvil cell, together with the lack of a suitable pressure-transmitting medium in the compression chamber, can lead to non-hydrostatic pressure conditions in the sample. Notwithstanding these practical complications, the second- and third-order Birch-Murnaghan equations of state are the most common for characterizing the pressure-dependent volume compression of materials in the high-pressure literature.

To summarize, the pressure-dependent study of materials presented in the following chapters consists of a few primary objectives. The first is to look for pressure-induced, first-order structural phase transitions. These are ultimately indicated by a discontinuity in the pressure-dependent volume, but in practice they are initially indicated by marked changes in powder x-ray diffraction images or Raman spectra. This discontinuity is the result of a change in the crystal structure (and correspondingly, the physical properties) of the material, so upon identifying a pressure-induced phase transition, the next step is to determine the crystal structure of the high-pressure phase. Once the crystal structure (or at the very least, the unit cell symmetry) has been determined, the pressure-dependent volume can be measured and subsequently fit to a second- or third-order Birch-Murnaghan equation of state to obtain B_{0T}, B_0', and V_0. These objectives are primarily realized by carrying out powder x-ray diffraction. However, to complement the diffraction studies, both Raman spectroscopy and first-principles calculations have been used to corroborate the proposed crystal structure of the high-pressure phases, to measure the pressure dependence of the optical phonon spectra, to provide complementary information on compression in the case of phases stable over a narrow pressure range, and to provide more appropriate equation of state parameters when complications associated with non-hydrostatic conditions arise.

2. On the order of gigapascals

The unit of pressure used throughout this work is the gigapascal (GPa). To gain an appreciation for the magnitude of the extreme static pressures reported in the following chapters, it is instructive to take note of a few pressure points in nature. First, atmospheric pressure is approximately 1×10^{5} Pa, or equivalently 1×10^{-4} GPa. To get the next few relevant points, one needs to head toward the earth's core. Figure 3 shows some of these points.

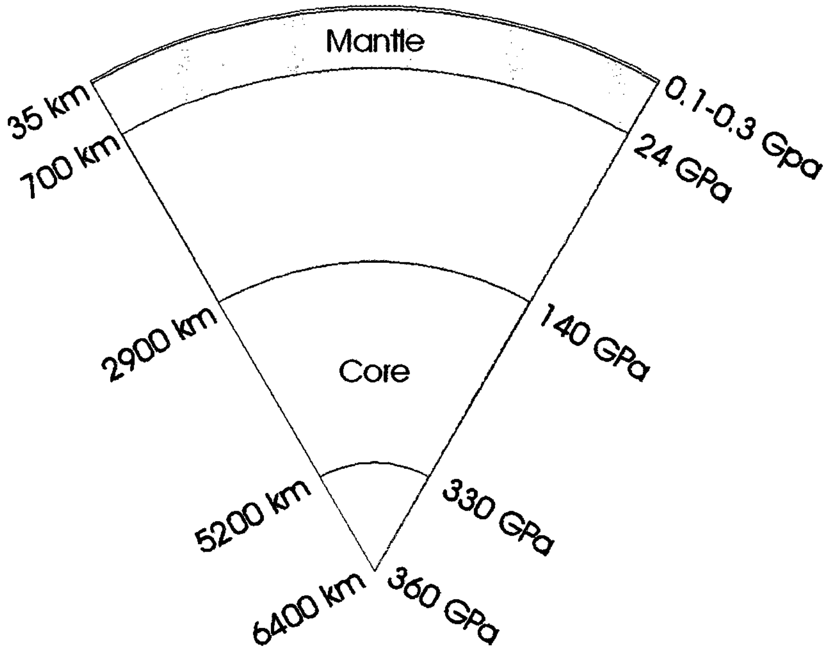

Figure 3: Pressures points within the earth.

At the deepest part of the Pacific Ocean, the bottom of the Mariana Trench (a depth of just over 11,000 m), the pressure is just over 0.1 GPa—1,000 times atmospheric pressure—and pressures at the crust-mantle boundary can reach as high as 1 GPa. The pressure at the core-mantle boundary is approximately 140 GPa, and estimates for the pressure at the centre of the earth put it at approximately 360 GPa (3.6 Mbar). The majority of the results on the hydrides presented in this work were obtained at pressures ranging from ambient pressure up to a few tens of GPa. The barium fluoride work goes as high as 80 GPa, while the experiments on strontium hydride mark the highest pressure achieved in this work, 120 GPa—well over one million atmospheres. The apparatus and techniques used to generate these extreme static pressures have been developed only recently—in the last fifty or so years. To understand the driving force leading up to these developments, one needs to go back almost another fifty years to the start of a single individual's study of materials at high pressure.

3. Generating extreme static pressures

The modern history of the study of materials at high pressure begins in the first half of the twentieth century and is essentially dominated by Percy W. Bridgman, a Professor at Harvard University from 1908 to 1961. His staggering scientific output and his innovations which facilitated his research led to the 1946 Nobel Prize in Physics "for the invention of an apparatus to produce extremely high pressures, and for the discoveries he made therewith in the field of high pressure physics."[2] The majority of his experiments were carried out using either a piston-cylinder device or Bridgman anvils, shown in Figure 4. For a piston-cylinder device, the material of interest is placed in the cylinder together with a pressure-transmitting medium and a large hydraulic press is used to drive the piston into the cylinder. Bridgman used this device primarily to study the compressibility of materials (note that he could also identify the occurrence of structural phase transitions due to a discontinuous volume collapse). Pressures as high as 3 GPa can be attained in piston-cylinder devices before catastrophic mechanical failure occurs. Bridgman anvils are simply two opposed anvils made of carboloy (tungsten with nickel or cobalt as a binder) and hardened steel. The material of interest is placed between the two anvils and a large hydraulic press is used to drive the two anvils together. Bridgman used this device primarily for pressure-dependent resistivity measurements. At the time, no other device could exceed the maximum pressures attained by Bridgman anvils, almost 10 GPa.

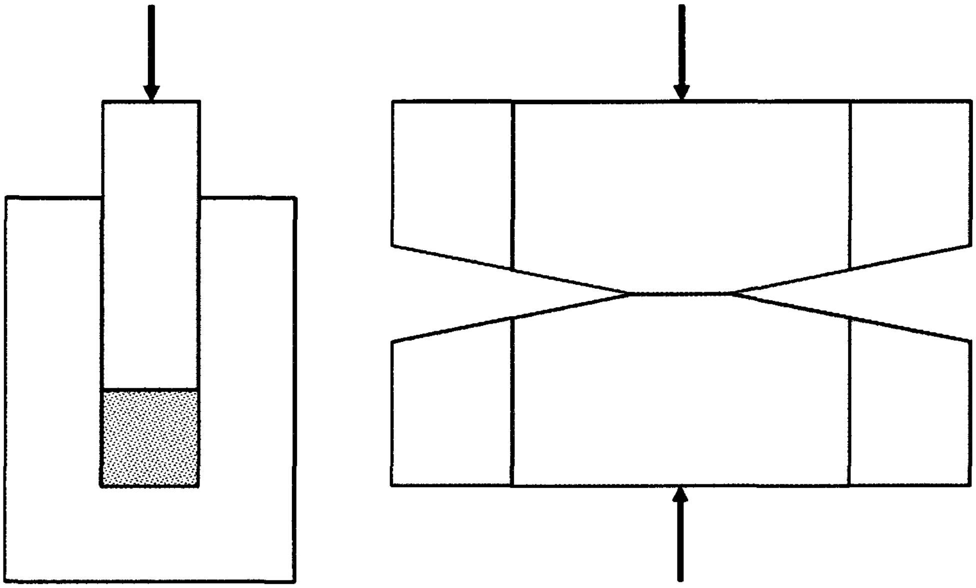

Figure 4: Schematic diagram of a piston-cylinder device (left) and Bridgman anvils (right) used by Percy W. Bridgman for the high-pressure study of materials.

The fact that an entire branch of experimental physics was, for almost half a century, dominated by a single individual is certainly a testament to Bridgman's abilities, but it is also a testament to the practical difficulties associated with high-pressure research. The costs associated with the installation, operation, and maintenance of the large hydraulic presses used to generate high static pressures was prohibitive. Leaving funding issues aside, the technical and safety requirements associated with the operation of the presses placed unusual demands on the experimentalist. Add to this the difficulties associated with accurate pressure determination and the limited practicable experimental techniques, and it is perhaps understandable that high-pressure research was carried out by relatively few individuals. If high-pressure research was to become a more widely practiced field of study, significant advances would be necessary to minimize the associated logistical difficulties, extend the maximum attainable pressures, and broaden the number of practicable experimental techniques. Remarkably, these challenges were met in 1959 by the introduction of a remarkably simple device, the diamond anvil cell.[3,4]

The diamond anvil cell (DAC) is essentially a miniature version of Bridgman anvils. Figure 5 shows the key elements of a DAC.

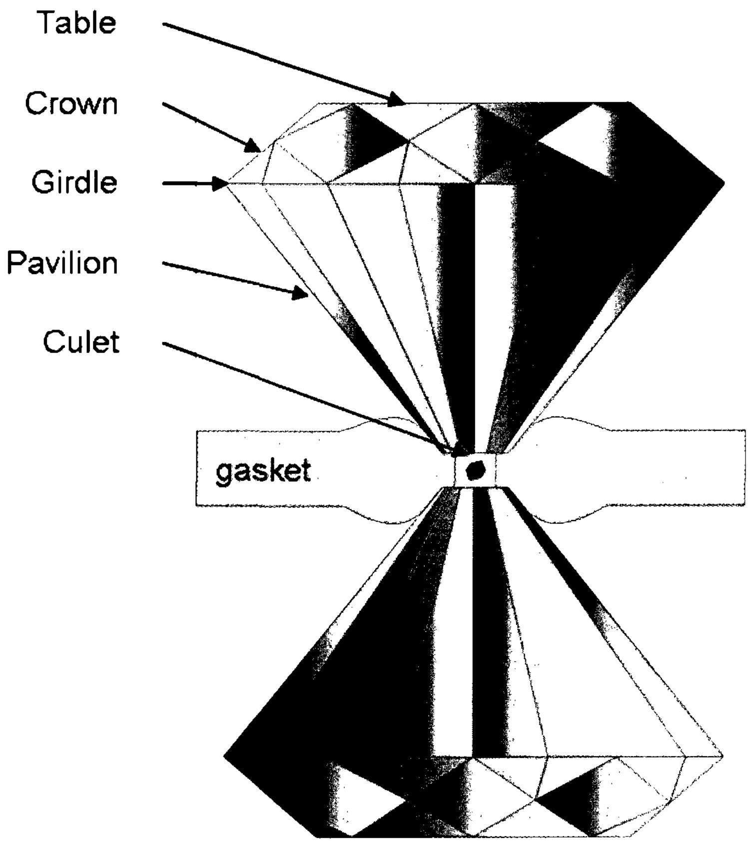

Figure 5: The core elements of the DAC: two opposed diamond anvils and a gasket. Also shown are the names, used frequently in the text below, of the various "parts" of the diamond anvil.

The basic design and operation of a DAC is quite simple. Typically, diamond anvils are made from brilliant-cut gemstones (although a number of other cuts and designs have been employed). The tip of the diamond is ground and polished to create a small, flat portion called the culet. The material to be studied is placed between the culets of two opposed diamond anvils and a force is applied to drive the anvils together. The mechanical advantage which facilitates the generation of extreme static pressures comes from the force being applied over the relatively large area of the anvil face (called the table) and subsequently transferred to the relatively small area over the culet. A number of different factors contribute to the maximum attainable pressure in a DAC. While these will be discussed in greater detail below, let it suffice here to say that with a modicum of care, experience, and expense on the part of the experimentalist, pressures in the tens of GPa can be routinely achieved. With the appropriate anvils and exceedingly careful preparation of the DAC, pressures exceeding 100 GPa can be routinely achieved. Reports of pressures above 200 GPa are exceedingly rare, and pressures approaching 500 GPa have been claimed,[5] although there is some controversy surrounding pressure "records," as accurate pressure measurement above approximately 175 GPa is quite challenging.

The DAC offers many advantages that in turn revolutionized the research of materials at extreme conditions. From a practical point of view, it is small—typically no more than a few centimeters in any dimension with a total mass of generally less than 1 kg. In the words of Jayaraman, ". . . a DAC capable of generating megabar pressures can fit into the palm of the hand . . ."[6] Large presses are not required to drive the anvils together; the force is applied by simply turning a few relatively small screws which bring the anvils' supporting structure together. The real revolution, however, comes from the properties of diamond. As the hardest known material, diamond is ideal for sustaining the large forces exerted on it in the DAC. Also, at the risk of sounding trite, the optical properties of diamond literally open up a window to the study of high-pressure materials. Specifically, diamond is optically transparent over a broad spectral range (for λ~300—2,500 nm), permitting pressure-dependent studies of optical absorption and reflectivity, infrared and Raman spectra, and Brillouin scattering. Furthermore, it provides the experimentalist with the extremely important advantage of observing the sample first-hand, *in situ*, during and after an increase or decrease in the sample pressure. Also, as a relatively low-Z (low atomic number) material, diamond is almost completely transparent to incident and diffracted x-rays (provided the x-ray wavelength is short), facilitating x-ray diffraction and absorption experiments. The diamonds also serve as excellent windows for heating the sample by means of laser irradiation; sample temperatures as high as 4000-5000 K have been achieved at very high pressures.[7] Modified DAC designs have also been employed for measurement of bulk properties including, for example, electrical resistivity and magnetic susceptibility. Much as dualisms are ubiquitous in philosophy, compromises are ubiquitous in experimental physics; there are certainly some drawbacks associated with the DAC that are discussed in more detail below. But in short, the DAC is a near-ideal tool for the study of materials subjected to extreme pressures. Below I expand on each of the particular components that comprise a DAC.

Diamond anvils

As mentioned above, diamond anvils are typically fashioned from brilliant-cut gemstones (the type shown in Figure 5). Other designs such as the Drukker anvil[8] include a vertical crown, providing a larger surface area for distributing the force applied to the anvil by the supports (called seats). A fairly recent innovation involves removing the facets from the crown by polishing and subsequently press-fitting the anvil into an angled seat. This provides a larger angular opening for better optical access as well as a wider scattering range for diffraction studies.[9] The overall weight of the diamond varies depending on the intended use of the anvil, maximum target pressure, and style of cut. Typical weights are about one-third of a carat, but can range from approximately 0.1—1 carat.

Diamond classification is also an important consideration. Routine optical and diffraction experiments can be carried out using Type Ia diamonds, which are characterized by having nitrogen impurities. However, care is taken to select diamonds relatively free of internal flaws or inclusions, and with low dislocation density (as estimated by birefringence), all of which could cause premature structural failure under load. Similarly, care is taken to select diamonds with low luminescence due to impurities to facilitate spectroscopic measurements. For spectroscopic measurements at pressures above approximately 50 GPa, nitrogen impurities in Type Ia diamonds give rise to a prohibitive level of background photo-excited luminescence, and it is necessary to use Type IIa diamonds, which are effectively free of nitrogen impurities. Type IIa diamonds are exceptionally rare and bear a hefty price tag. All of the diamonds used in this work were Type Ia diamonds carefully selected for ultra low luminescence and birefringence.

Culet size is a particularly important consideration, as it ultimately determines the maximum attainable pressure that can be achieved in a DAC. If one recalls that pressure is defined as a force per unit area, it is clear that for a given force applied to the anvil, the smaller the area of the culet, the greater the pressure on the sample. In his work *High Pressure Experimental Methods*,[10] Eremets gives some rough guidelines for culet size and corresponding pressure ranges, suggesting that culets 1 mm in diameter are suitable for work up to approximately 20 GPa, 600 μm culets are suitable for work up to about 50 GPa, and culets 200-300 μm are suitable for work up to 100 GPa or more. For routine work above 100 GPa, it is necessary to use a beveled culet, with a small flat region not more than 100 μm in diameter, with a beveled region (θ=7-8.5° with respect to the culet) approximately 300 μm in diameter. All of the diamonds used for this work had flat culets 300 μm in diameter, with the exception of the strontium hydride experiments for which diamonds with flat culets 200 μm in diameter were used. Figure 6 shows some of the different anvil and culet designs discussed in the preceding paragraphs.

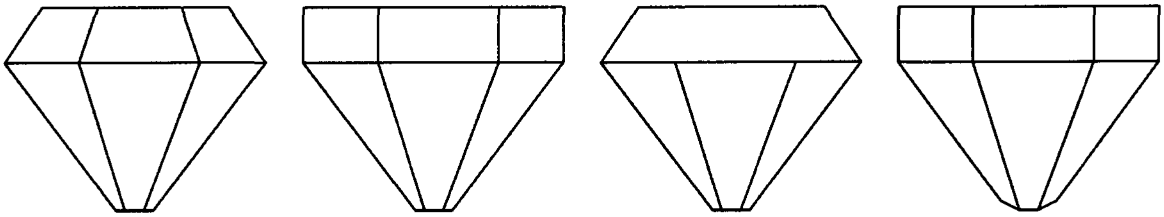

Figure 6: Diamond anvil designs. The first diamond anvils were made from brilliant-cut gemstones (far left), a design that is still commonly used today. The Drukker cut (middle left) features a vertical crown, providing a table with more surface area to bear the applied load. The polished crown of the Boehler-Almax anvil (middle right) bears the applied load, leaving the table open for improved optical access and a wide scattering angle. A beveled culet (far right) is crucial to obtaining ultra-high static pressures.

Gasket

Interestingly, the first report of using a gasket in conjunction with a DAC was in 1965,[11] a little more than five years after the first DACs were constructed. Prior to this, the material of interest was placed directly between the two diamonds. Some of the problems associated with not using a gasket include sample extrusion beyond the culets, inability to study liquids and gases (or to use liquids or gases as pressure-transmitting media), a small range for the compression stroke, and diamond failure due to direct contact between the diamond anvils. The gasket is an extremely important DAC component as it remedies all of these difficulties. It provides a well-defined compression chamber to prevent sample extrusion, it enables the study of liquid and gas phases, it allows the introduction of pressure-transmitting media, the thickness of the gasket gives a larger range for the compression stroke, and it provides both axial and lateral support for the diamond anvils. Gaskets are typically made from hard yet malleable metals. Common materials include hardened stainless steel, Inconel, and rhenium. For all of the research presented here, the gasket material was either ANSI T301 full-hard stainless steel (for pressures up to about 30 GPa) or rhenium (for pressures up to 120 GPa). Additional details regarding gaskets are provided below in the sections associated with sample preparation.

Seats

The direct supports which transfer the force to the anvils are called the seats (see zigzag hatching in Figure 7). The material used for seats is crucial, as it must be able to support the anvils without undergoing too much plastic or elastic deformation when a load is applied—

failure of the seats is a common reason for overall structural failure of the DAC at high pressures. Seats are typically made from either hardened steel or tungsten carbide. The tradeoff is to provide as much support as possible for the diamond, while still providing a reasonable amount of optical access to the sample. Other materials are used for seats in specialized applications. Seats made of low-Z materials such as beryllium or boron are used in some cells designed for x-ray scattering, as they are highly transparent to high-energy x-rays. However, given they are not as hard and rigid as more traditional materials their optical access is typically much smaller so as to provide a larger area to support the diamond table. All of the cells used for the present work were of a hybrid design; one of the anvils was supported by a tungsten carbide seat, providing a large opening for sample viewing and spectroscopic measurements, while the other anvil was supported by a beryllium seat, providing a large x-ray opening for x-ray diffraction experiments. The most common methods for mounting anvils to seats include gluing them directly to the seat, using a retaining ring, or press-fitting. The particular choice of mount depends on a number of factors (for example, sample loading at cryogenic temperatures can cause thermal cycling in the DAC components, disturbing the mounted position of the diamond anvils). In any case, it is extremely important that the surface of the seat, the table, and the culet be parallel to each other for optimum DAC performance.

Cell body

A number of different designs for the actual body of the DAC have been used, depending on the type of experiments to be performed. Here I shall only consider some of the most basic general requirements for the cell body and discuss the particular type used for the experiments described in the following chapters. In general, the cell body must provide a stable, robust platform for supporting the seats. However, the support for the seats must also be adjustable to facilitate the alignment of the anvils. Also, there must be some method to keep the parts of the cell body in proper alignment, even after repeated pressure cycling. Finally, the body must accommodate the mechanism for the application of pressure. The body of the DACs used for this work consists of a tight-fitting piston-cylinder design. The seat/anvil mounted in the cylinder side can be translated to bring it into alignment with the anvil on the piston side. The anvil on the piston side is mounted on a hemispherical seat, allowing tilt adjustment to ensure the culets are parallel (more details on cell alignment are provided in later sections). The DAC accommodates two methods for applying pressure; the piston can be pulled into the body by turning four screws, (this was the method most commonly used) or alternatively, the piston can be driven into the cylinder using a small pneumatic membrane. Figure 7 shows a technical drawing very similar to the DACs used for the experiments presented in this work, detailing many of the components discussed above.

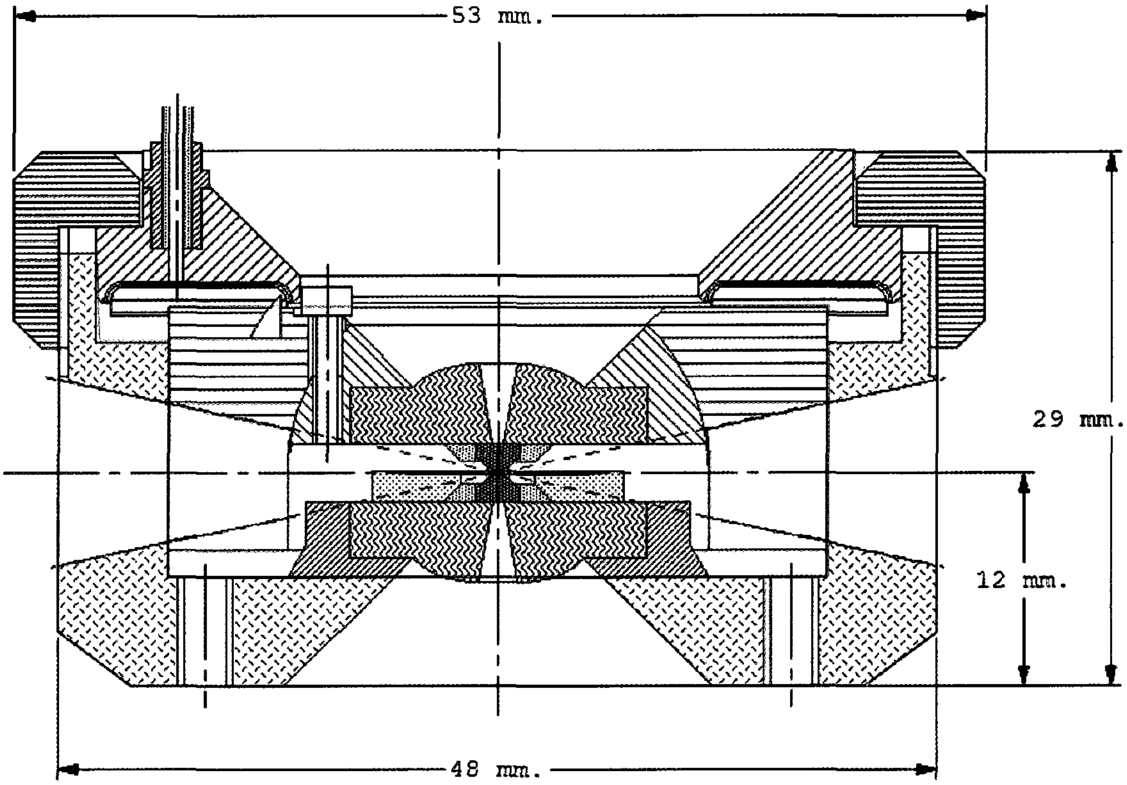

Figure 7: Technical drawing (courtesy of easyLab Technologies Ltd.) of a DAC very similar to those used for the experiments. The red, green, and blue regions correspond to the piston, cylinder, and membrane assembly, respectively (note, however, that the bottom seat assembly is mounted on the cylinder).

In summary, the emergence of the DAC was a seminal event in the history of high-pressure research. An entire branch of material physics which fifty years ago was dominated by a big name is today dominated by a little device. The DAC raised the maximum attainable static pressures by more than an order of magnitude, it substantially increased the number of practicable experimental techniques, and it significantly reduced many of the logistical burdens associated with high-pressure research. Of course, there are some limitations imposed by the DAC, the most obvious of which is the extremely small sample volume—on the order of 10^{-7} cc. For applications requiring larger sample volumes, there is still a place for the hydraulic giants and other moderately-sized pressure cells.

4. Measuring pressure

Although the DAC was immediately recognized as a revolutionary tool for high-pressure research, its widespread use was hindered by one major obstacle—it was extremely difficult to accurately measure the sample pressure. A direct measurement of pressure requires knowledge of the force applied as well as the area over which it is applied. In the case of the DAC, determining the actual applied force is not trivial, but even if the applied force is known, the design of the DAC is such that the applied force is distributed not only over the area of the culet but also to a lesser extent over the supporting structure and cell body. In 1972 Forman and coworkers[12] proposed the pressure dependence of the R-line photoluminescence of ruby (Al_2O_3:Cr^{3+}) could be used to measure pressure. Specifically, they measured the wavelength of ruby luminescence for the R_1-line at several known liquid-solid and solid-solid phase lines of various materials, up to about 2.2 GPa, and found that the shift in wavelength was approximately linear with pressure:

$$\frac{d\lambda}{dP} = 0.364\, nm/GPa \tag{8}$$

Interestingly, almost forty years after its appearance, ruby luminescence remains *by far* the most common method of pressure measurement in DAC applications (at least for pressures below approximately 175 GPa), however the pressure calibration has since undergone a few refinements. In 1978, Mao *et al.* proposed a new calibration obtained by measuring the wavelength of the R_1-line and comparing it against equations of state (obtained from shock wave experiments) for Cu, Mo, Pd, and Ag.[13] They proposed the following:

$$P(\text{GPa}) = \frac{a}{b}\left[\left(\frac{\lambda_0 + \Delta\lambda}{\lambda_0}\right)^b - 1\right];\ a = 1904\ \text{GPa},\ b = 5 \tag{9}$$

where λ_0 is the luminescence wavelength measured at ambient pressure and temperature and $\Delta\lambda$ is the shift in wavelength with respect to λ_0. Equation 9 is still commonly used (and was used for all pressure measurements in the following chapters, save the hydrostatic experiment on barium fluoride). It should be noted that the experiments used to obtain the calibration in Equation 9 were carried out under non-hydrostatic conditions, so the same research group proposed a modification, b = 7.665, for ruby luminescence measured under quasi-hydrostatic pressure conditions.[14] Note that Equation 8 and both modifications of Equation 9 are essentially in agreement up to approximately 15 GPa. Figure 8 compares the shift in the R_1-line as a function of the measured pressure for the three calibrations discussed above, as well as for a recent modification to the *a* and *b* parameters proposed by Dewaele *et al.*[15]

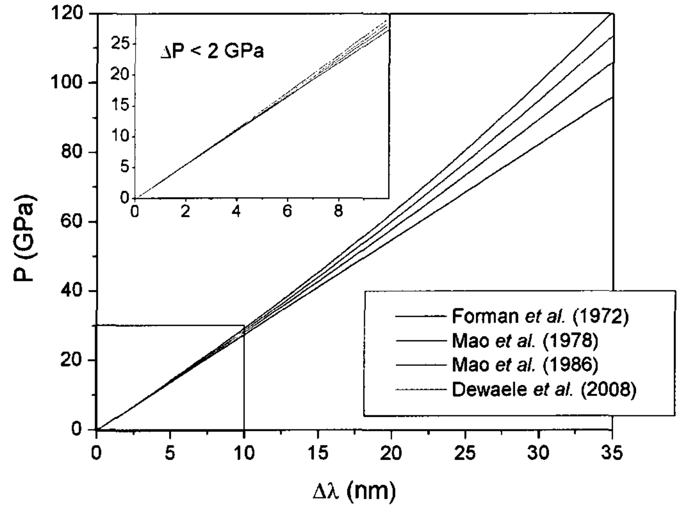

Figure 8: Pressure calibrations for the ruby pressure gauge. For pressures lower than approximately 15 GPa, there is little difference among the various calibrations (see inset). For higher pressures it is important to use the calibration most appropriate, dictated by the hydrostaticity of the sample.

Figure 9 shows the R-line doublet measured at ambient pressure and temperature (left) together with some spectra measured upon increasing pressure (right)

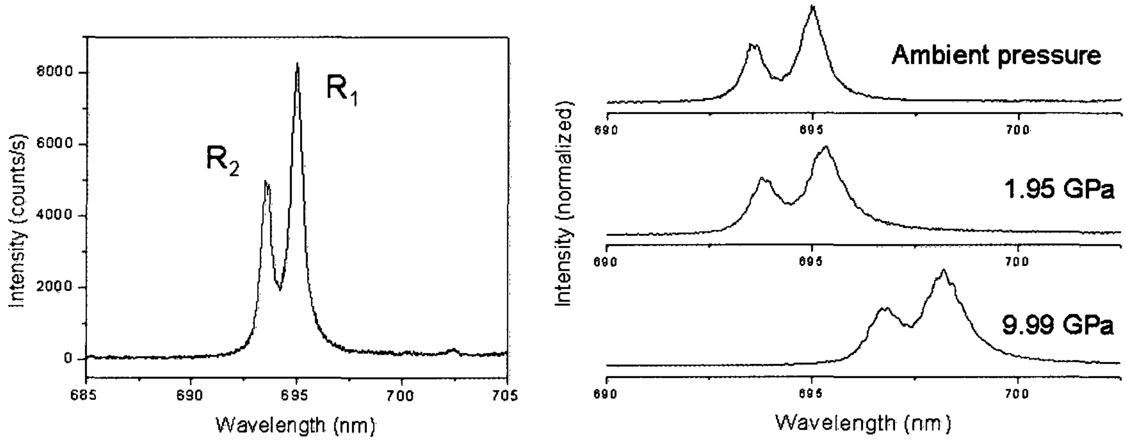

Figure 9: The luminescence of the ruby R-line doublet measured at ambient temperature and pressure (left). The pressure-dependent luminescence wavelength of the R_1 line is used to determine the sample pressure (right).

There are a few challenges associated with the ruby luminescence technique. First, the R-line can undergo substantial strain broadening at higher pressure (particularly in the case of non-hydrostatic pressure conditions) which can make an accurate and unambiguous assignment of the peak position quite difficult. Second, the R-line is temperature dependent, shifting approximately 0.007 nm/K,[16] so care must be taken to minimize heating the sample or gauge, or alternatively, to account for the change in temperature. Note here the biggest risk is actually heating the ruby with the laser used to stimulate the luminescence; laser power should be reduced at the source and further attenuated by filters if necessary, using the minimum power needed to acquire a reasonably intense spectrum. Third, the luminescence wavelength of the R-line is independent of the wavelength used for excitation, but the *efficiency* of the luminescence is not. The absorption band blue-shifts with pressure, so while at ambient pressure ruby can be satisfactorily pumped by a number of different laser lines (for example the 514.5 nm line of an argon ion laser or the 532 nm line of a frequency-doubled YAG laser), at pressures approaching 100 GPa ruby must be pumped using shorter wavelengths (for example the 488 or 458 nm line of an Ar ion laser).

Although not relevant to the research presented in this work, it should be noted that for measuring pressures above approximately 175 GPa, ruby luminescence is no longer reliable. At these ultra-high pressures, the most common method of pressure measurement is to carry out powder x-ray diffraction using an internal standard in the cell (Au and Pt are commonly used). The unit cell volume of the internal standard obtained from the diffraction measurement is compared to equations of state obtained from shock wave experiments to yield the corresponding pressure.

Hydrostatic pressure and pressure transmitting media

In order to make the most appropriate choice among the various calibrations for the ruby pressure gauge, the experimentalist must determine the degree of hydrostaticity in the compression chamber. To achieve the best possible hydrostatic conditions it is necessary to use a pressure transmitting medium (unless the sample material has properties similar to that of an ideal pressure transmitting medium). Nearly all of the data presented in the subsequent chapters were obtained from samples loaded without a pressure transmitting medium. The specific reasons for this are discussed in more detail throughout this work. However, the importance of carrying out experiments under the best possible hydrostatic conditions warrants a brief discussion, including some general remarks about pressure, methods for determining the degree of hydrostaticity in the sample chamber, and finally, common pressure transmitting media together with their approximate maximum hydrostatic pressure ranges.

The thermodynamic variable *P* as discussed in this opening chapter is, more specifically, hydrostatic pressure. It constitutes the special case for which the stress tensor is diagonal (i.e., there are no shear forces present in the system), and furthermore, each of the diagonal elements are equal. Thus the hydrostatic pressure of a system is one-third the trace of the stress tensor. It is a scalar quantity, and is the same throughout the entire system (recall that *P* is an intensive property). If one hopes to compare experimental results against theoretical predictions (obtained in terms of hydrostatic pressure), or similarly, model experimental data using equations of state derived from theory (e.g., the Birch-Murnaghan equation of state), then it is necessary to carry out the experiments under the best-possible hydrostatic pressure conditions.

There are a few common methods for determining if the pressure in the sample chamber is hydrostatic. First, several ruby micro-spheres can be distributed throughout the sample volume and the measured pressure from each ruby micro-sphere can be compared. Clearly, if hydrostatic pressure conditions prevail, the measurements should be in agreement (with appropriate consideration given to the uncertainty of the measurements). Alternatively, the full width at half the maximum intensity (FWHM) of the R_1-line can be monitored as the pressure of the sample is increased. In the case of non-hydrostatic pressure conditions, the non-isotropic strain on the ruby will cause moderate to significant broadening of the R_1-line. (The experimentalist should keep in mind, however, that this broadening could also be brought about by an extremely thin compression chamber leading to the ruby micro-sphere bridging the two diamond anvils.) Finally, the data obtained from the actual sample can indicate non-hydrostatic pressure conditions, for example, strain-induced broadening of x-ray diffraction peaks with increasing pressure.

To carry out experiments under the best possible hydrostatic conditions, it is generally necessary to load the sample together with a pressure transmitting medium. The ideal pressure transmitting medium is a chemically inert liquid, such that the force applied to the system is directly transferred to the material of interest, with no shear forces present in the pressure transmitting medium. Unfortunately, all liquids eventually solidify (at ambient temperature) upon increasing pressure, so the goal is to identify and use liquids which do not solidify up to relatively high pressures, and/or identify solids which do not sustain large shear forces under high pressures. Additional considerations affecting the particular choice of pressure transmitting medium include its possible contribution to the measurement, possible reaction with the sample material, and ease of loading.

After considering several possible candidates as pressure transmitting media, the DAC pioneers at the National Bureau of Standards (USA) proposed a mixture of methanol:ethanol in a ratio of 4:1 by volume.[17] At ambient temperature, the mixture remains liquid up to approximately 10.5 GPa. It was later proposed by Fujishiro *et al.*[18] that adding a small amount of water to the mixture to yield methanol:ethanol:water (MEW) in a ratio 16:3:1 by volume increased the solidification pressure to approximately 14.5 GPa at ambient temperature. MEW is still commonly used as a pressure transmitting medium. It is relatively easy to load, save the experimentalist must exercise some care to prevent from washing the sample and/or ruby out of the compression chamber during loading. Drawbacks associated with MEW include possible reaction with, or dissolution of, the sample material (the hydride samples studied in this work serve as particular examples) and above 10-15 GPa the hydrostatic qualities are greatly diminished such that little is gained by its use.

Another common class of pressure transmitting media is the noble gases. Although at ambient temperature they solidify at relatively low pressures (He has the highest solidification pressure of the noble gases at approximately 12.1 GPa), they remain relatively "soft" to quite high pressures, sustaining only low to moderate shear forces upon compression. In the case of He, sample conditions remain nearly hydrostatic up to 60 GPa or more.[6] Other benefits include limited possibility for reaction with the sample and the opportunity to reduce unwanted signal during measurements (for example, as a low-atomic number material with a high-symmetry crystal structure, He contributes very little to the scattering recorded during x-ray diffraction studies). The primary drawback associated with the noble gases is the difficulty of loading. They must be loaded cryogenically, or they must be loaded at extremely high pressures. The study of barium fluoride presented in Chapter 4 represents an excellent practical example of how using helium as a pressure transmitting medium can greatly improve the quality of the experimental data. More detailed information regarding the choice and use of pressure transmitting media can be readily found in the literature, for example, Jayaraman[6] has tabulated several common pressure transmitting media, including the solidification pressures at room temperature, pressure ranges of nearly hydrostatic behaviour, and remarks regarding ease of use. A more recent work by Klotz *et al.*[19] provides a simple, detailed, and systematic study of eleven different pressure transmitting media including those discussed in this section. In short, helium and hydrogen are by far the most superior pressure transmitting media for maintaining the best possible hydrostatic pressure conditions at extreme pressures.

5. Preparing and loading the diamond anvil cell

I here discuss several general considerations associated with the preparation and loading of diamond anvil cells. However, given the wide range of cell designs and applications, I will discuss these topics in the specific context of the piston-cylinder membrane diamond anvil cells used for the experiments presented hereafter. Figure 7 (shown above in Section 3) details the main components of the DAC used for all of the experiments presented in this work. While somewhat obvious, it should be said at the outset that the first step is to work with the highest quality cell and components possible. The cell should be expertly machined from the most reliable materials, should show no excessive wear or fatigue, and should be in good working order. If these prerequisites are not met, at best the time required to properly prepare the cell may be substantially extended, and at worst it may be altogether impossible to properly prepare the cell. In any case, the best possible outcome for the experiment can be significantly compromised.

Mounting the anvils on the seats

The first step is to mount the diamonds to the seats. The primary goal is to ensure that the culet is well-centred with respect to the optical opening of the seat, and that the table sits perfectly flat on the seat. To ensure the latter, both the seat and the diamond anvil must be perfectly clean, free of any visible debris or residue. If the seat is not already mounted in the cell body, it can be placed in an ultrasonic cleaner with acetone. Otherwise careful cleaning with a cotton swap wetted with acetone should be sufficient. Similarly, the diamond anvil can be cleaned in an ultrasonic cleaner. (Warning to reader: clean only one anvil at a time in the ultrasonic cleaner. *Never* clean two anvils at the same time, nor put any other component in with a diamond anvil. While I have never investigated the consequences myself, others have suggested during casual conversation that anvils have been damaged owing to diamond-diamond abrasion during the cleaning process.) Prior to placing the anvil table on the seat, both should be carefully examined under the microscope to confirm proper cleaning.

If the anvil is to be mounted using a retaining ring, the table can be placed on the seat with the culet centred over the optical access. The ring is then carefully put into position and slowly tightened while constantly checking and double-checking that the anvil remains properly centred (if not centred, one can loosen the ring slightly, reposition the diamond, and then retighten the ring). If the anvil is to be glued to the seat, a small jig must be made to hold the anvil securely in place against the seat during the gluing process. Note that the jig should be transparent to allow the alignment to be examined through a microscope in transmission (a reusable jig can be fashioned out of Plexiglas in a matter of an hour or two). Figure 10 includes an example of the jig used for these experiments. Once the jig is holding the anvil firmly in place, the glue can be applied and allowed to dry, after which the jig is removed.

Diamond anvil alignment

Once the diamond anvils have been properly mounted to the seats and the seats in turn have been mounted in the cell, it is necessary to align the diamond anvils. There are two compulsory aspects regarding alignment: the anvils must be coaxial and the culets must be perfectly parallel to each other. A third aspect that is not compulsory (and may not be feasible, depending on the type of cell and alignment mechanisms) is to ensure rotational symmetry, i.e., the points of the culets are aligned. As mentioned above, for the cells used in this work, the seat mounted on the cylinder side of the cell body allows for translational motion of the diamond to ensure coaxial alignment. The seat mounted on the piston side of the cell body rocks on a hemisphere, permitting adjustments to the culet angle to facilitate parallelism of the culet faces.

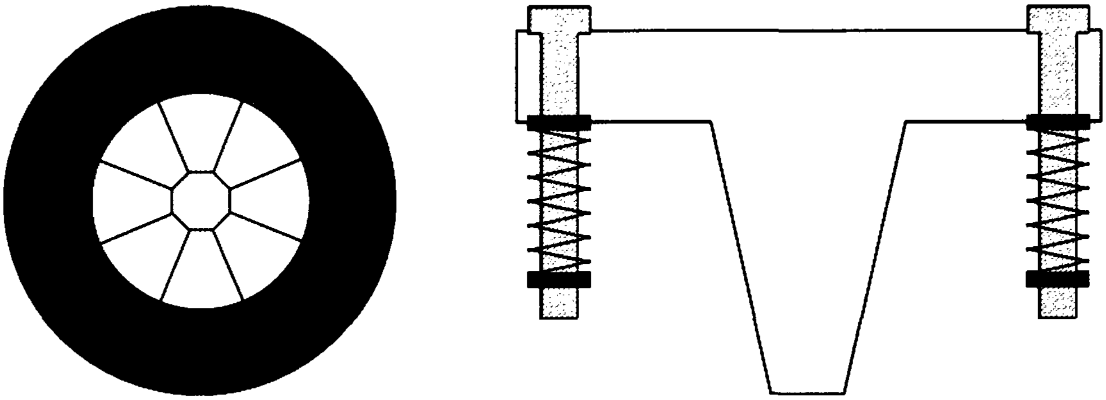

Figure 10: It is imperative that the culet be well-centred with respect to the optical opening of the seat (left) to ensure the applied load is distributed evenly over the table. The particular jig used to hold the anvils in position during gluing (right) is made from a transparent material to facilitate centring of the culet. The jig is tapered to allow side access to the anvils, required for making small adjustments to the anvil position and for gluing. The spring-loaded screws (which correspond to screw holes on the cell body) allow the jig to be carefully lowered without disturbing the anvil position.

The first step is to insert the (properly oriented) piston into the cylinder and bring the culets very close together (not more than 10 μm apart). This is done by observing (through a microscope) the anvils through the side port of the cell body while very gently turning a pressure screw. Extreme caution must be exercised during this procedure, as any contact between the culets can cause damage to the anvils. Once the anvils are at the proper distance, a brake screw (a screw that pushes on the piston the opposite direction of the pressure screw) is used to lock the position of the piston with respect to the cylinder. The cell is now viewed through the load axis—straight through the optical access of both seats and anvils—using both transmitted and reflected light from the microscope. Any translational misalignment will result in bright regions and shadows around the edges of the culets (see Figure 11).

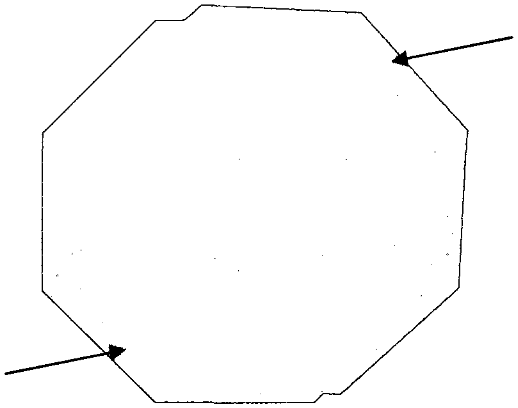

Figure 11: Translational misalignment of the anvils can sometimes be difficult to see under the microscope. Bright regions and dark shadows around the edges of the culet indicate slight misalignment.

The seat mounted in the cylinder of the cell is translated by loosening and tightening two sets of opposing screws until the culets are coaxial. Once they are coaxial the two sets of screws are firmly tightened to lock the seat in place, after which the coaxial alignment is verified (if misaligned during the final tightening of the translational screws, the above process is repeated until satisfactory alignment is achieved).

To ensure the culets are parallel to each other, they are observed under the microscope using monochromatic light (we use a sodium vapor lamp). Any deviation from parallelism will give rise to interference (Fizeau) fringes across the culets—the greater the number of fringes, the greater the misalignment. Figure 12 shows an example of culets that are not perfectly parallel. To correct the misalignment, the number of fringes is minimized by rocking the hemispherical seat in the piston side of the cell. Near-perfect parallelism is indicated by the complete absence of fringes across the culets. Once the fringes have been eliminated and the three screws used to rock the seat have been tightened, the parallelism can be confirmed by gently turning the brake screw to drive the culets apart. If the culets are parallel, one can observe what we call "breathing modes" (not necessarily a technical term); the intensity of the sodium lamp as observed across the culets will alternate from bright yellow to completely extinguished as the anvils are driven apart a few microns.

It should be noted that although the culets may be perfectly parallel to each other, they may not be perfectly normal to the load axis. It is extremely important that the culets are normal to the load axis, as any deviation from the normal can lead to translation of the compression chamber upon application of pressure. Unfortunately, there is no easy way for the experimentalist to verify this aspect of the alignment. I here reiterate that it is of the utmost importance to use a cell that has been expertly designed and machined to exact tolerances, such that the plane of the seat is normal to the load axis (determined by the stroke of the tight-fitting piston in the cylinder). Similarly, anvil suppliers go to great lengths to ensure the table of the anvil is parallel to the culet. These considerations, together with the care exercised by the experimentalist to properly mount and align the anvils, should ensure proper operation of the cell under extreme loads.

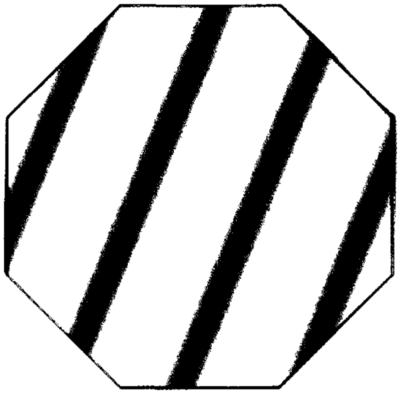

Figure 12: Interference (Fizeau) fringes indicate the culet faces are not perfectly parallel. In this case, three fringes across a 300 μm culet correspond to a misalignment of approximately 0.3°. By eliminating any visible fringes, one ensures the change in distance across the culet faces is less then one-half the monochromatic wavelength. For 300 μm culets and a sodium lamp, this would correspond to the targeted maximum deviation from parallelism, 0.05°.

Gasket preparation

Gasket preparation includes pre-indenting the gasket material, drilling a small compression chamber in the centre of the indentation, and then replacing the gasket on the anvil. For all of the experiments presented in the following chapters, either stainless steel ($P_{max} < 30$ GPa) or rhenium gaskets were used. The initial gasket material is typically 250 μm thick. For pre-indentation, the gasket is mounted atop the anvil on the cylinder side of the cell. Small bits of reusable putty are placed on each side of the anvil, the gasket is placed over the anvil (its edges supported by the putty), and it is then gently pushed down into the putty until it comes into contact with the culet. The piston is inserted such that its anvil is brought into contact with the top of the gasket, after which pressure is applied *via* the pressure screws until the appropriate indentation thickness is achieved.

The target thickness for the indented portion of the gasket is not less than 50 μm, but not more than 90 μm. There are a few different methods for estimating the indentation thickness during the actual indentation process. The method I used was to measure the width of the gasket extrusion shadow against the pavilion of the anvil. Specifically, as the anvil is driven into the gasket material, one can observe the edge of the gasket material (shown in Figure 13) moving up the pavilion. By measuring the distance between these edges on opposing sides of the pavilion, one can make a reasonable estimate of the indentation thickness. Of course, this must be initially calibrated by making indentations of different thicknesses and comparing the measured thicknesses against the distance between the edges measured across the pavilion; an example of this calibration in shown in Figure 13. The final gasket thickness is measured by removing the gasket from the cell and measuring directly with a small micrometer (precise to within 1 μm).

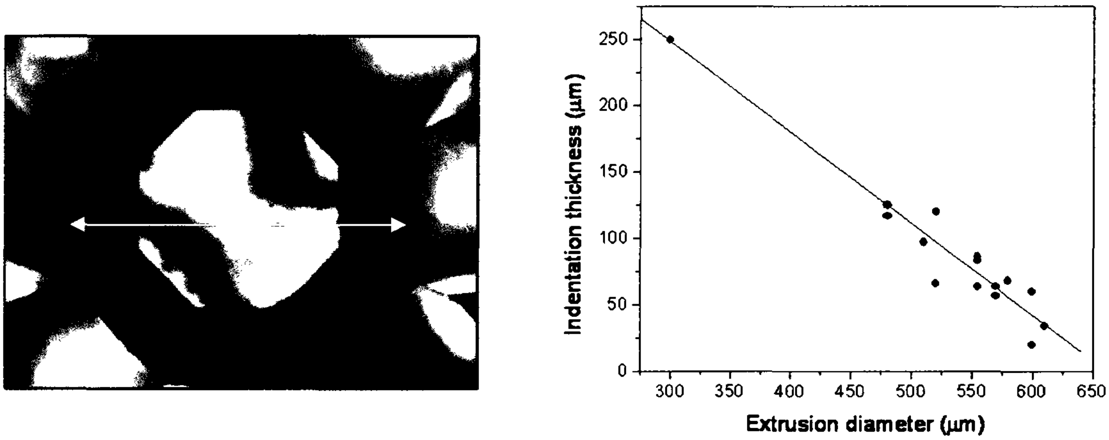

Figure 13: An estimate of the gasket indentation thickness can be made during the indentation process by measuring the extrusion diameter of the gasket material against the anvil pavilion (left) and comparing it to a calibration of gasket thickness *vs.* extrusion diameter obtained from several gasket indentations (right).

Gasket indentation accomplishes some very important goals. First, it cold-works the indented material, significantly increasing its hardness. This is important as the walls of the compression chamber must sustain extreme pressures. It is not uncommon for the pressure limit of an experiment to be dictated by sample extrusion through a failed gasket wall. Second, during indentation the gasket material flows out of the region between the culets and causes the gasket material to rise up around the pavilion of the anvils (see the raised portions of the gasket as depicted in Figure 5). This provides additional lateral support for the anvils. Gasket indentation is the key to reaching extreme static pressures with a DAC.

It is important to verify that the alignment of the cell holds throughout the indentation process. After the initial alignment of the cell, the first indentation should be done in iterative steps. The gasket should be indented about half way, the gasket is then removed and the alignment of the cell is verified, then the gasket is replaced and fully indented, after which a final check of the cell alignment is made. If the alignment does not hold, the experimentalist is compelled to start again with the alignment process and discard any gasket indentations made using a previous alignment.

Following indentation, the next step is to drill the compression chamber. As a rule of thumb generally accepted by DAC practitioners, the diameter of the compression chamber should not exceed approximately one-third the diameter of the anvil culet. Small, commercially manufactured precision tungsten carbide bits ranging from 75-150 μm were used. It is not possible to use a conventional drill press as the rotating head would introduce an intolerable degree of wobble in the tip of the bit. Instead the bits are mounted against V-grooves. A small rubber belt serves the dual purpose of keeping the bit securely against the V-grooves and turning the bit for drilling. For the stainless steel gaskets, precision mechanical drilling was used. The bit is lowered by way of a mechanical lever driven by turning a fine-thread screw. The compressed rhenium is too hard for mechanical drilling, so instead the chamber is "drilled" by electronic micro-spark erosion. Again, the bit is held in place against V-grooves by a rotating belt, but the bit is lowered by a computer-controlled actuator, using a LabView Virtual Instrument code.[20] The rate at which the bit lowers depends on feedback of the discharge voltage between the bit and the gasket.

While it perhaps goes without saying, great care must be exercised to ensure the hole is drilled in the centre of the indentation. The bit must be brought as close as possible to the gasket surface while its position is observed under a microscope. A stereoscope is ideal, as it provides the experimentalist with some depth perception. Alternatively, a monocular scope can be used, but the bit must be observed through the scope at various angles to ensure proper alignment in all directions.

After indentation and drilling, the final step is to replace the gasket atop the anvil on the body side of the cell. Prior to replacing the gasket, it must be cleaned thoroughly in an ultrasonic cleaner to ensure it is clean and free of any oil or debris from the drilling process. It is crucial that the gasket is replaced in the same orientation used for indentation (to facilitate this, a small mark can be scribed at one corner of the gasket, corresponding to an identifying mark on the cell body). Again, the putty is placed on either side of the anvil and the gasket is gently pushed down against the anvil. The gasket must be viewed under the microscope to ensure it is in contact with the culet and the indentation is perfectly coincident with the culet. Any positioning error should be visible due to the sharp angles on the gasket indentation. If there is a small discrepancy, the gasket can be gently nudged into position. If there is a large discrepancy, the gasket should be removed and cleaned, and the process should be repeated until the gasket is properly positioned. Once the gasket is indented, drilled, and properly seated against an anvil, the sample can be loaded.

Sample loading

The particular method employed for sample loading depends on a number of factors including the nature of the material to be loaded, as well as whether or not the material will be loaded with a pressure-transmitting medium. The heavy alkaline earth hydrides are extremely sensitive to moisture in the atmosphere, so they were loaded in an inert, argon atmosphere, and furthermore no pressure-transmitting medium was used. Below I discuss the specific procedure used for this work, however many of the more general concepts apply to loading other types of materials.

The first step in the sample loading procedure is to place a small piece of ruby in the compression chamber. Typically, experimentalists use chips ground from a large ruby, however, there are some associated difficulties. First, it is not always easy to properly judge the dimensions of a ruby chip. The length and width may appear acceptable under the microscope, but the height may well exceed the height of the compression chamber, so the experimentalist is compelled to carefully examine the chip in all dimensions prior to placing it in the compression chamber. Furthermore, if the sample material exhibits visible domains and boundaries, it can be difficult to locate the chip for pressure measurements if its position is disturbed during sample loading. I was fortunate to have access to small ruby spheres (10-15 μm in diameter) which eliminated both of these difficulties: it is easy to judge their volume (based on their diameter) while viewing under the microscope, and they are easily identifiable in a loaded sample. A sphere is picked up and placed in the compression chamber using a custom tool consisting of a dowel with an etched copper wire taped to the tip. Once the ruby is in place, the wavelength of the R-line at ambient pressure, *viz.*, λ_0, is measured.

For loading under an inert atmosphere, a medium-sized commercial glove bag was used. The glove bag was fitted with a vacuum line for purging, a gas line for inflating the bag with argon, and an optical fiber bundle for reflection illumination of the cell under a small stereoscope (also placed in the glove bag). All necessary loading components are cleaned and placed in the bag. Necessary components include the DAC cylinder and piston, pressure screws with key, sample vial, loading tool, packing needle, and tweezers. The bag is sealed using hand clamps, after which the atmosphere is repeatedly vacuum purged and refilled with argon. After four or five purging cycles, the sample vial is opened and the tweezers are used to put an exceedingly small amount of material on top of the gasket, well away from the compression chamber. The sample material is observed under the microscope with the goal of identifying a single, polycrystalline aggregate with the approximate volume of the compression chamber. The aggregate is picked up with (or alternatively pushed by) the loading tool and gently placed in the compression chamber. At this point some caution should be taken, as removal of the aggregate from the compression chamber carries with it the risk of also removing the ruby sphere used for pressure measurements. The aggregate is gently packed in the chamber using a needle, and if it appears that the chamber is not filled, additional, smaller aggregates can be added. Once the compression chamber is filled, the loading tool can be used to gently remove any small pieces of sample material that may be littering the gasket indentation.

Once the compression chamber is filled and the indentation is free of debris, the piston can be gently inserted into the cylinder. Before making contact between the piston anvil and the gasket, the pressure screws should be inserted and turned a few threads to ensure proper alignment of the piston with respect to the cylinder, after which the piston can be slowly driven into the gasket by hand. The screws can then be tightened just to the point that mechanical resistance is first met. Then, while viewing the sample through the microscope, the screws are further turned ever so slightly in an attempt to apply pressure to the sample. The first visual signs of pressure include the appearance of a bright, smooth gasket and a slight shrinking of the compression chamber diameter. The former indicates firm contact between the culet and the gasket, while the latter is the result of the chamber being not completely filled, so the gasket extrudes into the sample chamber to fill any empty space. It is critical that some pressure be applied to the sample to ensure the sample chamber is sealed; this prevents the atmosphere from reacting with and contaminating the hydride. However, for the purposes of a complete data set, it is important to apply the lowest possible pressure, ideally well below 1 GPa.

Upon completion of the loading procedure, the pressure is immediately measured to verify that some pressure has indeed been applied to the sample. The sample quality is then verified by obtaining a Raman spectrum. While I do not discuss this last step in detail here, let it suffice to say that prior to the high-pressure experiments, Raman spectra were obtained from hydrides prepared in sealed capillaries at ambient pressure. The capillary samples were then exposed to moisture in the ambient atmosphere, after which additional Raman spectra were obtained, providing a comparison of pure and contaminated hydride. Figure 14 shows a loaded sample of barium fluoride (note this is not immediately after loading but rather at a pressure of approximately 80 GPa, showing an example of the gasket extrusion which dictated the maximum pressure for this sample).

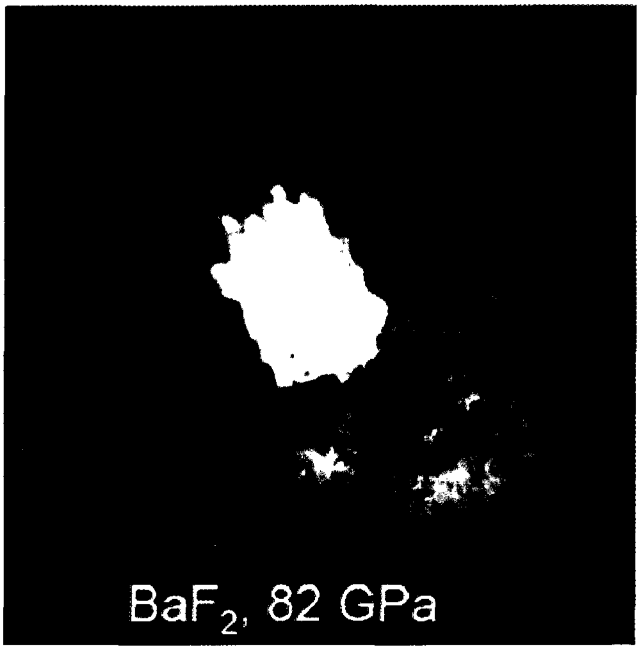

Figure 14: A sample of BaF_2 at high-pressure. The bright portion is the actual sample (made bright by transmitted light from underneath the DAC). The compression chamber (initially round) has extruded somewhat toward the upper-left edge of the culet. The ruby sphere is visible in the lower-left part of the sample, against the compression chamber wall. Some sample material (not properly removed during loading) *can be seen on the gasket surface. The blurry regions near the culet edge* are due to elastic deformation (curvature) of the culets under extreme pressure. Scale: culet is 300 μm in diameter.

If, by chance, this section detailing DAC preparation and sample loading has seemed somewhat long and tedious for the reader, I here offer as a slight comfort the assurance that the actual process is exceedingly long and tedious for the experimentalist. Regardless of how much one pores over the available literature, there is no substitute for the experience gained by sitting at the microscope and confronting the challenges associated with working on the scale of microns. While there is no quick, easy way to prepare and load a DAC, no part of the process is magical. With a steady hand, a little experience, and a lot of patience, one can prepare high-quality samples. With a loaded cell in hand, one is ready to explore the structure of materials submitted to extreme pressures.

6. Angle-dispersive powder x-ray diffraction using synchrotron radiation

The need for synchrotron radiation

While above I have gone to some effort to praise the virtues associated with the DAC, there are corresponding limitations, and here I consider some of these with respect to x-ray diffraction. First, the diamonds can absorb a substantial percentage of incident and diffracted x-rays. A pair of 1.5 mm-thick diamond anvils will absorb about 99% of the photons generated by a conventional copper x-ray tube. Also, the anvils' supporting structure severely limits the available reciprocal space. The cells used for this work offer about 30° 2θ (which is relatively large compared to that offered by the majority of DACs). Also, the sample volume is minute, on the order of 10^{-7} cc. In short, there just isn't much material to scatter from.

The degree to which synchrotron radiation mitigates these difficulties is remarkable. First, synchrotron radiation permits the use of high-energy (hard) x-rays. The benefit is two-fold. First, the diamond anvils become highly transparent to incident x-rays at high energy, and second, looking at the Bragg equation,

$$n\lambda = 2d\sin\theta \tag{10}$$

it is clear that the scattering from a particular set of lattice planes (spaced a distance *d* apart) will fall at smaller angles 2θ for higher energies (equivalently, shorter wavelengths). This two-fold benefit is shown graphically in Figure 15.

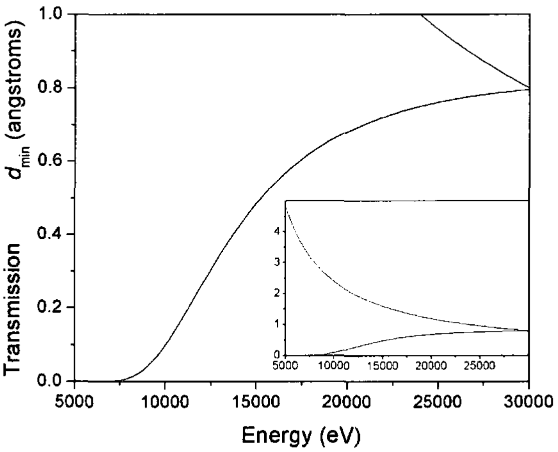

Figure 15: X-ray transmission through a pair of 1.5 mm diamond anvils (black) and minimum lattice spacing, or *d*-spacing, measured at 30° (red) as a function of energy. The hard x-rays available at synchrotron radiation sources mitigate both the absorption due to diamond and the limited scattering range available with a DAC.

Another great advantage offered by synchrotron radiation is the sheer number of photons incident on the sample. There are a couple of factors which account for this. To start, there are simply many photons generated at the source (from bend magnets, wigglers, or undulators), but moreover, the divergence of the radiation from the source is small. Radiation produced by the acceleration of a non-relativistic particle (hereafter, an electron will be used for discussion) is distributed over a large surface (i.e., it is radiated in almost all directions), but the radiation produced by the acceleration of a relativistic electron is distributed over a very narrow cone, normal to the direction of acceleration and parallel to its velocity (e.g., the plane of orbit of the electron in the case of a synchrotron source). For instance, the electrons in the synchrotron storage ring at the Canadian Light Source are traveling at approximately 99.9997% the speed of light. At this speed, the divergence is on the order of $1/\gamma$ ($=m_0c^2/E_{Particle}$), or just over 0.1 mrad. These combined factors, namely the production of many photons with small divergence from the source, result in orders of magnitude more flux (number of photons per unit time per unit area) incident on the microscopic samples contained in the DAC as compared to laboratory sources. Figure 16 shows the on-axis brilliance (closely related to photon flux) for several different synchrotron radiation-producing devices and compares it to that emitted from conventional x-ray tubes with copper and molybdenum targets.

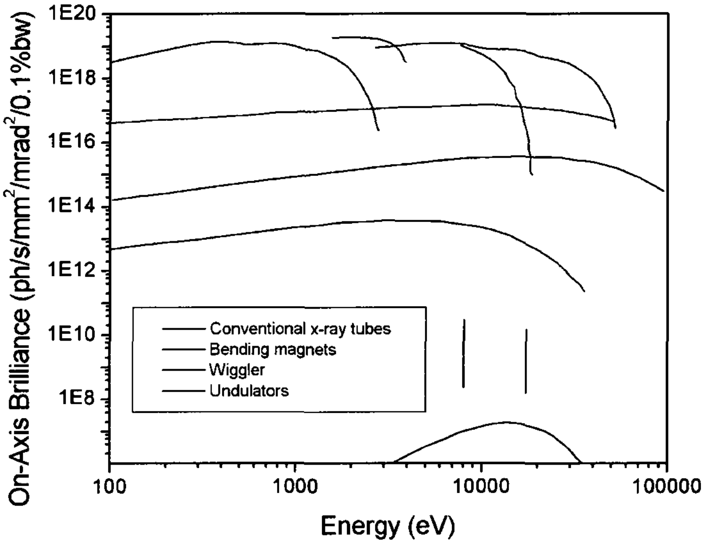

Figure 16: Synchrotron radiation sources offer orders of magnitude more photons (over the continuous spectrum) than conventional x-ray tubes with copper (vertical bar at ~8000 eV) or molybdenum (vertical bar at ~18,400 eV) targets. Note the black curve at the bottom of the plot is the continuous spectrum (Bremsstrahlung) from a conventional tube.

It should be noted that the high flux offered by synchrotron radiation is over the continuous spectrum. Keeping in mind the limited angular opening of the DAC, prior to the early 1990's, the primary method of high-pressure x-ray diffraction using synchrotron radiation was energy-dispersive. Specifically, an energy-discriminating detector would be positioned at a fixed scattering angle, and the continuous spectrum would scatter from the sample. From the Bragg equation above, it is clear that if the (fixed) scattering angle and the incident energy are known, the corresponding *d*-spacings of the crystal lattice can be obtained. The primary difficulty with energy-dispersive powder x-ray diffraction is the poor energy resolution of current detectors. Experimentalists could certainly identify a phase transition, perhaps obtain the unit cell of the high-pressure phase, and even study the pressure dependence of the volume, but crystal structure determination and the observation of subtle changes in the crystal structure were difficult, if not impossible.

Imaging plates

In the early 1980's, the imaging plate (a type of area detector) was introduced in the context of medical computed radiography.[21] Imaging plates consist of rare-earth doped phosphors which create colour centres when struck by x-rays. These colour centres can subsequently be stimulated by laser irradiation; the broad excitation spectrum for these colour centres is centred in the red, close to the emission wavelength of a HeNe laser, while the radiation emitted from the colour centres is in the in the blue, narrowly centred around 400 nm. This appreciable difference between the stimulation and emission wavelengths facilitates the intensity measurement of the emitted light. The image plate can be erased by exposing it to white light (to stimulate any colour centres remaining after the readout process) and can be reused. Imaging plates have a large dynamic range (e.g., 16 or 17 bits), a remarkably linear response, and can be scanned at high spatial resolution (small pixel size). The synchrotron radiation community was quick to take advantage of these benefits. In the field of high-pressure x-ray crystallography, imaging plates brought about a monumental shift from energy-dispersive methods to angle-dispersive methods.

Imaging offers several advantages discussed in some detail in Chapter 6, but I here point out some of the main advantages. First, even though the incident flux on the sample is significant, it does not change the fact that the scattering volume in the DAC is extremely small, and therefore there just aren't enough crystallites in the sample to ensure proper scattering statistics. By capturing entire Debye rings, the total intensity around a given Debye ring can be summed, yielding a more accurate intensity per unit length of the ring. Second, imaging gives the experimentalist immediate information about the quality of the sample, including the degree of random orientation among crystallites, number of phases contained in the DAC, strain broadening of reflections, and preferred orientation of crystallites, all of which provide useful information which may not be immediately appreciated when looking at a conventional intensity *vs.* 2θ pattern. Figure 17 shows an example of an image obtained from barium compounds at high pressure, detailing some of the very phenomena mentioned above.

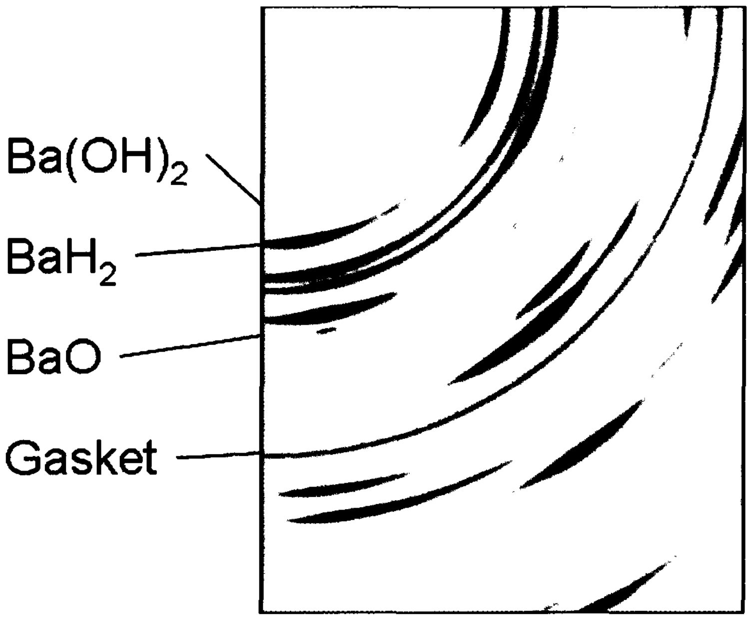

Figure 17: A portion of an x-ray diffraction image of barium compounds. Imaging is a powerful tool, as it facilitates the identification of multiple phases within a sample. In this case, the Debye rings from $Ba(OH)_2$ are faint, continuous, and diffuse; rings from BaH_2 exhibit marked changes in width and intensity; the ring from BaO is narrow, well-defined, and somewhat grainy; the ring from the gasket is broad and continuous.

Experimental configuration

The great majority of the diffraction results presented in this work were obtained at the Hard X-ray MicroAnalysis (HXMA) beamline at the Canadian Light Source (CLS, Canada). The works on calcium hydride and barium fluoride also include results from the National Synchrotron Light Source (NSLS, USA) and Super Photon ring-8 (SPring-8, Japan), respectively. I should note here that my first experiences as a synchrotron radiation user were at the Cornell High-Energy Synchrotron Source (CHESS, USA). Although results obtained at CHESS are not included in this work, much of the experience gained there has been useful for the present work. I here focus on the experimental configuration at the CLS, as I made significant contributions to the design, installation, and implementation of both hardware and software used to carry out all of the high-pressure powder x-ray diffraction experiments performed there to date.

The radiation source at HXMA is a 63-pole superconducting wiggler (a device which uses alternating magnetic poles to "wiggle" the electrons, providing the acceleration which gives rise to the emission of synchrotron radiation). The radiation produced by the wiggler passes through two hutches (radiation enclosures housing all optics and equipment in the beam's path), namely the optics hutch and the experimental hutch. The optics hutch contains permanently installed equipment maintained and operated by the CLS staff. It houses several general components including slits for defining the rough beam dimensions, cameras for monitoring beam position (as seen when transmitted through crystals which emit visible radiation when struck by high-energy x-rays), and filters for attenuating the beam intensity. The central components of the optics hutch consist of three specialized pieces of equipment used to condition the beam for experimental work. The first is a large plane-parabolic mirror used to collimate the incoming beam in the horizontal plane. The surface of the mirror consists of two metal strips, made of rhodium and platinum. The former is well-suited to reflect x-rays with energies less than approximately 22 keV, while the latter is used for x-rays with energies greater than approximately 20 keV. The purpose of the collimating mirror is to achieve the maximum efficiency out of the second of the three major components, the fixed-exit double-crystal monochromator. As the name suggests, the monochromator is used to select the desired wavelength of monochromatic radiation for x-ray diffraction. The available crystal pairs are the (111) and (220) crystals of silicon. The wide rocking curve of the (111) crystals offers higher flux, while the narrow rocking curve of the (220) crystals offers higher resolution.[22] The range of energies available for each crystal pair is limited by design and engineering. In selecting the energy (equivalently, the wavelength) to carry out the work presented below, the compromise was made to use the (111) crystals at the maximum design energy of approximately 24 keV, yielding high flux, acceptable energy resolution, and a sufficiently short wavelength (~0.5 Å). The final component is a toroidal mirror, again with both Rh and Pt strips, used to focus the beam. The mirror has a fixed curvature to focus the beam horizontally, and can be bent (adjustable) to control vertical focusing. From this last mirror the beam passes through a small beam pipe a few meters long into the experimental hutch, which contains all of the pertinent equipment needed to carry out high-pressure x-ray diffraction. A schematic diagram of the primary elements described above is presented in Figure 18.

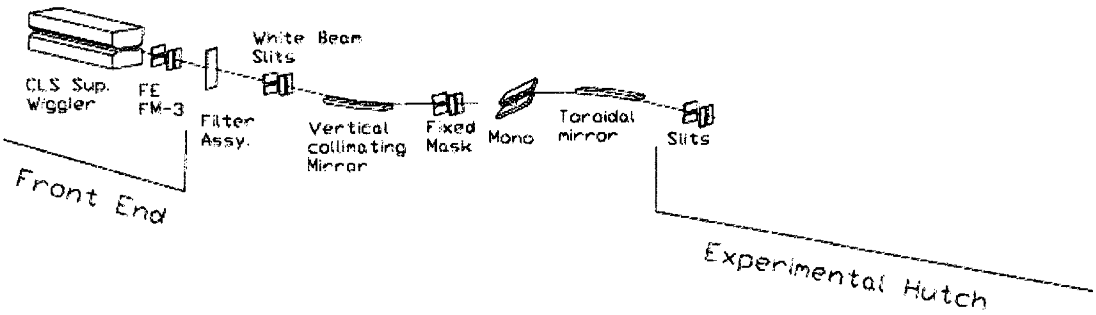

Figure 18: Permanently installed equipment which determines the general HXMA beamline characteristics. The 63-pole superconducting wiggler is housed in the front end. Between the front end and the experimental hutch is the optics hutch, which houses generic components used to control the beam size, position, and intensity, as well as specialized components used to focus and monochromatize the incident beam. Diagram courtesy of the Canadian Light Source, Inc.

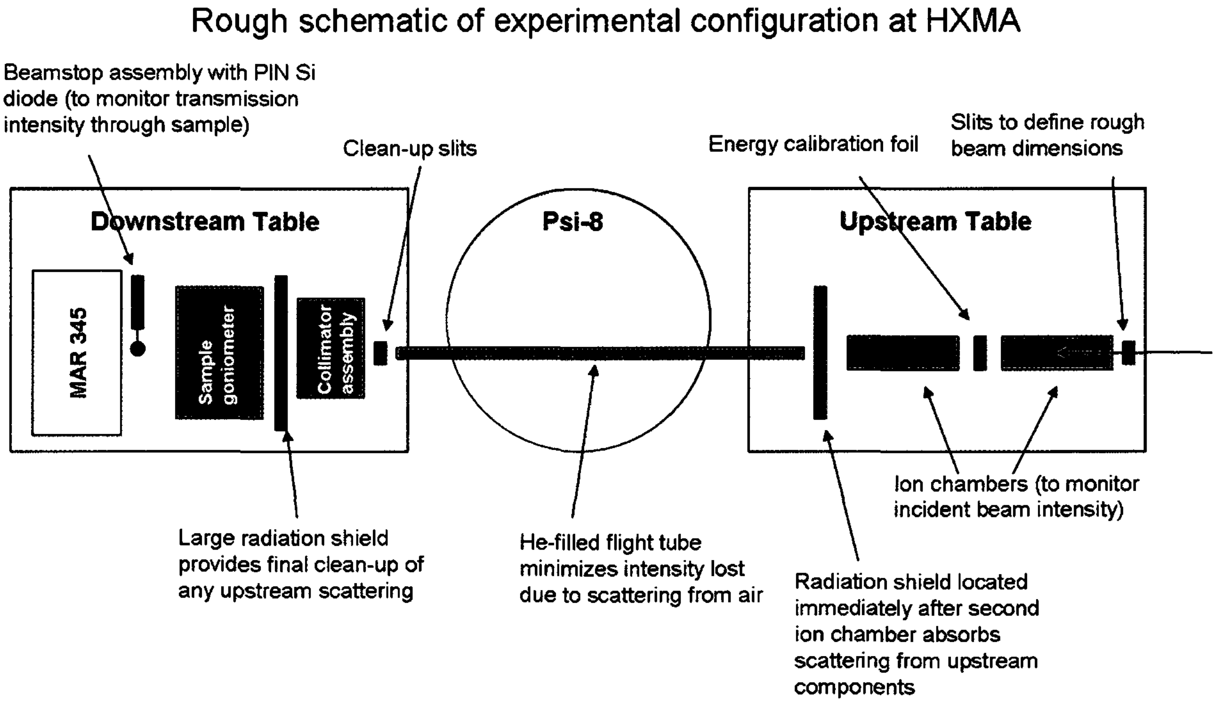

Figure 19: Basic components comprising the most recent equipment configuration in the experimental hutch. The total length from point of entry into the hutch to the Marresearch mar345 image plate detector is approximately 7 m.

The primary goal of the equipment configuration in the experimental hutch is to maximize scattering from the sample while at the same time minimizing scattering from all other sources. While some of the specific components in the configuration have changed over the past few years, the basic components and concepts have remained. Figure 19 shows a schematic of the configuration.

Upon entering the experimental hutch, the beam first encounters a set of motorized slits that serve to cut the beam dimensions down to a small square (generally 0.5x0.5 mm^2) and to absorb any stray scattering from the upstream optics. From there it travels through two ionization chambers used to monitor the intensity of the incoming beam. The purpose of having two ion chambers is to allow for energy selection. This is done by placing a thin, elemental calibration foil between the two chambers and scanning the motorized angle, and thus wavelength or energy, of the double-crystal monochromator. By monitoring the intensity of the respective ion chambers, the absorption edge of the foil can be used to correlate incident photon energy with motorized monochromator angle. Figure 20 shows an example of a measured absorption edge.

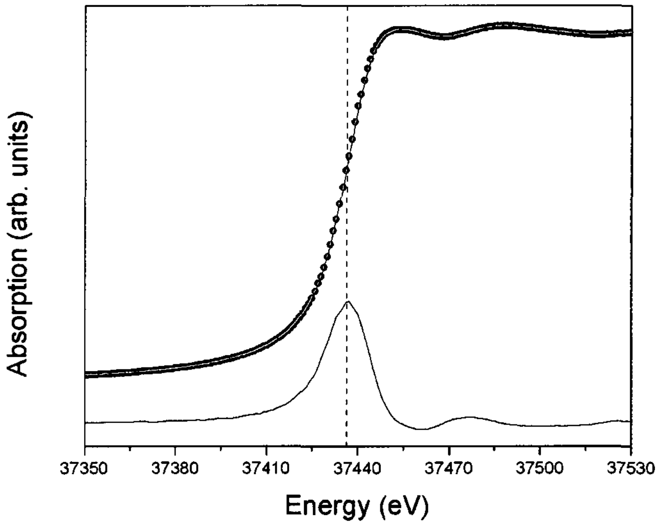

Figure 20: *K*-edge absorption spectra (such as this one obtained from barium fluoride powder) are used to calibrate the incident x-ray energy (equivalently, wavelength). In this plot, the measured data points (symbols) are smoothed (red curve) by adjacent averaging of a few points. The *K*-edge is defined (in this case) by the inflection point (the stationary point in the first derivative plot, shown by the blue curve) of the smoothed edge data.

By carrying out this process for several elements, the monochromator can be calibrated. We typically verified the calibration by scanning a foil with an absorption edge near (or at) the desired energy for the experiments (e.g., Pd with a *K*-edge at 24.350 keV), and checked the results against the beamline calibration. Following the ion chambers, the beam next passes through a beam pass (this is simply a He-filled pipe which maximizes transmission of the beam to the sample by minimizing the scattering from air), a second set of slits, and a radiation shield (again, to minimize stray scattering) before passing through a small, square-aperture collimator. Three sizes of custom-designed collimators were used, 15x15, 30x30, and 45x45 μm^2. These are constructed by sandwiching small foils of the desired thickness between two 1.4 mm-thick half-rounds of tungsten carbide, held together by a heat-shrinkable metal collar, to form slits. Two slit assemblies are brought together at right angles to create the aperture, shown in Figure 21.

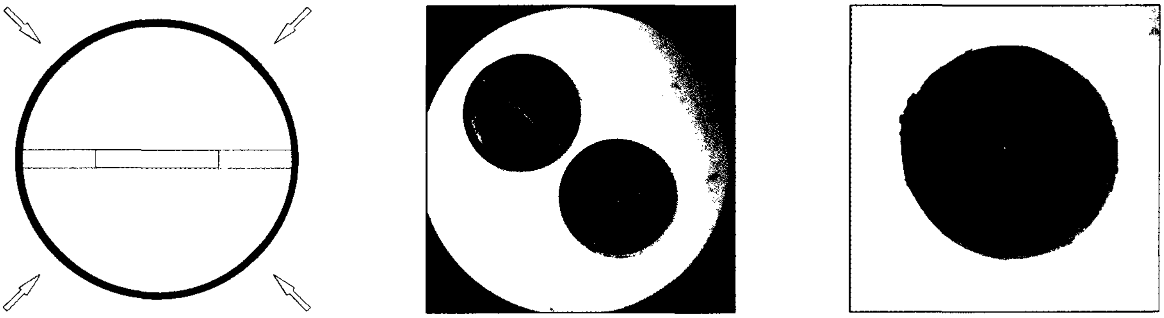

Figure 21: Custom-designed x-ray collimators. A slit of the desired width is made by sandwiching pieces of thin foil between two half-rounds; the assembly is held together tightly by a heat-shrinkable metal collar (left). Two of these assemblies are oriented with the respective slits normal to each other (centre), and are stacked to create a square aperture defining the final collimator dimensions (right). Collimator shown at right is approximately 3 mm in diameter, with a 30x30 μm^2 square aperture.

After leaving the collimator, the beam next encounters the sample in the DAC. Following the sample, a beamstop assembly is used to protect the detector from the intense transmitted beam. The beamstop is fitted with a small PIN Si diode, connected to a current amplifier, to monitor the intensity of the transmitted beam. The last component is the imaging plate. For the earlier works (the calcium and barium hydride studies presented in Chapters 2 and 3) a bare imaging plate was held in place on a flat vacuum plate (visible in Figure 22), and after exposure it was taken to a nearby scanner to obtain an image file. For the latter works (the barium fluoride, strontium hydride, and the centring and rocking studies presented in Chapters 4-6), a fully integrated imaging plate system, the Marresearch mar345 detector, was used (visible in Figure 23). Photographs showing many of the relevant components discussed above are presented in Figures 22 and 23.

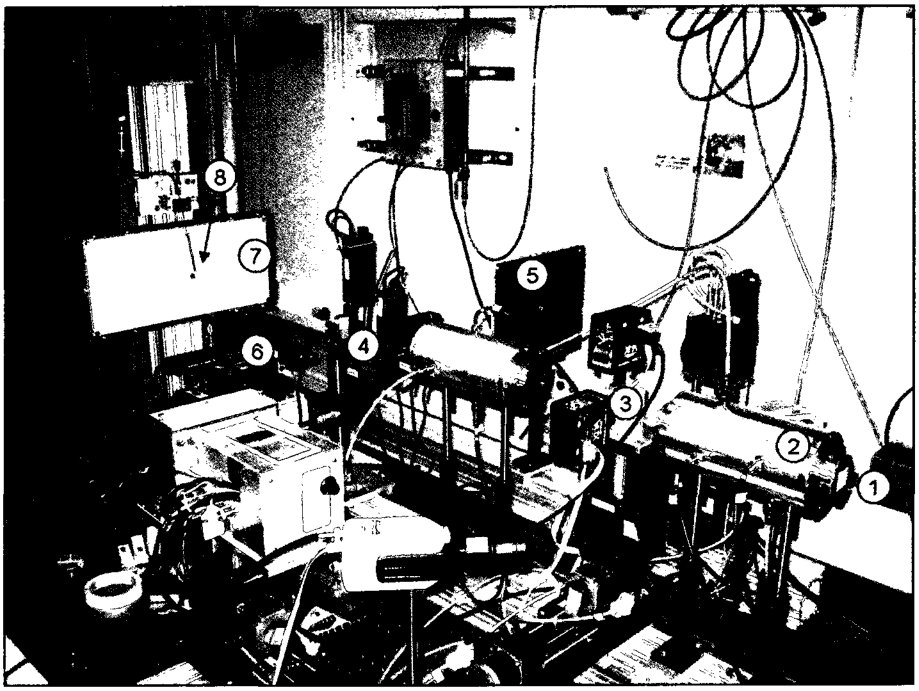

Figure 22: A photograph (first-generation configuration) showing some of the components in the experimental hutch, including (1) the location of the slits used to define the beam, (2) ion chambers, (3) calibration foil, (4) collimator positioning assembly, (5) radiation shield (off-line), (6) sample goniometer (without mounted DAC), (7) imaging plate mount, and (8) beamstop assembly with diode.

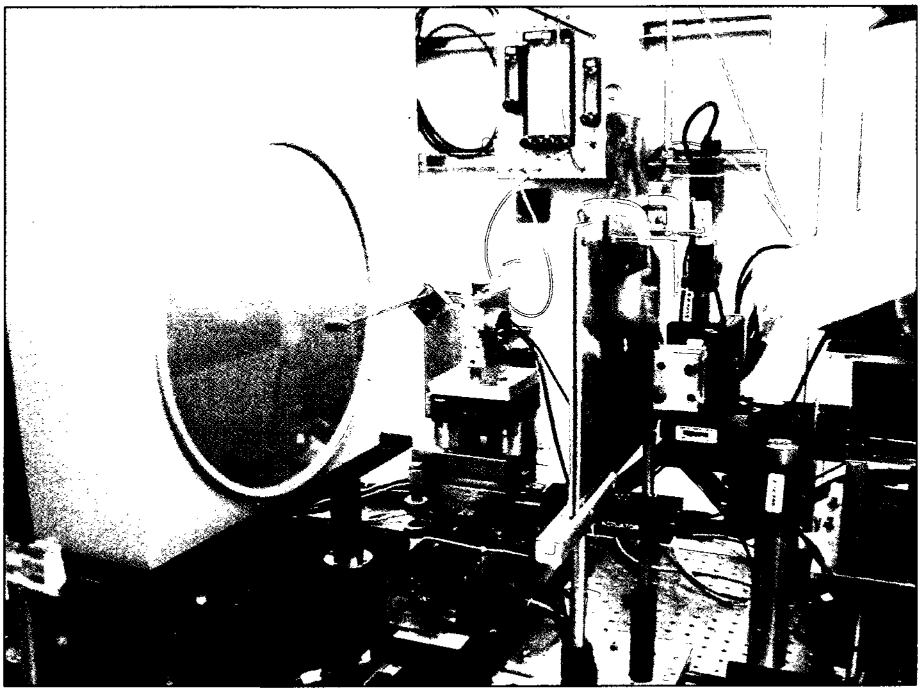

Figure 23: A photograph (second-generation configuration) showing some of the same equipment above as well as the mar345 imaging plate detector. Note that the collimator is visible (the short brass rod on the collimator positioning assembly), and a DAC (with thermocouple) is mounted atop the sample goniometer.

Installing the experimental equipment

While I do not offer here a complete description regarding the installation and alignment of all of the various components of the experimental configuration, a brief description of the general strategy and procedure is perhaps appropriate. At the outset, I should point out that I frequently refer to *scanning* a component. This simply consists of translating (or sometimes rotating) a component in small, discrete steps while measuring the transmission of the x-ray beam through the component by means of an ion chamber or diode downstream. Scans are done successively in the vertical and horizontal directions normal to the beam, with the purpose of eventually positioning the component in the most intense region of the incident x-ray beam. A screenshot from a LabView Virtual Instrument code used to scan various components is shown in Figure 24.

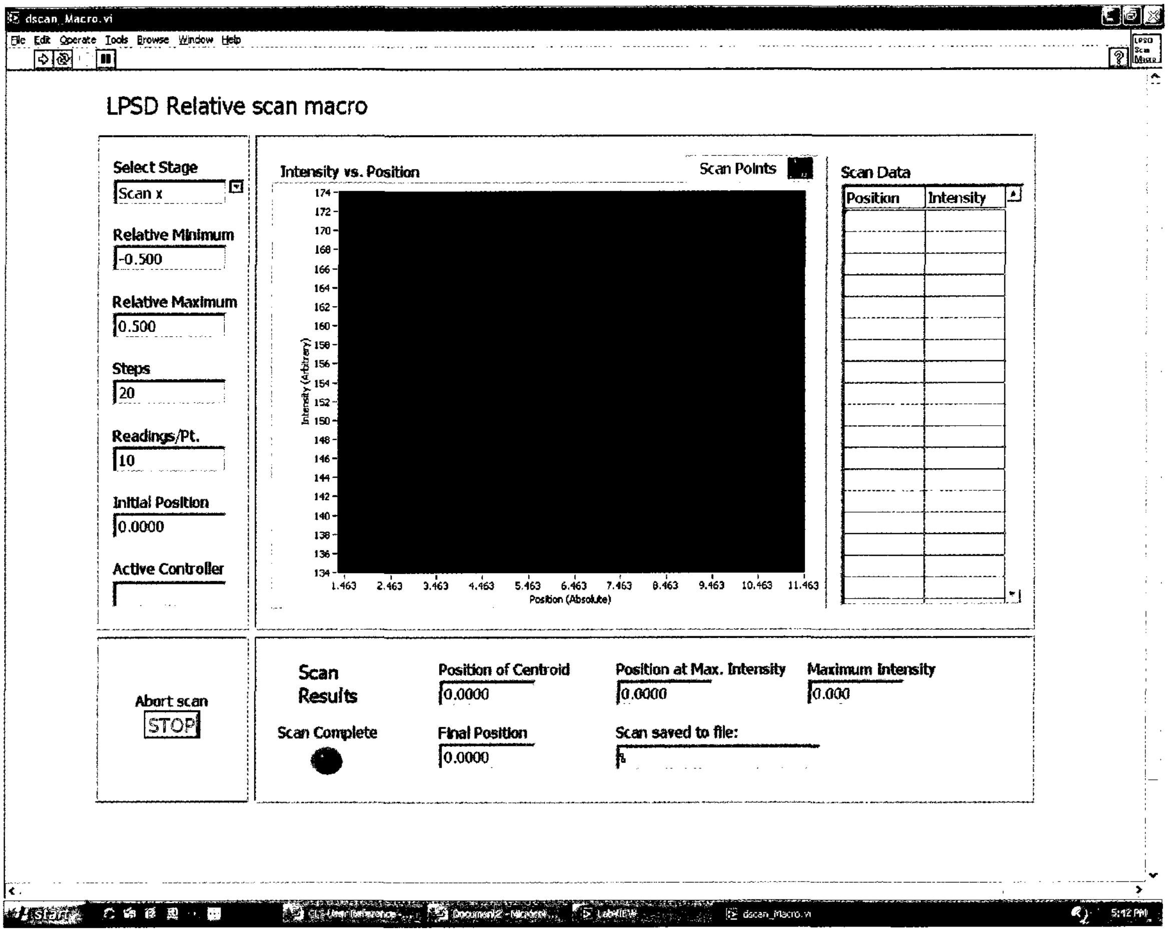

LPSD Relative scan macro

Select Stage: Scan x

Relative Minimum: -0.500

Relative Maximum: 0.500

Steps: 20

Readings/Pt.: 10

Initial Position: 0.0000

Active Controller:

Position of Centroid: 0.0000

Position at Max. Intensity: 0.0000

Maximum Intensity: 0.000

Final Position: 0.0000

Scan saved to file:

Figure 24: The macro used for scanning the collimator and samples (see Chapter 6 for more details, as well as examples of sample scans).

The first step is to install what I refer to as the coarse components (components for which the alignment tolerances are on the order of millimeters). This includes the motorized slit assemblies, ion chambers, calibration foil, beam pass, and radiation shield. The proper elevation for each of the components can be readily obtained using a laser level mounted on a surveying tripod. The beam elevation is determined by exposing burn paper (specialized paper that bears a mark upon being irradiated by high-energy x-rays) to the beam for a minute or two, after which the laser level is adjusted to the same elevation. At this point, each of the components is mounted using the laser as a guide. The motorized slit assembly can be set to the desired dimensions to define the beam size entering the hutch, after which the entire optical table is scanned and subsequently located at the position yielding the most counts in the ion chamber. After this, the collimator positioning assembly (without collimator) and sample goniometer (without mounted DAC) are installed, the detector is moved into position (note the detector must have full radiation shielding for protection during the alignment process), and the beamstop assembly is mounted. The beamstop assembly is then scanned and subsequently positioned in the path of the beam (defined by the motorized slits upstream).

The next step is to install the remaining components, which must be positioned to micron tolerances. To align the collimator, first a blank (a short metal rod with the same diameter as the collimator mount, but with a large hole to facilitate positioning) is scanned and positioned. The blank is then carefully removed and replaced by the actual collimator. In order to obtain the desired beam dimensions and maximum transmission through the collimator, it is crucial that it be perfectly normal to the incident beam. To achieve this, the collimator positioning assembly includes four degrees of freedom (vertical and horizontal translation, pitch and yaw tilt). All four degrees of freedom are repeatedly scanned until the experimentalist is satisfied that the maximum number of counts per unit time is incident upon the beamstop PIN diode. With this complete, the radiation shield can be removed from the detector and the DAC can be mounted atop the goniometer. Positioning the sample in the path of the beam is done in the same manner as the collimator, namely, by scanning the sample in the plane normal to the beam and monitoring the transmission intensity as recorded by the PIN diode in the beamstop assembly. However, for work at the highest resolution, it is not sufficient to simply locate the sample in the path of the beam. The position of the sample *along* the beam must also be carefully adjusted; the motivation and procedure for carefully positioning the sample along the beam is described in detail in Chapter 6.

Once the components are installed and aligned and the sample has been mounted and positioned, the photon shutters are closed and the imaging plate of the detector is erased to ensure the final image is not contaminated by scattering recorded during the alignment process. Once the plate is erased, the photon shutters are opened and the sample exposure is carried out. Exposure time depends on the particular sample, detector, and source. The goal is to expose as long as possible without saturating the detector. At HXMA, typical exposure times range from 5-25 minutes, depending on the sample volume and Z-value of the sample material. At a very specialized high-pressure diffraction beamline at the European Synchrotron Radiation Facility (ESRF, France), exposure times are on the order of 10 seconds.[23] At the other end of the spectrum, images obtained with a conventional molybdenum tube take 24-36 hours (and offer much less resolution).[24] Upon reaching the end of the exposure time, the photon shutters are closed and the imaging plate is scanned to yield the high-pressure powder x-ray diffraction image. Series of images are taken upon increasing (and if possible, decreasing) sample pressure. With a complete data set, the experimentalist is ready to begin the data analysis process, which in turn reveals the pressure-dependent behavior of the sample at extreme pressures. Before discussing this process, however, it is worth briefly considering just how it is the image made it to the detector in the first place.

7. A *very* brief introduction to x-ray diffraction

A complete and comprehensive introduction to x-ray scattering in general, and x-ray diffraction in particular, is well beyond the scope of this introduction. However, I want to highlight some of the most basic concepts in an effort to account for the nature of the powder x-ray diffraction images obtained for this work. Throughout this section I state without demonstration a number of results to facilitate the discussion; a complete description can be found by consulting the works listed in the topical bibliography at the end of this chapter.

X-ray scattering from an electron

When x-rays encounter an electron, there are a number of different scattering processes that can occur. I here consider only the case of elastic scattering, for which the wavelength of the incident and scattered x-rays are the same. The intensity of the scattered x-rays depends on a number of factors, and is given by the Thomson equation:

$$I = I_0\left(\frac{\mu_0}{4\pi}\right)^2\left(\frac{e^4}{m^2r^2}\right)\sin^2\alpha \qquad (11)$$

Here I_0 is the intensity of the incident beam, μ_0 is the permeability of free space, e is the charge of the electron, m is the mass of the electron, r is the distance between the electron and the position of the measured intensity, and α is the angle between the direction of scattering and the direction of the electron acceleration giving rise to the scattering. (Note that the mass term in Equation 11 makes it clear that x-ray scattering is an electron phenomena, as the mass of the proton is about 2000 times the mass of an electron, such that the ratio of scattering from a proton to that of an electron is approximately $3\text{x}10^{-7}$.) The x-rays generated by a conventional x-ray tube are randomly polarized, which will modify the intensity:

$$I = I_0\left(\frac{\mu_0}{4\pi}\right)^2\left(\frac{e^4}{m^2r^2}\right)\left(\frac{1+\cos^2 2\theta}{2}\right) \tag{12}$$

Here 2θ is the familiar scattering angle of x-ray diffraction measurements.

X-ray scattering from an atom

The x-ray scattering from an atom is simply the sum of the scattering from the atoms' individual electrons, and is described by a number f called the atomic scattering factor:

$$f = \frac{\text{amplitude of the wave scattered by an atom}}{\text{amplitude of the wave scattered by an electron}} \tag{13}$$

However, because the scattering from the individual electrons is elastic and coherent, the amplitude of the wave scattered by an atom is modified by destructive interference. This is shown schematically in Figure 25. For scattering in the forward direction, there is no path difference for the waves scattered by different electrons, so the amplitude of the scattered wave from Z electrons is simply the amplitude scattered by one electron (Equation 12) multiplied by Z. However, for scattering at some angle, a path difference is introduced, and the total scattering is reduced. Note that the magnitude of the path difference will depend on both the scattering angle and the wavelength; for a fixed wavelength, the path difference is larger for larger scattering angles. Similarly, for a fixed scattering angle, the path difference is larger for shorter wavelengths.

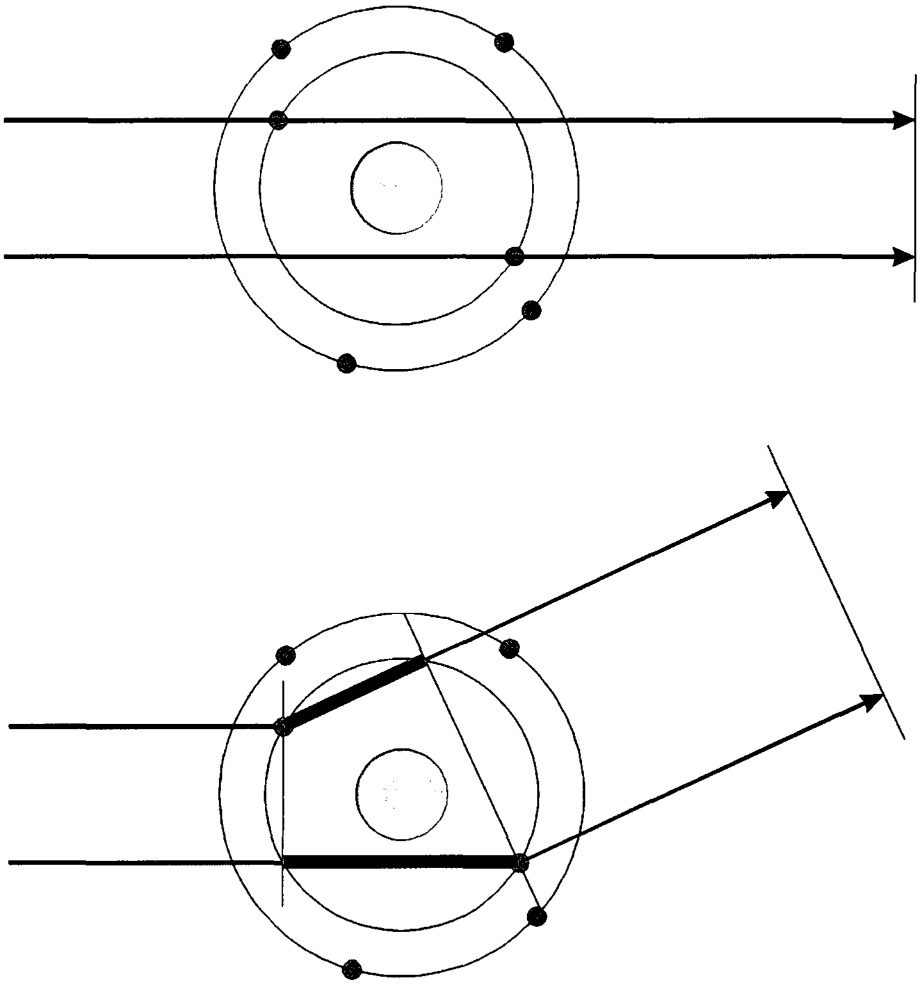

Figure 25: X-ray scattering from an atom. There is no difference in the path length, and hence no destructive interference, for x-rays scattered in the forward direction (top). The path difference (the difference between the two blue segments) introduced by scattering at an angle (bottom) results in decreased scattering intensity because of destructive interference.

Values for f are tabulated in the International Tables for Crystallography, Volume C.[25] Figure 26 shows a plot of f for germanium. Note that the abscissa units account for both the scattering angle and wavelength, and for scattering in the forward direction, f = 32 (the number of electrons in germanium).

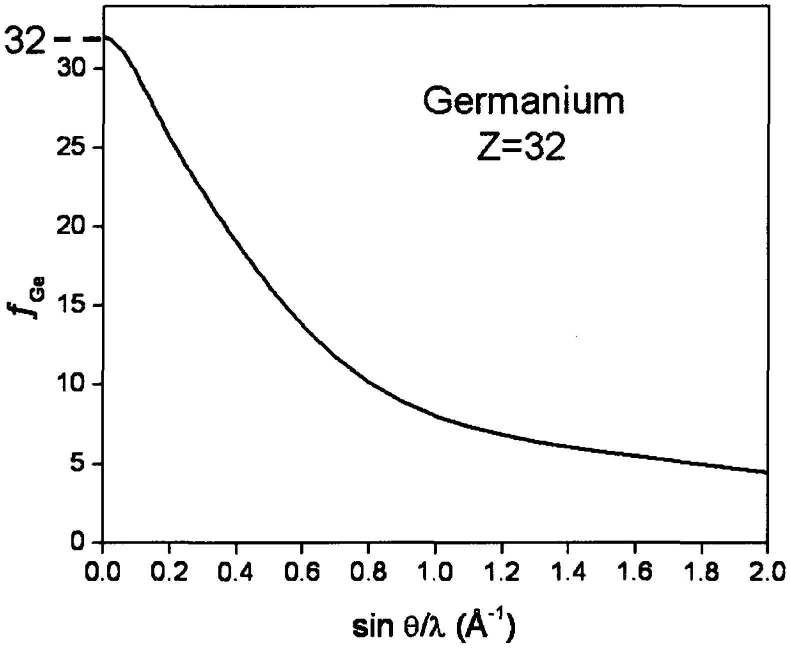

Figure 26: Atomic scattering factor for germanium.

X-ray scattering from atoms in a unit cell

A crystalline solid consists of a unique arrangement of atoms that is repeated periodically in space. The structure of a crystalline solid can be described completely by its crystal lattice shape (the basic geometric motif, or *unit cell*, that is repeated periodically) and contents (type, number, and position of the atoms within each unit cell). Analogous to the scattering from an atom, the scattering from a unit cell is described by a number F called the structure factor:

$$|F| = \frac{\text{amplitude of the wave scattered by all atoms in the unit cell}}{\text{amplitude of the wave scattered by one electron}} \tag{14}$$

Here, too, destructive interference of the coherently scattered x-rays plays a very important role. In fact, because of the sheer number of atoms, the intensity of the scattered wave is zero almost everywhere; for every atom that scatters a wave in a given direction, there is another atom that is located at just the right position in space to produce a scattered wave exactly out of phase with the first. For certain orientations of the crystal, however, the scattered waves from all of the atoms interfere constructively. Figure 27 shows two rays from an incident beam striking the most basic two-dimensional lattice (the basic building block, or unit cell, is a square, and each unit cell contains a single atom).

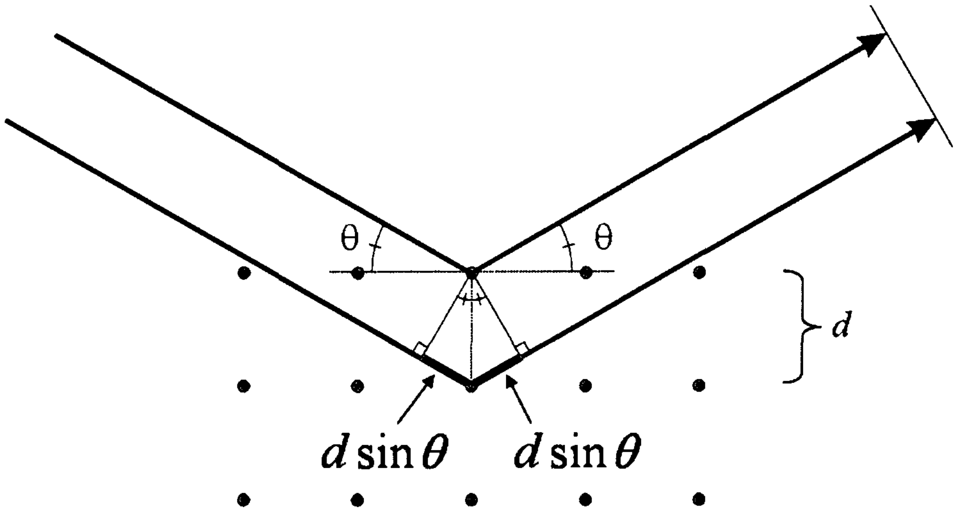

$$n\lambda = 2d\sin\theta$$

Figure 27: Bragg's law. Scattered x-rays will interfere constructively for the special case when the path difference (constituted by the two blue segments) between two rays is equal to an integer multiple of the x-ray wavelength.

The repeated atoms form planes with spacing *d*. In the special case that the path difference (shown in blue in Figure 27) between the two scattered rays is an integer multiple of the incident x-ray wavelength, there will be constructive interference, and hence a measured intensity. In this special case Bragg's Law (or similarly, the Bragg condition) is satisfied. Note that the scattering angle with respect to the incident beam is 2θ—the sum of the angles between the incident beam and the atomic planes (θ) and between the atomic planes and the detector (θ). Because these angles are equal, the scattered intensity is commonly referred to as a *reflection.*

One crystal, many planes (and possible many atoms)

In Figure 27 above, the planes with spacing *d* were defined in a particular way. Specifically, I started with an atom (e.g., top row, left) and then repeatedly moved horizontally by one atom and vertically by zero atoms to define a plane. But there are many other sets of planes that could be similarly defined by simply changing the number of horizontal and vertical steps, and each of these planes would (in general) have a different interplanar spacing. To identify the different sets of planes, the number of horizontal and vertical steps can be used as indices, such that the planes defined in Figure 27 could be denoted d_{10}. Figure 28 below shows some other sets of planes, identified by the indices used to generate them.

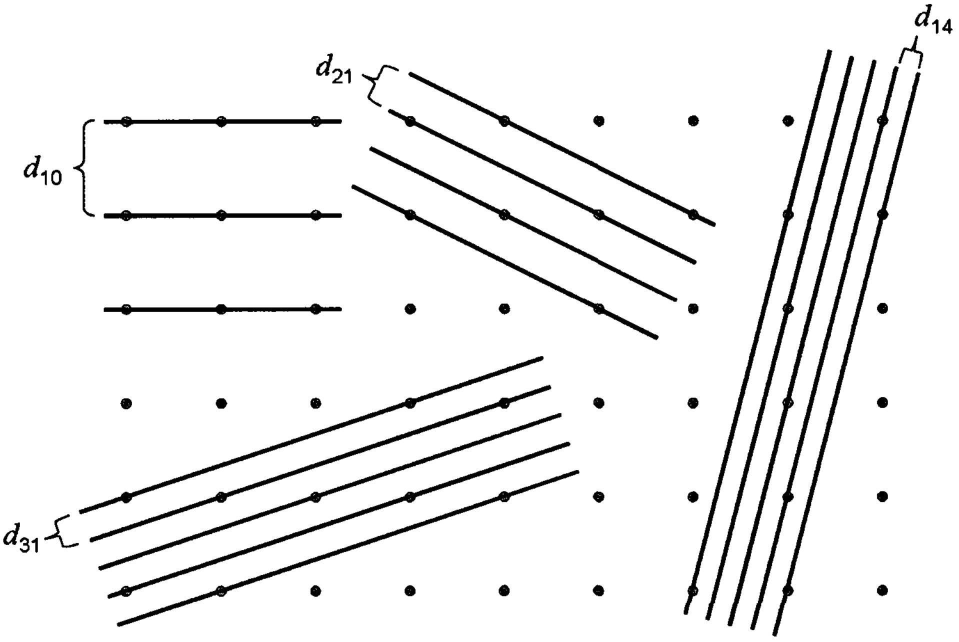

Figure 28: A crystalline lattice contains several different sets of planes with different interplanar spacings.

Note that in Figure 28 above, the Bragg condition is satisfied for the d_{10} planes, but not for the other planes. However, by rotating the lattice in the plane of the paper, the Bragg condition can be satisfied for each of the different sets of planes. The angle between the incident beam and the various planes d_{hk} is determined by the Bragg equation. The indices crystallographers use to identify the various sets of planes are called Miller indices h, k, and l.

In addition to many planes, a single unit cell can have many atoms. Figure 29 shows an example of a rectangular lattice with three atoms per unit cell. There are a few points worth illustrating here. First, in the case of the square lattice, the spacing between the d_{10} and d_{01} planes was the same, but in the case of a rectangular lattice, $d_{10} \neq d_{01}$. Second, note that regardless of the choice of origin, the size and shape of the basic building block is always the same, and contains three atoms (although the type and location of the particular atoms changes). And finally, the total scattering from the unit cell now depends on more than the scattering from just one atom.

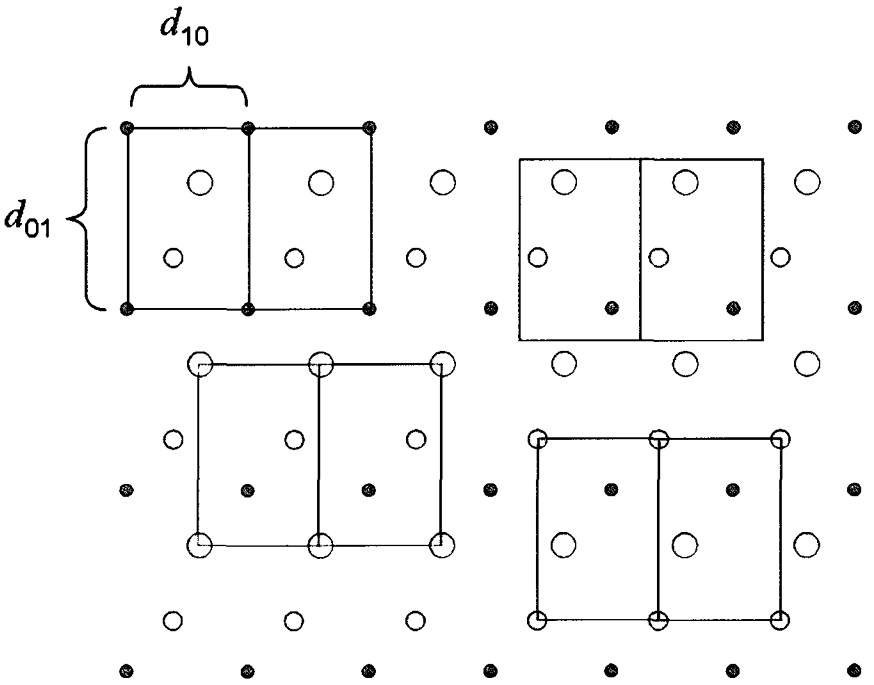

Figure 29: A crystalline lattice based upon a rectangular unit cell, with each unit cell containing three atoms. Four separate groups of two unit cells have been shown to demonstrate that the choice of origin for the unit cell is arbitrary. Note that while it may appear that some unit cells contain six atoms (four at the corners and two inside), the atoms at the corners are actually shared among four unit cells. Each of these four corner atoms contributes ¼ of an atom—or collectively, 4x1/4=1 atom—per unit cell.

In short, the structure factor presented above in Equation 14 is different for each set of planes d_{hkl}, and depends on all of the atoms contained in the unit cell. This can be concisely expressed:

$$F_{hkl} = \sum_{1}^{N} f_n e^{2\pi i(hu_n + kv_n + lw_n)} \tag{15}$$

Where the summation is over the N atoms contained in the unit cell, f_n is the atomic scattering factor of the n^{th} atom, u, v, and w are the fractional positional coordinates of the n^{th} atom in the unit cell, and h, k, l are the Miller indices of the set of planes $\{hkl\}$ giving rise to a particular reflection. It should be noted that inasmuch as the atomic scattering factors are well-characterized for the elements, if one is given a crystal structure (i.e., the number, type, and position of the atoms in a particular unit cell), the calculation of the diffracted intensities for various planes $\{hkl\}$ is straightforward. This is sometimes referred to as the forward problem. The reverse problem, taking a set of scattered intensities and determining the crystal structure which gave rise to them, is not straightforward. I do not discuss this here in more detail, but let it suffice to say this constitutes the central problem in crystallography.

The two-dimensional powder x-ray diffraction image

This brief introduction to x-ray scattering and x-ray diffraction has been provided with the hope that it will facilitate an explanation of the characteristic Debye rings which constitute a two-dimensional powder x-ray diffraction image. Figure 30 shows the situation described above in Figure 27, only the crystal lattice has been shrunk somewhat, the incident beam is normal to the edge of the page, and an area detector has been introduced to capture any scattered x-rays.

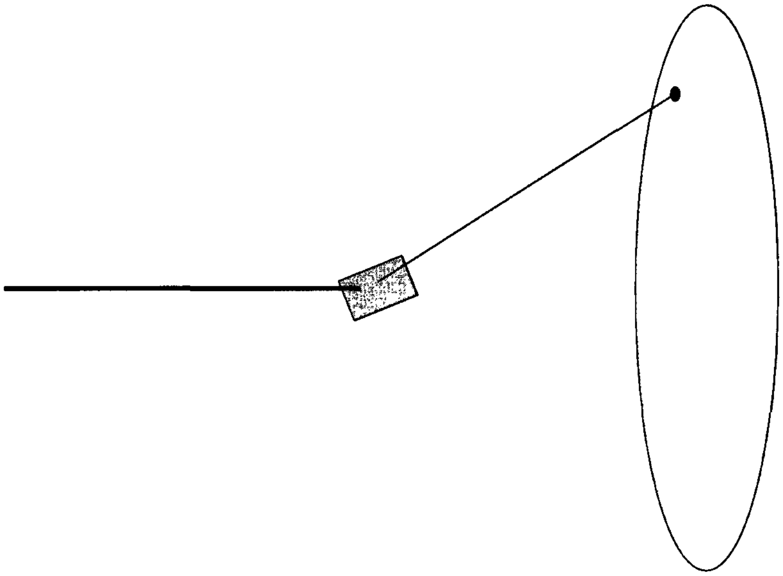

Figure 30: Bragg spot from a single crystal. When the Bragg condition is satisfied for a single crystal, a single Bragg spot of measured intensity will be recorded by the area detector. The destructive interference among scattered x-rays results in zero recorded intensity everywhere else (i.e., at all other scattering angles).

With the Bragg condition satisfied, there will be a measured intensity at a discrete point on the area detector, with an angle 2θ between the incident and scattered beam. This intense spot on the detector is called a Bragg spot. Now imagine that the crystal is rotated about an axis collinear with the incident beam. The Bragg condition will still be satisfied and the diffracted intensity will still be at an angle 2θ, but now the Bragg spot will move, tracing out an arc on the detector. If the crystal is rotated 360° about the beam, a complete circle, called a Debye ring, will be traced out on the plane of the detector, shown in Figure 31.

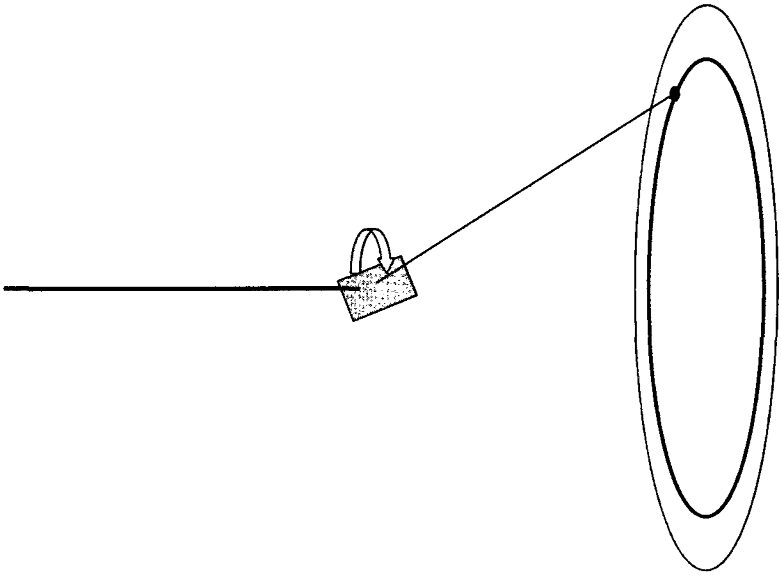

Figure 31: From Bragg spot to Debye ring. Assuming the Bragg condition is satisfied, rotating the single crystal about an axis collinear to the incident beam will yield a Debye ring (with a constant scattering angle 2θ).

Other rings with different radii could be obtained by first rotating the crystal in the plane of the page to satisfy the Bragg condition for a different set of crystallographic planes, after which the crystal could be rotated 360° about the axis defined by the incident beam to trace out the Debye ring. This is essentially the manner in which single crystal x-ray diffraction is executed, save there is no reason to trace out the rings. Instead, the crystal is rotated about other axes and the intensities of the Bragg spots are measured. In the case of powder x-ray diffraction, the goal is to have many small crystal domains, or crystallites. Ideally, there are a sufficient number of randomly oriented crystallites such that somewhere in the sample the Bragg condition is satisfied for each of the sets of planes *{hkl}*, with all of the possible orientations about the axis of the beam. If this is the case, the diffracted intensity will form a family of cones (shown in Figure 32), with each cone having a semi-angle 2θ corresponding to the scattering angle dictated by the wavelength of the incident radiation and the spacing between the atomic planes.

By measuring the scattering angle 2θ of the cones, the spacing between planes can be calculated, which in turn allows for the identification of the unit cell. This is an extremely important point. The Bragg equation doesn't tell us anything about the intensity of the Debye rings; it is independent of the type, number, and position of atoms in the unit cell.

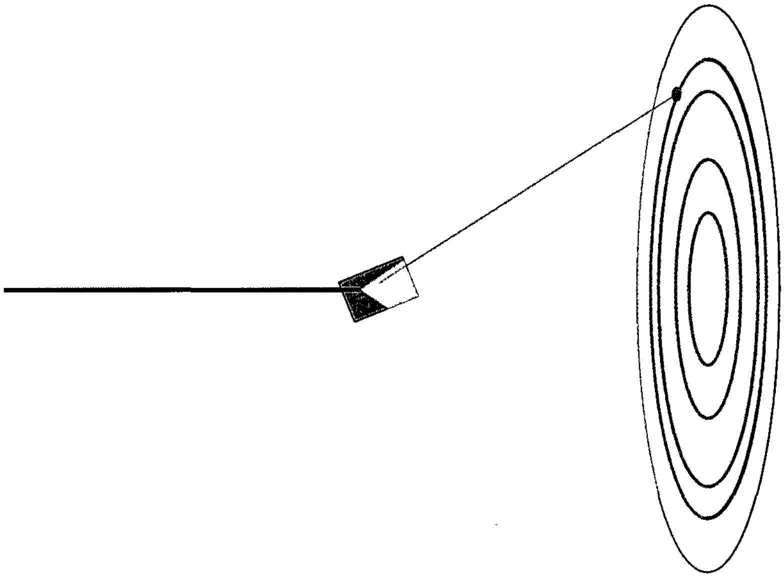

Figure 32: Diffraction from an ideal polycrystalline sample. Provided there are a sufficient number of randomly oriented grains (polycrystalline aggregates with single-crystal domains) satisfying the Bragg condition, the scattered x-ray intensity will constitute a family of cones giving rise to a set of Debye rings recorded by the detector.

The size and shape of the unit cell—the basic geometric motif that constitutes the volume (a state variable) of a crystalline solid—can be determined solely from the scattering angle of the Debye rings. (The previous statement is a bit of a generalization, as atoms located in special symmetry positions within the unit cell can result in zero measured intensity at a particular scattering angle for which a reflection would otherwise be expected; these are called systematic absences, and are very important in identifying the unit cell). But similarly, because the Bragg equation doesn't tell us anything about the intensity of the observed diffraction, the scattering angles of the Debye rings are not sufficient to completely determine the structure of a crystalline solid. The intensities of the Debye rings must be measured and compared against those expected based on the structure factor calculation for a particular arrangement of atoms. An exposition of methods for coming up with a possible structure goes well beyond the scope of this introduction, however Chapter 3 on barium hydride provides an example of one method for coming up with a possible structure.

8. Powder x-ray diffraction data reduction and analysis

From two-dimensional image to one-dimensional data

The process of scanning the image plate, which yields the two-dimensional powder x-ray diffraction image captured by the area detector, consists of binning the recorded intensity into an array of small pixels. The mar345 offers the user a few options; for all of the data presented in this work, the highest available resolution of 100x100 μm^2 pixels was used. At this resolution, the resulting image (345 mm in diameter) consists of almost 9.4 million pixels identified by (x, y) Cartesian coordinates. The task, shown schematically in Figure 33, is to rebin this square array into annular bins of equal width $\Delta 2\theta$, generating a conventional intensity *vs.* 2θ powder x-ray diffraction pattern. This pattern can be subsequently analyzed in the usual manner, i.e., unit cell indexing or full-pattern refinement. There are a few available software packages designed to carry out the rebinning process (also called image integration or image folding). By far the most widely used program is called Fit2d,[26] which was used for integrating all of the images for this work.

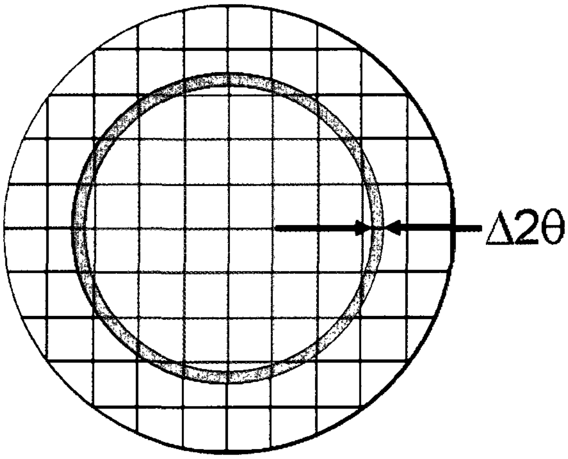

Figure 33: Rebinning a square array. The intensity recorded by the imaging plate is binned into a square array of pixels during the image scanning process. This data must be rebinned into annular regions of equal step size 2θ for the purpose of generating a conventional intensity *vs.* 2θ diffraction pattern.

Before the integration can be carried out correctly, a number of parameters from the experimental configuration must be known, including the distance between the sample and detector, the x-ray wavelength, the position of the beam incident on the detector (hereafter, the beam centre), and the angle of the detector plane with respect to the transmitted beam. With the exception of the x-ray wavelength (independently determined using calibration foils as previously discussed) all of these parameters can be determined using a powder x-ray diffraction image of a calibration standard. The standards most commonly used are sold by the National Institute of Standards and Technology (NIST, USA) as Standard Reference Materials (SRM). The SRMs are certified to have (at ambient pressure and temperature) a lattice parameter accurately measured to extremely high precision, and also a well-characterized mean particle size and strain. The SRMs used for this work were LaB_6, Si, and CeO_2. Each is cubic; the high symmetry ensures reasonable distance between neighboring reflections, allowing each reflection to be unambiguously identified by the software's peak-search algorithm. Figure 34 shows an example of a calibration image obtained from LaB_6 (simple cubic, a=4.1569 Å). Note that this image will be used throughout the rest of this section to demonstrate the basic steps of data reduction and analysis.

Characterizing the experimental configuration

The first step is to identify the beam centre. If a direct beam spot is visible on the detector, the user can simply identify the approximate position (done by clicking on a pixel using the Graphical User Interface), and the position is refined by fitting the recorded intensity in a small region about the pixel to a two-dimensional Gaussian. Note that a direct beam spot can be obtained by using a semi-transparent beamstop or by moving the beamstop momentarily to allow the transmitted beam to directly strike the detector. In either case, caution should be exercised to avoid overexposure which can damage the detector. In the absence of a direct beam spot, the approximate beam centre can be obtained by identifying at least three points on a single Debye ring. The centre of the unique circle determined by these points constitutes the beam centre on the detector.

The next step is to determine the angle of the detector plane with respect to the beam. Recalling that the diffraction intensity recorded by the detector arises from diffraction cones with apexes located at the sample, in the special case that the detector plane is perfectly orthogonal to the incident beam, the intersection of the detector plane with the cones will yield circles. However, it is not possible in practice to achieve perfect orthogonality, such that the intersection of the detector plane with the diffraction cones yields ellipses (for a well-positioned detector, as was the case for Figure 34, this eccentricity is not visible to the eye).

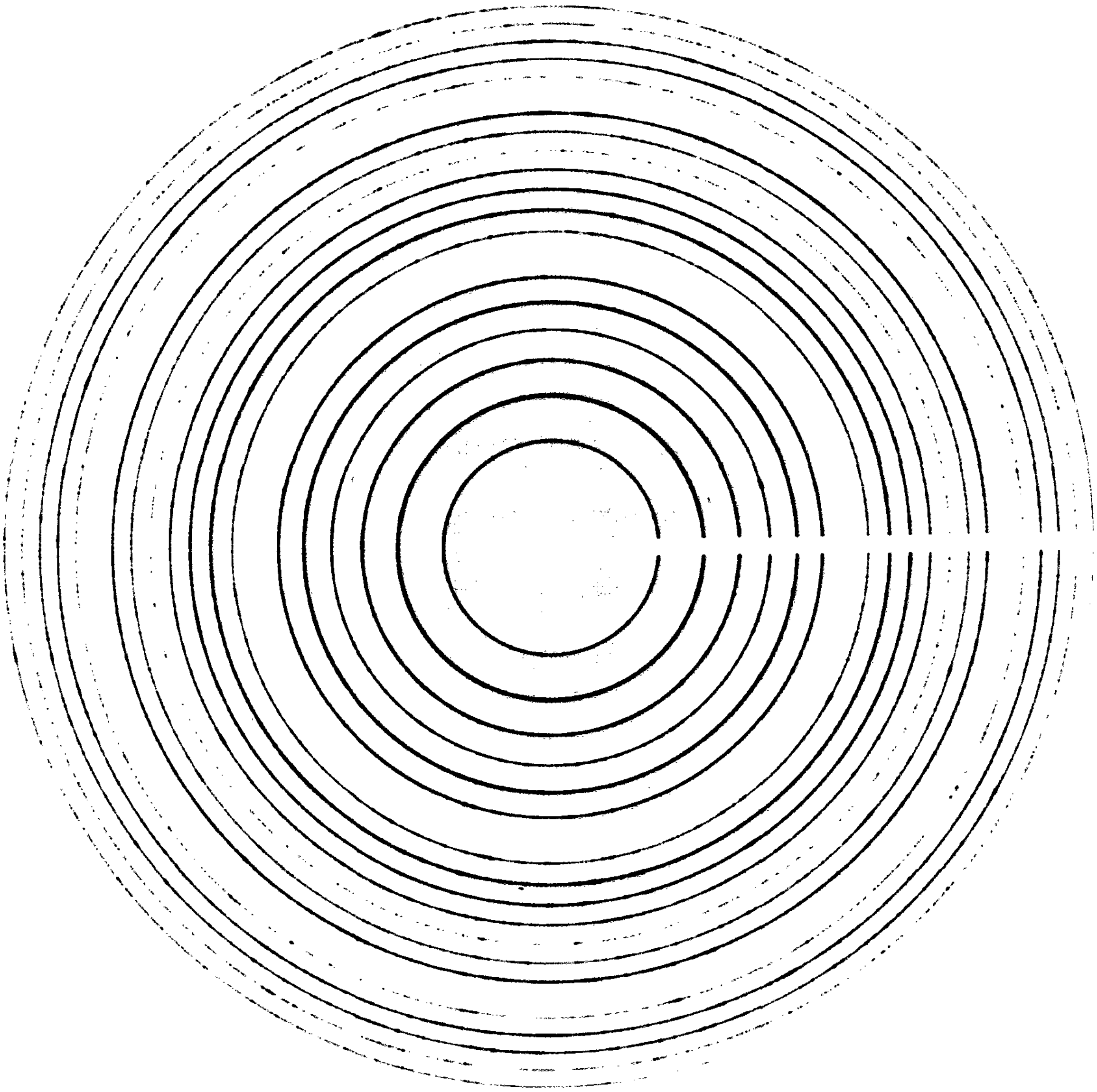

Figure 34: Powder x-ray diffraction image of LaB_6. Actual image diameter is 345 mm. The beamstop assembly blocks the scattered radiation from reaching the detector; its shadow can be seen from the centre to the right edge of the image.

The angle of the detector with respect to the incident beam can be described by two parameters, rotation and tilt, defined in Figure 35. With an approximate beam centre defined, the user identifies one or (preferably) more Debye rings on the diffraction image. Starting with the assumption that the detector is perfectly orthogonal to the incident beam, the algorithm determines through a least-squares refinement the rotation and tilt necessary to account for the eccentricity of the Debye rings.

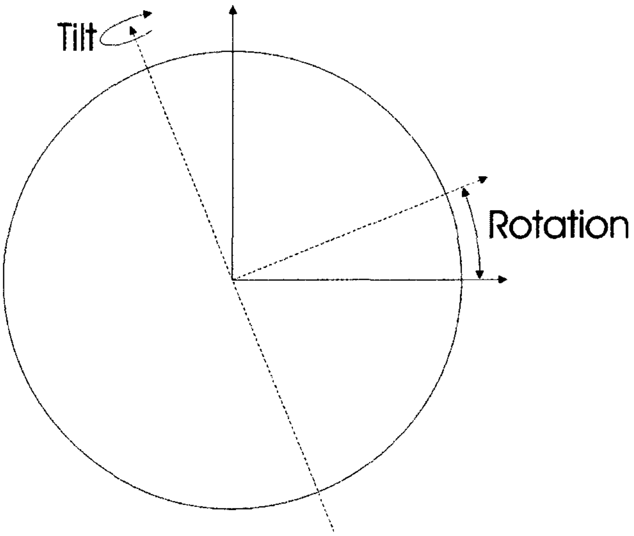

Figure 35: Definition of the detector tilt plane. The angle of the detector plane can be defined using two orthogonal rotation axes, called the rotation and tilt axes.

Finally, the distance between the sample and detector (hereafter, *D*) must be determined. This is a crucial parameter in the experimental configuration. In many conventional diffraction geometries, a point detector is situated at a constant distance from the sample (and moreover, it is always facing the sample—a consideration that will be further discussed below). In the case of a flat, two-dimensional detector, however, points on the detector surface are not at a constant distance from the sample; the proper conversion of a point on the detector (at a radial distance *r* with respect to the beam centre) to the appropriate scattering angle 2θ depends on *D*:

$$2\theta = \tan^{-1}\left(\frac{r}{D}\right) \tag{16}$$

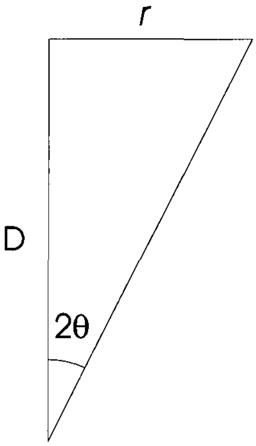

Figure 36: The scattering angle 2θ for a Debye ring with radius *r* depends on *D*.

For an SRM with known cubic lattice parameter *a*, the interplanar spacings for various planes {hkl} can be readily calculated:

$$d_{hkl} = \frac{a}{\sqrt{h^2 + k^2 + l^2}} \tag{17}$$

With these interplanar spacings and an independently known x-ray wavelength, the Bragg equation can be used to calculate the scattering angle for each of the observed Debye rings in the calibration image shown in Figure 34.

$$2\theta_{hkl} = 2\sin^{-1}\left(\frac{\lambda}{2d_{hkl}}\right) \tag{18}$$

Similarly, the radial distance *r* of the rings can be measured directly from the diffraction image. All of the Debye rings observed in the calibration image are used to obtain a unique value for *D* such that the calculated scattering angles and observed radii of the Debye rings simultaneously satisfy Equation 16. Note that while I have discussed the steps for determining the various experimental parameters separately, in practice, once the approximate position of the beam centre has been identified, the beam centre, rotation/tilt angles, and the sample-to-detector distance can be simultaneously refined using the calibration procedure in Fit2d. Figure 37 shows a screen shot immediately following the completion of the calibration procedure.

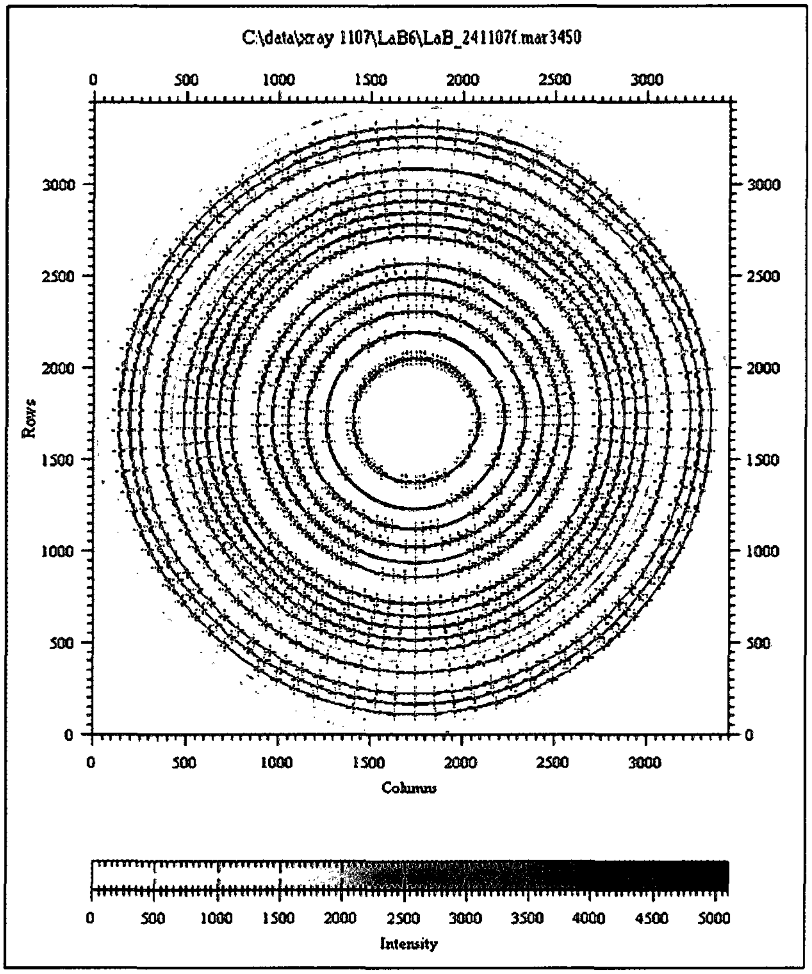

Figure 37: Characterization of the experimental configuration. The peak-search algorithm in Fit2d locates each of the Debye rings in the diffraction image. The beam centre and detector rotation angles are refined to yield the best fit to the elliptical Debye rings. The calculated *d*-spacings for LaB_6, together with the radial position of the Debye rings, are used to refine the distance between the sample and the detector.

With the calibration procedure complete, the next step is to integrate the calibration image (i.e., rebin the data to generate a conventional intensity *vs.* 2θ pattern). Figure 38 shows the resulting pattern. Assuming the calibration was done correctly, the resulting diffraction pattern should yield sharp, narrow diffraction peaks. Small errors in the tilt/rotation parameters or the beam centre will result in oddly shaped peaks (broader than expected peak width or asymmetric peak shape), while gross errors may generate a pattern with no recognizable peaks. Similarly, analysis of the pattern should yield the expected lattice parameter. Errors in either *D* (sample-to-detector distance) or λ (wavelength of the monochromatic x-rays) will result in an incorrect (small errors) or impossible to determine (large errors) lattice parameter due to a non-linear shift in peak positions as a function of 2θ.

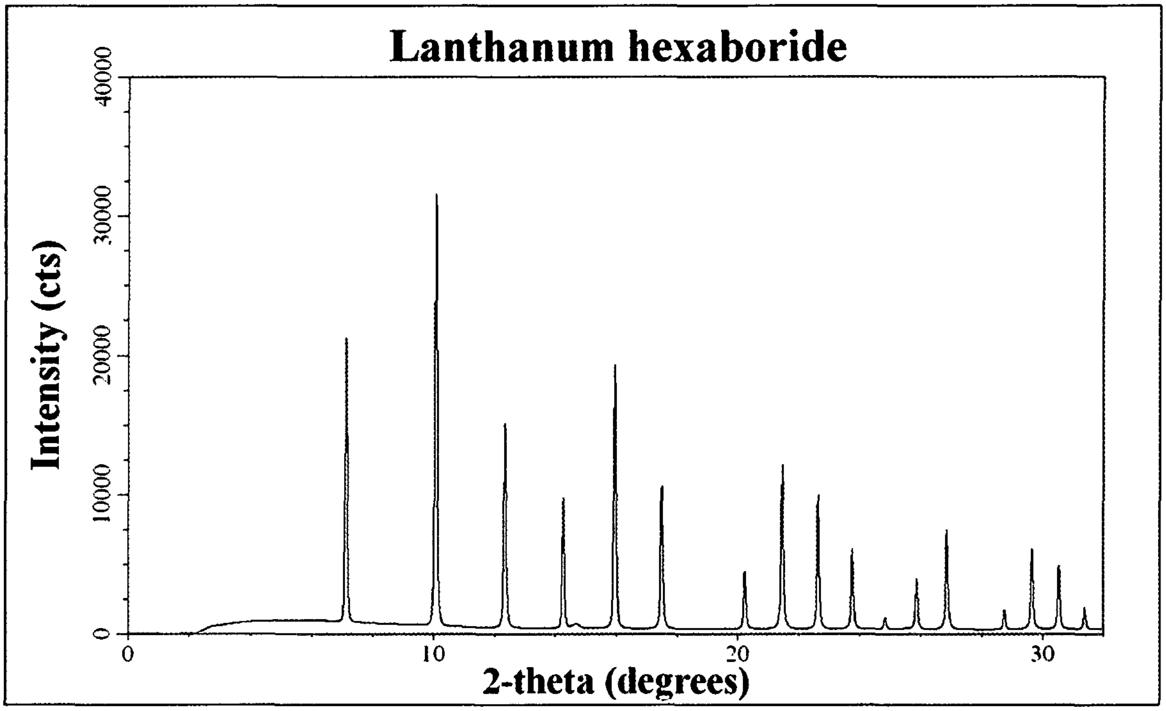

Figure 38: Intensity *vs.* 2θ diffraction pattern obtained by integrating the powder x-ray diffraction image shown above in Figure 34 (after properly characterizing the experimental configuration).

Integration parameters

When carrying out the actual integration of the image using Fit2d, two successive screens (shown below in Figure 39), called *control forms*, give the user a number of options. The *experimental geometry control form* (Figure 39, left) includes all of the experimental parameters obtained during the calibration process, together with the x-ray wavelength and the pixel size of the image. The *control of radial, 2-theta, or Q scan re-binning parameters* (Figure 39, right) contains a number of different options that further affect the integration output. Below, these are treated individually.

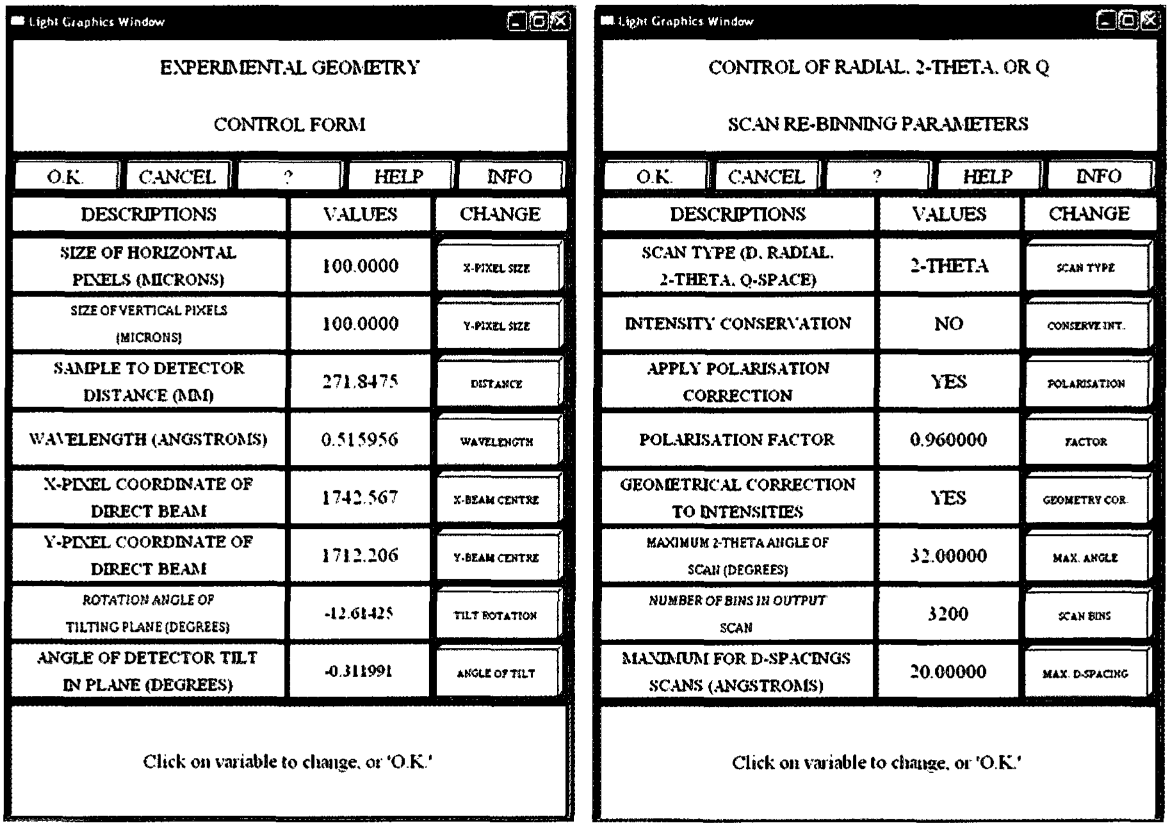

EXPERIMENTAL GEOMETRY

CONTROL FORM

DESCRIPTIONS	VALUES	CHANGE
SIZE OF HORIZONTAL PIXELS (MICRONS)	100.0000	X-PIXEL SIZE
SIZE OF VERTICAL PIXELS (MICRONS)	100.0000	Y-PIXEL SIZE
SAMPLE TO DETECTOR DISTANCE (MM)	271.8475	DISTANCE
WAVELENGTH (ANGSTROMS)	0.515956	WAVELENGTH
X-PIXEL COORDINATE OF DIRECT BEAM	1742.567	X-BEAM CENTRE
Y-PIXEL COORDINATE OF DIRECT BEAM	1712.206	Y-BEAM CENTRE
ROTATION ANGLE OF TILTING PLANE (DEGREES)	-12.61425	TILT ROTATION
ANGLE OF DETECTOR TILT IN PLANE (DEGREES)	-0.311991	ANGLE OF TILT

Click on variable to change, or 'O.K.'

CONTROL OF RADIAL, 2-THETA, OR Q

SCAN RE-BINNING PARAMETERS

DESCRIPTIONS	VALUES	CHANGE
SCAN TYPE (D, RADIAL, 2-THETA, Q-SPACE)	2-THETA	SCAN TYPE
INTENSITY CONSERVATION	NO	CONSERVE INT.
APPLY POLARISATION CORRECTION	YES	POLARISATION
POLARISATION FACTOR	0.960000	FACTOR
GEOMETRICAL CORRECTION TO INTENSITIES	YES	GEOMETRY COR.
MAXIMUM 2-THETA ANGLE OF SCAN (DEGREES)	32.00000	MAX. ANGLE
NUMBER OF BINS IN OUTPUT SCAN	3200	SCAN BINS
MAXIMUM FOR D-SPACINGS SCANS (ANGSTROMS)	20.00000	MAX. D-SPACING

Click on variable to change, or 'O.K.'

Figure 39: Fit2d Integration control forms. The *experimental geometry control form* (left) includes all of the experimental parameters from the calibration process. The *control of radial, 2-theta, or Q scan re-binning parameters* (right) offers the user several options affecting the output of the rebinned data, including choice and range of the scattering variable, as well as a number of corrections to the recorded intensity. Note that the various parameters are the actual values yielded by the calibration procedure (left) as carried out on the image in Figure 34, as well as those used to generate the intensity vs. 2θ pattern (right) shown in Figure 38.

Scan type allows the user to choose the abscissa units. For all purposes of discussion, I consider the case of 2θ. However, it should be noted that the other choices sometimes offer flexibility not available in a 2θ plot. For example, in the work on barium fluoride presented in Chapter 5, Figure 4 compares diffraction patterns obtained using different x-ray wavelengths. The plot in Q-space facilitates a wavelength-independent comparison of the respective patterns.

Intensity conservation gives the user the option to normalize the intensity in a given radial bin by the number of contributing pixels in the bin (*NO*) or to output the sum without normalization, i.e., conserve total intensity (*YES*). For most data analysis, it is appropriate to normalize the intensity as this yields intensity data equivalent to the type obtained using conventional diffractometers or x-ray cameras. More will be said on this matter later, but let it suffice to point out here that conventional diffractometers and cameras have a fixed slit width and film width, respectively, such that as the scattering angle 2θ increases, the ratio of the recorded intensity to the intensity around the complete Debye ring decreases. This is shown schematically in Figure 40.

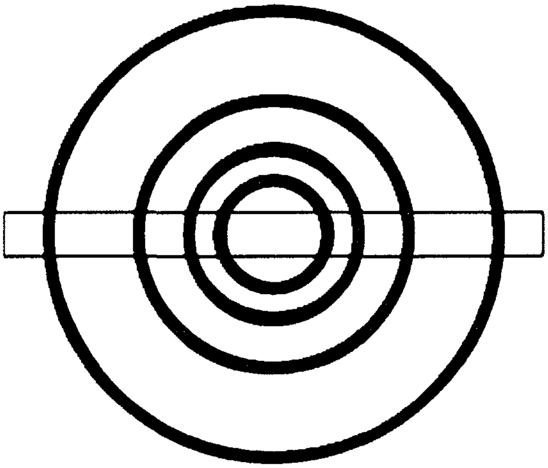

Figure 40: As the scattering angle increases, the fixed slit or film width (depicted by the rectangle) of diffractometers or cameras captures a smaller portion of the total intensity around Debye rings. Normalizing the rebinned intensity during the image integration process mimics this effect.

Apply polarisation correction and *Polarisation factor* allow the user to correct for variations in the recorded x-ray intensity owing to the polarization of the incident x-ray beam. X-rays generated by a conventional x-ray tube are randomly polarized, and the effect on the measured diffraction intensity depends on the scattering angle 2θ:

$$P = \frac{1}{2}\left(1 + \cos^2 2\theta\right) \tag{19}$$

Note that this is the last term in the equation for the scattering of randomly polarized x-rays (i.e., x-rays emitted from a conventional x-ray tube) from an electron, presented above in Equation 12.

Synchrotron radiation, however, is not randomly polarized. In fact, it is almost totally plane-polarized (in the plane of the electron acceleration—the horizontal plane for most synchrotron radiation production devices). The modified polarization correction required was first made explicit by Kahn *et al.*[27]

$$P = P_0 - P' = \frac{1}{2}\left(1 + \cos^2 2\theta\right) - \frac{1}{2}\mathscr{F}\cos 2\rho \sin^2 2\theta; \tag{20}$$

$$\mathscr{F} = \frac{E_\sigma^{\ 2} - E_\pi^{\ 2}}{E_\sigma^{\ 2} + E_\pi^{\ 2}} \tag{21}$$

Here 2θ is the usual scattering angle, ρ is (for the purposes of this work) the azimuthal angle on the area detector (these angles are shown schematically in Figure 41), E_σ is the amplitude of the incident x-rays in the horizontal plane ($\rho=0^\circ=180^\circ$), and E_π is the amplitude of the incident x-rays in the vertical plane (perpendicular to E_σ). Note that P_0 is simply the usual polarization correction for randomly polarized x-rays, and P' is the modification required due to the plane-polarized incident beam.

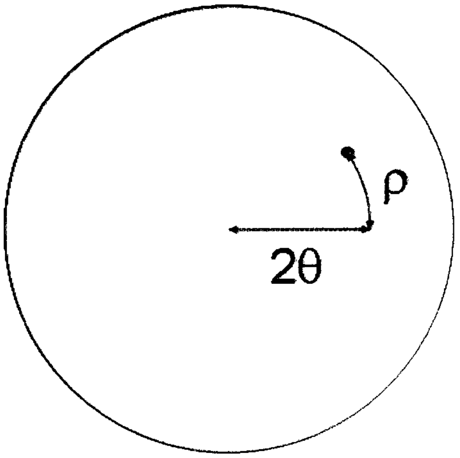

Figure 41: The correction to the observed intensity required by the plane-polarized x-ray beam from a synchrotron radiation source depends on both the scattering angle 2θ and the azimuthal detector angle ρ.

If a conventional θ-2θ geometry is used in conjunction with a point detector, the detector essentially travels along an arc in 2θ space and ρ=constant. In the case of a powder x-ray diffraction image captured on an area detector, however, the range of ρ is $[0, 2\pi]$, i.e., the correction continually varies about the circumference of the Debye ring at a given scattering angle 2θ.

The range of $\mathscr{F}$ (Equation 21) is [-1, 1]. Ideally, synchrotron radiation is totally plane-polarized in the plane of the electron acceleration (this would correspond to $\mathscr{F}=1$), but in practice the finite size and emittance of the electron beam, and the angles of the focusing optics and monochromator with respect to the beam, reduce this value somewhat (note: emittance is the beam divergence due to the electron-electron repulsion in the beam, and the focusing done to correct for this repulsion). The appropriate value for $\mathscr{F}$ can be determined by measuring it experimentally, or calculating it based on the design parameters of the radiation source and configuration of the optical components. I have made extensive measurements of the source polarization at the HXMA beamline of the CLS *via* the traditional method employing a polarimeter, as well as a novel technique using the total scattering from an amorphous material as measured by the area detector (this constitutes the subject of an article in preparation for publication, but not included in the present work). Without going into greater detail here, I simply report that the value of $\mathscr{P}$= 0.96 is appropriate when carrying out integration of the two-dimensional diffraction images relevant to this work. Note that $\mathscr{P}$=0 and $\mathscr{P}$= -1 would correspond to randomly polarized x-rays and totally plane-polarized x-rays in the vertical plane, respectively. Finally, although mentioned below in the subsection concerning Rietveld refinement, it must be said here that because the polarization correction to the recorded intensities is carried out during the image integration process, it is imperative that no polarization correction be included during full-pattern refinement.

Geometrical correction to intensities accounts for modifications to the observed intensity that are due to the use of a flat area detector. In a conventional θ-2θ diffraction geometry, the point detector swings on a radial arm, such that the detector is situated at a constant distance from the sample, normal to the scattered x-rays incident on the detector. In the case of a flat area detector, the distance between the sample and the detector plane, and the oblique angle of the scattered x-rays with respect to the detector plane, increase with increased scattering angle. The appropriate correction to the intensity has been described by Barna *et al.*[28]

$$I_{corrected} = \frac{I_{observed}}{\left(\cos^2 2\theta\right)\left(\cos 2\theta\right)\left(e^{-\alpha/\cos 2\theta}\right)} \qquad (22)$$

Here 2θ is the usual scattering angle and $\alpha=(D_{2\theta}-D)\mu$ (where $D_{2\theta}$ is the distance between the sample and the detector at a scattering angle 2θ and μ is the linear attenuation coefficient for air). The cosine squared term accounts for the $1/r^2$ falloff of intensity (recall Equation 12) due to the increased distance between sample and detector, the cosine term accounts for the apparent reduced width of a pixel due to the oblique incidence of the beam, and the exponential term accounts for absorption in air owing to the increased path length between sample and detector. This last term for absorption in air brings about an exceedingly small correction, and is not included in the correction applied in Fit2d.

Maximum 2θ angle of scan (in degrees) and *Number of bins in output scan* are self-explanatory, however, some consideration should be given to the choice of values, as the total range will be divided among the number of bins. With this in mind, the maximum range should not far exceed the actual edge of the detector (so as to not waste resolution by essentially dedicating some of the bin width to empty space) and the number of bins should be chosen such that the bin width (or step size, in the nomenclature of conventional geometries) can be expressed by a "round" number with relatively few numerals (e.g., 0.01° as opposed to 0.01002852°). This latter consideration prevents round-off errors which can be introduced (and propagated as a function of 2θ) during subsequent indexing and full-pattern refinement, due to truncation of large strings by analysis software.

Assuming the experimentalist has carefully characterized the experimental geometry *via* the calibration process, and has made the relevant choices regarding the corrections to intensity, the intensity *vs.* 2θ pattern yielded by the integration of the two-dimensional diffraction image should be equivalent to that obtained from a conventional θ-2θ Bragg-Brentano diffractometer, save the conventional pattern will not be corrected for polarization whereas the pattern obtained from the image will be corrected for polarization. An example of a resulting pattern has already been presented above in Figure 38. At this point, the experimentalist can proceed with unit cell indexing and full-pattern refinement using software designed for conventional intensity *vs.* 2θ powder x-ray diffraction patterns.

Analysis of the powder x-ray diffraction pattern

A comprehensive treatment of unit cell indexing and full-pattern refinement goes well beyond the scope of this introduction. Below I will present the most basic concepts associated with the analysis of the powder x-ray diffraction pattern, together with examples of typical results, in an effort to provide a basic background for the results and analyses that are presented in the following chapters.

Unit cell indexing

The first step in pattern analysis is to index the unit cell. As discussed above, the unit cell is the basic, three-dimensional geometric motif, containing one or more atoms at particular positions, that is repeated periodically. It should be noted that for a given crystalline structure, there may be several possible motifs that could be repeated periodically to yield the crystal structure, so a further restriction is that the proposed unit cell must be the smallest, simplest motif that can be used to generate the crystal structure through periodic repetition.

In general, the positions (angles) of the observed diffraction peaks depend on the unit cell size and shape; they do not depend on the number of atoms in the unit cell, nor do they depend on the positions of the atoms (although atoms located in particular positions may result in the absence of peaks that would otherwise be expected for a particular unit cell).

Assuming for the moment that one has a possible candidate for the correct unit cell, the expected positions for observed diffraction peaks can be readily calculated, so the problem of indexing consists of determining a possible unit cell size and shape, calculating the expected peak positions, and comparing the calculated positions against the observed positions in the diffraction pattern. If the proposed unit cell is correct, all of the observed diffraction peaks will be accounted for by the calculated peaks, but moreover, there will (in general) be no additional peaks predicted by the calculation yet not observed in the pattern.

There are many methods for coming up with candidate unit cells for testing against the observed pattern, however the most common method involves taking advantage of the computational power and search-match algorithms currently available. Specifically, the scattering angles of the observed peaks are measured, and using the Bragg equation, the corresponding interplanar spacings, or *d*-spacings, are calculated. These observed *d*-spacings are then used as input for programs which test a large number of possible unit cells based on a number of initial constraints dictated by the user. For each unit cell tested by the software, the calculated *d*-spacings are compared against the observed *d*-spacings, and the software (hopefully) outputs a number of possible candidates for the correct unit cell. It is then incumbent upon the user to go back and manually test one or more of the possible solutions to see if any fulfill the criteria of accounting for all observed peaks, but not predicting any unobserved peaks. It should be noted that the software does not always provide the correct solution, and sometimes provides no solutions! Working with accurate, complete data is the key to successful indexing. Forsaking a more detailed discussion of obtaining possible solutions to difficult or challenging problems with indexing, below I provide an example of a correct result, together with an example of an incorrect result.

For the purposes of illustration I will use the diffraction pattern shown above in Figure 38, obtained by integrating the two-dimensional diffraction image shown in Figure 34. The image comes from a Standard Reference Material, LaB_6. The unit cell for LaB_6 is cubic, and each unit cell contains one lanthanum atom and six boron atoms. The length of one side of the cube (at ambient pressure and temperature) is a=4.1569 Å. Figure 42 shows this basic unit cell.

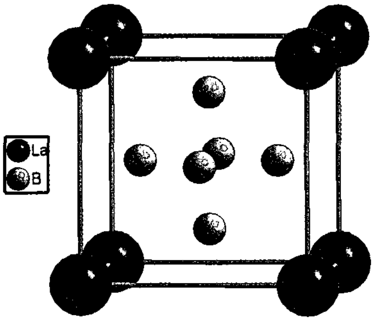

Figure 42: A unit cell of LaB_6 contains one La and six B (recall that each of the eight La atoms in the corners is shared by eight unit cells, working out to one La per unit cell).

Knowing in advance the unit cell size and shape (i.e., a candidate unit cell proposed by the indexing software), expected *d*-spacings of the various diffraction peaks can be readily calculated using Equation 17 presented earlier; these are shown below in Table 1.

Miller indices			*d*-spacing (Å)
h	*k*	*l*	
1	0	0	4.1569
1	1	0	2.9394
1	1	1	2.4000
2	0	0	2.0785
2	1	0	1.8590
2	1	1	1.6970
2	2	0	1.4697
2	2	1	1.3856
3	0	0	1.3856
3	1	0	1.3145

Table 1: *d*-spacings (calculated using Equation 17) for various planes {*hkl*} for LaB_6 (cubic lattice parameter a=4.1569 Å).

With these expected *d*-spacings and the x-ray wavelength, the Bragg equation can in turn be used to calculate the expected scattering angle 2θ for each of the diffraction peaks. A comparison of the expected peak positions against the diffraction pattern is shown in Figure 43.

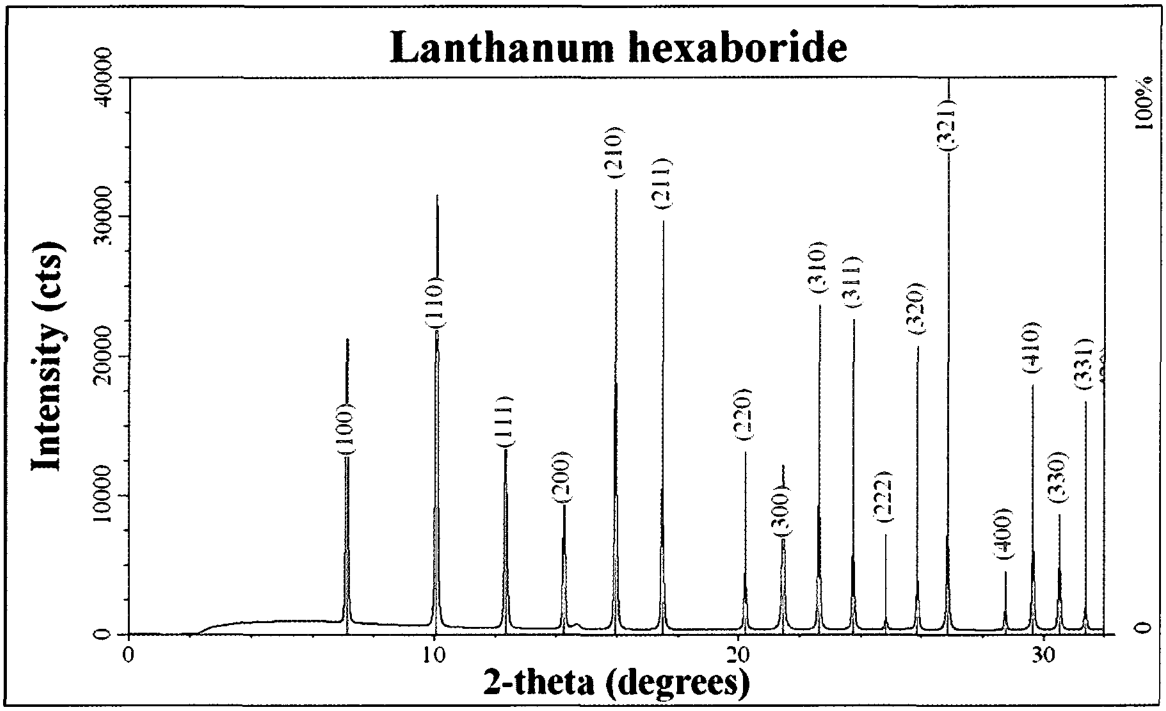

Figure 43: A comparison of expected peak positions (based on the unit cell obtained from the pattern-indexing software) against the observed peak positions strongly suggests the correct unit cell has been determined. The expected peaks account for all of the observed peaks, and furthermore, there are no additional expected peaks without corresponding observed peaks.

At first glance the comparison looks excellent. There is a small problem, however, as there is a weak, broad peak just beyond the (200) peak that is unaccounted for. There are a couple of possibilities. First, the candidate unit cell may be incorrect, or second, the peak may come from a different phase, e.g., an impurity in the sample. It turns out that in this case, it comes from the gasket material surrounding the sample. As an aside, it is worth noting again the advantage of using imaging plates. Looking at Figure 34 above, it is clear that just beyond (200) reflection (the fourth Debye ring starting from the centre) there is a very faint ring. While the rest of the Debye rings are intense and even a little spotty, this Debye ring is faint and diffuse. The stark contrast in the appearance of the rings strongly suggests that the respective reflections come from different materials.

An incorrect unit cell

I here show an example of an incorrect unit cell for LaB_6, that might possibly be found by automatic indexing. Recall from above that there are possibly several motifs that can be repeated periodically to generate the crystal structure. Take for example two cubic unit cells of LaB_6 end to end. In this case, the unit cell would be tetragonal (a cube stretched or compressed along one axis), with lattice parameters *a*=4.1569 Å, *c*=2*a*=8.3138 Å, as shown in Figure 44.

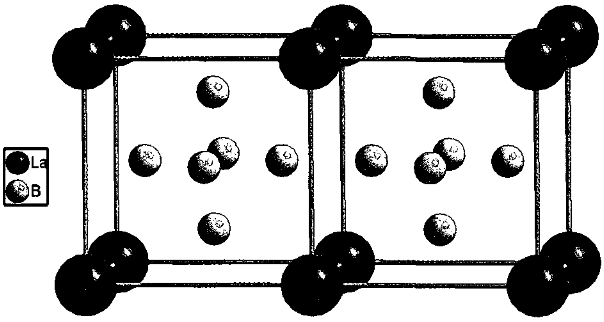

Figure 44: The periodic repetition of a doubled (along one axis) unit cell of LaB_6 would lead to exactly the same crystalline solid generated by a periodic repetition of the cubic unit cell shown above in Figure 42.

If this motif were repeated periodically, it would yield precisely the same crystal structure obtained from periodic repetition of the unit cell shown above in Figure 42. The *d*-spacings for the expected peaks can be calculated using the following equation:

$$\frac{1}{d_{hkl}{}^2} = \frac{h^2 + k^2}{a^2} + \frac{l^2}{c^2} \tag{23}$$

A comparison of the calculated peak position against the observed peak positions is shown in Figure 45. Note that each of the observed peaks is accounted for by a calculated peak, however there are many calculated peaks with no corresponding observed peak. In this case the proposed unit cell is closely related to the correct unit cell, however, it is not the smallest, simplest cell that can be periodically repeated to generate the crystal structure.

Crystal structure determination

Once the unit cell is indexed, the next step is to determine the number, type, and position(s) of the atom(s) within each unit cell; this constitutes a complete description of the crystal structure. In the case of unit cell indexing, one comes up with a proposed unit cell and compares the positions of the calculated peaks against the positions of the observed peaks. Similarly, in the case of crystal structure determination, one comes up with a proposed crystal structure and compares the calculated *intensities* of the peaks against the observed intensities of the peaks.

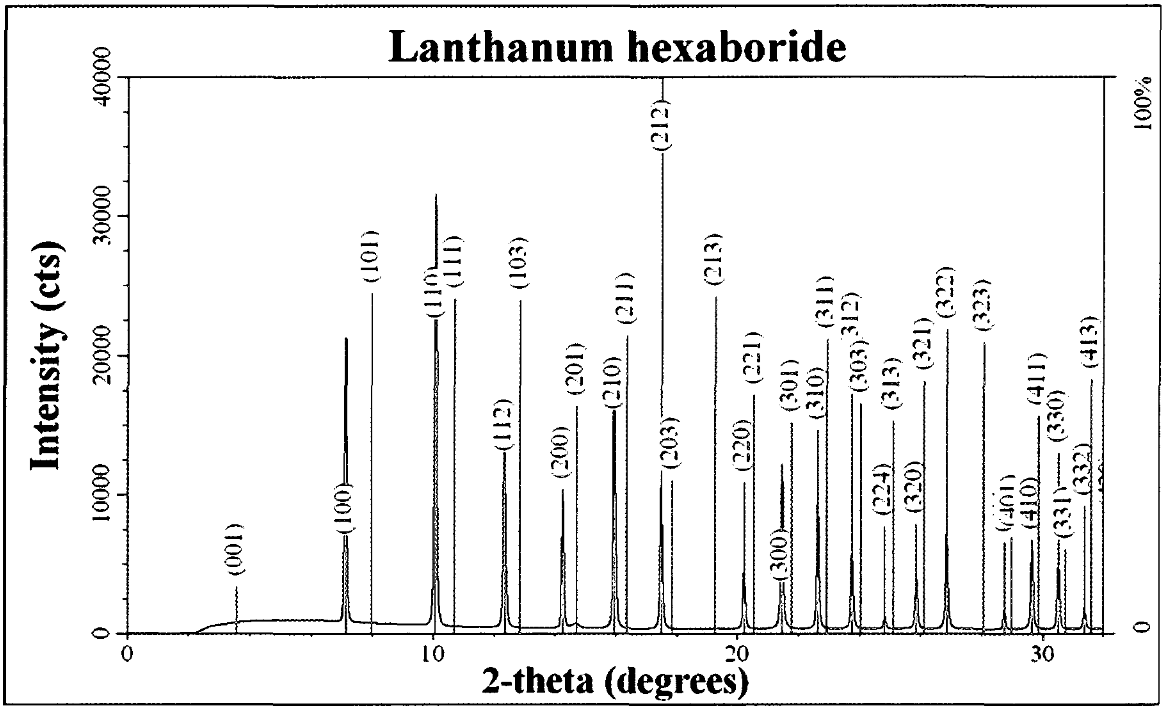

Figure 45: A comparison of expected peak positions (based on the unit cell possibly obtained from the pattern-indexing software) against the observed peak positions clearly shows an incorrect unit cell has been proposed. The expected peaks account for all of the observed peaks, however, there are additional expected peaks without corresponding observed peaks.

In general, powder x-ray diffraction data is not ideal for intensity comparison because of overlapping reflections. Consider, for example, the case of LaB_6 for which the (300) peak and the (221) peak have the same *d*-spacing, namely 1.3856 Å (see Table 1). The result is that the diffracted intensity from each of these crystalline planes will scatter at the same angle 2θ. Unfortunately, there is no way of determining how much of the total integrated intensity at the particular scattering angle 2θ is due to the {300} planes and how much is due to the {221} planes. Because of this difficulty, single crystal x-ray diffraction is the preferred experimental technique for crystal structure determination. While it is true that for a single crystal each of these reflections will still have the same scattering angle, they can nevertheless be distinguished because the single crystal will have a unique *orientation* which gives rise to each reflection (conversely, recall that in the case of an ideal powder, *all* possible orientations of the crystal are simultaneously present, giving rise to the ambiguity).

Of course, there are many instances for which it is not possible to grow a single crystal of suitable size and/or quality. Notably, in the case of high-pressure crystallography, samples are frequently prepared *in situ* under high-pressure conditions, *viz.*, a pressure-induced phase transition. Even if the initial sample were a single crystal, the volume collapse associated with a pressure-induced phase transition frequently results in a polycrystalline sample following the transition. Because single crystal x-ray diffraction is sometimes simply not feasible, it is extremely important to have a method which facilitates the refinement and corroboration of proposed crystal structures based on powder diffraction data. Such a method was introduced by Rietveld in 1966.[29]

Rietveld refinement

A powder x-ray diffraction pattern can be thought of as a set of discrete data points of measured intensity. The measured intensity of each data point is the sum of the background and possibly one or more diffraction peaks. The basic idea is to start with a model that describes the total scattered intensity of each point. This model includes structural information (for example, the unit cell size and shape, the type, number, and positions of the atoms) as well as information about the experimental configuration (for example, the wavelength and spectral width of the monochromatic radiation). The model is used to generate a calculated diffraction pattern and this calculated intensity (at each point) is compared against the observed intensity (at each corresponding point). The disagreement between the observed and calculated patterns can be quantified by a sum of the weighted square of the difference at each point:

$$S_y = \sum_i w_i (y_i - y_{ci})^2 \tag{24}$$

where y_i and y_{ci} are the observed and calculated intensities of the i^{th} point in the diffraction pattern and $w_i = 1/y_i$ is the weight given to the i^{th} point. The quantity S_y is minimized by a least-squares refinement of the various parameters that constitute the model for the calculated diffraction pattern. Note that there can be many parameters in the model (i.e., the refinement is non-linear), so the refinement is carried out iteratively, adjusting the various parameters by small steps until convergence is reached.

The intensities for each point in the calculated diffraction pattern are given by:

$$y_{ci} = s \sum_K L_K |F_K|^2 \phi(2\theta_i - 2\theta_K) P_K A + y_{bi} \tag{25}$$

s is the scale factor

K represents the Miller indices hkl for each Bragg reflection

L_K includes corrections for the Lorentz, polarization, and multiplicity factors

F_K is the structure factor of the K^{th} Bragg reflection

$\phi(2\theta_i - 2\theta_K)$ is the reflection profile function (i.e., a quantitative description of peak width)

P_K is a correction for preferred orientation
A accounts for absorption in the sample
y_{bi} is the background intensity at the i^{th} point

Below I discuss each of these terms in greater detail, and where appropriate, they are discussed in the specific context of FullProf,[30] the software used to carry out the full-pattern refinements presented in this work. The input file for FullProf consists of several input parameters that constitute the model for the calculated profile. Some of the input parameters (e.g., the x-ray wavelength) are fixed, whereas the remaining parameters (e.g., the lattice parameters) can be varied to carry out the least-squares refinement. Each of the variable parameters can be turned on or off (i.e., varied or fixed) at various stages of the refinement process. This is important, as during the early stages of refinement, the observed and calculated patterns may be quite different, and the refinement may diverge if there are too many free parameters. (Specific strategies for which parameters to vary, and when to vary them, can be found in the references at the end of this chapter.)

Turning first to the scale factor s, it is important to note that an accurate calculation of the *absolute* intensity for an experimentally observed Bragg reflection would be extremely difficult, as it would require accurate knowledge of the number of electrons in the sample (or more appropriately, in the scattering volume), the intensity of the incident beam, the energy-dependent response of the detector, etc. Fortunately, because the crystal structure consists of a repeated unit cell, the calculated intensity of one Bragg reflection *relative* to another Bragg reflection is relatively straightforward. Therefore, if the correct crystal structure is used in the model, the relative intensities of *all* of the Bragg reflections for a given phase in the pattern can be multiplied by a single scale factor s to yield agreement between the observed and calculated *absolute* intensities. Note also that the scale factor can serve as a powerful tool in quantitative phase analysis (assuming satisfactory agreement between the observed and calculated patterns upon completion of the refinement process).

L_K includes corrections for the Lorentz, polarization, and multiplicity factors. As discussed above, for the diffraction patterns presented in this work, a correction due to the polarization of the incident beam has already been applied, and should not be applied during the refinement process. The multiplicity factor accounts for planes of the same family {*hkl*} contributing to the reflection. For example, in a cubic crystal, there are six unique atomic planes, namely the (100), (010), (001), (-100), (0-10), and (00-1), that all have the same *d*-spacing and structure factor. These make up the family of planes {100}. In the case of single crystal x-ray diffraction, the intensity from each "member" of the family can be measured at six unique crystal orientations, but in the case of powder x-ray diffraction, all of the planes of a given family contribute equally (in the case of an ideal powder) to the observed (100) reflection. (Note this is *not* the same as peak overlap discussed above, for which the structure factors of the planes are *not* the same.) So the multiplicity factor for the {100} family is 6. The multiplicity factor for other families is different, e.g., the multiplicity factor for the {111} family is 8. The appropriate multiplicity factor for each family of planes *{hkl}* is applied to the calculated reflection (*hkl*). The Lorentz factor accounts for variations in intensity owing to the particular experimental geometry. In the case of the transmission geometry used for the present work, there are three separate terms which contribute to the overall Lorentz factor.

$$\text{Lorentz Factor} = \left(\frac{1}{\sin 2\theta}\right)(\cos 2\theta)\left(\frac{1}{\sin 2\theta}\right) = \frac{1}{4\sin^2\theta\cos\theta} \tag{26}$$

Without providing additional details I here simply state that the first term is due to the decreased angular region over which the Bragg condition is satisfied for reflections at higher scattering angles, the second term is due to the fact that a perfect, randomly oriented powder will have fewer planes favorably oriented for reflections at higher scattering angles as compared to the number of planes favorably oriented for reflections at lower scattering angles, and the third is due to the fact that for a fixed slit width (or similarly, for intensity normalized to the number of pixels contributing to an annular bin), the fraction of the total Debye ring contributing the recorded intensity will be smaller at higher scattering angles (recall Figure 40). Using trigonometric identities, the three terms can be combined into a single term shown on the right-hand side of Equation 26. With regard to corrections made by FullProf, the multiplicity factor is automatically applied based on the unit cell type used in the model. There are a number of different Lorentz-polarization (*Lp*) factor corrections that can be applied, depending on the choice of experimental geometry. For the refinements presented in the following chapters, the *Bragg-Brentano or Debye-Scherrer Geometry* option was employed. The correction applied is given by:

$$Lp = \frac{1/2 + 1/2\cos^2 2\theta_{Mono}\cos^2 2\theta}{2\sin^2\theta\cos\theta} \tag{27}$$

The $\cos^2 2\theta_{Mono}$ term (part of the polarization correction term) is calculated by the user and input directly. Because a polarization correction was applied during image integration, this term can be set to zero, in which case Equation 27 reduces to Equation 26, which is precisely the Lorentz correction required.

The structure factor F_K is similar to that presented above in Equation 15, only in this case it also includes a correction for reduced intensity due to the oscillation of the atoms about their mean position (i.e., it accounts for thermal vibrations):

$$F_K = Fe^{-M}$$
$$M = 8\pi^2 u^2 \left(\frac{\sin\theta}{\lambda}\right)^2 \tag{28}$$

Where u^2 is the mean-squared displacement of the atom from its equilibrium position, θ is the Bragg angle (i.e., half of 2θ), and λ is the wavelength of monochromatic radiation.

There are many different types of peak profile functions $\phi(2\theta_i\text{-}2\theta_K)$ that can be employed using FullProf. The study of appropriate peak profile functions for different types of scattering (e.g., diffraction from synchrotron sources, conventional x-ray tubes, neutron sources, or electrons) makes up a significant topic of study in its own right. It is extremely important to be able to correctly model the peak shape of the observed diffraction pattern, as it determines the integrated intensity of the diffraction peak. The two most basic peak profile shapes are Gaussian and Lorentzian

$$G = \frac{C_0^{1/2}}{H_K \pi^{1/2}} e^{-C_0(2\theta_i - 2\theta_K)^2/H_K}; \; C_0 = 4\ln 2 \tag{29}$$

$$L = \frac{C_1^{1/2}}{H_K \pi} 1 \bigg/ \left[1 + C_1 \frac{(2\theta_i - 2\theta_K)^2}{H_K{}^2}\right]; \; C_1 = 4 \tag{30}$$

Here the H_K term describes the full width of the peak at half the maximum peak intensity (FWHM) of the K^{th} reflection. H_K varies with scattering angle, and the most common function used to model this variation was introduced by Cagliotti *et al.*[31]

$$H^2 = U\tan^2\theta + V\tan\theta + W \tag{31}$$

where U, V, and W are parameters in the least-squares refinement.

In practice, generally neither the Gaussian nor the Lorentzian profile function can provide an ideal fit to the observed peaks, so several other functions have been employed. The function used to model the peak profiles in the patterns presented in later chapters is called the pseudo-Voigt profile function. The Voigt function is a convolution of Gaussian and Lorentzian functions. The use of a true Voigt function, however, would require substantial computing power as each point in the calculated pattern would involve computing an integral. The pseudo-Voigt is simply a linear combination of a Gaussian and a Lorentzian function. It is employed in Rietveld software because it is a relatively good approximation to a Voigt function and it is computationally much less expensive. The pseudo-Voigt function is given by:

$$pV = \eta L + (1-\eta)G \tag{32}$$

where η has a range [0, 1] and is a parameter in the refinement.

Preferred orientation is a very common problem in powder x-ray diffraction. An ideal powder consists of a very large number of small crystallites with completely random orientations. However, because of a number of factors including the shape of the unit cell and sample preparation methods (i.e., packing a powder), the preferred orientation of crystallites is the rule rather than the exception. This affects the observed relative intensities of the various reflections as some of the reflections will be favored by the predominant orientation, while others with be discriminated against. Preferred orientation is particularly troublesome in the case of DAC crystallography as, again, samples are frequently "prepared" *in situ* under high-pressure conditions. The problem is exacerbated by the fact that the compression is uniaxial (i.e., parallel to the direction of the compression stroke determined by the cell design), and the high-pressure conditions are almost always non-hydrostatic. An example of preferred orientation as seen in a diffraction image is shown above in Figure 17, where the Debye rings associated with BaH_2 show marked variations in intensity as a function of the detector azimuthal angle. The function used during refinements to correct for this is given by:

$$P_K = e^{-G_1 \alpha_K{}^2} \tag{33}$$

where G_1 is the refinable parameter and α_K is the angle between the K^{th} reflection and the direction of preferred orientation (also called the fiber axis).

In general, the absorption correction *A* accounts for variations in intensity due to the absorption by the sample. The particular form of the correction depends on the particular diffraction geometry. No absorption correction was used for the refinements presented in this work. This is because the absorption due to the sample is insignificant compared to the absorption due to the anvils and seat, given the sample's small relative thickness. Note that the seats used were hemispherical to minimize the dependence of the absorption on the scattering angle. The increased path length through the diamond, however, will result in reduced intensity at increased scattering angles. This, however, is mitigated (or rather, overcompensated for) by the increased absorption of the imaging plate detector at increased scattering angles. Specifically, the x-rays striking the imaging plate at an angle "see" an effectively thicker imaging plate, resulting in increased intensity as compared to normal incidence. This constitutes the dominant 2θ-dependent absorption (although this is not absorption in the usual sense). The appropriate correction is given by:[32]

$$I_{corr} = \frac{I_{obs}}{[1-e^{(\ln T_{\perp}/\cos 2\theta)}]/1-T_{\perp}} \tag{34}$$

where $T_{\perp}$ is the transmission through the imaging plate at normal incidence and 2θ is the usual scattering angle. Again, in the case of images taken from samples contained in a DAC the approximation here is that the two effects mentioned above approximately cancel each other. The possibility of choosing an ideal x-ray wavelength, based on both the thickness of the diamonds and the thickness and composition of the imaging plate, for DAC crystallography is something I hope to explore in more detail in the near future.

Ideally, the model for the background, y_b, has a physical basis which models the various scattering phenomena (Compton scattering, temperature diffuse scattering) which gives rise to the background. In most cases, however, this is not feasible. This is particularly the case for DAC x-ray diffraction using an imaging plate, as the imaging plate records not just the scattering (both elastic and inelastic) from the sample, but also the scattering from the diamond anvils and parasitic scattering from upstream in the experimental configuration (e.g., the scattering of x-rays from air along the beam path). The most common methods for modeling the background use either a polynomial (with refinable coefficients) or a linear interpolation between a set of refinable background points. The latter method was used for most of the data in the following chapters.

The criteria most commonly used for assessing the quality of fit are called the R-factors and the goodness of fit:

$$R_{wp} = \left[\frac{\sum w_i(y_i - y_{ci})^2}{\sum w_i y_i^2}\right]^{1/2} \tag{35}$$

$$R_e = \left[(N-P)/\sum w_i y_i^2\right]^{1/2} \tag{36}$$

$$\chi^2 = \left[S_y/(N-P)\right] = \left[R_{wp}/R_e\right]^2 \tag{37}$$

R_{wp} is called *R weighted-pattern*, R_e is called *R expected*, *N* is the number of points *i* in the diffraction pattern, *P* is the number of refined parameters in the model, and χ^2 is called the *goodness of fit* (all other terms have been defined above). I will not discuss the significance of these criteria in any detail. However, in general a good fit is characterized by a χ^2 value close to 1, with a value significantly larger than 1 indicating a poor model and a value significantly less than 1 indicating there are more refined parameters in the model than appropriate given the nature of the experimentally observed diffraction pattern. These raw values for the various criteria must be viewed with some caution, and should only be considered as rough guidelines, as they can be significantly influenced by a number of factors that do not depend on model for the actual crystal structure (e.g., an intense background, counting statistics limited by the dynamic range of the detector, etc.). Because of this, a difference plot (the difference between the observed and calculated pattern) can serve as an equally powerful tool for determining the quality of the proposed structural model.

Figure 46 is an example of a Rietveld refinement carried out on the diffraction pattern of LaB_6 from Figure 38. Table 2 contains a list of the several of the refined parameters, values, and accompanying comments.

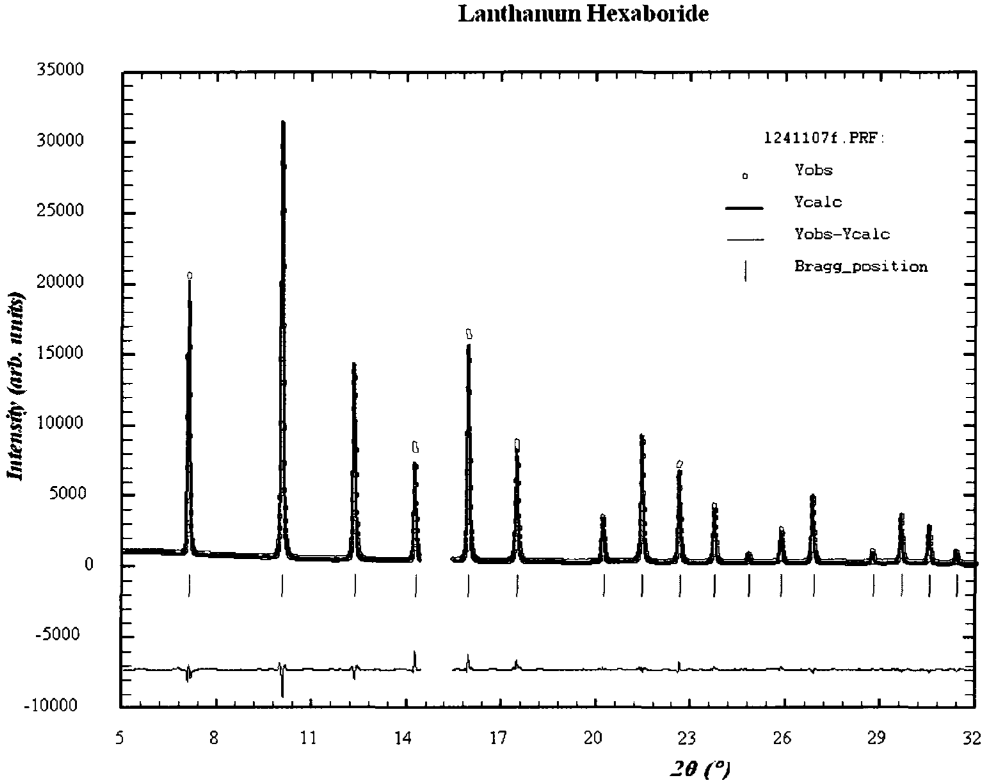

Figure 46: Rietveld refinement of the powder x-ray diffraction pattern of LaB_6 (obtained from the powder x-ray diffraction image shown in Figure 34) used as an example throughout this section on data reduction and analysis.

Model parameter	Value	Comments
Fixed parameters		
X-ray wavelength (Å)	0.515956	Determined from foil calibration
Scattering geometry	Debye-Scherrer	Employs *Lp* correction from Eq. 28
Polarization correction	None	Applied during integration, Eq. 28 reduces to Eq. 27
Background position (°)	51 points	Care taken not to position points in a reflection
Peak-width range (FWHM)	8	Cutoff for the purpose of intensity calculations
Excluded region (°)	14.5-15.5	Ignores gasket region for criteria of fit calculations
Number of phases	1	Fit only LaB$_6$ (not gasket)
Space group	*Fm-3m*	Defines a cubic lattice (+ symmetry considerations)
Wyckoff positions	1*a* (La), 6*f* (B)	Symmetry positions for atoms
Atom positions	Constrained	By symmetry, except B fractional *x*-coordinate
Occupancy (La and B)	Full	SRM carefully prepared (not sub-stoichiometric)
Variable parameters		
Scale	0.0018	Multiplied by calculated pat. to match observed pat.
Background intensity	Various	
Lattice parameter (Å)	4.1571	$\Delta a/a = 4\times10^{-5}$ (compared to NIST value)
Peak profile parameters		Pseudo-Voigt w/ peak asymmetry and $\eta(2\theta)$
U	-0.044	For these U, V, W: H (i.e., FWHM) ranges from 0.074-0.081° (exceptionally narrow due to synchrotron radiation)
V	0.010	
W	0.006	
η	0.272	Peak profile is predominantly Gaussian
X	0.192	A small variation of η *vs.* 2θ yields better fit
Asym. 1	-0.006	Allows for slight asymmetry in profile shape
Asym. 2	-0.007	Same as above
La isotropic disp. (Å^2)	0.950	Accounts for thermal vibration of La atoms
B isotropic disp. (Å^2)	0.194	Accounts for thermal vibration of B atoms
B fractional *x*-coordinate	0.192	In excellent agreement with published values
Criteria of fit		
R$_{wp}$ (%)	4.57	(Equation 35)x100
R$_e$ (%)	3.27	(Equation 36)x100
χ^2	1.95	Not ideal, but difference pattern is convincing

Table 2: Parameters, both fixed and variable, used for the Rietveld refinement shown above in Figure 46. Also shown are the criteria of fit.

I should make it clear at this point that a Rietveld refinement requires a proposed structure, and furthermore, if the structure is incorrect (i.e., the calculated and observed patterns do not agree), a Rietveld refinement does not yield an alternative structure. In short, it is a method for structure refinement, *not* structure solution. There are many methods for arriving at a proposed crystal structure, however, a description of these methods will not be presented here. I here mention that the proposed high-pressure structure (adopted by each of the heavy alkaline earth hydrides and barium fluoride) presented in the following chapters was arrived at by an iterative process. First, computational results on CaH_2 (the first compound studied, presented in Chapter 2) suggested a pressure-induced structural phase transition, but because of a close relationship between the ambient- and high-pressure structures, the calculations did not yield the unit cell of the high-pressure structure (specifically, there was a marked shift of the atomic positions in the coordinate system of the ambient-pressure unit cell). However, the experimental data from CaH_2 could be indexed (in the manner described in the previous section) to a hexagonal unit cell, and because of the relationship between the respective structures, a coordinate transformation of the atomic positions from the ambient-pressure structure to the high-pressure hexagonal unit cell was possible. During the analysis of BaH_2 (the next compound studied), an isostructural comparison with BaF_2[24] led to the high-pressure phase being explicitly identified as the Ni_2In structure. It is this proposed structure that was used as the starting point for the Rietveld refinements for the high-pressure phase.

9. Complementary methods

The primary focus of my research has been on carrying out angle-dispersive powder x-ray diffraction, using synchrotron radiation, on materials submitted to extreme pressure conditions in a diamond anvil cell. As such, the introduction has been similarly focused. However Chapters 2-5 include the results of Raman spectroscopy experiments and first-principles calculations which served a crucial role in the overall breadth and scope of the respective chapters. Here I present some of the most basic concepts associated with these complementary experimental and theoretical methods, and discuss their specific role in the studies presented in the following chapters.

Raman spectroscopy

Raman spectroscopy is a type of vibrational spectroscopy that probes the optical phonon spectrum a solid. The scattering process is inelastic; the incident photons (monochromatic) gain (anti-Stokes scattering) or lose (Stokes scattering) a small amount of energy upon scattering from the sample. The scattered light is spectrally dispersed using a spectrograph, and recorded using a charge-coupled device (CCD) detector. The wavelength of the scattered light with respect to the incident wavelength depends on the vibrational frequency of the atoms in the crystal. Raman spectroscopy is a powerful tool used, for example, in chemical analysis and the study of lattice dynamics. In the context of the work presented in the following chapters, Raman spectroscopy served three primary purposes. First, it was used to confirm the successful loading of pure hydrides. Second, it was used to identify structural phase transitions. And third, it was used to corroborate the proposed Ni_2In structure observed at high pressure in each of the heavy alkaline earth hydrides. Each of these aspects is briefly discussed below.

As mentioned above, the heavy alkaline earth hydrides are very sensitive to moisture in the atmosphere. Specifically, they react with water to form a hydroxide, releasing hydrogen gas in the process:

$$MH_2 + 2H_2O \rightarrow M(OH)_2 + 2H_2 \tag{38}$$

where M is the alkaline earth metal. Immediately after loading a hydride sample, Raman spectroscopy was carried out to ensure the characteristic Raman spectrum associated with the ambient-pressure phase was observed.

The occurrence of a structural phase transition in the heavy alkaline earth hydrides was clear from the Raman spectra, as they exhibited a marked change in the number of observed Raman modes. It is important to note here that the Raman spectra from the ambient- and high-pressure phases show such marked differences that the transition is clear even without any structural information about the respective phases.

In general, the number of Raman-active modes for a solid depends only on the number and position of the atoms in the unit cell (the observed frequency and intensity depend on a number of factors including the frequency and magnitude of the atomic vibrations, the orientation of the crystal(s) in the sample, the polarization state of the incident photons, etc.). For the proposed high-pressure Ni_2In structure, only two Raman modes should be observed. All of the high-pressure Raman spectra for the hydrides (save CaH_2) as well as those of barium fluoride exhibited two Raman modes. Note that there are certainly other possible structures that would give rise to only two modes, so it is for this reason I describe this as structure corroboration as opposed to structure confirmation.

Finally, as the pressure is increased, the total energy of the system increases (recall Figure 1). As a result, the frequencies of the atomic vibrations increase. This is indicated by the shift of Raman modes to higher frequencies with increasing pressure. The pressure-dependence of these shifts is reported in the following chapters for the benefit of other researchers who may use the data, for example, to characterize the lattice dynamics associated with the compression and phase transition(s) of a particular material or class of materials.

First-principles calculations

A discussed above in Section 1, a thermodynamic system will always adopt the state which minimizes the energy for the system (provided there are no barriers preventing the system from reaching this ground state). The experimental approach to determining this state is to measure (e.g., diffraction, spectroscopy, etc.). However this fails to appreciate that from a theoretical point of view, if one has an understanding of why a system adopts a particular state, one should be able to quantitatively predict what ground state a particular system will adopt, and furthermore, this prediction should be based on a physically meaningful model or explanation. In short, one should not have to measure, one should be able to calculate (at least, this is how one experimentalist views the situation).

Determining the ground state of a system involves finding the minimum of an equation which describes the energy of the system, *viz.*, the Schrödinger equation. The problem is that a real system (i.e., a material) has many particles, each of which may adopt any one of many possible energy states. It is an extremely complex (in the technical sense) problem. It turns out that the problem can be simplified considerably be expressing the energy of a system as a function of its electron density in space (i.e., the many body problem of the Schrödinger equation is reduced to a three-dimensional problem). This is what constitutes *Density Functional Theory.*

As suggested by the name of the theory, the electron density (the argument of the Energy function) has for its argument a function, called the *energy exchange correlation function*; it describes the potential between the electrons in the system. The problem is that the proper form of the exchange correlation function (i.e., the form that would yield the same ground state as that obtained by solving the many-bodied Schrödinger equation) is not known. However, approximations have been developed which yield very satisfactory results. Additional approximations have also been incorporated to reduce the computational expense of finding the minimum energy of the system. For example, rather than considering all of the electrons in the system in the calculation, the core electrons are kept fixed or “frozen”, and only the valence electrons are considered as part of the potential. The potential is then referred to as a pseudopotential.

While it is important from a theoretical point of view to be able to calculate the ground state of a system, it is sometimes also extremely practical. As an experimentalist, my approach is to measure, but it turns out that sometimes this is not feasible, or worse, the measurement may be compromised. I here provide a few specific examples. In Chapter 3 a phase transition is reported for barium hydride at a relatively low pressure. Recall that in order to properly characterize the compressibility of a material, it is necessary to have a relatively large compression over a relatively large pressure range. In the case of barium hydride, this was not possible due to the phase transition. Using first-principles calculations, the compression of the phase can be explored up to higher pressures by constraining the system (i.e., forcing it to adopt a particular structure), allowing a larger compression for determining the equation of state parameters. The experimental data can then be analyzed keeping some parameters (e.g., B_0') fixed to a reasonable value based on the first-principles calculations. Another excellent example of how first-principles calculations benefited this study is presented in Chapter 4 on barium fluoride. I first carried out diffraction experiments up to about 80 GPa under non-hydrostatic pressure conditions. The experimental data, however, did not agree with my collaborators' calculations. They repeated the calculations using a slightly more (computationally) expensive pseudopotential, and the new results were in accord with their previous calculations. Suspecting complications due to non-hydrostatic pressure conditions, subsequent experiments were carried out using helium as a pressure-transmitting medium, and the resulting data were in excellent agreement with the first-principles calculations. This was particularly important in clearing up difficulties with previous results on BaF_2, as it has served as an important structural archetype for proposing the Ni_2In structure for the high-pressure phases of the hydrides. In short, I am very grateful for (and the present work has benefited greatly from) the theoretical calculations carried out by my collaborators.

10. The heavy alkaline earth hydrides

The alkaline earth metals constitute Group II of the periodic table of the elements, which includes beryllium, magnesium, calcium, strontium, barium, and radium. All except radium are known to bond with hydrogen to form binary hydrides, MH_2 (M=alkaline earth metal). A casual search of the scientific literature reveals much research on the alkaline earth hydrides in a wide variety of contexts. The motivation for studying them as a function of pressure is multifaceted. I repeat here some of the contexts mentioned earlier, for example, hydrogen storage and exchange, hydrogen lattice dynamics, systematics in ionic AX_2 compounds, and insulator-metal transitions. The initial motivation, however, came from an article on MgH_2.

Shortly before the experiments presented in the following chapters were started, a structural study of MgH_2 at high pressure was published by Moriwaki *et al.*,[33] who reported several pressure-induced phase transitions, and specifically, reported that above approximately 17 GPa MgH_2 adopts the cotunnite-type structure. This structure was stable up to the maximum pressure of the study, 57 GPa. Interestingly, CaH_2, SrH_2, and BaH_2 all adopt this structure at ambient conditions (it is this shared structure which constitutes the classification of the heavy alkaline earth hydrides). The initial motivation for studying CaH_2 was to look for high-pressure phases which, in turn, might suggest the structure of a possible high-pressure phase in MgH_2 above 57 GPa. After identifying a pressure-induced structural phase transition in CaH_2, it was a natural continuation to investigate the other heavy alkaline earth hydrides, and as it turns out, barium fluoride—an important structural analogue. The additional motivation prompting a systematic study of these compounds goes well beyond the search for possible structures of MgH_2 at pressures greater than 57 GPa. Inasmuch as this interest developed over time, with each successive series of experiments, the following chapters present the related articles in the order they were published (save Chapter 6, which deals not with a specific compound, but with selected experimental techniques employed in each of the prior articles). My hope is that this will clearly show the continued and growing interest which culminated in the systematic study that constitutes this work. Following the articles, a short concluding chapter brings together the combined results of the individual works.

---

[1] J. P. Poirier, *Introduction to the Physics of the Earth's Interior*, Cambridge University Press, Cambridge, 1991.
[2] http://nobelprize.org/nobel_prizes/physics/laureates/
[3] J. C. Jamieson, A. W. Lawson, and N. D. Nachtrieb, Rev. Sci. Ins. **30**, 1016 (1959).
[4] C. E. Weir, R. E. Lippincott, A. Van Valkenburg, and E. N. Bunting, J. Res. Natl. Bur. Stand., Sec. A **63**, 55 (1959).
[5] A. L. Ruoff, H. Xia, and Y. Vohra, Rev. Sci. Ins. **61**, 3830 (1990).
[6] A. Jayaraman, Rev. Mod. Phys. **55**, 65 (1983).
[7] V. B. Prakapenka, A. Kubo, A. Kuznetsov, A. Laskin, O. Shkurikhin, P. Dera, M. L. Rivers, and S. R. Sutton, High Press. Res. **28**, 225 (2008).
[8] D. Drukker and Zn N. V., Amsterdam.
[9] R. Boehler and K. De Hantsetters, High Press. Res. **24**, 391 (2004).
[10] M. Eremets, *High Pressure Experimental Methods*, Oxford University Press, Oxford, 1996.
[11] A. Van Valkenburg, *Conference internationale sur les hautes pressions*, Le Creusot, Saone-et-Loire, France (1965).
[12] R. A. Forman, G. J. Piermarini, J. D. Barnett, and S. Block, Sicence **176**, 284 (1972).
[13] H. K. Mao, P. M. Bell, J. W. Shaner, and D. J Steinberg, J. Appl. Phys. **49**, 3276 (1978).
[14] H. K. Mao, J. A. Xu, and P. M. Bell, J. Geophys. Res. **91**, 4673 (1986).
[15] A. Dewaele, M. Torrent, P. Loubeyre, M. Mezouar, Phys. Rev. B **78**, 104102 (2008).
[16] D. E. McCumber and M. D. Sturge, J. Appl. Phys. **34**, 1682 (1963).
[17] G. J. Piermarini, S. Block, and J. D. Barnett, J. Appl. Phys. **44**, 5377 (1973).

---

[18] I. Fujishiro, G. J. Piermarini, S. Block, and R. G. Munro, Proc. 8th AIRAPT Conference Uppsala, **II**, 608 (1982).

[19] S. Klotz, J-C Chervin, P. Munsch, and G. Le Marchand, J. Phys. D: Appl. Phys., **42**, 075413 (2009).

[20] LabView Virtual Instrument code written by R. Bolen.

[21] M. Sonoda, M. Takano, J. Miyahara, and H. Kato, Radiology **148**, 833 (1983).

[22] P. Coppens (with contributions from D. Cox), *Synchrotron radiation crystallography*, Academic Press, London, 1992.

[23] M. Mezouar, W. A. Crichton, S. Bauchau, F. Thurel, H. Witsch, F. Torrecillas, G. Blattmann, P. Marion, Y. Dabin, J. Chavanne, O. Hignette, C. Morawe, and C. Borel, J. Synchrotron Rad. **12**, 659 (2005).

[24] J. M. Leger, J. Haines, A. Atouf, O. Schulte, and S. Hull, Phys. Rev. B **52**, 13247 (1995).

[25] A. J. C. Wilson, ed, *International tables for crystallography, Volume C*, Dordrecht, Boston, 1992.

[26] A. P. Hammersley, S. O. Svensson, M. Hanfland, A. N. Fitch, and D. Häusermann, High. Press. Res. **14**, 235 (1996).

[27] R. Kahn, R. Fourme, A. Gadet, J. Janin, C. Dumas, and D. Andre, J. Appl. Cryst. **15**, 330 (1982).

[28] S. L. Barna, M. W. Tate, S. M. Gruner, and E. F. Eikenberry, Rev. Sci. Ins. **70**, 2927 (1999).

[29] H. M. Rietveld, Acta Cryst. **21**, A228 (1966).

[30] J. Rodriguez-Carvajal, Physica B **192**, 55 (1993).

[31] G. Cagliotti, A. Paoletti, and F. P. Ricci, Nucl. Inst. Methods **35**, 223 (1958).

[32] J. Zaleski, G. Wu, and P. Coppens, J. Appl. Cryst. **31**, 203 (1998)

[33] T. Moriwaki, Y. Akahama, H. Kawamura, S. Nakano, and K. Takemura, J. Phys. Soc. Jpn. **75**, 074603 (2006).

Topical Bibliography

The following is a list of selected works which explore in greater detail each of the various topics presented in the introduction. Of course, the list is not exhaustive. Rather, it includes works that I have found particularly helpful in my own studies.

The study of materials as a function of pressure

Lin-gun Liu and William A. Bassett. *Elements, oxides, and silicates: high-pressure phases with implications for the earth's interior* (Oxford University Press, Oxford, 1986).

The bulk of this work comprises a reference of P-T phase diagrams, grouped in such a way as to facilitate a presentation of general trends for various classes of elements and compounds (e.g., the relationship among the molar volume, cation-anion distance, and coordination number in ionic compounds). It also includes a concise introduction to thermodynamics from the pressure point of view, static and dynamic pressure generating methods, and a list of the various types of experiments that can now be carried out as a function of pressure.

Jean-Paul Poirier. *Introduction to the physics of the earth's interior* (Cambridge University Press, Cambridge, 1991).

An excellent introduction to a number of topics related to the pressure-dependent study of materials, with particular emphasis on theory. It includes a number of issues not covered in this introduction, such as elastic moduli and lattice vibrations, melting, dynamic pressure experiments, and several different types of equations of state.

The diamond anvil cell and related experimental techniques

Mikhail I. Eremets. *High pressure experimental methods* (Oxford University Press, Oxford, 1996).

This is arguably the most complete, up-to-date reference for the high-pressure experimentalist. It includes very detailed and meticulously referenced sections on static pressure generation, design and operation of high-pressure devices (with particular emphasis on diamond anvil cells), pressure measurement techniques, general experimental techniques (e.g., DAC and gasket preparation), and basic concepts related to a number of different experimental methods (e.g., low-temperature applications, optical measurements, etc.)

Wilfried B. Holzapfel and Neil S. Isaacs, Editors. *High-pressure techniques in chemistry and physics: a practical approach* (Oxford University Press, Oxford, 1997).

This is also a fine reference for the high-pressure experimentalist. It focuses less on experimental design and techniques, and more on the different experimental methods and resulting data.

A. Jayaraman. *Diamond anvil cell and high-pressure physical investigations*, Review of Modern Physics **55**, 65-107 (1983).

Although not quite as up to date as the previous works, this review article is a classic in the high-pressure literature, and contains a wealth of information regarding types of DACs, types of high-pressure measurements, and a number of important experimental techniques.

Andrzej Katrusiak and Paul McMillan, editors. *High-pressure crystallography* (Kluwer Academic Publishers, Dordrecht, 2004).

An excellent reference containing articles on a number of topics including data analysis strategies and workflow, various types of equations of state, high-pressure experimental methods and techniques, structure determination in the context of high-pressure crystallography, etc.

Synchrotron radiation

Grant S. Henderson and Don R. Baker, editors. *Synchrotron radiation: earth, environmental and material sciences applications* (Mineralogical Association of Canada, Ottawa, 2001).

Written specifically with the Canadian Light Source in mind, the introduction covers the production and basic properties of synchrotron radiation. Subsequent chapters consider specific experimental techniques made possible by the Phase I beamlines at the CLS.

Dennis M. Mills. *Third-generation hard x-ray synchrotron radiation sources: source properties, optics, and experimental techniques* (Wiley, New York, 2002).

A treatment of the innovations particular to third-generation sources (e.g., insertion devices) and the corresponding innovations in experimental methods.

Herman Winick, editor. *Synchrotron radiation sources: a primer* (World Scientific, Singapore, 1994).

A detailed and technical work perhaps intended more for synchrotron radiation facility staff than for the users who visit to carry out research. Nevertheless, there are some lucid and informative sections describing basic properties of synchrotron radiation.

Powder x-ray diffraction

Philip Coppens (with contributions from David Cox). *Synchrotron radiation crystallography* (Academic Press Ltd., London, 1992).

An invaluable resource to the crystallographer using synchrotron radiation, this work examines problems in x-ray crystallography that are well-met by the use of synchrotron radiation. In includes excellent discussions on technical aspects (e.g., beamline optics, beamline polarization, monochromator design and performance, etc.)

B. D. Cullity and S. R. Stock. *Elements of x-ray diffraction, third edition* (Prentice Hall, New Jersey, 2001).

As introductory texts go, this is a *tour de force*, covering x-ray scattering, crystallography, diffractions techniques, and practical applications. Given the wide scope of the work, some of the discussions are not exhaustive, but they nevertheless serve as an excellent foundation.

B. E. Warren. *X-ray diffraction* (Addison-Wesley, Reading, 1969).

This is a classic text, containing a more detailed mathematical treatment of many of the topics covered in Cullity and Stock.

Rietveld refinement

R. A. Young, editor. *The Rietveld method* (Oxford University Press, Oxford, 1995).

A comprehensive work on Rietveld refinement, covering basic principles, a mathematical description, details regarding the various parameters which constitute the complete model, quality of fit criteria, refinement strategies, etc

Raman spectroscopy

Ian R. Lewis and Howell G. M. Edwards, editors. *Handbook of Raman spectroscopy: from the research laboratory to the process line* (Marcel Dekker, New York, 2001).

A comprehensive reference including an exposition of the Raman effect, thorough descriptions of various spectrograph geometries, detectors, excitation sources (lasers), data collection, and data analysis, and a section on Raman spectroscopy on samples contained in a diamond anvil cell.

Richard L. McCreery. *Raman spectroscopy for chemical analysis* (John Wiley & Sons, New York, 2000).

An excellent reference including concise discussions on the Raman effect, suitable equipment, data collection and analysis, etc. As the title suggests, much of the work is dedicated to chemical analysis.

First-principles calculations (density functional theory)

Robert G. Parr and Weitao Yang. *Density functional theory of atoms and molecules* (Oxford University Press, Oxford, 1994).

A thorough reference which starts with a review of the many-particle problem in quantum mechanics to motivate a detailed treatment of density functional theory. The work includes a review of the early development of density functional theory, together with the developments of Kohn and Sham in the 1960's. From there it explores a number of different approaches to first-principles calculations in the context of density functional theory.

See also several chapters in *High-pressure crystallography* referenced above.

Metal hydrides

Kenneth M. Mackay. *Hydrogen compounds of the metallic elements* (Spon, London, 1966).

Although an older text, this work includes much useful information including classification of metallic hydrides by bond type, hydride synthesis, safety considerations, etc.

Maurizio Peruzzini and Rinaldo Poli, editors. *Recent advances in hydride chemistry* (Elsevier Science Ltd., Amsterdam, 2001).

Although broad in scope, this work includes much useful information about hydrogen bonding, common crystal structure types, hydrogen storage and exchange systems, etc.

Chapter 2 Structural phase transition in CaH_2 at high pressures

as published in Physical Review B, Volume 75, Article Number 134108, 2007.

PHYSICAL REVIEW B **75**, 134108 (2007)

Structural phase transition in CaH_2 at high pressures

J. S. Tse,[1] D. D. Klug,[2] S. Desgreniers,[3] J. S. Smith,[3] R. Flacau,[3] Z. Liu,[4] J. Hu,[4] N. Chen,[5] and D. T. Jiang[6]
[1]*Department of Physics and Engineering Physics, University of Saskatchewan, Saskatoon, Saskatchewan, Canada S7N 5E2*
[2]*Steacie Institute for Molecular Sciences, National Research Council of Canada, Ottawa, Ontario, Canada K1A 0R6*
[3]*Laboratoire de physique des solides denses, Department of Physics, University of Ottawa, Ottawa, Ontario, Canada K1N 6N5*
[4]*Geophysical Laboratory, Carnegie Institution of Washington, 5251 Broad Branch Road Northwest, Washington, DC 20015, USA*
[5]*Canadian Light Source, University of Saskatchewan, Saskatoon, Saskatchewan, Canada S7N 0X4*
[6]*Department of Physics, University of Guelph, Guelph, Ontario, Canada N1G 2W1*

(Received 12 October 2006; revised manuscript received 16 February 2007; published 26 April 2007)

The structural and vibrational properties of CaH_2 have been examined up to 30 GPa at room temperature. Under ambient conditions, CaH_2 has a *Pnma* (cotunnite-type) structure. A structural phase transformation was observed around 15 GPa and completed at 20 GPa. The high pressure structure is identified as hexagonal $P6_3/mmc$. First-principles calculations reproduced the first-order nature of the transition. Since $P6_3/mmc$ is a supergroup of *Pnma* the structural change can be traced back to gradual displacements of the hydrogen atoms from the 4*c* positions in the cotunnite structure to the special 2*a* and 2*d* positions in the hexagonal structure. The observed phase transition pressure is much lower than that predicted for MgH_2.

DOI: 10.1103/PhysRevB.75.134108 PACS number(s): 62.50.+p, 61.10.−i

INTRODUCTION

Alloys of metal hydrides are potential efficient hydrogen storage materials.[1] Simple group I and II hydrides such as LiH and MgH_2, due to low atomic weights of the cations, have been seriously considered as good contenders. On the other hand, hydrides of heavier elements, such as the alkaline metal hydride CaH_2, even with the heavier metal ion, have a favorable H_2 specific mass for safe and efficient generation of hydrogen gas from the reaction with water. Therefore, CaH_2 remains a competitive hydrogen carrier medium.[2] Many properties of metal hydrides have been well characterized. There is substantial interest to explore possible metastable high pressure polymorphs with novel structures and properties that may be quenched to ambient conditions for practical applications.[3,4] Recently, it was predicted that metallic hydrides under high pressure can also be good candidate materials with very high superconducting critical temperatures.[5] These materials are suggested to be potential candidates since it is possible that electronic bands associated with the hydrogen may strongly couple with optical phonons. It was proposed that high-frequency hydrogen vibrations and the low-frequency motions of the metal ions will help to enhance the electron-phonon coupling processes. Metal hydrides are insulators under normal condition. However, like many other materials, it is plausible that they may undergo insulator-metal transitions under pressure. For metal hydrides with heavier and more polarizable ions such as CaH_2 and BaH_2, the metallization transition may even occur at moderate pressures.

Recently, structural transformations have been reported for MgH_2 at high pressure.[6] MgH_2 exists in the rutile structure under ambient pressure.[6] Upon compression, it undergoes successive solid-to-solid transformations. Above 17 GPa it transforms to a cotunnite structure (space group *Pnma*) which is stable up to at least 57 GPa. A high pressure transformation sequence was first suggested from first-principles calculations.[6] Although the exact route found computationally for the structural transition was not identical to that observed, nonetheless the stability of the high pressure cotunnite phase was correctly predicted. Interestingly, another higher pressure phase with the Ni_2In (hexagonal $P6_3$) structure was predicted from the calculations to exist at much higher pressure but has not yet been observed.[4] It should be noted that in the proposed $P6_3$ structure[4] the atoms are located in symmetry sites and the space group is identical to $P6_3/mmc$. In comparison, CaH_2 under ambient conditions already adopts the cotunnite structure.[7,8] The main objective of this study is to investigate the possibility of the existence of a hexagonal phase at moderate pressure.

In this paper, results on x-ray diffraction and Raman spectroscopy and theoretical investigations on the high pressure stability of CaH_2 are reported. A high pressure phase with a hexagonal unit cell was found at pressures higher than 15 GPa. In the next section, the experimental and theoretical procedure will be described. Details of the structure and lattice vibrations and comparison with theoretical calculations will be made in the ensuing paragraphs.

EXPERIMENTAL AND THEORETICAL DETAILS

CaH_2 (99.9%, Sigma Aldrich) was loaded into a diamond anvil cell (DAC) under an Ar inert atmosphere without a pressure medium; since the sample is highly moisture sensitive it hydrolyzes readily with commonly used pressure transmitting media like methanol/ethannol mixture or silicone oil. X-ray diffraction patterns were obtained at beamline X17C at the National Synchrotron Light Source (run 1) and the Hard X-ray Micro-Analysis (HXMA) beamline (run 2) at the Canadian Light Source (CLS). The X17C beamline is equipped with a seven-pole superconducting wiggler with 17.4 cm period operating at 4.2 T. Synchrotron radiation monochromatized to 0.4066 Å with a pair of sagitally bent Si (001) Laue crystals was further focused on the sample with Kirkpatrick-Baez 100 mm × 100 mm mirrors. At the HXMA beamline (run 2), synchrotron radiation from a 63–

pole superconducting wiggler was monochromatized to 0.48595 Å with Si (220) crystals and focused by a Rh coated torodial mirror, further collimated to a spot with a diameter of 30 μm. X-ray diffraction images were recorded on FUJI and ST-VI imaging plates and processed with FIT2D.[9] X-ray diffraction patterns were analyzed using XRDA[10] and Rietveld refinements were performed with FullProf.[11] High pressure diamond anvil cells were used for all experiments. The culets of the diamond anvils were 300 μm in diameter. The ruby fluorescence technique[12] was used to measure pressure. High-pressure Raman measurements were made using a Coherent Innova 90 Plus argon ion laser to obtain the Raman spectra with the 514.5 nm laser line being used for excitation. The scattered light from the sample was focused into a Jobin-Yvon spectrograph equipped with a CCD detector.

First-principles electronic structure calculations were carried out using the plane-wave pseudopotential method within the framework of density functional theory with the software package VASP.[13] Projected augmented wave pseudopotentials[14] for Ca and H from the pseudopotential library were used. For Ca, $2p$ and $3s$ electrons were treated as valence. The Perdew-Wang 91 generalized gradient approximation exchange-correlation functional was employed. Monkhorst-Pack grids[15] of $12\times12\times12$ and $6\times12\times8$ were used for the electronic Brillouin zone integration in the hexagonal and orthorhombic structure, respectively. The cell shape and atomic positions were optimized at selected volumes and the corresponding pressures were computed from the stress tensor. Phonon calculations at the Brillouin zone center were carried out with the program ABINIT.[16] Trouiller-Martins-type pseudopotentials[17] employing an energy cutoff of 65 Hartree with the generalized gradient approximation of Perdew *et al.*[18] were employed.

RESULTS AND DISCUSSION

In run 1, x-ray diffraction patterns were collected after the loading of CaH_2 in the DAC. The pressure was initially at 16 GPa. The complicated powder x-ray diffraction pattern was found to be a mixture of the starting cotunnite structure with a minor unknown phase [Fig. 1(a)]. The intensity of the x-ray diffraction features attributed to the minority phase weakened when the pressure was released gradually from 16 GPa, which led to a full recovery of the pure cotunnite phase below 12 GPa. At 5 GPa the lattice parameters for the orthorhombic unit cell were $a=5.68(4)$, $b=3.51(2)$, and $c=6.66(2)$ Å. The sample was then recompressed from 5 GPa. Again, the diffraction patterns indicated the existence of a mixed phase at 15 GPa, but above 20 GPa the pattern became very simple, indicating the complete transformation to a higher symmetry phase. The diffraction pattern at 25 GPa was indexed to a hexagonal unit cell with $a=3.54(1)$ and $c=4.58(1)$ Å. The hexagonal cell can also be expressed as an equivalent orthorhombic cell with $a=4.58(1)$, $b=3.54(1)$, and $c=6.13(2)$ Å. The experimental equation of state shown in Fig. 2 indicates a first-order transition with a volume change of about 8% across the transition.

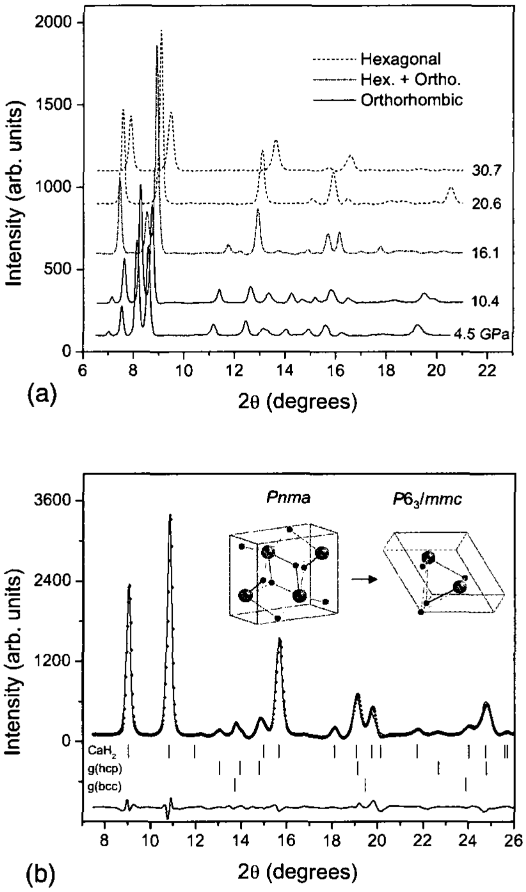

FIG. 1. (Color online) (a) (Top panel) X-ray diffraction pattern from run 1. Note that the initial pressure was 16 GPa in which the sample was already a mixture of the low pressure *Pnma* phase and high pressure $P6_3/mmc$ phase. The sample pressure was then decreased to 5 GPa and subsequently increased to finally reach 30 GPa. Background has been subtracted from all patterns and offsets have been introduced for clarity. (b) (Bottom panel) X-ray diffraction pattern (symbols) recorded at 22.9 GPa in run 2 and Rietveld fit (solid line) considering a mixture of three phases, namely, high-density CaH_2 ($P6_3/mmc$), hexagonal stainless steel gasket T301 ($P6_3/mmc$), and cubic stainless steel gasket T301 (Im-$3m$). For the CaH_2 phase, Ca atomic positions as fixed by symmetry and full site occupancies are assumed. Preferred orientation for the high-pressure hydride and the stainless steel gasket, both hexagonal phases, has been taken into account. The R factors for the Rietveld fit (FullProf) are $R_{\text{exp}}=7.8\%$, $R_{\text{wp}}=10.3\%$, and $R_{\text{wp}}/R_{\text{exp}}=1.3$. The bottom trace shows the difference between the Rietveld fit and the experimental data. The inset illustrates the low- and high-density structure models for CaH_2.

Significantly higher quality powder x-ray diffraction patterns [Fig. 1(b)] were subsequently measured on the HXMA beamline at CLS. In run 2, the initial pressure following loading of the sample in the DAC was below 1 GPa. The x-ray diffraction images could thus be recorded progressively as a function of increasing pressure. The x-ray diffraction pattern obtained at 5.2 GPa showed only the Bragg reflections from the ambient cotunnite structure giving unit cell parameters $a=5.760(9)$, $b=3.502(8)$, and $c=6.68(1)$ Å. In-

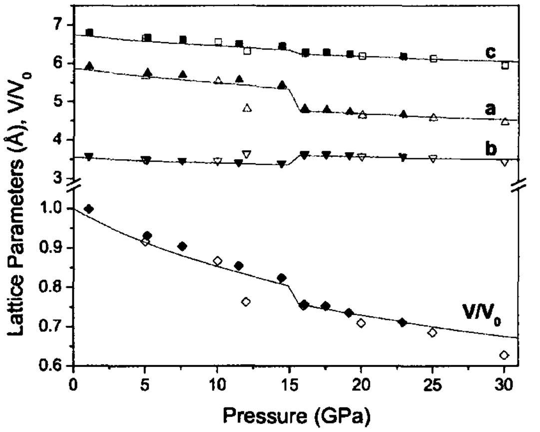

FIG. 2. (Color online) Room temperature pressure dependence of lattice parameters and relative unit cell volume of the orthorhombic *Pnma* and hexagonal $P6_3/mmc$ (in the orthorhombic setting) phases of CaH_2. Open and solid symbols distinguish results obtained in run 1 and run 2, respectively. Data points below 16 GPa were recorded with decreasing pressures in run 1. Solid lines represent theoretical calculations.

creasing pressure showed a phase transition at 14–16 GPa. Once again, the x-ray diffraction pattern of the high pressure phase can be indexed to a hexagonal unit cell ($P6_3/mmc$) with atoms at Wyckoff positions 2*c* (Ca), 2*d* (H), and 2*a* (H). At 22.9 GPa the equivalent orthorhombic cell parameters are $a=4.667(1)$, $b=3.571(3)$, and $c=6.185(6)$ Å. The x-ray diffraction pattern for the $P6_3/mmc$ phase observed at 22.9 GPa and the corresponding Rietveld fit are shown in Fig. 1(b). The Rietveld refinement was carried out with Ca^{+2} located at symmetry positions 2*c* (1/3, 2/3, 1/4) and full site occupancy and by taking into account preferred orientation, as was observed in the x-ray diffraction images of hexagonal CaH_2. X-ray scattering from hydrogen atoms was neglected. The small mismatch between the observed and model patterns [Fig. 1(b)] and x-ray diffraction arising for the gasket material can be explained most likely by preferred orientation not fully corrected and by less-than-optimal x-ray beam collimation. Owing to the better quality sample, improved x-ray diffraction resolution and the lack of overlapping patterns near the phase transition pressure, a more precise equation of state was obtained (Fig. 2). Results of run 2 confirmed the previous observation that a first-order structural phase transition occurs in CaH_2 and is found complete at 16 GPa.

High pressure Raman spectra for CaH_2 are reported in Fig. 3. In run 1, at 16.1 GPa, the Raman spectrum in the region 150–1000 cm^{-1} shows four bands centered at 180, 239, 290, and 840 cm^{-1} and a weak feature at 214 cm^{-1}. The four band Raman spectrum is in good agreement with a reported spectrum recorded under ambient condition.[6] Upon the release of pressure, the weak feature disappears below 12 GPa. This observation closely follows the variation of the diffraction patterns in run 1. Therefore, this weak band is almost certainly associated with the high pressure hexagonal phase which was mixed with the cotunnite phase from 12 to 16 GPa. When the CaH_2 sample is recompressed from 4.5 GPa, the four band Raman spectrum of the cotunnite structure is maintained until 15.3 GPa, upon which the small band at 200 cm^{-1} reemerges indicating the onset of the structural phase transition. At 20 GPa, the initial cotunnite spectral features vanished and a very simple one band Raman spectrum was observed up to 30.7 GPa, the highest pressure reached in run 1. The simplicity of the Raman spectrum again confirms that the high pressure phase indeed possesses a space group symmetry higher than the lower pressure orthorhombic *Pnma* phase. The variation of Raman band frequencies with pressure is shown in Fig. 3(b).

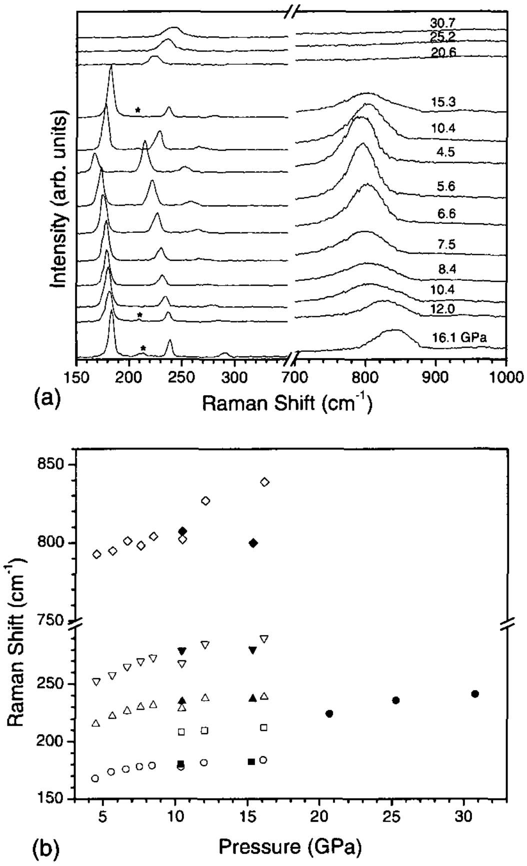

FIG. 3. (Color online) Raman data for run 1. (a) (Top panel) Raman spectra as a function of pressure, following the sequence of pressure changes from bottom to top. The asterisk indicates the Raman line due to the high-pressure phase in the case of phase mixtures. (b) (Bottom panel) Pressure dependence of the Raman shifts for decreasing pressures (open symbols) and increasing pressures (solid symbols).

All experimental evidence unambiguously indicates that a first-order structural transformation occurs around 16 GPa in CaH_2. Analysis of the x-ray diffraction data suggests the high pressure phase has a hexagonal unit cell, which can also be represented by an orthorhombic unit cell. To characterize the structure of the high pressure phase and the mechanism of the transformation, first-principles electronic structure calculations were performed. The starting point of the calculation

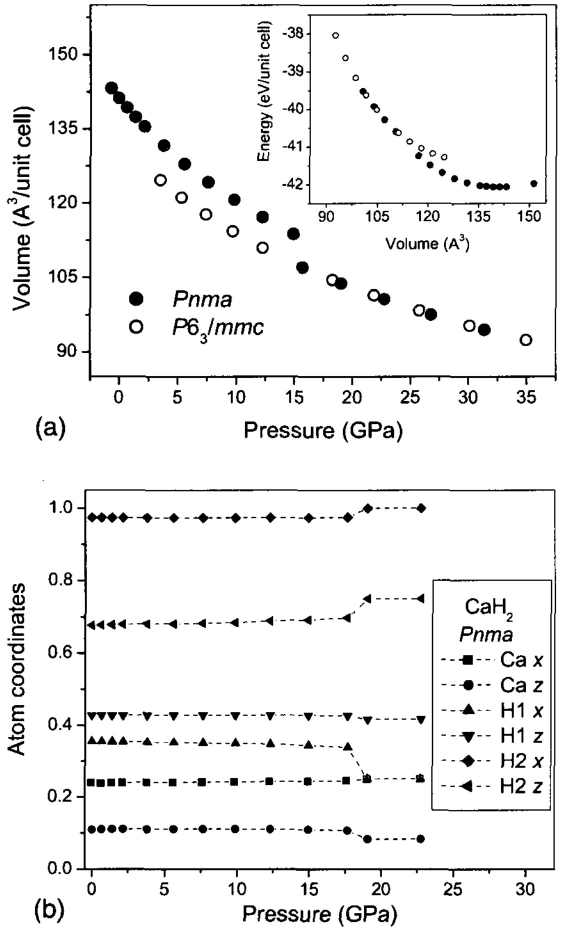

FIG. 4. (Color online) (a) (Top panel) Unit cell volume calculated as a function of pressure. The data points (open symbols) for the $P6_3/mmc$ are those for the equivalent orthorhombic setting. The inset illustrates the change of total energy for both phases. (b) (Bottom panel) Atomic coordinates calculated as a function of pressure.

was the ambient *Pnma* structure. Geometry optimization at 0 GPa gave a unit cell $a=5.881$, $b=3.559$, and $c=6.751$ Å and the following atomic positions: Ca ($x=0.2394$, $z=0.1104$), H_I ($x=0.3556$, $z=0.4276$), and H_2 ($x=0.9742$, $z=0.6770$). These values compare favorably with the experimental neutron structure of CaD_2 (Ref. 8) of $a=5.925(1)$, $b=3.581(1)$, and $c=6.776(1)$ Å and Ca [$x=0.2378(13)$, $z=0.1071(8)$], D_I [$x=0.3573(6)$, $z=0.4269(7)$], and D_2 [$x=0.9739(6)$, $z=0.6766(5)$]. Variation of the total energy and the volume of the *Pnma* phase of CaH_2 with pressure are shown in Fig. 4(a). These curves show a normal volume-pressure and energy-volume dependence until the pressure reaches 15 GPa. At this pressure the curves deviated and followed a different trend to higher pressures. The abrupt change in the energy is due to a structural phase transition. In the *Pnma* space group the Ca atoms and two unique H atoms occupy the Wyckoff 4*c* positions. The change in the internal atomic coordinates with pressure is shown in Fig. 4(b). At pressures below 17 GPa there are no significant changes in the atomic positions. However around 17 GPa, sudden shifts of the H_I x coordinate and H_2 z coordinate to the special positions $\frac{1}{4}$ and $\frac{3}{4}$, respectively, were observed. Simultaneously the Ca position shifts to $(\frac{1}{4},\frac{1}{4},0)$. Analysis of the atomic positions revealed that the *Pnma* structure has transformed to hexagonal $P6_3/mmc$ with both the Ca and H located in special positions: 2*c* (Ca), 2*d* (H_I), and 2*a* (H_2). First-principles calculations in the higher symmetry $P6_3/mmc$ space group led to almost identical energies and unit cell volumes with the *Pnma* structure at pressures above 19 GPa [Fig. 4(b)]. Significantly, the calculated unit cell parameters in the orthorhombic representation are almost in quantitative agreement with the experimental observation as illustrated in Fig. 2. The discontinuities in the unit cell parameters observed at 16 GPa are clearly reproduced by the calculations. Since all the atoms are in symmetry sites, a Rietveld fit was carried out with preferred orientation of CaH_2 crystallites as the main correction, as shown in Fig. 1(b). The calculated diffraction patterns are in good agreement with experiment. In the high pressure hexagonal structure, the Ca atom is surrounded by three nearest neighbor H atoms and six second nearest neighbor H atoms. At 23 GPa, the calculated closest Ca [Fig. 1(b), inset] and H separations are 2.045, 2.315, and 2.350 Å. Each H atom is surrounded by five Ca atoms in a trigonal-pentagonal environment.

The theoretical high pressure CaH_2 structure is also consistent with spectral changes observed in the Raman spectra. It is expected the number of vibrational modes be reduced from a low- to high-symmetry structure. A factor group analysis on the $P6_3/mmc$ structure shows that only one Raman active band is expected in the 150–1000 cm^{-1} region. This prediction is verified by experiment as only one Raman peak is observed at pressure higher than 16 GPa. In fact, the calculated frequency for this band of 211 cm^{-1} at 19 GPa corresponds very well to the Raman band observed at 225 cm^{-1} at 20.6 GPa.

CONCLUSIONS

The crystalline structure of CaH_2 has been studied under high pressure up to 30 GPa. A structural phase transition from the ambient cotunnite *Pnma* structure to a hexagonal $P6_3/mmc$ structure has been unambiguously identified around 16 GPa from x-ray diffraction and Raman experiments and first-principles electronic calculations. The hexagonal phase is structurally identical to the $InNi_2$ structure ($P6_3$) predicted for high pressure MgH_2, however it has not been observed at pressures up to 57 GPa.[6] In contrast, in CaH_2, the phase transition occurs at substantially lower pressure. The present results suggest that the hexagonal structure should be achievable in MgH_2 at higher pressure. The hexagonal structure, however, remains an insulator and much higher pressure is needed to achieve metallization. Therefore, group II hydrides may not be convenient candidates for the exploration of superconductivity property at low pressure.

Note added in proof. We have been made aware of a previous high pressure x-ray study on CaH_2 (Ref. 19). The x-ray diffraction, spectroscopic, and theoretical results presented here are in agreement with the x-ray diffraction results of Kinoshita *et al.*

ACKNOWLEDGMENTS

J.S.T. and S.D. acknowledge the financial support of NSERC. J.S.T. also wishes to thank the CFI and the Canada Research Chair Program for support. Raman and preliminary x-ray measurements were performed at the U2A and X17C beamlines at the NSLS of BNL (DOE Contract No. DE-AC02-98CH10886). The U2A and X17C beamlines are supported by COMPRES, the Consortium for Materials Properties Research in Earth Sciences under NSF Cooperative Agreement Grant No. EAR01-35554, and the U.S. Department of Energy (DOE) (CDAC Contract No. DE-FC03-03N00144). Additional x-ray experiments were performed at the Canadian Light Source, which is supported by NSERC, NRC, CIHR, and the University of Saskatchewan.

---

[1] A. W. MaClaine, U.S. Department of Energy, Office of Energy Efficiency and Renewable Energy, FY 2003, Progress Report of Hydrogen Fuel Cell and Technologies, Progress Report, 2003 (unpublished).

[2] V. C. Y. Kong, D. W. Kirk, F. R. Foulkes, and J. T. Hinatsu, Int. J. Hydrogen Energy **28**, 205 (2003).

[3] Y. Fukai and N. Okuma, Phys. Rev. Lett. **73**, 1640 (1994).

[4] P. Vajeeston, P. Ravindran, A. Kjekshus, and H. Fjellvåg, Phys. Rev. Lett. **89**, 175506 (2002).

[5] N. W. Ashcroft, Phys. Rev. Lett. **92**, 187002 (2004).

[6] T. Moriwaki, Y. Akahama, H. Kawamura, S. Nakano, and K. Takemura, J. Phys. Soc. Jpn. **75**, 074603 (2006); P. Vajeeston, P. Ravindran, B. C. Hauback, H. Fjellvåg, A. Kjekshus, S. Furuseth, and M. Hanfland, Phys. Rev. B **73**, 224102 (2006).

[7] E. Zintl and A. Harder, Z. Elektrochem. Angew. Phys. Chem. **41**, 33 (1935).

[8] A. F. Anderson, A. J. Maeland, and D. Slotfeldt-Ellingsen, J. Solid State Chem. **20**, 93 (1977).

[9] A. P. Hammersley, S. O. Svensonn, M. Hanfland, A. N. Fitch, and D. Häusermann, High Press. Res. **14**, 235 (1996); FIT2D, European Synchrotron Radiation Facility, 1998.

[10] S. Desgreniers and K. Lagarec, J. Appl. Crystallogr. **27**, 432 (1994); J. Appl. Crystallogr. **31**, 109 (1998).

[11] J. Rodrigues-Carvajal, Physica B **192**, 55 (1993); FullProf, version 3.70.

[12] H. K. Mao, J. Xu, and P. M. Bell, J. Geophys. Res., [Solid Earth Planets] **91B**, 4673 (1986).

[13] G. Kresse and J. Furthmüller, Comput. Mater. Sci. **6**, 15 (1996); Phys. Rev. B **54**, 11169 (1996).

[14] D. Vanderbilt, Phys. Rev. B **41**, 7892 (1990).

[15] H. J. Monkhorst and J. D. Pack, Phys. Rev. B **13**, 5188 (1976).

[16] X. Gonze, Phys. Rev. B **55**, 10337 (1997); X. Gonze and C. Lee, *ibid.* **55**, 10355 (1997); X. Gonze *et al.*, Comput. Mater. Sci. **25**, 478 (2002).

[17] N. Troullier and J. L. Martins, Phys. Rev. B **43**, 1993 (1991).

[18] J. P. Perdew, K. Burke, and M. Ernzerhof, Phys. Rev. Lett. **77**, 3865 (1996).

[19] K. Kinoshita *et al.*, *Proc 20th AIRAPT Conference*, (2005).

Chapter 3 High-pressure phase transition observed in barium hydride

as published in the Journal of Applied Physics, Volume 102,
Article Number 043520, 2007.

JOURNAL OF APPLIED PHYSICS **102**, 043520 (2007)

High-pressure phase transition observed in barium hydride

Jesse S. Smith[a] and Serge Desgreniers
Laboratoire de physique des solides denses, Department of Physics, University of Ottawa, Ottawa, Ontario K1N 6N5, Canada

John S. Tse
Department of Physics and Engineering Physics, University of Saskatchewan, Saskatoon, Saskatchewan S7N 5E2, Canada

Dennis D. Klug
Steacie Institute for Molecular Sciences, National Research Council of Canada, Ottawa, Ontario K1A 0R6, Canada

(Received 25 May 2007; accepted 17 July 2007; published online 28 August 2007)

The pressure-dependent structural and vibrational properties of barium hydride have been studied up to 22 GPa at room temperature by means of powder x-ray diffraction, Raman spectroscopy, and first-principles calculations. At ambient conditions, BaH_2 crystallizes in the cotunnite structure (*Pnma*). A reversible, first-order structural phase transition is observed at 1.6 GPa. The high-pressure phase can be indexed by a hexagonal unit cell with a proposed Ni_2In structure ($P6_3/mmc$), with the Ba and H atoms in special positions. The experimental volume compression of the high-pressure phase yields an isothermal bulk modulus $B_0=24(1)$ GPa (B_0' fixed at 4.13). This compares favorably with the results of the first-principles calculations, which reproduce the first-order nature of the transition. The relevance of these results is discussed in the contexts of metal hydrides in particular and ionic AX_2 ($A=$metal) compounds in general. © *2007 American Institute of Physics*. [DOI: 10.1063/1.2772427]

I. INTRODUCTION

There has been much recent research activity surrounding metal hydrides, perhaps primarily motivated by their potential to serve as efficient energy storage materials.[1,2] Light metal hydrides such as LiH and MgH_2 are attractive because of their high hydrogen content per unit mass. However, the restrictive thermodynamic conditions for hydrogen exchange in these light hydrides make them impractical for commercial use. In the case of the heavy alkaline earth hydrides (HAEH), namely CaH_2, SrH_2, and BaH_2, the conditions for hydrogen exchange become more restrictive with increasing cation mass. However, it is possible that the pressure-temperature conditions required to obtain higher-density phases are at the same time relaxed. Furthermore, in a recent study of Pt-doped heavy alkaline earth manganites ($AMnO_3$, $A=$Ca, Sr, or Ba) it was found that introduction of the heaviest cation, Ba, facilitated a remarkable uptake in hydrogen as compared to the equivalent Sr and Ca compounds.[3] Together, these considerations lead to the suggestion that a compromise might be reached between efficient hydrogen storage and convenient hydrogen exchange in heavier hydrogen compounds.

In a more fundamental context, an interesting relationship between the molar volume, mean cation-anion distance, and cation coordination number has been established for many ionic AX_2 compounds ($A=$metal).[4] Specifically, the molar volume is linearly proportional to the cube of the mean cation-anion distance and inversely proportional to the cation coordination number. It is of interest to determine if, as AX_2 compounds, the HAEHs can be characterized by the same relationship. Furthermore, HAEHs have been the subject of recent low-temperature, ambient-pressure theoretical and incoherent inelastic neutron scattering studies elucidating the role of hydrogen in these compounds.[5] Extending such studies to moderate pressures could be particularly interesting if any of the HAEHs were found to undergo a pressure-induced phase transition over the relevant pressure regime.

A recent study showed that MgH_2, which crystallizes in the rutile structure ($P4_2/mnm$) at ambient conditions, undergoes successive pressure-induced structural phase transitions.[6] Above 17 GPa, it adopts the cotunnite structure, which remains stable up to at least 57 GPa. Inasmuch as the HAEHs exhibit the cotunnite structure at ambient conditions,[7,8] pressure-induced phase transitions in these hydrides may suggest the possibility of a similar high-density phase of MgH_2 above 57 GPa. Such a phase transition has already been reported for CaH_2 (Refs. 9 and 10) and SrH_2.[9] The primary purpose of the present study was to look for such a phase transition in BaH_2.

Since undertaking this study, a recently reported powder x-ray diffraction experiment has demonstrated that indeed, BaH_2 undergoes successive pressure-induced structural phase transitions at 2.5 GPa and approximately 50 GPa at room temperature.[11] Following a brief description of the experimental and theoretical details of the present work, we present the results of powder x-ray diffraction experiments corroborating the reported phase transition at approximately 2.5 GPa. In addition, we present the results of Raman spectroscopy measurements and first-principles calculations to

---

[a] Electronic mail: jsmit068@uottawa.ca

further elucidate the lattice dynamics and structural properties of BaH_2 at pressures up to 22 GPa. In short, we show that BaH_2 undergoes a reversible, first-order structural phase transition at 1.6 GPa. The high-pressure phase can be indexed by a hexagonal unit cell. The proposed structure (based in part on isostructural comparison) is Ni_2In-type ($P6_3/mmc$) with Ba and H atoms occupying special positions. The phase transition is reproduced well by first-principles calculations. The pressure dependence of the unit cell volume is fit to a third-order Birch-Murnaghan equation of state, which compares favorably with the equation of state obtained from first-principles calculations. The work concludes with a brief discussion of the results as outlined in this introduction.

II. EXPERIMENTAL AND THEORETICAL DETAILS

Barium hydride powder (99.5% metals analysis, Strem Chemicals) was loaded into gasketed diamond anvil cells (DAC) under an inert gas (argon) atmosphere. The diamond anvils had a culet diameter of 300 μm and the ANSI T-301 (full hard) stainless-steel gaskets were preindented to thicknesses of 50–80 μm, with drilled sample chambers 75 –125 μm in diameter. In each case, a single ruby microsphere was placed in the sample chamber prior to loading and subsequent pressure measurements were carried out using the ruby luminescence technique.[12] BaH_2 is extremely sensitive to moisture and readily hydrolyzes with common pressure-transmitting media such as methanol/ethanol or silicone oil. As these were the only options available at the time of the experiment, no pressure-transmitting medium was used. In addition, BaH_2 was loaded into capillaries for ambient-condition measurements.

Angle-dispersive powder x-ray diffraction measurements were carried out using synchrotron radiation at the Hard X-ray MicroAnalysis (HXMA) beamline at the Canadian Light Source (CLS). The radiation source at the multipurpose HXMA beamline is a 63-pole superconducting wiggler with a critical energy around 10 keV. Wavelength was selected using the (111) crystals of a double-crystal silicon monochromator; for all x-ray diffraction images in the present study, a wavelength of 0.485 94(2) Å or 0.563 56(3) Å was used. The monochromatic beam was focused using a Pt-coated toroidal mirror, and further collimated to a 30 μm spot using a tungsten carbide collimator similar in design to that described elsewhere.[13] A sample-to-detector distance of 254.75(10) mm was consistently verified using several x-ray diffraction images of lanthanum hexaboride (National Institute of Standards and Technology, Standard Reference Material 660a). BaH_2 samples were then located at the same position as the standard using a centering technique based on the x-ray transmission profile of the gasket. X-ray diffraction images were recorded, with exposure times ranging from 5 to 25 min, on Fuji ST-VI image plates read at 100 μm pixel resolution on a Fuji BAS2500 scanner. X-ray diffraction images were processed and integrated with FIT2D (Ref. 14) to obtain x-ray diffraction patterns of intensity versus 2θ. Patterns were then analyzed and indexed using the XRDA program.[15] Whole-pattern refinements were performed on selected patterns using FULLPROF,[16] applying LeBail fitting for known structures and Rietveld refinement for the high-pressure phase of BaH_2.

Raman spectroscopy measurements were performed following the powder x-ray diffraction measurements. For the majority of pressurized samples, the 532 nm line of a solid-state frequency-doubled YAG laser was used for excitation. Raman spectra in the 400–1300 cm^{-1} range were collected in near-backscattering geometry using a Rayleigh edge filter with a Jobin-Yvon 0.64 m spectrograph equipped with a nitrogen-cooled charge-coupled device (CCD) detector. The spectral resolution was 4 cm^{-1}. For samples at room conditions in a capillary, as well as a one of the pressurized samples, the 488 or 514.5 nm line of an Ar ion laser was used for excitation, and spectra in the 50–1300 cm^{-1} range were collected using a triple-grating subtractive spectrograph to facilitate the collection of Raman spectra at the lowest wavenumbers.

First-principles calculations of the electronic structure were performed with the plane-wave pseudopotential method, within the framework of density functional theory, using the software package VASP.[17] For Ba and H, projected augmented wave pseudopotentials from the pseudopotential library were used.[18] For Ba, $5p$ and $6s$ electrons were treated as valence. The Perdew-Wang 91 generalized gradient approximation exchange-correlation function was employed. For electronic Brillouin zone integration, Monkhorst-Pack grids[19] of $6\times12\times8$ and $12\times12\times12$ were used for the orthorhombic and hexagonal structures, respectively. For selected volumes the cell shape and lattice parameters were optimized and the corresponding pressures were computed from the stress tensor.

III. RESULTS AND ANALYSIS

A. X-ray diffraction: Crystalline structure phase stability and equation of state

Figure 1 shows an x-ray diffraction pattern obtained from a sample at ambient conditions. The primary phase present is attributed to BaH_2 (cotunnite structure, *Pnma*). The orthorhombic lattice parameters $a=6.798(3)$, $b=4.172(4)$, and $c=7.868(4)$ Å are in agreement with previous neutron diffraction studies.[8] As seen in Fig. 1, a significant contribution arises from a secondary phase, attributed to barium oxide (NaCl structure, $Fm3m$). The lattice parameter $a=5.535(2)$ Å is again consistent with previous x-ray diffraction studies.[20] A quantitative phase analysis of independent capillary samples yielded a contribution of slightly less than 15% BaO by weight. The most plausible explanation for such a significant contribution from the oxide is that it was present in the sample as supplied. The additional small peaks, particularly noticeable at low 2θ, are attributed to trace amounts of $Ba(OH)_2$ (which was not considered in the quantitative analysis). Again, the contribution from barium hydroxide can be explained by its presence in the initial material and/or residual moisture on the capillary walls as the reaction of BaH_2 with water yields $Ba(OH)_2$ and hydrogen gas.

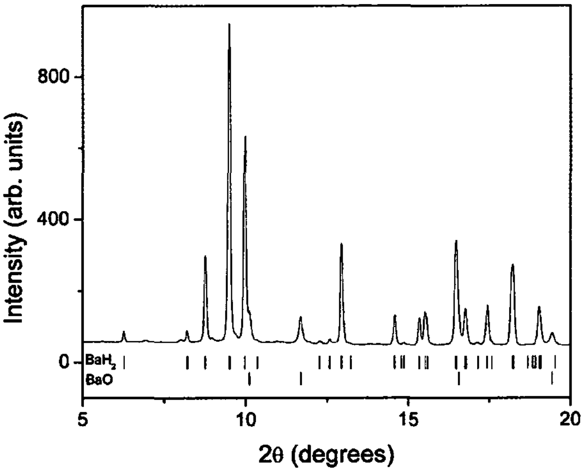

FIG. 1. Observed powder x-ray diffraction pattern of BaH_2 (cotunnite-type) with minority phase BaO (NaCl-type) obtained under ambient conditions, $\lambda=0.563\,56$ Å. Note the x-ray diffraction due to trace amounts of barium hydroxide (*).

After loading BaH_2 into DACs, samples were observed under a microscope. The samples exhibited two distinct regions. The central portion was approximately circular and appeared light-brown and grainy. The second region consisted of a narrow ring separating the gasket and the central portion of the sample. The ring was highly transparent as compared to the central portion and exhibited little visible texture. The ring was believed to be $Ba(OH)_2$, again due to the reaction of BaH_2 with residual moisture on the gasket walls. Due to limitations of the nominal beam size, it was not possible to collect x-ray diffraction images from only the central portion of the sample, and this presented some difficulty in obtaining unambiguous x-ray diffraction patterns of the *Pnma* phase of BaH_2 under pressure. Figure 2(a) shows a LeBail fit of an x-ray diffraction pattern obtained at 0.6 GPa. Based on a recent high-pressure study,[21] $Ba(OH)_2$ is assigned to the space group $P2_1/n$. Where the capillary sample shows only small peaks and shoulders from the contaminating hydroxide phase, the pressurized sample shows a significant contribution, as detailed by the inset of Fig. 2(a). Interestingly, phase identification and pattern indexing is facilitated by the Debye rings observed in the x-ray diffraction image, illustrated partially in Fig. 2(b). The characteristic hydride rings show a marked variation in both intensity and breadth as a function of azimuthal angle (i.e., along a given Debye ring), most likely due to a combination of preferred orientation and anisotropic strain. Debye rings attributed to the oxide are narrow and well-defined, with a grainy appearance. Finally, the contaminating hydroxide rings are broad, continuous, and diffuse. At 0.6 GPa, the resulting lattice parameters for BaH_2 are $a=6.730(3)$, $b=4.146(9)$, and $c=7.830(4)$ Å.

Upon increasing pressure, a structural phase transition was observed in BaH_2. While there was no appreciable change in the appearance of the sample as viewed under a microscope, the transition was noticeable due to changes in both the number and position of the intense, characteristic

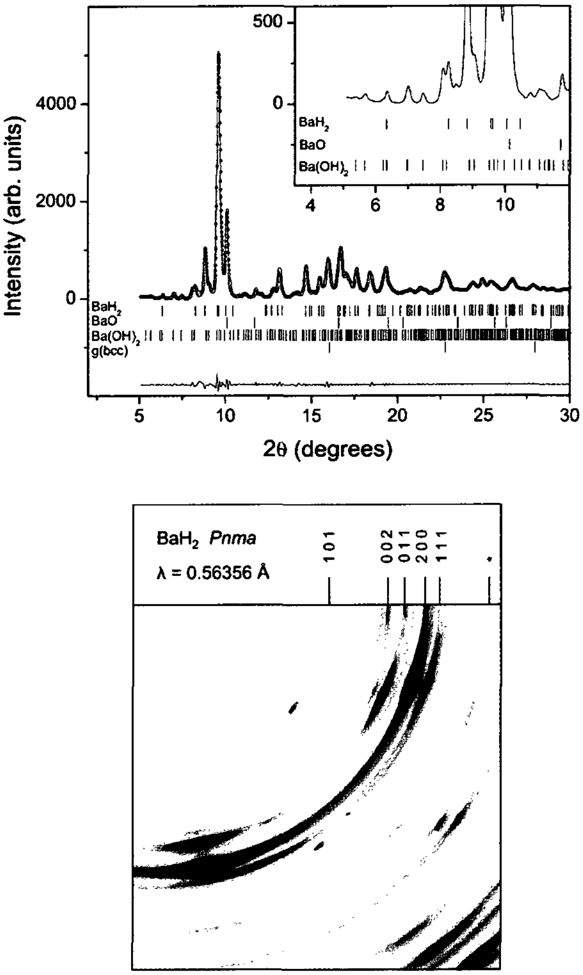

FIG. 2. (Color online) (a) Observed (symbols) and calculated (solid line) x-ray diffraction patterns with difference curve (bottom) obtained at 0.6 GPa. The ambient-pressure phase of BaH_2, together with BaO, $Ba(OH)_2$, and stainless-steel gasket, are modeled by LeBail fitting. (b) Portion of the x-ray diffraction image (equivalent to $0° < 2\theta < 12°$) detailing the difference between Debye rings associated with the low-pressure phase of BaH_2 (indexed), BaO (*), and $Ba(OH)_2$ (unindexed).

Debye rings. The high-pressure phase can be indexed with a hexagonal unit cell, $a=4.359(2)$ and $c=5.850(5)$ Å at 3.7 GPa. Considering the position of the observed peaks together with systematic absences, the x-ray diffraction pattern is consistent with the space group $P6_3/mmc$. Figure 3(a) shows a combined Rietveld refinement (high-pressure BaH_2) and LeBail fit [BaO, $Ba(OH)_2$, and gasket] carried out on an x-ray diffraction pattern obtained at 4.8 GPa. Refined parameters for each phase included lattice constants and pseudo-Voigt peak profile parameters. For BaH_2, Ba^{2+} was assigned to the special position $2c$ and additional refined parameters included a scale factor, B_{overall}, and a Rietveld-Toraya correction for preferred orientation. The resulting criteria of fit are $R_{wp}=11.5\%$, $R_e=9.5\%$, and $\chi^2=1.46$. The quality of the overall fit is likely overestimated inasmuch as discrepancies between the observed and calculated high-pressure BaH_2 phase may, in some regions, be minimized by the LeBail fit

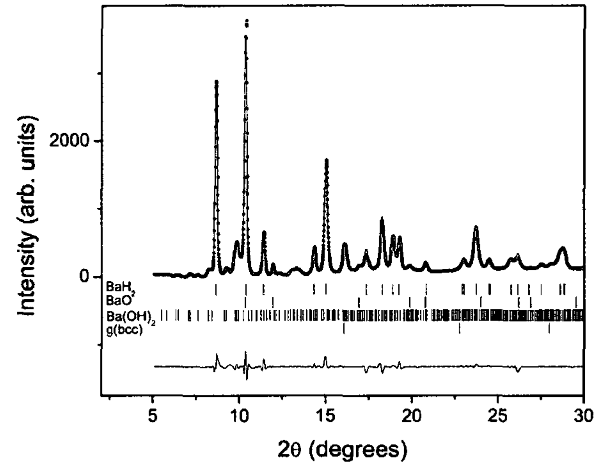

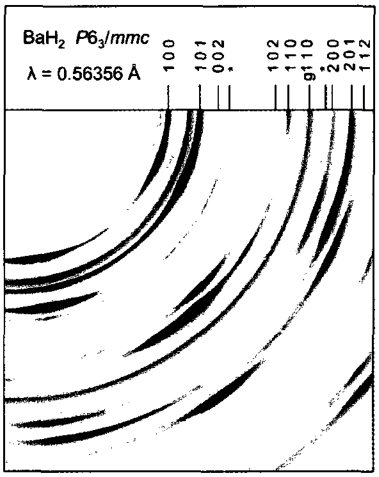

FIG. 3. (Color online) (a) Observed (symbols) and calculated (solid line) x-ray diffraction patterns with difference curve (bottom) obtained at 4.8 GPa. High-pressure BaH_2 is modeled by Rietveld refinement; BaO, $Ba(OH)_2$, and stainless-steel gasket are modeled by LeBail fitting. (b) Portion of the x-ray diffraction image (equivalent to $0° < 2\theta < 19°$) detailing the difference between Debye rings associated with the high-pressure phase of BaH_2 (indexed), BaO (*), $Ba(OH)_2$ (unindexed), and stainless-steel gasket (g).

of $Ba(OH)_2$. Nevertheless, the result of the Rietveld fit obtained indicates likelihood for the proposed positions of the Ba atoms. The refined lattice parameters for BaH_2 are $a = 4.315(3)$ and $c = 5.676(5)$ Å at 4.8 GPa. Figure 3(b) shows a portion of the x-ray diffraction image, again showing the marked contrast in the appearance of the Debye rings among the four contributing phases.

Because the H atoms effectively do not contribute to the scattered x-ray intensity observed in the diffractions experiments, it is not possible to make a complete structure determination of the high-pressure phase based solely on x-ray diffraction data. The calculated x-ray diffraction pattern obtained by assigning the Ba atoms to the special position $2c$ of space group $P6_3/mmc$ agrees with the observed x-ray diffraction data. Specifically, the Ba atoms occupy a hexagonal close-packed (hcp) lattice. In an effort to propose plausible positions for the H atoms, an examination of isostructural compounds was carried out. A structural study of BaF_2 at room temperature confirmed that it undergoes a pressure-induced phase transition from the cubic fluorite structure to the cotunnite structure at approximately 3 GPa, and furthermore reported a transition to the Ni_2In structure at pressures above 15 GPa.[22] Given its close relation to BaH_2 with respect to the mass and valence electron configuration of the cation and anion, respectively, BaF_2 is an ideal candidate for an isostructural comparison. Further investigation of the two compounds reveals further similarities. In both compounds, the anion-anion distances are such that in the cotunnite phase, the compressibility along the a axis is large compared to the compressibility along the b and c axes (see, for example, the above-reported lattice parameters for BaH_2 at ambient conditions compared with those at 0.6 GPa). Upon transforming to the Ni_2In phase, both compounds have approximately the same c/a ratio, 1.32 for BaH_2 at 4.8 GPa and 1.30 for BaF_2 at 20.5 GPa. Perhaps one notable difference is that in BaF_2 the c/a ratio increases slightly with pressure, whereas in BaH_2 it decreases slightly with pressure, *viz.*, 1.34–1.28 over the pressure range 3.7–17.9 GPa. Taking these similarities into account, the proposed structure is the Ni_2In-type ($P6_3/mmc$) with three atoms in the asymmetric unit, located at Wyckoff special positions $2c$(Ba), $2d$(H), and $2a$(H), as established for the case of BaF_2.[22]

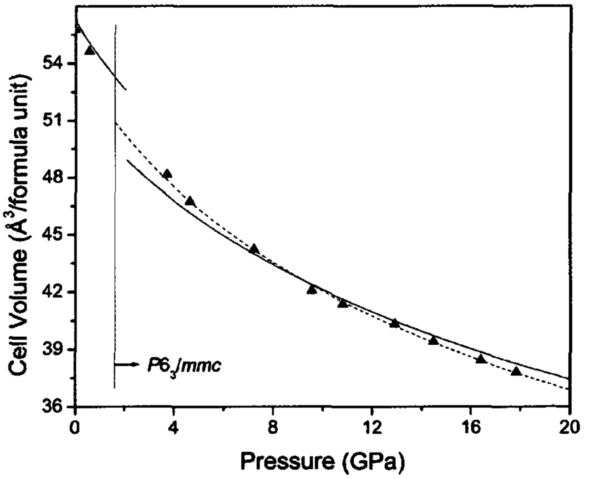

FIG. 4. Experimental unit cell volume (symbols) as a function of pressure, compared with the theoretical (solid line) and experimental (dashed line) equations of state.

It has not been possible to carry out Rietveld refinements on patterns corresponding to sample pressures above 5 GPa inasmuch as $Ba(OH)_2$ undergoes a structural phase transition around this pressure and the high-pressure structure has not yet been unambiguously determined.[21] However, the characteristic Debye rings of the high-pressure phase of BaH_2 have allowed for straightforward indexing of patterns, and consequently the measurement of the pressure-induced changes in lattice parameters, up to 18 GPa, the highest pressure reached in the diffraction measurements of this study.

Figure 4 shows the experimentally determined unit cell volume as a function of pressure, together with the theoretically and experimentally determined isothermal (300 K) equations of state. The theoretical equation of state for the high-pressure phase was determined by fitting the data points obtained from the calculations to a third-order Birch-Murnaghan equation of state, yielding $B_0=31.1(2)$ GPa, $B_0'=4.13(3)$, and $V_0=103.8(1)$ Å^3. Similarly, the experimental data were fit to a third-order Birch-Murnaghan equation of state with B_0' fixed at 4.13, yielding $B_0=24(1)$ GPa and $V_0=108(1)$ Å^3. The theoretical equation of state differs slightly from the experimental one, underestimating the compressibility and consequently overestimating the transition pressure. However, for measured pressures exceeding 10 GPa, the *R*-lines of the ruby luminescence spectra exhibited moderate strain-induced broadening. Consequently, the pressure of these points may have been slightly underestimated. It is therefore reasonable to conclude that under true hydrostatic conditions the actual equation of state for the high-pressure hexagonal phase would lie somewhere between the theoretical and experimental curves. The number of data points obtained for the low-pressure phase was insufficient for determining an experimental equation of state, and furthermore the transition pressure was not narrowly determined. However, examination of the calculated data shows an abrupt volume decrease of approximately 7% across the transition, in accord with that found for CaH_2.[9,10]

B. Raman spectroscopy: Phase transition and transition pressure

To complement the x-ray diffraction study, Raman spectroscopy measurements were performed to further characterize the *Pnma*–*P*6$_3$/*mmc* transition, as well as to determine more precisely the transition pressure. A group theoretical analysis indicates a reduction in the number of observable Raman-active modes as a result of the *Pnma*–*P*6$_3$/*mmc* phase transition; the irreducible representations of the Raman-active modes are $\Gamma_{\mathrm{Raman}}=6A_g+3B_{1g}+6B_{2g}+3B_{3g}$ and $\Gamma_{\mathrm{Raman}}=2E_g$ for the *Pnma* and *P*6$_3$/*mmc* phases, respectively. In the *Pnma* phase, 6 of the total 18 modes are associated with vibrations involving Ba atoms and consequently should be observed at relatively low wavenumbers. Following the transition at high pressure to the *P*6$_3$/*mmc* phase, two single modes of vibration are expected—one each associated with Ba and H.

A search of the literature failed to yield a Raman study of BaH_2, so the Raman spectrum of BaH_2 (Fig. 5, middle) was compared to that of CaH_2 (Fig. 5, top), both recorded under ambient conditions, to establish that the spectrum was in fact due to BaH_2 and not, for instance, $Ba(OH)_2$. The Raman spectrum of CaH_2 presented here is consistent with that reported elsewhere.[6,10] Both calcium and barium hydrides adopt the cotunnite structure (*Pnma*) at ambient conditions, and therefore show marked similarities in their Raman spectra. In both cases, two groups of narrow and broad Raman-active lines were observed at low and high wavenumbers, which were attributed to vibrations of the heavier alkaline metals and hydrogens, respectively. A lack of spectral resolution and/or efficient detection prevented a complete count of all possible predicted Raman-active modes in either hydride at ambient conditions.

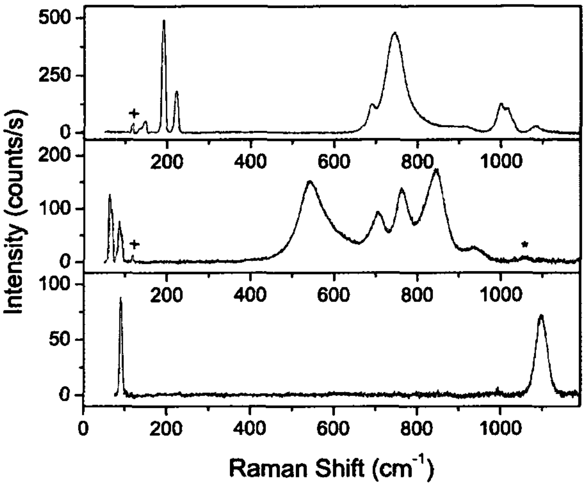

FIG. 5. Raman spectra of CaH_2 (top) and BaH_2 (middle) obtained under ambient conditions, $\lambda_0=488$ nm, as well as high-pressure BaH_2 (bottom) obtained at 9.2 GPa and room temperature, $\lambda_0=514.5$ nm. Additional lines are due to Ar plasma lines (+) and contamination by $Ba(OH)_2$ (*).

A Raman spectrum of BaH_2 recorded at 9.2 GPa and at room temperature, in the *P*6$_3$/*mmc* phase, is shown in Fig. 5 (bottom). As predicted by the group theoretical analysis, only two Raman-active modes were observed: a sharp line at 95 cm^{-1}, attributed to vibrations of Ba atoms, and a broader line at around 1100 cm^{-1}, which arises from hydrogen vibrations. Figure 6 shows several Raman spectra over the 400–1200 cm^{-1} range for one sample at selected pressures. At the initial loading pressure of 7.5 GPa the spectrum exhibited a single peak at 1073 cm^{-1}, consistent with the high-wavenumber peak expected from the group theoretical analysis for the high-pressure *P*6$_3$/*mmc* phase. Upon decreasing pressure, the peak shifted to lower wavenumbers, with the peak remaining the sole spectral feature down to 1.7 GPa. Below 1.7 GPa, the low-pressure *Pnma* phase characterized

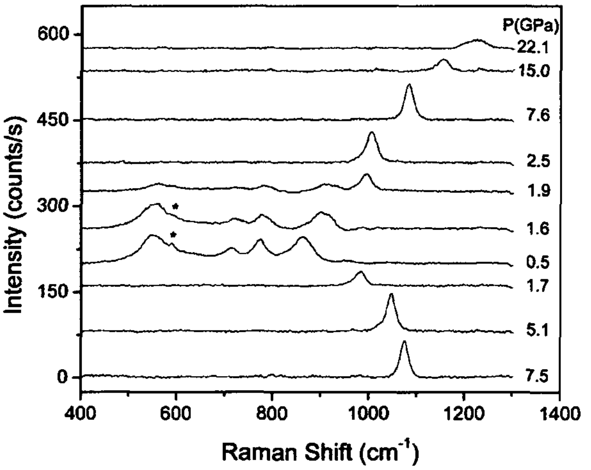

FIG. 6. Raman spectra of one BaH_2 sample starting at the loading pressure of 7.5 GPa and continuing with selected pressures in the order of collection, up to the maximum pressure, 22.1 GPa, of the Raman study, $\lambda_0=532$ nm. Small peaks are due to contamination from $Ba(OH)_2$ (*).

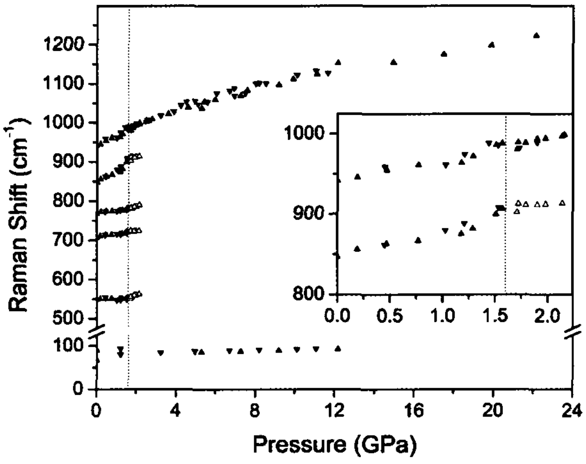

FIG. 7. Raman shifts as a function of pressure. Symbols pointing up and down represent data taken on increasing and decreasing pressure, respectively. Open symbols indicate persistent low-pressure peaks resulting in a phase mixture. Inset details assignment of the transition pressure at 1.6 GPa, marked by the discontinuity in the pressure derivative of the Raman shift.

by the five broad bands in the 500–1000 cm^{-1} range was recovered. Upon increasing pressure, the peak associated with the high-pressure phase reappeared at 1.8 GPa; however, remnants of the low-pressure phase persisted up to approximately 2.3 GPa, after which the spectra again exhibited a single peak up to 22.1 GPa, the highest pressure reached in the Raman measurements of this study.

The pressure dependence at room temperature of wavenumbers of all observable Raman lines is presented in Fig. 7. It should be noted that the data shown in Fig. 7 correspond to several different samples and are presented for increasing and decreasing pressures. Starting from ambient conditions, as the pressure was increased, the first three Raman lines of the high-wavenumber group at 508, 706, and 766 cm^{-1} (0.1 MPa) exhibited only a slight increase of 2, 13, and 13 cm^{-1}, respectively, up to 1.6 GPa. Conversely, the two lines with the highest wavenumbers at 847 and 940 cm^{-1} showed a marked increase of 57 and 46 cm^{-1} over the same pressure regime, with the bulk of the observed shift occurring just below the transition pressure (see also the progression from 0.5 to 1.6 GPa in Fig. 6). The assignment of the transition pressure is detailed in the inset of Fig. 7, where the position of the persistent low-pressure peak around 910 cm^{-1} remained relatively constant above 1.6 GPa. The transition pressure of 1.6 GPa was determined based on this discontinuity in the pressure derivative of the Raman shift. From ambient conditions to the transition pressure, the Raman lines at the lowest wavenumbers, associated with motion of cations, showed modest pressure shifts. Given the limited spectral resolution of those Raman lines, we have plotted the pressure shift of two wavenumbers corresponding to the peak intensity of Raman "bands" comprising convoluted individual Raman lines, as seen in Fig. 5 (middle). Actual pressure coefficients for the two bands have not been calculated due to the lack of data points over the pressure range. It should be noted that we have observed a merging of the two Raman bands recorded in the *Pnma* phase into a single Raman line at the transition pressure. For the high-pressure phase, the position of this Raman line increased by about 1 cm^{-1}/GPa, whereas the position of the Raman line associated with H vibrations increased by about 12 cm^{-1}/GPa.

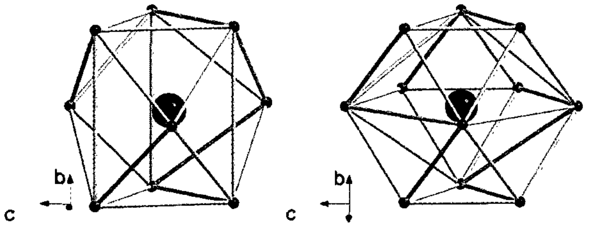

FIG. 8. (Color online) Detail of cation coordination number for the cotunnite structure (left) and the Ni_2In structure (right). In both structures the cation is surrounded by six anions forming a trigonal prism. The remaining anions, three for the cotunnite structure and five for the Ni_2In structure, lie in the plane of the cation, resulting in coordination numbers of 9 and 11, respectively. Connections between anions are included to highlight the geometric arrangement of atoms; they are not intended to represent bonds.

IV. DISCUSSION AND CONCLUSIONS

The study on BaF_2 was significant as it was the first explicitly reported example of cation coordination number 11 in ionic AX_2 compounds. A number of other examples of pressure-induced cotunnite→Ni_2In transitions have since been reported, such as Na_2S (Ref. 23) and notably the HAEHs.[9–11] The characteristics of the closely related cotunnite and Ni_2In structures have been described in detail elsewhere.[22,23] To briefly summarize, both structures are characterized by cations arranged on a hcp lattice, surrounded by trigonally arranged anion prisms. In the case of the cotunnite structure, the cation hcp lattice is distorted, and adjacent anion prisms are tilted 25° with respect to each other. In the Ni_2In structure the cations occupy a proper hcp lattice, and the neighboring anion prisms are no longer tilted with respect to each other. Figure 8 details the cation coordination of each structure. In both cases, the cation is surrounded by six anions forming a trigonal prism. Additionally, in the plane of the cation lie three anions in the cotunnite structure and five anions in the Ni_2In structure, resulting in cation coordination numbers 9 and 11, respectively. For BaH_2 at ambient conditions, the Ba-H distances range from 2.499(1)–3.001(2) Å, with a mean cation-anion distance of 2.791 Å. In the high-pressure hexagonal phase there are three unique Ba-H distances of 2.517(2), 2.911(2), and 2.925(3) Å at 3.7 GPa, with a mean cation-anion distance of 2.806 Å. The more efficient packing required for the abrupt decrease in volume across the phase transition is due to the increase in coordination number of the cation, as it is clear that the mean cation-anion distance actually increases across the phase transition.

A linear relationship between the molar volume, the cube of the mean cation-anion distance, and the cation coordination number has been established for dioxides and fluorides: $V_{\text{molar}}=k(d_0)^3/N$, where $k=14.4(6)$, d_0 is the mean cation-anion distance, and N is the cation coordination number. In their work on BaF_2, the authors add several chlorides, bromides, and iodides to the group, demonstrating that the

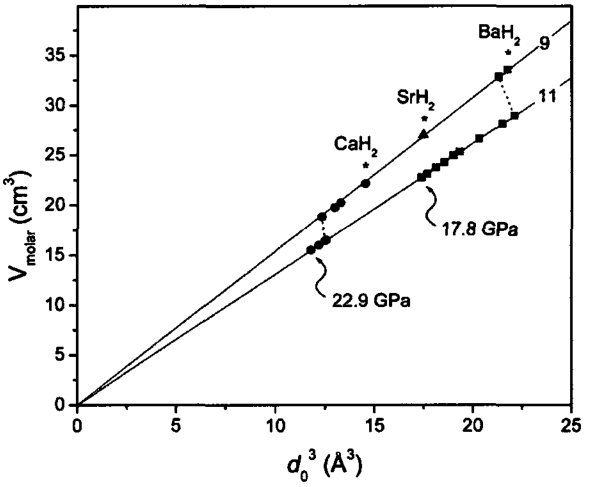

FIG. 9. Molar volume as a function of the cube of the mean cation-anion distance for CaH_2 (circles), SrH_2 (triangle), and BaH_2 (squares). Ambient-pressure data are indicated by asterisks. Upon increasing pressure, data tend toward the origin within a given stable pressure regime, or increase in coordination number across the transition, as indicated by dotted lines. The relationship holds up to the maximum pressures of the respective studies (as indicated on the graph).

relationship holds for over a dozen ionic AX_2 compounds for various ambient-pressure and high-pressure phases with coordination numbers ranging from 4–11.[22] Notably, the authors also add a hydride, YbH_2, to the coordination number 11 compounds based on a previous study.[24] Figure 9 shows that the relationship holds for the HAEHs as well, with data for CaH_2, SrH_2, and BaH_2 obtained from Refs. 10 and 7, and the present study, respectively. Data for ambient conditions are indicated with asterisks. As the pressure is increased, data points progress toward the origin (or to higher coordination number across the phase transition). In this case, $k=13.9$ for coordination number 9 and 14.4 for coordination number 11. It is worth noting that not only does the relationship hold for each of the HAEHs at ambient pressure, and for CaH_2 and BaH_2 immediately following the phase transition, but it also holds for each phase, as a function of pressure, throughout the stable pressure regime of the given phase (at least up to the maximum pressure of the respective studies, as indicated on the graph). With CaH_2 and BaH_2 serving as the bookends of the HAEHs, it is reasonable to suggest that SrH_2 would follow a similar trend upon increasing pressure.

Considering the HAEHs in the context of hydrogen storage, if the problem of large-scale, commercial hydrogen storage is ultimately solved by the use of a metal hydride, it is unlikely the solution will take the form of a simple binary hydride. Nevertheless, the present study, together with studies on the other group II hydrides, provides examples of how substitution of a heavier cation in an isostructural group can reduce the cost associated with obtaining a higher-density phase. The obvious tradeoff is the decrease in hydrogen content per unit mass. In the case of BaH_2 and other group II hydrides the cost of substitution is too high, particularly in light of the increased restrictions governing hydrogen exchange. However, in more complex hydrides and related hydrogen-bearing compounds, the tradeoff may yet prove to be advantageous.

Considering the HEAHs in the context of neutron studies, BaH_2 is an ideal candidate for pressure-dependent neutron diffraction and incoherent inelastic scattering studies. The observed transition pressures of CaH_2 at 16 GPa and SrH_2 at 10 GPa are certainly within the pressure limitations of current medium-volume pressure cells. However, the relative ease of generating pressures below 10 GPa, together with the more nearly hydrostatic conditions attainable at low pressures, make BaH_2 the ideal HAEH for such studies. A neutron diffraction study of BaH_2 (or similarly BaD_2) could provide timely corroboration or correction of the hydrogen positions proposed in the current work.

In conclusion, the powder x-ray diffraction, Raman spectroscopy, and theoretical results unambiguously indicate that BaH_2 undergoes a reversible, first-order phase transition at 1.6 GPa. The x-ray diffraction results, together with an isostructural comparison with BaF_2, are sufficient to propose the $Ni_2In(P6_3/mmc)$ structure for the high-pressure phase, with the atoms occupying special positions $2c$(Ba), $2d$(H), and $2a$(H). The phase transition was reproduced well by first-principles calculations. Raman spectroscopy results support the proposed structure, as the two Raman-active modes predicted for $P6_3/mmc$ were observed following the phase transition. In addition, the Raman spectroscopy data allowed for a more precise determination of the transition pressure. The results of the HAEHs suggest that a similar transition may be observed in MgH_2, perhaps at pressures approaching 100 GPa.

ACKNOWLEDGMENTS

S.D. and J.S.T. acknowledge the financial support of the Natural Sciences and Engineering Research Council of Canada. J.S.T. also wishes to thank the Canada Foundation for Innovation and the Canada Research Chair Program for support. Portions of the research described in this article were performed at the Canadian Light Source, which is supported by NSERC, NRC, CIHR, and the University of Saskatchewan. The authors also gratefully acknowledge the work of Dr. Ning Chen and Dr. De-Tong Jiang in facilitating experiments carried out at the HXMA beamline of the Canadian Light Source.

[1] A. W. MacLaine, U.S. Department of Energy, Office of Energy Efficiency and Renewable Energy, FY 2003, Progress Report of Hydrogen Fuel Cell and Technologies (unpublished).
[2] A. Zaluska, L. Zaluski, and J. O. Ström-Olsen, Appl. Phys. A **72**, 157 (2001).
[3] T. K. Mandal, L. Sebastian, J. Gopalakrishnan, L. Abrams, and J. B. Goodenough, Mater. Res. Bull. **39**, 2257 (2004).
[4] L. G. Liu and W. A. Bassett, *Elements, Oxides, and Silicates: High-Pressure Phases with Implications for the Earth's Interior* (Oxford University Press, Oxford, 1986).
[5] D. Colognesi, G. Barrera, A. J. Ramirez-Cuesta, and M. Zoppi, J. Alloys Compd. **427**, 18 (2007).
[6] T. Moriwaki, Y. Akahama, H. Kawamura, S. Nakano, and K. Takemura, J. Phys. Soc. Jpn. **75**, 074603 (2006).
[7] T. Sichla and H. Jacobs, Eur. J. Solid State Inorg. Chem. **33**, 453 (1996).
[8] G. J. Snyder, H. Borrmann, and A. Simon, Z. Kristallogr. **209**, 458 (1994).
[9] K. Kinoshita, M. Nishimura, Y. Akahama, and H. Kawamura, in Proceed-

ings of the 20th AIRAPT T10–P048 (2005).
[10] J. S. Tse, D. D. Klug, S. Desgreniers, J. S. Smith, R. Flacau, Z. Liu, J. Hu, N. Chen, and D. T. Jiang, Phys. Rev. B **75**, 134108 (2007).
[11] K. Kinoshita, M. Nishimura, Y. Akahama, and H. Kawamura, Solid State Commun. **141**, 69 (2007).
[12] H. K. Mao, P. M. Bell, J. W. Shaner, and D. J. Steinberg, J. Appl. Phys. **49**, 3276 (1978).
[13] A. L. Ruoff, H. Luo, C. Vanderborgh, H. Xia, K. Brister, and V. Arnold, Rev. Sci. Instrum. **64**, 3462 (1993).
[14] A. P. Hammersley, S. O. Svensson, M. Hanfland, A. N. Fitch, and D. Häusermann, High Press. Res. **14**, 235 (1996).
[15] S. Desgreniers and K. Lagarec, J. Appl. Crystallogr. **27**, 432 (1994).
[16] J. Rodriguez-Carvajal, *FULLPROF, version 3.70, July 2006.*
[17] G. Kresse and J. Furthmüller, Comput. Mater. Sci. **6**, 15 (1996).
[18] D. Vanderbilt, Phys. Rev. B **41**, 7892 (1990).
[19] H. J. Monkhorst and J. D. Pack, Phys. Rev. B **13**, 5188 (1976).
[20] L. G. Liu and W. A. Bassett, J. Geophys. Res. **77**, 4934 (1972).
[21] A. Friedrich, M. Kunz, R. Miletich, and P. Pattison, Phys. Rev. B **66**, 214103 (2002).
[22] J. M. Leger, J. Haines, A. Touf, O. Schulte, and S. Hull, Phys. Rev. B **52**, 13247 (1995).
[23] A. Vegas, A. Grzechnik, K. Syassen, I. Loa, M. Hanfland, and M. Jansen, Acta Crystallogr. B **57**, 151 (2001).
[24] B. Lebech, N. H. Andersen, S. Steenstrup, and A. S. Pedersen, Acta Crystallogr. C **39**, 1475 (1983).

Chapter 4 High-pressure structures and vibrational spectra of barium fluoride: Results obtained under nearly hydrostatic conditions

as published in Physical Review B, Volume 79, Article Number 134104, 2009.

PHYSICAL REVIEW B **79**, 134104 (2009)

High-pressure structures and vibrational spectra of barium fluoride: Results obtained under nearly hydrostatic conditions

Jesse S. Smith,[1,*] Serge Desgreniers,[1] John S. Tse,[2] Jian Sun,[3,†] Dennis D. Klug,[3] and Yasuo Ohishi[4]
[1]*Laboratoire de physique des solides denses, Department of Physics, University of Ottawa, Ottawa, Ontario, Canada K1N 6N5*
[2]*Department of Physics and Engineering Physics, University of Saskatchewan, Saskatoon, Saskatchewan, Canada S7N 5E2*
[3]*Steacie Institute for Molecular Sciences, National Research Council of Canada, Ottawa, Ontario, Canada K1A 0R6*
[4]*Materials Science Division, Japan Synchrotron Radiation Research Institute (JASRI), SPring-8, Sayo, Hyogo 679-5198, Japan*
(Received 22 November 2008; published 6 April 2009)

Powder x-ray diffraction and Raman spectroscopy experiments, together with first-principles calculations, have been carried out to corroborate and clarify the pressure-dependent structural evolution of barium fluoride. X-ray diffraction experiments were performed both with and without a pressure-transmitting medium. The latter serve to reproduce past experimental results, while the former show a marked difference. Specifically, the experiments employing helium as a pressure-transmitting medium yield observed relative intensities and volume compression consistent with the proposed Ni_2In structure of barium fluoride at pressures greater than 14 GPa. The Raman spectroscopy measurements corroborate the proposed Ni_2In structure, as the spectra exhibit the two modes expected for the high-pressure phase. The experiments also demonstrate that barium fluoride remains an insulator up to at least 77 GPa, and the results of first-principles calculations suggest that a subsequent insulator-metal transition may not be expected well into the megabar regime.

DOI: 10.1103/PhysRevB.79.134104 PACS number(s): 61.50.Ks, 62.50.−p, 78.30.−j

I. INTRODUCTION

The pressure-dependent properties of ionic AX_2 compounds are of considerable interest in a number of applied and fundamental respects. For example, many of the oxides are relevant in various industrial[1] and geological[2] contexts, and several of the hydrides have been examined as possible systems for hydrogen storage and exchange[3] and for elucidating hydrogen lattice dynamics.[4] Furthermore, as relatively simple binary compounds, many AX_2 compounds are well suited to powerful computational methods over a broad range of thermodynamic conditions. BaF_2 has played an important role in the study of these materials. It served as the first explicit example of a pressure-induced structural phase transition for which the high-pressure structure is characterized by a cation coordination number of 11 (Ref. 5) and both computational[6] and experimental[7] studies have predicted an insulator-metal transition at the relatively modest pressures (modest with respect to the current limits of static high-pressure techniques) of 33 and 87 GPa, respectively.

At ambient conditions, BaF_2 adopts the cubic fluorite structure ($Fm3\text{-}m$, Z=4) (Ref. 8). A pressure-induced phase transition at approximately 3 GPa was first identified by Smith and Chen[9] and shortly thereafter confirmed and clarified by Seifert,[10] who proposed the cotunnite structure (orthorhombic, *Pnam*, Z=4) for the high-pressure phase. This proposed structure was later corroborated by the Raman spectroscopy measurements of Kessler *et al.*,[11] carried out at low temperature (77 K) and high pressure (up to approximately 3 GPa).

Upon undertaking powder x-ray and neutron-diffraction studies, Leger *et al.*[5] reported they could expect, based on their previous work,[12] that at yet higher pressures BaF_2 would adopt a monoclinic structure. This would follow the structural progression cubic → orthorhombic → monoclinic which in turn would be characterized by a progression in the cation coordination number $8 \rightarrow 9 \rightarrow 10$. Instead they found upon increasing pressure that at approximately 15 GPa, BaF_2 undergoes a first-order structural phase transition with a proposed Ni_2In structure (hexagonal, $P6_3/mmc$, Z=2). As mentioned above, this was the first explicit example of cation coordination number 11 among AX_2 compounds, although Leger *et al.* noted that the structure proposed by Lebech *et al.* for YbH_2 at pressures greater than approximately 14.3 GPa (Ref. 13) is the same as that proposed for BaF_2 at pressures greater than approximately 15 GPa, and would therefore also constitute an example of cation coordination number 11 in ionic AX_2 compounds. Furthermore, by extending their study up to 40 GPa, they demonstrated that if BaF_2 does undergo a subsequent insulator-metal transition, the later work of Kanchana *et al.*[6] which predicted a metallization pressure of 33 GPa was certainly an underestimate. Table I summarizes the structural details of the three observed phases of BaF_2 for various pressures at ambient temperature.

The work of Leger *et al.*[5] has been influential as it has served as the archetype for the cotunnite → Ni_2In structural progression in a number of experimental and computational studies on AX_2 compounds. This has been of particular importance, for example, in the case of recent experimental work on the heavy alkaline-earth hydrides[14–17] which adopt the cotunnite structure at ambient conditions and subsequently transform to the Ni_2In structure upon increasing pressure. In these instances, powder x-ray diffraction measurements alone were not sufficient to locate the position of hydrogen. Similarly, it has been important in computational works (see, for example, that on Li_2O) (Ref. 18), where proposed transition pressures approach or exceed the limits of routine static pressure experiments.

A close examination of Ref. 5, however, reveals some difficulties with the proposed Ni_2In structure. Specifically, the cotunnite structure is such that throughout the stable pressure regime, the *a* axis should be substantially more

TABLE I. Summary of the known structures of BaF_2 at ambient temperature. The refined x and z coordinates of the cotunnite phase are from data obtained at 7.9 GPa.

Type	Symmetry	Space group	Z-value	Atom	Wycoff site	x	y	z	Stability range (GPa)
Cubic fluorite	Cubic	$Fm3\text{-}m$	4	Ba^{2+}	$4a$	0	0	0	0–3
				F^{1-}	$8c$	1/4	1/4	1/4	
Cotunnite	Orthorhombic	$Pnma$	4	Ba^{2+}	$4c$	0.246(2)	1/4	0.119(1)	3–14
				F^{1-}	$4c$	0.370(3)	1/4	0.415(4)	
				F^{1-}	$4c$	0.987(5)	1/4	0.705(3)	
Ni_2In	Hexagonal	$P6_3/mmc$	2	Ba^{2+}	$2c$	1/3	2/3	1/4	14–77+
				F^{1-}	$2a$	0	0	0	
				F^{1-}	$2d$	1/3	2/3	3/4	

compressible than the b and c axes, which is precisely what was observed. Similarly, upon transformation to the Ni_2In structure, the c axis should be more compressible than the a axis (due to the close relationship between the two respective structures), resulting in a decreasing c/a ratio with increasing pressure. The *opposite* pressure dependence was observed. Furthermore, the observed relative diffraction intensities for the Ni_2In phase differ significantly from those expected based on the proposed structure; the observed differences can only be accounted for by severe or essentially total preferred orientation. Finally, there has been no subsequent account of complimentary experimental techniques to corroborate the proposed structure. With the above in mind, it is expedient to revisit the pressure-dependent structural progression of BaF_2.

The following work presents angle-dispersive powder x-ray diffraction and Raman spectroscopy experiments, together with first-principles calculations, in an effort to resolve the aforementioned difficulties. In the case of the diffraction experiments, samples were prepared both with and without a pressure-transmitting medium; the respective experiments revealed marked differences. In the absence of a pressure-transmitting medium, the x-ray diffraction results reproduced well the results (including the difficulties mentioned above) reported in Ref. 5. Conversely, with the use of helium as a pressure-transmitting medium, the pressure dependence of the lattice parameters evolved in accord with that expected for the Ni_2In structure, viz., the c/a ratio decreased with increasing pressure. Also, the observed relative intensities were more consistent with those expected from the structural model. Furthermore, subtle precursor phenomena proposed by Kunc *et al.*[18] were observed for the cotunnite structure at pressures just below the Ni_2In transition. The Raman spectroscopy results further corroborate the Ni_2In structure, as the two expected Raman-active modes were observed. Finally, our observations indicate that BaF_2 remains an insulator up to at least 77 GPa—the maximum experimental pressure attained in this study—and if a possible insulator-metal transition occurs in the same manner as observed for BaH_2 (Ref. 15), calculations suggest it is not expected to take place well into the megabar regime.

II. EXPERIMENTAL AND THEORETICAL DETAILS

Three separate samples were prepared from the same bulk powder sample of BaF_2 (Sigma-Aldrich, 99.999% trace metals analysis). Membrane-type diamond-anvil cells with 300 μm flat culet anvils were used. Rhenium gaskets with an initial thickness of 250 μm were preindented to 45–70 μm, after which compression chambers 75–125 μm in diameter were drilled using electric spark erosion. Two of the three samples were loaded without a pressure-transmitting medium. For the first sample, the primary objective was to collect diffraction data up to the highest pressure possible (perhaps as high as 100 GPa) in an effort to find the proposed insulator-metal transition. It should be noted that pressure-transmitting media (with the exception of helium or similarly hydrogen) offer marginal benefit at such high pressures and can complicate the diffraction data with unwanted x-ray scattering. For the second sample, the primary objective was to collect unambiguous Raman spectra to corroborate the Ni_2In structure, consequently no pressure-transmitting medium was used (at the expense of not obtaining the pressure dependence of the Raman-active modes under hydrostatic conditions). The third sample was loaded with helium using a high-pressure gas loading system available at the BL10XU beamline at SPring-8. We here note that although the sample cannot be characterized as truly hydrostatic upon solidification of the helium pressure-transmitting medium, we hereafter refer to this sample and the corresponding experimental results as hydrostatic. In each sample, a single ruby microsphere was placed in the compression chamber prior to loading and pressure measurements were carried out using ruby luminescence, $P=A/B[(\lambda/\lambda_0)^B-1]$, selecting appropriate parameters for pressure calculations based on the use (or lack) of a pressure-transmitting medium ($A=1904$ GPa with $B=5$ for nonhydrostatic conditions[19] and $B=7.665$ for hydrostatic conditions).[20]

Two separate angle-dispersive powder x-ray diffraction experiments were performed using synchrotron radiation. The first was carried out at the HXMA beamline at the CLS (Ref. 21) on one of the samples loaded without a pressure-transmitting medium. An incident wavelength of 0.515 96 Å was selected using the Si (111) crystals of a fixed-exit double-crystal monochromator. Beamline optics were used for collimating and focusing the white beam and monochromatic radiation, respectively, and a final beam size of 30 $\times 30$ μm^2 was defined using a square-aperture tungsten carbide collimator. Powder x-ray diffraction images were captured on a Marresearch mar345 imaging plate detector (scanned at 100 μm pixel resolution) located 271.71(2) mm from the sample. The sample-to-detector distance was determined using x-ray diffraction images of silicon (National Institute of Standards and Technology, Standard Reference Material 640c), and research samples were located at the same position as the standard using a centering technique based on the x-ray transmission of the gasket.[22] During a typical exposure of 8 min, the sample was rocked over 6° to minimize detector saturation and to improve the intensity distribution along Debye rings.[22] Starting at ambient pressure, images were collected upon increasing pressure up to a maximum pressure of 77.1 GPa.

The second diffraction experiment was carried out at the BL10XU beamline at SPring-8 (Ref. 23) on the sample loaded with helium as a pressure-transmitting medium. A wavelength of 0.352 69 Å was selected using the diamond (111) crystals of a double-crystal monochromator. The x-ray beam was focused using glassy carbon compound refractive lenses (CRL) followed by another CRL made of an SU-8 polymer (an epoxy-based negative photoresist) providing a final beam spot 20×20 μm^2 at the sample. Powder x-ray diffraction images were captured on a Rigaku R-Axis IV imaging plate detector (scanned at 100 μm pixel resolution) located 307.74(2) mm from the sample. The sample-to-detector distance was determined using powder x-ray diffraction images of CeO_2, and research samples were located at the same position as the standard using automated microscopy. During a typical exposure of 10 min, samples were rocked over 10°. Starting at 0.7 GPa, images were collected upon increasing pressure up to a maximum pressure of 32.7 GPa.

All powder x-ray diffraction images were processed and integrated using FIT2D (Ref. 24) to obtain x-ray diffraction patterns of intensity vs 2θ. XRDA (Ref. 25) was used for pattern analysis and indexing. Whole-pattern refinements were performed on all patterns using FULLPROF.[26] Due to several complicating factors (see Sec. III A for more details), the Le Bail method of profile matching was applied to diffraction patterns of the high-pressure phases collected from the sample without a pressure-transmitting medium. Refined parameters included background, scale, lattice parameters, and pseudo-Voigt peak profile parameters. Rietveld refinements were carried out on all other patterns. Additional refined parameters included an overall isotropic displacement parameter, a Rietveld-Toraya correction for preferred orientation for the high-pressure phases, and fractional atomic coordinates for the cotunnite structure.

Raman spectroscopy measurements were performed on the two samples loaded without a pressure-transmitting medium. Spectra were collected from the same sample used in the diffraction experiment (starting at the maximum pressure of 77.1 GPa) upon decreasing pressure down to ambient pressure. For the second sample, spectra were collected from 0.3 GPa upon increasing pressure up to 31.5 GPa. Raman spectra were collected in near-backscattering geometry using a Jobin-Yvon S3000 triple-grating subtractive spectrograph equipped with a nitrogen-cooled charge-coupled device (CCD) detector. The 488 nm line of an Ar ion laser was used for excitation. All diffraction and spectroscopy experiments were carried out at ambient temperature.

First-principles calculations of the electronic structure were performed using the software package VASP.[27] Perdew-Becke-Erhenzof (PBE) projected augmented potentials (PAW) (Ref. 28) were used in all calculations. The $5s^25p^66s^2$ electrons of Ba were treated as valence. Monkhorst-Pack k meshes[29] of $10 \times 8 \times 12$, $12 \times 12 \times 8$, and $8 \times 8 \times 12$ were used for the cotunnite, Ni_2In, and AlB_2 structures, respectively. The unit-cell size (and fractional atomic coordinates, in the case of the cotunnite structure) was optimized for selected volumes, and the corresponding pressures were calculated directly from the stress tensor. In all cases, the plane-wave energy cutoff was set at 875 eV. The convergence criterion for energy calculations was 10^{-7} eV and for geometry optimizations, the residual forces on the atoms were smaller than 1.0×10^{-3} eV/Å. Phonon frequencies and eigenvectors for the Ni_2In phase were obtained using the ABINIT code[30] using the generalized gradient approximation[28] employing the pseudopotential plane-wave density-functional method on $8 \times 8 \times 8$ Monkhorst-Pack k meshes.[29] Troullier-Martins pseudopotentials[31] were employed for the phonon calculations treating the $6s^2$ electrons as valence. Equations of state data were obtained with Troullier-Martins and Hartswigsen-Goedecker-Hutter pseudopotentials[32] treating $6s^2$ and $5s^25p^66s^2$ electrons of Ba as valence, respectively.

III. RESULTS AND ANALYSIS

A. Powder x-ray diffraction

An x-ray diffraction image was first obtained from BaF_2 at ambient pressure and temperature conditions. The resulting pattern revealed no signs of impurity; the refined lattice parameter of the cubic fluorite structure was $a = 6.197\,7(5)$ Å consistent with previous measurements.[8] Figure 1 shows representative whole-pattern refinements from each of the three phases (cubic fluorite, cotunnite, and Ni_2In structures) from the nonhydrostatic (left) and hydrostatic (right) diffraction experiments. As expected, the characteristic features of the respective experiments showed marked contrast. The diffraction patterns of the high-pressure phases obtained from the nonhydrostatic sample exhibited substantial strain broadening as compared to those obtained from the hydrostatic sample (compare, for example, the resolution of closely spaced peaks at even modest 2θ values). Similarly, the nonhydrostatic experiment suffered from severe preferred orientation, as evidenced by the remarkable differences in relative intensities for the Ni_2In phase. Perhaps less expected was the nature of the pressure-induced phase transitions. In the nonhydrostatic case, the phase transitions were distinct and complete. The patterns obtained at 5.2 and 18.5 GPa (the first pressure points above the expected transition pressures of approximately 3 and 14 GPa) exhibited

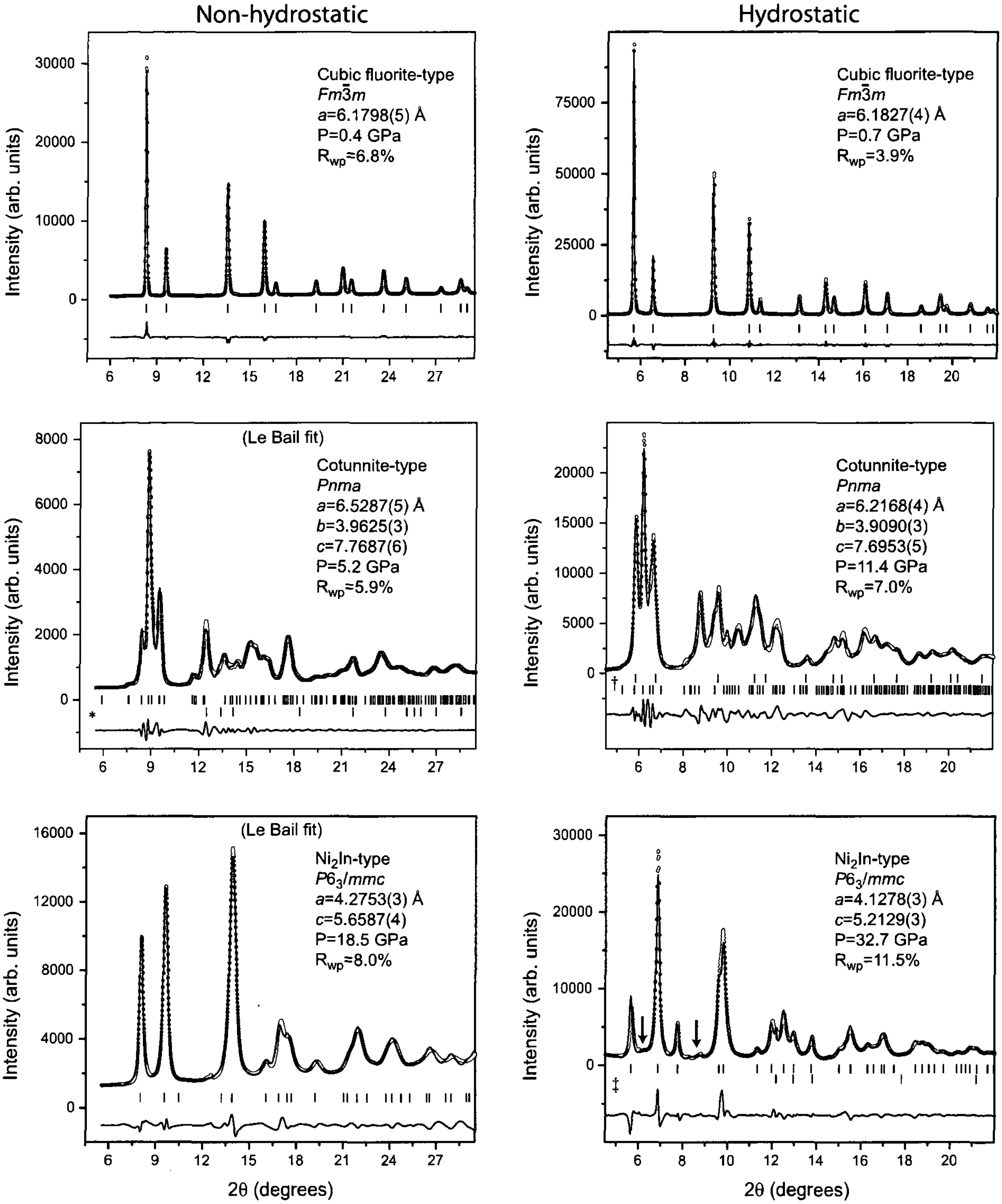

FIG. 1. (Color online) Representative Rietveld (or Le Bail, where indicated) refinements for the three observed phases of BaF_2 from the nonhydrostatic (left) and hydrostatic (right) powder x-ray diffraction experiments. Each plot includes the observed diffraction intensity (symbols), corresponding fit (solid line), expected Bragg peaks (vertical bars), and difference (bottom solid line). Additional Bragg peaks account for the scattering from the rhenium gasket (*), the persistent cubic fluorite phase (†), or solid helium (‡). Trace amounts of the persistent cotunnite phase are indicated by arrows (bottom right). Note that the background has been subtracted from the plots obtained under hydrostatic conditions (right) to facilitate comparison against the expected Bragg peaks.

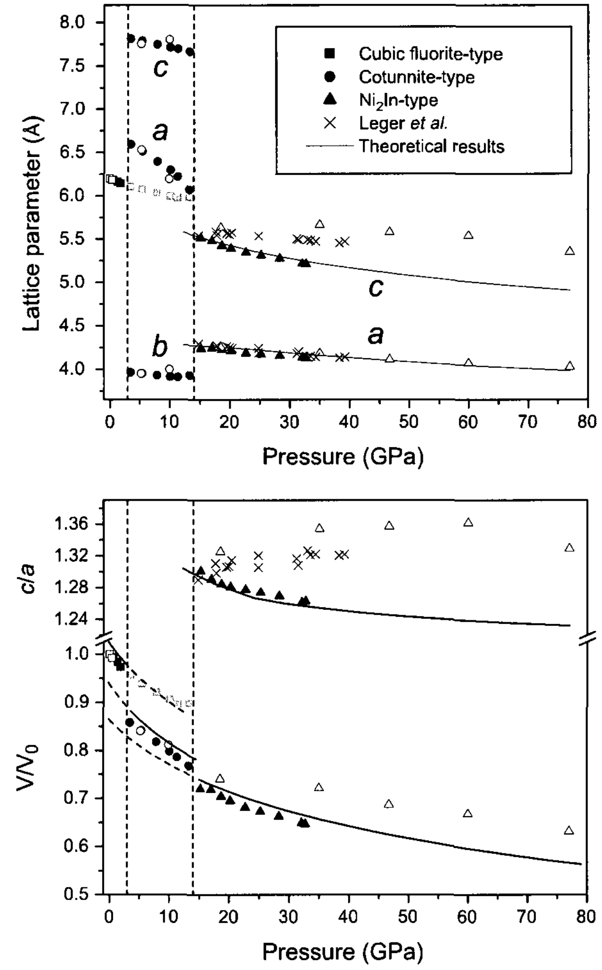

FIG. 2. Pressure dependence of the lattice parameters (top) and relative volume (bottom) for each of the three phases, as well as the c/a axial ratio for the Ni_2In phase (bottom). Open and closed symbols denote data from the nonhydrostatic and hydrostatic diffraction experiments, respectively. The gray squares represent the refined lattice parameter for the persistent cubic fluorite phase in the stable pressure regime of the cotunnite phase for the hydrostatic experiment.

peaks only from the cotunnite and Ni_2In structures, respectively. Conversely, in the case of the hydrostatic experiment, the phase transitions were extremely sluggish. The first (trace) sign of the cotunnite phase appeared at approximately 2 GPa but did not constitute the majority phase (based on quantitative analysis) until approximately 5.5 GPa, and the cubic fluorite phase persisted as a minority phase up to at least 13 GPa, nearing the onset of the cotunnite→Ni_2In phase transition. Similarly, trace amounts of the cotunnite phase persisted throughout the stable pressure regime of the Ni_2In phase up to the maximum sample pressure of 32.7 GPa. As further discussed below, this introduced complications with carrying out structural refinements and with obtaining accurate experimental equations of state.

1. Cubic fluorite phase

The cubic fluorite phase was stable up to approximately 3 GPa. Full structural refinements were carried out on patterns from both the nonhydrostatic and hydrostatic experiments, as shown in Fig. 1 (top). Figure 2 shows the refined lattice parameters and relative volume for each of the three phases, together with the results of the first-principles calculations. While the narrow pressure range and correspondingly small volume compression of the pure cubic fluorite phase precluded obtaining a meaningful experimental equation of state, the data nevertheless agree well with the equation of state obtained by fitting the results of the first-principles calculations to a third-order Birch-Murnaghan equation of state. The resulting isothermal bulk modulus $B_0=58.2(3)$ GPa is in good agreement with that obtained from ultrasonic measurements obtained at ambient pressure.[33] See Table II for complete experimental and theoretical equation of state parameters for all phases.

2. Cotunnite phase

Above approximately 3 GPa, a pressure-induced phase transition was indicated by the marked change in the x-ray diffraction images. Indexing the orthorhombic cotunnite phase was straightforward for patterns from both of the diffraction experiments. Note that here the indexing is consistent with the *Pnma* permutation (as opposed to *Pnam* per-

TABLE II. Equation of state parameters for the three phases of BaF_2 obtained by fitting $P(V)$ data to a third-order Birch-Murnaghan equation of state. $V_0=59.52(1)$ Å^3/BaF_2 based on the x-ray diffraction data obtained at ambient conditions.

	Expt.			Theor.		
	B_0 (GPa)	B_0'	V/V_0	B_0 (GPa)	B_0'	V/V_0
Fluorite	57[a]	n/a	n/a	58.2(3)	4.67(2)	1.022(1)
Cotunnite	51(4)	4.7[b]	0.92(1)	52(1)	4.7(3)	0.937(1)
Ni_2In	56(5)	4.67[b]	0.86(2)	69(1)	4.67(2)	0.864(2)

[a] Reference 33.

[b] Assumed, based on theoretical results.

mutation used in Refs. 10 and 5; for a detailed discussion on the various permutations of the *Pnma* space group, see Hybler's work[34] with regard to α-$PbCl_2$). As shown in Fig. 2 (top), there is a marked difference in the pressure dependence among the various lattice parameters. Specifically, the a axis is much more compressible than the b and c axes, decreasing by approximately 0.046 Å/GPa as compared to 0.008 and 0.016 Å/GPa, respectively. Despite the relatively narrow stable pressure regime for the cotunnite phase, the experimental data were fit to a third-order Birch-Murnaghan equation of state, yielding an isothermal bulk modulus $B_0 = 51(4)$ GPa (B_0' fixed at 4.7, the value obtained from the theoretical calculations). This result is less than 79(10) GPa reported in Ref. 5, however, the underestimate here is likely due to the coexistence of the cubic fluorite and cotunnite phases. A volume collapse of approximately 10% was observed at the transition pressure of 3 GPa.

Of the three stable structures of BaF_2 studied in this work, the cotunnite structure is the only one for which the atoms are not located in special positions. Specifically, each of the three atoms in the asymmetric unit occupies the $4c$ position, with only the y coordinate constrained by symmetry. Unfortunately, the preferred orientation present in the nonhydrostatic experiment precluded a full structural refinement, as ambiguity was introduced by the strong correlation between the degree/direction of the preferred orientation and the fractional x and z coordinates of the respective atoms. Similarly, the coexistence of phases in the hydrostatic experiment does not rule out ambiguity in the refined atomic positions. Nevertheless, to obtain full structural refinements, the atomic positions obtained from the first-principles calculations were initially used. These atomic positions are in excellent agreement with the refined positions reported in Ref. 5. Table I includes the refined atomic positions for data obtained at 7.9 GPa. Figure 1 (middle) shows representative Le Bail and Rietveld refinements for the nonhydrostatic and hydrostatic experiments, respectively.

In their first-principles investigation of Li_2O, Kunc *et al.*[18] suggested precursor phenomena that accompany the cotunnite→Ni_2In transition. At ambient conditions, Li_2O adopts the cubic antifluorite structure and undergoes a pressure-induced structural phase transition to the anticotunnite structure at approximately 50 GPa (Ref. 35). (Note the antiphase nomenclature refers to A_2X, as opposed to AX_2, compounds.) Their computational results suggested that Li_2O will subsequently transform to the Ni_2In structure at approximately 135 GPa, with precursor phenomena to the phase transition characterized by distinct nonlinearities in the c/b and a/b axial ratios (the latter more so than the former) of the anticotunnite structure. Interestingly, they specifically suggested that BaF_2 would serve as a good candidate to explore these phenomena experimentally. Figure 3 (top) shows these axial ratios for the cotunnite phase of BaF_2 (from the hydrostatic experiment) over the stable pressure range of 3–14 GPa, which exhibit the proposed nonlinearities. Furthermore, as shown in Fig. 3 (bottom), these nonlinearities are the result of a sharp decrease in a, together with a slight *increase* in b, just before the phase transition—precisely as suggested in Ref. 18.

To summarize the x-ray diffraction results for the cubic fluorite and cotunnite phases, the results of the nonhydrostatic and hydrostatic experiments—as well as the results of the first-principles calculations—are essentially in agreement, and moreover, are in general agreement with the results of Ref. 5. We here add to the description the precursor phenomena for the cotunnite phase just prior to transforming to the Ni_2In structure. It is upon transforming to the Ni_2In structure that the various results begin to show marked differences.

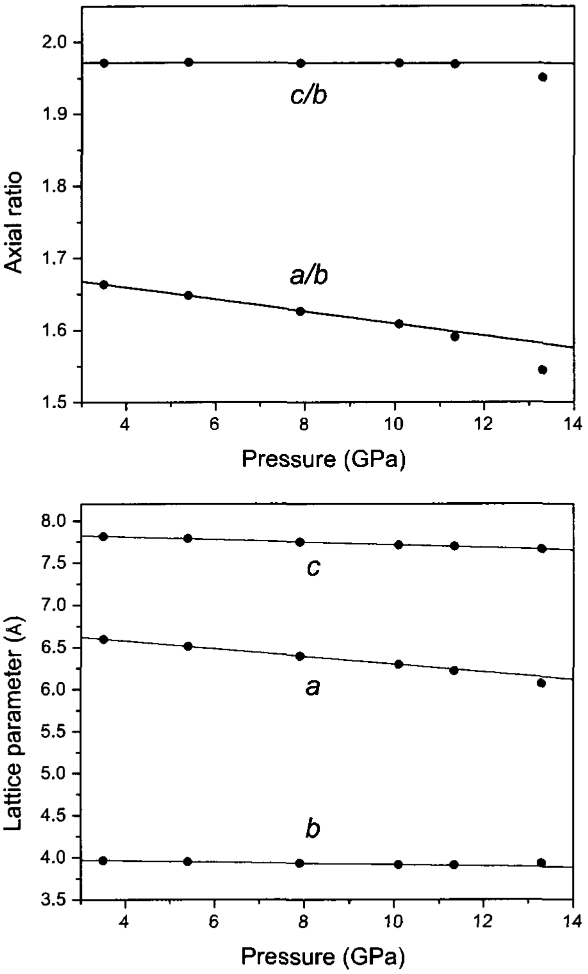

FIG. 3. Pressure dependence of the axial ratios (top) and lattice parameters (bottom) of the cotunnite phase from the hydrostatic experiment, detailing the precursor phenomena observed just prior to the Ni_2In transformation. The solid lines represent linear fits obtained from the first four data points of the respective ratios or lattice parameters.

3. Ni_2In *phase*

Above approximately 14 GPa, a subsequent phase transition was observed, indicated again by distinct changes in the x-ray diffraction images. The resulting x-ray diffraction patterns were readily indexed to a hexagonal unit cell. As shown in Fig. 2 (top), there was excellent agreement for the refined values of the a axis among the nonhydrostatic and hydro-

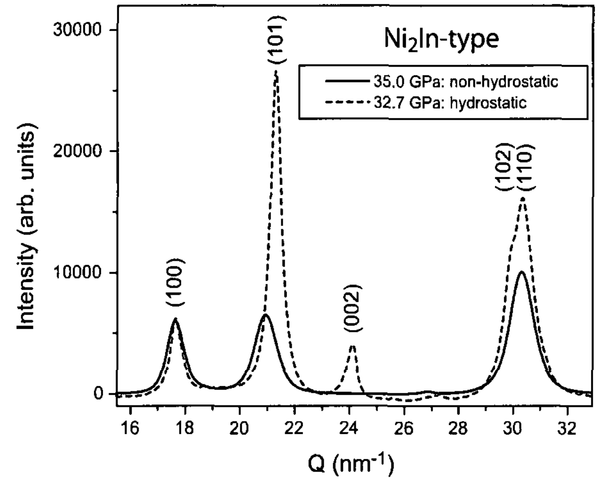

FIG. 4. (Color online) A comparison of x-ray diffraction patterns of the Ni_2In phase from the nonhydrostatic and hydrostatic diffraction experiments reveals marked differences in intensity and line position due to severe preferred orientation and atypical axial compression.

static experiments, the results of Ref. 5, and the theoretical results. The same cannot be said about the c axis. A significantly larger c axis was observed in the nonhydrostatic experiment and (to a lesser extent) in Ref. 5, as compared to the hydrostatic and theoretical results. Furthermore, the former two showed an increase in the c/a ratio with increasing pressure, while the latter two showed the opposite pressure dependence. As already discussed, the close relationship between the high-pressure structures suggests that the highly compressible a axis in the cotunnite structure should in turn result in a highly compressible c axis in the Ni_2In structure.

These observed differences can be accounted for by preferred orientation. With the c axis of the Ni_2In phase normal to the load axis—and consequently the incident x-ray beam—the $(00l)$ reflections would be absent, and (hkl) reflections with $l \neq 0$ would show marked decreases in intensity. Furthermore, upon compression along the load axis of the cell, the compression along the a axis would be close to what would be observed even under hydrostatic conditions, while the compression along c would be minimized due to the orientation of the crystallites. This is well illustrated in Fig. 4, which compares intensities over a selected region of Q space from the nonhydrostatic and hydrostatic experiments at approximately the same pressure, viz., 35.0 and 32.7 GPa, respectively. It is important to note that the background has been subtracted from the pattern obtained under hydrostatic conditions, and a small Q shift in the nonhydrostatic experiment of 0.15 nm^{-1} (equivalent to 0.07° 2θ) has been applied to aid in comparing peak positions; however, no intensity scaling has been applied to either pattern. The intensities of the (100) reflection [i.e., an $(hk0)$ plane] are in excellent agreement. However, the (101) reflection shows extreme differences in intensity and position due to preferred orientation and minimized compression along the c axis, respectively. The effect on intensities is most extreme in the case of the (002) peak [i.e., a $(00l)$ peak], which is completely absent in the nonhydrostatic case.

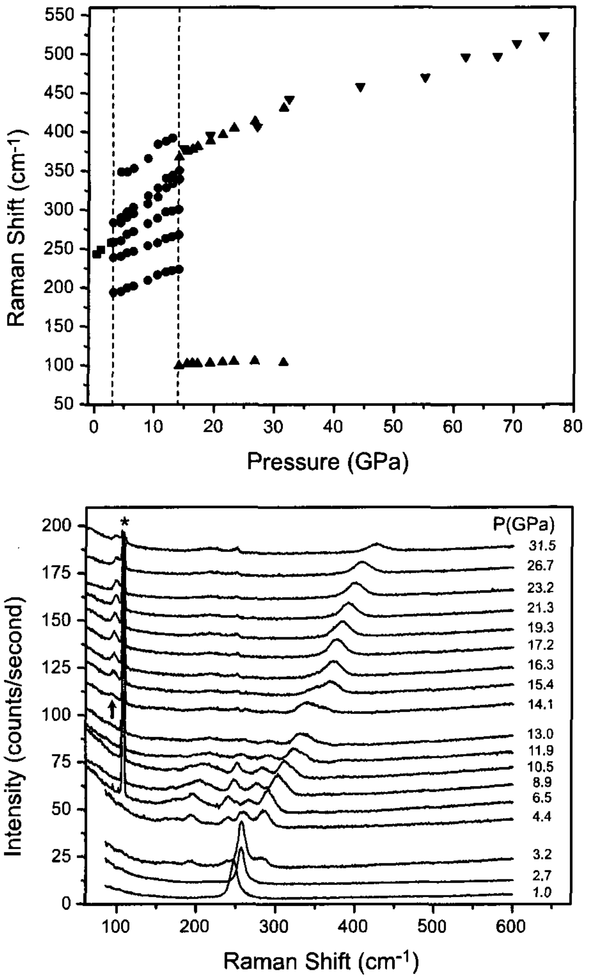

FIG. 5. The pressure dependence of the observed Raman modes (top) and several Raman spectra obtained upon increasing pressure (bottom). The inverted triangles represent data collected upon decreasing pressure; all other data were collected upon increasing pressure. The arrow indicates the first sign of the low-wave-number mode associated with the Ni_2In phase. The intense narrow peak at approximately 105 cm^{-1} (*) arises from stray light associated with collecting spectra from very low wave numbers (its position remains constant with pressure). For clarity, the intensity of the bottom two spectra has been halved and a vertical offset has been added to all spectra.

The pressure-dependent volume of the Ni_2In phase was fit to a third-order Birch-Murnaghan equation of state, yielding $B_0=58(5)$ GPa (B_0' fixed at 4.67, the value obtained from the theoretical calculations). Again, this is likely an underestimation due to the coexistence with the cotunnite phase up to the maximum pressure of the study. But nevertheless, it is clear after measuring the compression under the best possible hydrostatic conditions that the Ni_2In phase of BaF_2 is much more compressible than previously reported. The volume collapse at the transition pressure of 14 GPa was approximately 5%.

B. Raman spectroscopy

The primary purpose of the Raman experiments was to corroborate the proposed Ni_2In structure of BaF_2. A group theoretical analysis indicates that only two modes should be observed, according to the irreducible representation $\Gamma_{Raman} = 2E_g$. Similarly, for the cubic fluorite and cotunnite phases, the irreducible representations of the Raman-active modes are $\Gamma_{Raman}=T_{2g}$ (a single mode) and $\Gamma_{Raman}=6A_g+3B_{1g} +6B_{2g}+3B_{3g}$ (18 modes), respectively. Figure 5 shows the pressure dependence of the observed Raman modes from the two nonhydrostatic samples (top), together with several Raman spectra from the experiment taken upon increasing pressure (bottom). Considering first the data taken upon increasing pressure, at ambient pressure the spectrum exhibited a single peak at 240 cm^{-1}. The peak shifted to higher wave numbers with increasing pressure at a rate of just over 8 cm^{-1}/GPa, in excellent agreement with that observed in Ref. 11. At 3.2 GPa, the peak intensity fell sharply and several broad peaks appeared on either side, indicating the onset of the transition to the cotunnite structure. Given the experiment was carried out at ambient temperature, it was not possible to resolve the many peaks in the 150–300 cm^{-1} range, and furthermore, many of the modes observed by Kessler *et al.*[11] at lower wave numbers were not observed. Nevertheless, the broad multimode band at $\sim$200 cm^{-1}, together with the triplet in the 225–300 cm^{-1} range, was consistent with the previous study. The pressure dependence of these modes over the stable pressure regime ranged from approximately 3–6 cm^{-1}/GPa, in agreement with that observed for α-PbF_2 (Ref. 11). Above 10 GPa, the intensity of the peaks again decreased significantly, and an asymmetry of the doublet at approximately 325 cm^{-1} developed, with a small shoulder emerging on the high-wave-number side. These developments may constitute the Raman manifestation of the precursor phenomena observed in the x-ray diffraction experiments. At 14.1 GPa, a weak peak emerged at approximately 95 cm^{-1} (indicated by the arrow in Fig. 4, bottom) and the weak shoulder of the peak at 325 cm^{-1} became dominant. Above 16 GPa, the phase transition was complete and the two peaks remained the only Raman features in the spectra up to the maximum pressure of 31.5 GPa. First-principles calculations of the two expected Raman modes for the Ni_2In phase at 40 GPa yielded expected frequencies of 115 and 590 cm^{-1}. While these calculated frequencies are higher than the observed values, the general range is nevertheless consistent with what was observed experimentally.

For the next sample studied upon decreasing pressure (the same as that used in the nonhydrostatic diffraction experiment), at 77.1 GPa, the spectrum had a single, weak, and broad peak at approximately 525 cm^{-1}. The peak shifted to lower wave numbers with decreasing pressure; however, due to the poor signal-to-background ratio and the breadth of the peak, it was difficult to obtain a satisfactory fit for the peak, hence the observed scatter in the data. However, the observed peak was consistent with the high-wave number peak observed for the Ni_2In phase in the companion experiment. The low-wave-number peak was not observed, however. Below 5 GPa, the group of peaks characteristic of the cotunnite phase emerged about this single peak. The group remained down to ambient pressure, and the peak associated with the cubic fluorite phase emerged, indicating a mixture of phases.

IV. DISCUSSION

As mentioned in Sec. I, a computational study predicted metallization of BaF_2 at 33 GPa (Ref. 6); however, it had already been demonstrated by Leger *et al.* that the Ni_2In phase was stable, and the sampled remained completely transparent to visible light, up to at least 40 GPa. More recently, *in situ* conductivity measurements on BaF_2 were carried out by Hao *et al.*[7] up to a pressure of approximately 60 GPa. While no metallization was observed, it was suggested that BaF_2 could be characterized as a wide-gap semiconductor at pressures above 25 GPa (with a band gap of approximately 1.2 eV) and based on extrapolation of the measured band gap as a function of pressure, metallization (zero band gap) would occur at approximately 87 GPa. However, no conclusion was made as to whether this would be accompanied by a first-order structural phase transition.

A high-pressure powder x-ray diffraction study of BaH_2 by Kinoshita *et al.*[15] was the first to report a post-Ni_2In structure for an ionic AX_2 compound. Specifically, the onset of the pressure-induced structural phase transition appeared at approximately 50 GPa, with the phase transformation completed at approximately 65 GPa, and furthermore the transition was reversible (however, large hysteresis was observed). The AlB_2 structure (hexagonal, $P6/mmm$) was proposed for the post-Ni_2In phase. The authors' unpublished research of BaH_2 agrees with Kinoshita *et al.*, and we here add to the characterization of the high-pressure phase by noting that upon transforming to the AlB_2 structure, the band gap is narrow enough that the sample is no longer transparent to visible light. It is reasonable to suggest that if BaF_2 is to undergo a subsequent structural phase transition, it might be characterized by the same structure as BaH_2. However, the current study demonstrates that the Ni_2In structure remains stable up to at least 77 GPa, and furthermore the sample remains transparent to visible light, viz., the band gap must still be significantly larger than 1 eV. We thus conclude that BaF_2 does not transform to a metallic state up to the maximum pressure reached in this study.

A linear relationship between the molar volume and the cube of the mean cation-anion distance has been established for several ionic AX_2 compounds: both at ambient- and high-pressure conditions (see, for example, Refs. 1 and 5). Specifically, $V_{molar}=kd_0^3/N$, where $k=14.4(6)$, d_0 is the mean cation-anion distance, and N is the cation coordination number. It has been shown for CaH_2 and BaH_2 that the relationship holds not only at ambient pressure and immediately following a pressure-induced phase transition, but also throughout the stable pressure range of a given phase.[17] Figure 6 shows this relationship also holds for each of the three phases of BaF_2 throughout the respective stable pressure ranges. Notably, the relationship suggests that the ionic nature of the bonding is maintained up to the maximum pressure of 77.1 GPa; further suggesting that BaF_2 remains an insulator.

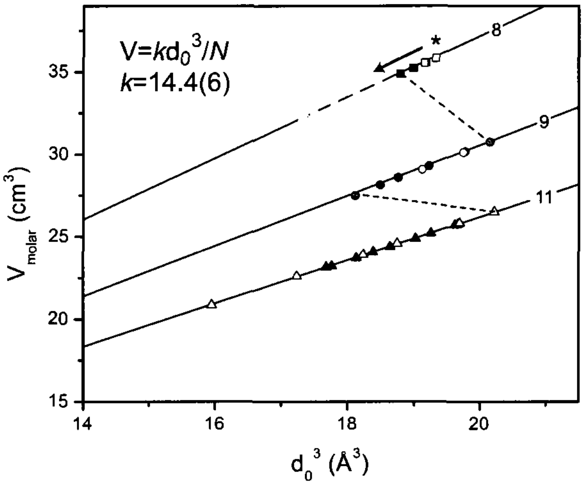

FIG. 6. (Color online) Molar volume vs the cube of the mean cation-anion distance for 8-, 9-, and 11-coordinated Ba^{2+}. Open and closed symbols denote data from the nonhydrostatic and hydrostatic diffraction experiments, respectively. The asterisk (*) indicates ambient pressure. Upon increasing pressure, data tend toward the origin, or in the case of a phase transition, increase in coordination number (as well as mean cation-anion distance) as indicated by the dotted lines. The relationship holds throughout the stable pressure regimes of the respective phases, up to the maximum pressure of the study (77.1 GPa), indicating that the bonding remains characteristically ionic.

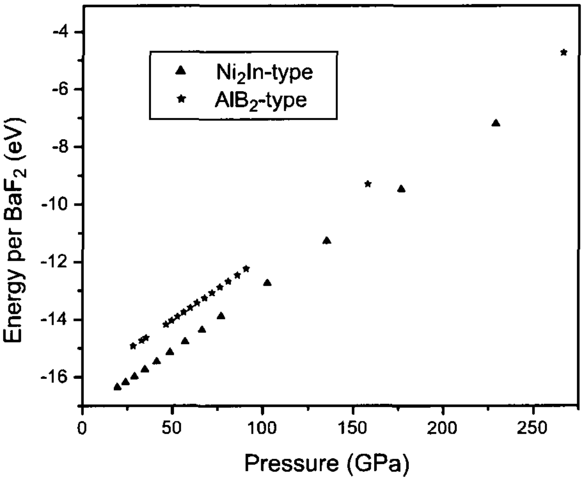

FIG. 7. (Color online) The calculated energy vs pressure for the observed Ni_2In structure and hypothetical AlB_2 structure of BaF_2 suggest that BaF_2 does not undergo an insulator-metal transition analogous to that observed for BaH_2.

Figure 7 shows a comparison of the calculated energy vs pressure for the observed Ni_2In phase and the hypothetical high-pressure AlB_2 phase for BaF_2. The results clearly show a transition to the AlB_2 structure as observed for BaH_2 is not expected to occur for BaF_2 up to at least 250 GPa. Furthermore, our calculations of the band gap suggest that the Ni_2In phase remains insulating at pressures greater than 500 GPa. In short, if BaF_2 does undergo a subsequent pressure-induced phase transition, it is either at pressures which exceed current experimental static pressure limits or it is characterized by a different structure than that observed for BaH_2.

Difficulties arising from nonhydrostatic pressure conditions, such as anisotropic strain broadening and preferred orientation, are frequently encountered. As hexagonal structures are particularly prone to texture, it is not necessarily surprising that the nonhydrostatic and hydrostatic experiments exhibited marked contrast for the Ni_2In data (although the magnitude of the contrast is certainly surprising, e.g., a difference of almost 10% in the c axis at approximately 35 GPa). On the other hand, difficulties arising from hydrostatic pressure conditions are less frequently encountered; in this particular case, hydrostatic conditions gave rise to extremely sluggish pressure-induced phase transitions. As for a possible explanation, we here suggest that microscopic domains may be present in the sample, and these domains are preserved by the hydrostatic conditions. As a portion of the sample in a given domain transforms to a higher-density phase, the corresponding local volume collapse permits a portion of the sample in the same domain to persist in the lower-density phase. Conversely, the shear forces present under nonhydrostatic conditions are sufficient to break down the domain boundaries, resulting in distinct, complete phase transitions. The same result could likely be achieved in the hydrostatic case through annealing by means of laser heating or a conventional furnace. A more thorough exploration of phase coexistence over such a broad pressure range presents an opportunity for further study.

V. CONCLUSION

The primary purpose of the current work was to corroborate the proposed Ni_2In structure of BaF_2 for pressures above 14 GPa. Compression under nonhydrostatic conditions gave rise to atypical compression of the lattice parameters in the high-pressure phase, as well as poor agreement between observed and expected relative intensities due to preferred orientation. These difficulties were resolved by carrying out the experiment under the best possible hydrostatic conditions. The Raman experiments further support the proposed structure, as the spectra exhibited two Raman-active modes as expected for the Ni_2In phase. The previously proposed precursor phenomena accompanying the cotunnite $\rightarrow$ Ni_2In transition were clearly observed in the hydrostatic x-ray diffraction study and this may be further indicated by the marked decrease in intensity of the majority of the observed Raman modes prior to the Ni_2In transition. Finally, the Ni_2In phase of BaF_2 remained stable up to at least 77 GPa and no indications of metallization were observed. If BaF_2 is to undergo a subsequent pressure-induced phase transition in a manner similar to BaH_2, it is likely that this will not occur until well into the multimegabar regime, or alternatively, it will be characterized by a different crystal structure.

ACKNOWLEDGMENTS

Synchrotron-radiation experiments described in this work were performed in part at the Canadian Light Source, which is supported by NSERC, NRC, CIHR, and the University of Saskatchewan, and in part at the beamline BL10XU at SPring-8, with the approval of the Japan Synchrotron Radiation Research Institute (JASRI). S.D., J.S.T., and J.S. wish to acknowledge the financial support of NSERC.

---

*Author to whom correspondence should be addressed. jsmit068@uottawa.ca

†Present address: Lehrstuhl für Theoretische Chemie, Ruhr-Universität Bochum, 44780 Bochum, Germany.

[1] *Metal Oxides: Chemistry and Applications*, edited by J. L. G. Fierro (Taylor & Francis, Florida, 2006).

[2] L. G. Liu and W. A. Bassett, *Elements, Oxides, Silicates: High-Pressure Phases with Implications for the Earth's Interior* (Oxford University Press, New York, 1986).

[3] B. Sakintuna, F. Lamari-Darkrim, and M. Hirscher, Int. J. Hydrogen Energy **32**, 1121 (2007).

[4] D. Colognesi, G. Barrera, A. J. Ramirez-Cuesta, and M. Zoppi, J. Alloys Compd. **427**, 18 (2007).

[5] J. M. Leger, J. Haines, A. Atouf, O. Schulte, and S. Hull, Phys. Rev. B **52**, 13247 (1995).

[6] V. Kanchana, G. Vaitheeswaran, and M. Rajagopalan, J. Alloys Compd. **359**, 66 (2003).

[7] A. M. Hao, C. X. Gao, M. Li, C. Y. He, X. W. Huang, D. M. Zhang, C. L. Yu, G. T. Zou, Y. C. Li, X. D. Li, and J. Liu, Chin. Phys. Lett. **23**, 2917 (2006).

[8] A. H. Swanson and E. Tatge, Natl. Bur. Stand. Circ. (U. S.) **539**, 1 (1953).

[9] H. I. Smith and J. H. Chen, Bull. Am. Phys. Soc. **11**, 414 (1966).

[10] K. F. Seifert, Fortschr. Mineral. **45**, 214 (1967).

[11] J. R. Kessler, E. Monberg, and M. Nichol, J. Chem. Phys. **60**, 5057 (1974).

[12] J. M. Leger, J. Haines, and A. Atouf, Phys. Rev. B **51**, 3902 (1995); J. Appl. Crystallogr. **28**, 416 (1995); J. Phys. Chem. Solids **57**, 7 (1996).

[13] B. Lebech, N. H. Andersen, S. Steenstrup, and A. S. Pedersen, Acta Crystallogr., Sect. C: Cryst. Struc. Commun. **39**, 1475 (1983).

[14] K. Kinoshita, M. Nishimura, Y. Akahama, and H. Kawamura, Proceedings of 20th AIRAPT Conference, 2005 (unpublished).

[15] K. Kinoshita, M. Nishimura, Y. Akahama, and H. Kawamura, Solid State Commun. **141**, 69 (2007).

[16] J. S. Tse, D. D. Klug, S. Desgreniers, J. S. Smith, R. Flacau, Z. Liu, J. Hu, N. Chen, and D. T. Jiang, Phys. Rev. B **75**, 134108 (2007).

[17] J. S. Smith, S. Desgreniers, J. S. Tse, and D. D. Klug, J. Appl. Phys. **102**, 043520 (2007).

[18] K. Kunc, I. Loa, and K. Syassen, Phys. Rev. B **77**, 094110 (2008).

[19] H. K. Mao, P. M. Bell, J. W. Shaner, and D. J. Steinberg, J. Appl. Phys. **49**, 3276 (1978).

[20] H. K. Mao, J. A. Xu, and P. M. Bell, J. Geophys. Res. **91**, 4673 (1986).

[21] S. Desgreniers, J. S. Smith, J. S. Tse, C. Y. Kim, N. Chen, D. T. Jiang, and D. D. Klug, Canadian Light Source Activity Report 2007, p. 132 (unpublished).

[22] J. S. Smith and S. Desgreniers, J. Synchrotron Radiat. **16**, 83 (2009).

[23] Y. Ohishi, N. Hirao, N. Sata, K. Hirose, and M. Takata, High Press. Res. **28**, 163 (2008).

[24] A. P. Hammersley, S. O. Svensson, M. Hanfland, A. N. Fitch, and D. Häusermann, High Press. Res. **14**, 235 (1996).

[25] S. Desgreniers and K. Lagarec, J. Appl. Crystallogr. **27**, 432 (1994); **31**, 109 (1998).

[26] J. Rodriguez-Carvajal, Physica B **192**, 55 (1993).

[27] G. Kresse and J. Furthmuller, Comput. Mater. Sci. **6**, 15 (1996); Phys. Rev. B **54**, 11169 (1996).

[28] J. P. Perdew, K. Burke, and M. Ernzerhof, Phys. Rev. Lett. **77**, 3865 (1996).

[29] H. J. Monkhorst and J. D. Pack, Phys. Rev. B **13**, 5188 (1976).

[30] X. Gonze, Phys. Rev. B **55**, 10337 (1997); X. Gonze and C. Lee, *ibid.* **55**, 10355 (1997); X. Gonze *et al.*, Comput. Mater. Sci. **25**, 478 (2002).

[31] N. Troullier and J. L. Martins, Phys. Rev. B **43**, 1993 (1991).

[32] M. Krack, Theor. Chem. Acc. **114**, 145 (2005).

[33] C. Wong and D. E. Schuele, J. Phys. Chem. Solids **29**, 1309 (1968).

[34] J. Hybler, Cryst. Res. Technol. **23**, 1127 (1988).

[35] K. Kunc, I. Loa, A. Grzechnik, and K. Syassen, Phys. Status Solidi B **242**, 1857 (2005).

Chapter 5 High-density strontium hydride: an experimental and theoretical study

as published in Solid State Communications, Volume 149,
pages 830-834, 2009.

Solid State Communications 149 (2009) 830–834

Contents lists available at ScienceDirect

Solid State Communications

journal homepage: www.elsevier.com/locate/ssc

High-density strontium hydride: An experimental and theoretical study

Jesse S. Smith [a,*], Serge Desgreniers [a], Dennis D. Klug [b], John S. Tse [c]

[a] Laboratoire de physique des solides denses, Department of Physics, University of Ottawa, Ottawa, Ontario, Canada K1N 6N5
[b] Steacie Institute for Molecular Sciences, National Research Council of Canada, Ottawa, Ontario, Canada K1A 0R6
[c] Department of Physics and Engineering Physics, University of Saskatchewan, Saskatoon, Saskatchewan, Canada S7N 5E2

ARTICLE INFO

Article history:
Received 17 January 2009
Accepted 17 March 2009 by P. Hawrylak
Available online 25 March 2009

PACS:
61.50.Ks
62.50.-p
78.30.-j

Keywords:
A. Strontium hydride
B. Diamond anvil cell
D. Phase transitions
E. High pressure

ABSTRACT

Powder x-ray diffraction experiments and first-principles calculations have been carried out to investigate the possibility of a structural phase transition, characterized by a change from ionic to covalent bonding, in strontium hydride at pressures greater than 50 GPa. The powder x-ray diffraction results confirm a previously reported transition from the cotunnite structure to the Ni_2In structure at approximately 8 GPa. The Ni_2In phase remained stable up to the maximum experimental pressure of 113 GPa. The first-principles calculations, however, predict that under hydrostatic conditions a transition from the Ni_2In structure to the AlB_2 structure will occur at 115 GPa. A comparison of the pressure-dependent volume yielded by the respective experimental and theoretical studies suggests that in many cases the bulk modulus obtained from experiments carried out under non-hydrostatic conditions may be overestimated. Raman spectroscopy experiments corroborated the previously proposed Ni_2In structure, as the spectra obtained at pressures greater than 8 GPa exhibited two Raman-active modes, consistent with those expected from the Ni_2In structure.

1. Introduction

The heavy alkaline earth hydrides (HAEHs) consist of the Group II (alkaline earth metal) hydrides, namely CaH_2, SrH_2, and BaH_2, which adopt the cotunnite structure (orthorhombic, $Pnma, Z = 4$) at ambient conditions [1–3]. Recent studies of the HAEHs show that each undergoes a pressure-induced, first-order structural phase transition, with a proposed Ni_2In structure (hexagonal, $P6_3/mmc, Z = 2$) for the high-pressure phase [4–7]. The cotunnite $\rightarrow Ni_2In$ transition is characterized by an increase in the cation coordination number from 9 to 11, which facilitates the necessary finite volume collapse across the phase transition. A cation coordination number of 11 in ionic AX_2 compounds was first reported in BaF_2 by Leger et al. [8]. This marked the highest cation coordination number observed in this class of compounds until Kinoshita et al. reported a post-Ni_2In structure in BaH_2 at a pressure of approximately 50 GPa [6]. The AlB_2 structure (hexagonal, $P6/mmm, Z = 1$) was proposed for the high-pressure phase, and the transition was characterized by a change in the nature of the bonds from ionic to covalent. Subsequent first-principles calculations by Li et al. predicted the same transition in CaH_2 at approximately 138 GPa [9]. As SrH_2 is the intermediate HAEH, it is reasonable to suppose it will undergo the same transition at an intermediate pressure; the primary purpose of this study is to look for such a transition in SrH_2 in the pressure range 50 to 138 GPa. Secondary purposes include corroborating the proposed Ni_2In structure by means of Raman spectroscopy and providing equation of state parameters for all relevant SrH_2 phases.

2. Experimental and theoretical details

Membrane-type diamond anvil cells were used for all experiments. Diamond anvils with flat culets 200 μm and 300 μm in diameter were used for the powder x-ray diffraction and Raman spectroscopy experiments, respectively. Rhenium gaskets with an initial thickness of 250 μm were pre-indented to thicknesses ranging from 50 to 70 μm, after which compression chambers approximately 100 μm in diameter were drilled using spark erosion. The SrH_2 powder used to prepare samples came from two separate commercial sources: Cerac (diffraction experiment) and Chemos (Raman experiment—note that this is the sample used in the inelastic neutron scattering experiment by Colognesi et al. [10]). SrH_2 was loaded into the compression chambers under an inert (argon) atmosphere. No pressure transmitting medium was used; SrH_2 is extremely sensitive to moisture, which precluded the use of a conventional pressure transmitting medium, and no gas loading apparatus was available, which precluded the use a of noble gas medium such as helium. A single ruby microsphere was loaded

---

[*] Corresponding author. Tel.: +1 613 562 5800; fax: +1 613 562 5190.
E-mail addresses: jesse.smith@rogers.com, jsmit068@uottawa.ca (J.S. Smith).

0038-1098/$ – see front matter © 2009 Elsevier Ltd. All rights reserved.
doi:10.1016/j.ssc.2009.03.021

Table 1
Summary of structural information for the observed cotunnite and Ni_2In phases (used for Rietveld refinements presented in Fig. 1) and the predicted AlB_2 phase of SrH_2. Note that the fractional atomic coordinates for the cotunnite phase were obtained from the first-principles calculations.

Type	Symmetry	Space group	Z-value	Atom	Wycoff site	x	y	z	Stability range (GPa)
Cotunnite	Orthorhombic	*Pnma*	4	Sr^{2+}	4*c*	0.2399	1/4	0.1108	0–8.3
				H^-	4*c*	0.3543	1/4	0.4274	
				H^-	4*c*	0.9735	1/4	0.6797	
Ni_2In	Hexagonal	$P6_3/mmc$	2	Sr^{2+}	2*c*	1/3	2/3	1/4	8.3–113+
				H^-	2*a*	0	0	0	
				H^-	2*d*	1/3	2/3	3/4	
AlB_2	Hexagonal	$P6/mmm$	1	Sr	1*a*	0	0	0	115+
				H	2*d*	1/3	2/3	1/2	

with each sample, and pressure measurements were carried out via ruby luminescence using a pressure calibration appropriate for non-hydrostatic pressure conditions [11].

Angle-dispersive powder x-ray diffraction measurements were carried out at the HXMA beamline of the Canadian Light Source. A wavelength of 0.51660 Å was selected using the Si (111) crystals of a fixed-exit double monochromator. Plane parabolic and toroidal mirrors were used to focus the incident beam, with a final beam spot of $30 \times 30\ \mu m^2$ defined by a square-aperture tungsten carbide collimator. Powder x-ray diffraction images were captured by a Marresearch mar345 imaging plate detector located 307.73(2) mm from the sample. During a typical exposure time of 10 min, samples were rocked over 5 ° to minimize detector saturation and to improve the intensity distribution around Debye rings [12]. Image integration (yielding a pattern of intensity *vs.* 2θ), pattern indexing and analysis, and full-pattern refinements were carried out using Fit2d [13], XRDA [14], and FullProf [15], respectively. Le Bail fits were carried out on the majority of the x-ray diffraction patterns; refined parameters included the scale, background, pseudo-Voigt peak profile parameters, and lattice parameters. Rietveld refinements were carried out on selected patterns; additional refined parameters included a Rietveld–Toraya correction for preferred orientation, an overall isotropic displacement parameter, and atomic structural data listed in Table 1. Starting at an initial pressure of 2.4 GPa, images were taken upon increasing pressure up to 113 GPa, after which the diamond anvils failed.

Raman spectroscopy was carried out on several samples upon both increasing and decreasing pressure from ambient pressure up to 22.4 GPa. Spectra were collected in near-backscattering geometry using a Jobin Yvon S3000 triple-grating subtractive spectrograph equipped with a liquid-nitrogen-cooled CCD detector. The 488 nm line of an Ar ion laser was used for excitation.

Structural optimization calculations for the equations of state and enthalpies of the *Pnma*, $P6_3/mmc$, and $P6/mmm$ structures were performed with VASP [16], employing the projected augmented wave (PAW) potential [17]. Gradient corrected potentials employing 4s4p5s electron valence states were used for Sr to optimize the initial structures. Monkhorst–Pack (MP) meshes [18] were used for the first Brillouin zone (BZ) sampling. Calculations to obtain the phonon spectra were performed with the ABINIT [19] code using the generalized gradient approximation employing the pseudopotential planewave method. Troullier–Martins [20] gradient-corrected [21] pseudopotentials were employed. Phonon frequencies were obtained using density functional perturbation theory (DFT) as implemented in the ABINIT DFT code.

3. Results and discussion

The initial powder x-ray diffraction pattern obtained at 2.4 GPa showed no signs of strontium impurity phases (e.g., $Sr(OH)_2$ or SrO); however, there was a strong contribution from the Re gasket due to the small compression chamber diameter (less than 50 μm) required to reach extreme pressure conditions. Fig. 1 (top) shows a Rietveld refinement of a pattern obtained at 5.0 GPa. In the cotunnite structure, each of the three atoms in the asymmetric unit occupies the Wyckoff 4*c* position, with only the fractional *y*-coordinate constrained by symmetry. Preferred orientation in the sample precluded an unambiguous refinement of the Sr^{2+} positions, and x-ray diffraction is not suitable to determine the H^- positions, so the atomic positions yielded by the first-principles calculations (listed in Table 1) were used for (and kept fixed during) the refinement.

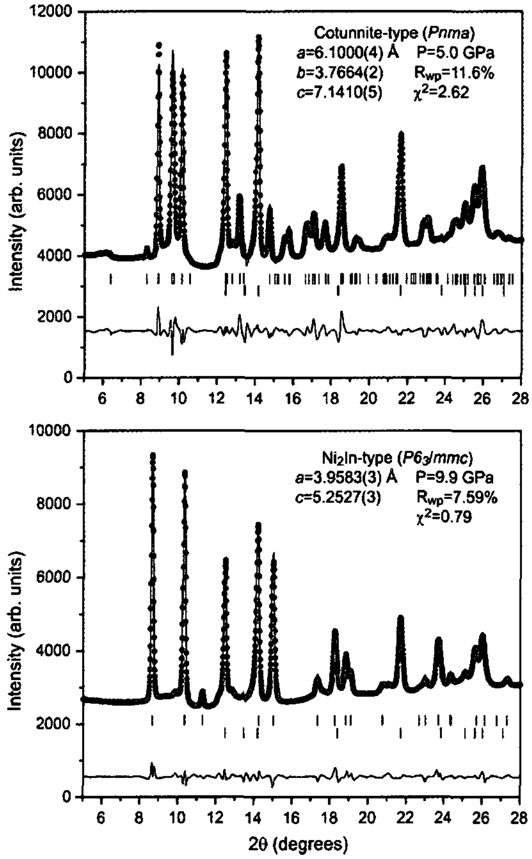

Fig. 1. (Color online) Rietveld refinements of the cotunnite (top) and Ni_2In (bottom) phases of SrH_2. Plots include observed (symbols) and calculated (solid line) diffraction patterns, difference curve (bottom solid line), and positions of expected Bragg reflections (vertical bars). The bottom set of Bragg reflections in each plot accounts for reflections from the rhenium gasket.

The appearance of new Debye rings in the diffraction image obtained at 7.8 GPa indicated the onset of the cotunnite→Ni_2In phase transition. Fig. 1 (bottom) shows a Rietveld refinement of the pattern obtained at the next pressure point, 9.9 GPa, with the

Table 2
Summary of experimental and theoretical equation of state parameters obtained from a third-order Birch–Murnaghan equation of state. Note that the experimental bulk moduli are overestimated due to non-hydrostatic pressure conditions.

	Theoretical			Experimental		
	B_0 (GPa)	B_0'	V_0 (Å^3/SrH$_2$)	B_0 (GPa)	B_0'	V_0 (Å^3/SrH$_2$)
Cotunnite	41.4(2)	3.13(5)	43.53(1)	57(4)	3.13*	44.3(3)
Ni_2In	41.3(2)	3.87(1)	40.72(3)	75(6)	3.87*	37.8(7)
AlB_2	39(1)	3.92(2)	38.5(3)	*Not experimentally observed*		

* Experimental B_0' based on theoretical results.

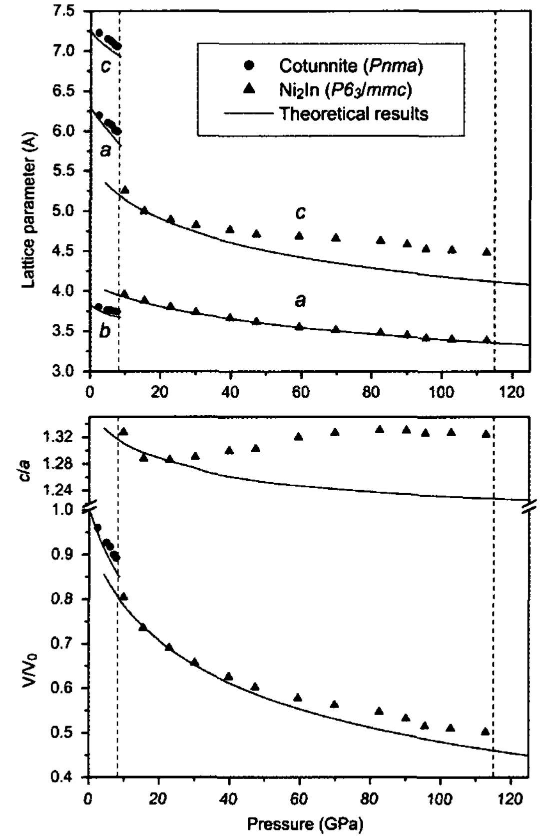

Fig. 2. Pressure dependence of the lattice parameters (top) and relative volume (bottom) of the cotunnite and Ni_2In phases of SrH_2, together with the c/a ratio (bottom) for the Ni_2In phase. The disparities between the experimental and theoretical results above 30 GPa are due to severe preferred orientation (see text). The dashed vertical lines at 8.3 and 115 GPa correspond to the observed and calculated transition pressures for the Ni_2In and AlB_2 structures, respectively.

transition to the Ni_2In phase completed. In the Ni_2In structure, all of the atoms are located in special positions (listed in Table 1). The Ni_2In phase remained stable up to the maximum pressure, 113 GPa, for the powder x-ray diffraction experiment.

Fig. 2 shows the pressure dependence of the lattice parameters (top) and the relative volume (bottom) for the cotunnite and Ni_2In phases, as well as the c/a ratio for the Ni_2In phase (bottom), from both the diffraction experiment (symbols) and the first-principles calculations (solid lines). Up to approximately 30 GPa, the agreement between theory and experiment is quite good. Furthermore, with regard to the Ni_2In phase, there is excellent agreement for the a-axis throughout the entire stable pressure regime. The c-axis, however, shows a marked disparity above 30 GPa, resulting in a corresponding disparity between theory and experiment for both the c/a ratio and relative volume. This disparity is brought about by severe preferred orientation in the crystallites. Specifically, upon uniaxial compression of the sample under non-hydrostatic conditions, the (00l) planes became oriented parallel to the incident beam. The result of this orientation could be readily seen in the diffraction patterns, as the (002) reflection observed at 9.9 GPa (the small peak at approximately 11.2° 2θ in Fig. 1, bottom) was absent in all subsequent diffraction patterns. With the c-axis normal to the compression axis, subsequent increases in pressure resulted in flattening the crystallites rather than compressing them. The result is that the a-axis decreased as expected, while the c-axis did not decrease as much as would be expected under hydrostatic pressure conditions. This is precisely the compression trend observed in a recent study of BaF_2 [22]. Specifically, under non-hydrostatic pressure conditions, the c/a ratio of the Ni_2In phase of BaF_2 (stable from 14 GPa up to at least 77 GPa) increased with increasing pressure, whereas a sample prepared with helium as a pressure transmitting medium showed the opposite pressure dependence, and was consistent with the accompanying first-principles calculations reported in that work.

Experimental and theoretical equation of state parameters, listed in Table 2, were obtained for both the cotunnite and Ni_2In phases by fitting the respective pressure-dependent volume data to a third-order Birch–Murnaghan equation of state. Because the cotunnite phase is stable over a relatively narrow pressure range, and because of the atypical compression of the c-axis in the Ni_2In phase, the pressure derivative of the bulk modulus obtained from the first-principles calculations was used when fitting the experimental data. The experimental bulk moduli are significantly larger than those obtained from the first-principles calculations. This is not surprising, however, as it is clear that the atypical compression brought about by severe preferred orientation gives the appearance of the material being less compressible. These results, together with our results on BaF_2, suggest that the bulk moduli reported for other Ni_2In structures in the literature may be significantly overestimated in the case of non-hydrostatic pressure conditions.

The primary purpose of the Raman spectroscopy experiments was to corroborate the proposed Ni_2In structure of SrH_2 observed at pressures greater than 8 GPa. A group theoretical analysis of the cotunnite structure predicts 18 Raman-active modes—6 modes associated with strontium and 12 modes associated with hydrogen. Fig. 3 (top) shows a Raman spectrum obtained at ambient pressure and temperature. While it is not possible to distinguish 18 individual modes, the spectrum is nevertheless consistent with that observed for CaH_2 and BaH_2 at ambient conditions [5,7,23]. Specifically, there is a group of relatively narrow modes around 100 cm^{-1} associated with the heavier cations, and several broad modes in the 500–1200 cm^{-1} range associated with the lighter hydrogen atoms. Upon transforming to the Ni_2In structure, only two Raman-active modes should be present—one associated with strontium and one associated with hydrogen. Above 8 GPa, the spectra changed significantly, with only two modes remaining. Fig. 3 (middle) shows a Raman spectrum obtained at 12.5 GPa. The narrow mode at approximately 120 cm^{-1} was clearly visible, but unfortunately the tail of the

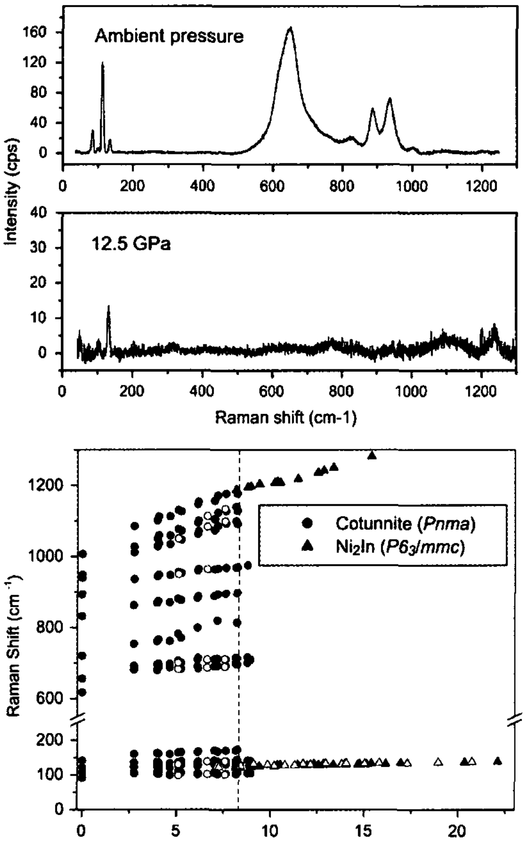

Fig. 3. Raman spectra (background subtracted) of SrH_2 in the cotunnite phase (top) and the Ni_2In phase (middle), together with the pressure dependence of the observed Raman modes (bottom). Closed and open symbols indicate data taken upon increasing and decreasing pressure, respectively.

strong Raman peak from diamond (centered at approximately 1330 cm^{-1}) almost completely washed out the high-wavenumber mode. However, the coincidence of this mode with the highest-wavenumber mode of the cotunnite structure, as well its pressure dependence, are in excellent agreement with that observed for BaH_2 [7]. The pressure dependence of all observed Raman modes is presented in Fig. 3 (bottom).

Fig. 4 shows the calculated enthalpies for the cotunnite, Ni_2In, and AlB_2 structures as a function of pressure. The intersection of the enthalpy curves for the cotunnite and Ni_2In structures (detailed in the inset of Fig. 3) at 8.3 GPa is in excellent agreement with the transition pressure observed in the diffraction and Raman experiments. Interestingly, the Ni_2In and AlB_2 enthalpy curves intersect at 115 GPa—just beyond the maximum pressure of the diffraction study. The authors' unpublished research on BaH_2 confirmed the transformation to the AlB_2 structure at approximately 50 GPa (in agreement with that reported by Kinoshita et al. [6]). We here add to the characterization of the high-pressure phase, noting that after the phase transition the sample appeared completely opaque, transmitting no visible light (this would be consistent with the change from ionic to covalent bonding suggested in Ref. [6]). Although 113 GPa marked the last static pressure point for which diffraction data was obtained for SrH_2, the diamond anvils actually failed at approximately 120 GPa, at which point the sample remained transparent to visible light. Given the under-compressed c-axis, the corresponding density was not high enough to bring about the phase transition. Significant further compression may have been required to bring about the predicted phase transition in the non-hydrostatic sample of SrH_2.

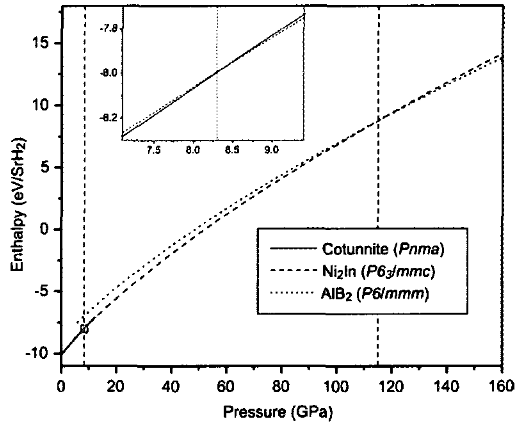

Fig. 4. (Color online) Calculated enthalpy vs. pressure for the cotunnite, Ni_2In, and AlB_2 phases of SrH_2. The intersection of the cotunnite and Ni_2In curves (inset) is in excellent agreement with the observed transition pressure. The intersection of the Ni_2In and AlB_2 curves predicts a subsequent phase transition at approximately 115 GPa (at zero temperature, under hydrostatic pressure conditions).

4. Summary

The results presented above confirm the previously reported cotunnite→Ni_2In phase transition in SrH_2 at 8.3 GPa. The proposed Ni_2In structure was corroborated by the Raman spectroscopy results, as the spectra exhibited two Raman-active modes. The marked contrast between the experimental and theoretical pressure-dependent volume suggests that equation of state parameters obtained under non-hydrostatic pressure conditions can be significantly overestimated. The first-principles calculations predict a $Ni_2In \rightarrow AlB_2$ transition at approximately 115 GPa. Although this was not observed experimentally up to almost 120 GPa, it is likely that the actual transition pressure may be significantly higher in the case of non-hydrostatic pressure conditions.

Acknowledgements

The authors gratefully acknowledge Dr. Daniele Colognesi for providing the strontium hydride used for the Raman spectroscopy experiments presented in this work. SD thanks NSERC of Canada for their financial support. The synchrotron radiation experiments described in this work were performed at the Canadian Light Source, which is supported by NSERC, NRC, CIHR, and the University of Saskatchewan. The authors gratefully acknowledge Dr. Ning Chen and Dr. Chang-Yong Kim for facilitating the diffraction experiments carried out at the CLS.

References

[1] J. Bergsma, B.O. Loopstra, Acta Cryst. 15 (1962) 92.
[2] E. Zintl, A. Harder, Z. Elektrochem. 41 (1935) 33.
[3] G.J. Snyder, H. Borrmann, A. Simon, Z. Kristallogr. 209 (1994) 458.
[4] K. Kinoshita, M. Nishimura, Y. Akahama, H. Kawamura, Proc. 20th AIRAPT T10-P048.
[5] J.S. Tse, D.D. Klug, S. Desgreniers, J.S. Smith, R. Flacau, Z. Liu, J. Hu, N. Chen, D.T. Jiang, Phys. Rev. B 75 (2007) 134108.

[6] K. Kinoshita, M. Nishimura, Y. Akahama, H. Kawamura, Solid State Commun. 141 (2007) 69.

[7] J.S. Smith, S. Desgreniers, J.S. Tse, D.D. Klug, J. Appl. Phys. 102 (2007) 043520.

[8] J.M. Leger, J. Haines, A. Atouf, O. Schulte, S. Hull, Phys. Rev. B 52 (1995) 13247.

[9] Y. Li, B. Li, T. Cui, Y. Li, L. Zhang, Y. Ma, G. Zou, J. Phys: Condens. Mater. 20 (2008) 045211.

[10] D. Colognesi, G. Barrera, A.J. Ramirez-Cuesta, M. Zoppi, J. Alloys Compounds 427 (2007) 18.

[11] H.K. Mao, P.M. Bell, J.W. Shaner, D.J. Steinberg, J. Appl. Phys. 49 (1978) 3276.

[12] J.S. Smith, S. Desgreniers, J. Synchrotron. Radiat. 16 (2009) 83.

[13] A.P. Hammersley, S.O. Svensson, M. Hanfland, A.N. Fitch, D. Häusermann, High. Press. Res. 14 (1996) 235.

[14] S. Desgreniers, K. Lagarec, J. Appl. Cryst. 27 (1994) 432; J. Appl. Cryst. 31 (1998) 109.

[15] J. Rodriguez-Carvajal, Physica B 192 (1993) 55.

[16] G. Kresse, J. Furthmüller, Phys. Rev. B 54 (1996) 11169.

[17] G. Kresse, D. Joubert, Phys. Rev. B 59 (1999) 1758;
P.E. Blöchl, Phys. Rev. B 50 (1994) 17953.

[18] H.J. Monkhorst, J.D. Pack, Phys. Rev. B. 13 (1976) 5188.

[19] X. Gonze, J.-M. Beuken, R. Caracas, F. Detraux, M. Fuchs, G.-M. Rignanese, L. Sindic, M. Verstraete, G. Zerah, F. Jollet, M. Torrent, A. Roy, M. Mikami, Ph. Ghosez, J.-Y. Raty, D.C. Allan, Comput. Mater. Sci. 25 (2002) 478.

[20] N. Troullier, J.L. Martins, Phys. Rev. B 43 (1991) 1993.

[21] J.P. Perdew, K. Burke, M. Ernzerhof, Phys. Rev. Lett. 77 (1996) 3865.

[22] J.S. Smith, S. Desgreniers, J.S. Tse, J. Sun, D.D. Klug, Y. Ohishi, Phys. Rev. B (in press).

[23] B. Li, Y. Li, K. Yang, Q. Cui, Y. Ma, G. Zou, J. Phys: Condens. Mater. 19 (2007) 226205.

Chapter 6 Selected techniques in diamond anvil cell crystallography: centring samples using X-ray transmission and rocking powder samples to improve X-ray diffraction image quality

as published in the Journal of Synchrotron Radiation, Volume 16, pages 83-96, 2009.

Journal of
Synchrotron Radiation
ISSN 0909-0495

Received 27 March 2008
Accepted 24 September 2008

Selected techniques in diamond anvil cell crystallography: centring samples using X-ray transmission and rocking powder samples to improve X-ray diffraction image quality

Jesse S. Smith* and Serge Desgreniers

Laboratoire de physique des solides denses, University of Ottawa, Ottawa, Ontario, Canada K1N 6N5. E-mail: jsmit068@uottawa.ca

The distinct X-ray transmission profile obtained by scanning a sample in a diamond anvil cell across a collimated X-ray beam is used to monitor sample displacement brought about by rotation. This measured displacement can in turn be used to calculate, and subsequently correct, the sample position with respect to a centre of rotation. This centring method differs from others also based on transmission in that it does not require a 180° sample rotation, nor does it require prior positioning of the rotation axis in the path of the X-ray beam. After a full description of the method, an example is presented together with an extended record of use to evaluate the method in a practical setting. The practice and benefits of rocking polycrystalline samples during X-ray exposure have also been quantitatively examined. Changing the orientation of the sample grains with respect to the incident beam yields the expected result of a more homogeneous intensity distribution along Debye rings. Interestingly, by limiting the amount of time large grains assume a particular orientation, rocking brings about the added effect of significantly reducing detector saturation. Sample rocking yields more reliable relative intensities, a more appropriate line shape and narrower line width. Data are presented for a calibration standard at ambient pressure as well as a research sample at high pressure.

Keywords: centring; diamond anvil cell; high pressure; X-ray diffraction; X-ray diffraction methods; rocking.

1. Introduction

The diamond anvil cell (DAC) is a remarkable tool in that it combines conceptual simplicity in design and operation with exceptional results in attainable pressures and practicable methods. In the context of high-pressure crystallography, however, these virtues are accompanied by a number of technical challenges. Difficulties such as X-ray absorption by the diamond anvils, the limited scattering range imposed by the anvils' supporting structure, and minute sample volumes are mitigated by the use of synchrotron radiation, as the small source size, near-parallel beam and high particle storage-ring energy of a typical synchrotron source allow a tremendous flux of high-energy X-rays to be delivered to microscopic samples. The threefold advantage is that the anvils become almost transparent, the accessible range of reciprocal space is significantly increased for a fixed DAC aperture, and intense scattering can be recorded from minute samples in a matter of minutes.

The use of synchrotron radiation, however, does not overcome all of the obstacles presented by the DAC. The severely limited sample volume necessary to reach high-pressure conditions puts finite limits on the number of diffracting crystallites in polycrystalline samples. Furthermore, polycrystalline samples are often 'prepared' *in situ* (*e.g.* a pressure-induced structural phase transition), under non-hydrostatic pressure conditions. In short, they are frequently far from ideal powders. These difficulties can even be exacerbated by the use of synchrotron radiation, as the highly parallel beam further limits the number of crystallographic planes which satisfy the Bragg condition (as compared with beams with moderate divergence, typically encountered in laboratory X-ray sources). It is therefore imperative that the user employ a number of experimental techniques to obtain data of the highest quality and, hence, structural parameters of the highest accuracy. The present work constitutes a detailed study of two of these experimental techniques: reproducible sample positioning at the centre of rotation in the experimental configuration, and rocking polycrystalline samples to improve the quality of powder X-ray diffraction images.

Following a brief description of the synchrotron radiation source, experimental configuration and analysis software common to the study as a whole, separate sections, each including a more detailed overview, experimental procedure, results and summary, are dedicated to the respective selected techniques. Although these techniques are presented in the context of DAC crystallography, their generic nature is such that they could likely be beneficially applied or adapted to a broad range of experimental configurations in the field of X-ray scattering.

2. Source and software

All data presented in this work were collected at the Hard X-ray Microanalysis (HXMA) beamline at the Canadian Light Source. HXMA is a multipurpose beamline providing users with EXAFS, microprobe, imaging and diffraction capabilities. The source is a 63-pole superconducting wiggler with a critical energy of approximately 10 keV. Wavelength is selected using either the Si(111) or (220) crystals of a fixed-exit double-crystal monochromator. Optional beamline optics include a plane parabolic mirror for collimating the continuous spectrum in the horizontal plane, as well as a toroidal mirror for focusing the monochromatic beam in both the horizontal and vertical planes. The final beam size is defined by square-aperture collimators [similar in design to those described by Ruoff *et al.* (1993)] ranging from 15 × 15 µm to 45 × 45 µm. Specific details regarding incident X-ray energy, beamline configuration and collimator size are provided in the respective descriptions of the centring and rocking studies. All X-ray diffraction images were obtained using transmission geometry, with scattering recorded on a Marresearch mar345 imaging-plate detector (located approximately 270 mm from the sample), and were scanned at 100 µm pixel resolution.

FIT2D (Hammersley *et al.*, 1996) was used extensively for data analysis and image processing. For the centring study, it was used to determine the sample-to-detector distance, based on powder X-ray diffraction images from calibration standards. For the rocking study, it was used to convert diffraction images into conventional diffraction patterns of intensity *versus* 2θ, and to produce the figures containing portions of powder diffraction images. With regard to the latter, it is important to note for each figure containing sets of images that each image is presented with the same intensity scaling. Furthermore, it is important to note that, for all images, saturated pixels were masked prior to any data analysis. *FullProf* (Rodriguez-Carvajal, 2006) was used to carry out Rietveld refinements on the LaB_6 diffraction patterns for the rocking study. Refined parameters included the background, scale factor, lattice constant, asymmetric pseudo-Voigt peak profile, B (overall) and fractional x-coordinate of boron.

3. Centring

3.1. Overview

Accurate reproducible sample positioning is a prerequisite for practically any X-ray diffraction experiment. A number of different positioning methods have been devised, depending on factors such as the source, geometry or specific type of measurement to be performed. When carrying out diffraction using a DAC in transmission geometry with an area detector, the sample-to-detector distance, D, is a crucial experimental parameter as it is required to convert the spatial position of observed Bragg spots or the radial position of observed Debye rings into the appropriate scattering variable. A fractional uncertainty in D will result in approximately the same fractional uncertainty in d-spacings. Typically, D is determined by recording a powder X-ray diffraction image of a calibration standard with well known lattice constants (*e.g.* Si, LaB_6 or CeO_2) at ambient conditions. The radial position of the recorded Debye rings, together with monochromatic radiation of known wavelength (independently determined, for example, by scanning an absorption edge of an elemental calibration foil), can be used to accurately determine D. The goal, of course, is to subsequently place research samples at the same position as the standard, such that all share a unique and well defined D. Making this unique position a centre of rotation is a natural choice, both for conventional multi-circle diffractometers as well as for custom multi-stage goniometers often employed for high-pressure studies at synchrotron radiation facilities.

Traditionally, optical methods are used for positioning a sample at the centre of rotation. The sample is rotated while observed through a microscope, and any initial displacement of the sample from the centre of rotation results in both lateral and telescopic motion of the sample upon rotation. Corrections are made to the sample position to minimize the observed motion upon rotation. Optical methods are not practical when using DACs because the optical access to the sample is severely limited by the anvils' supporting structure, and furthermore the high refractive index of diamonds introduces additional challenges, particularly as the optical path length increases upon rotation. Alternatively, Hamilton (1974) showed that the sample position with respect to the centre of rotation could be determined from the observed angles of pairs of single-crystal reflections. An adaptation of this method was first applied to DACs by King & Finger (1979), and further generalized by Dera & Katrusiak (1999). The obvious limitation of a method based on single-crystal reflection pairs is that the problem of positioning polycrystalline samples is not resolved. Furthermore, these methods are based on traditional geometries which include a point detector situated at a constant distance from the centre of rotation.

The method of centring presented in this work is related to the optical method in that it relies upon the observed sample displacement upon rotation; however, it does not rely on the eye to monitor this displacement but rather on the characteristic transmission profile obtained by scanning a gasketed DAC sample across a spatially well defined X-ray beam. Specifically, the sample position with respect to the fixed X-ray beam is measured at three separate sample rotation angles, and the corresponding sample displacement is used to calculate the position of the sample with respect to the centre of rotation. Similar methods for sample centring based on X-ray transmission through the DAC have been described by Budzianowski & Katrusiak (2004) and Kunz *et al.* (2005); however, in both cases centring is carried out in a step-wise fashion: the sample must first be centred along one (or both) of the axes normal to the beam, after which the sample is centred along the axis parallel to the beam. To accomplish this first step, Bunzianowski & Katrusiak prescribe a 180° sample rotation, whereas Kunz *et al.* do not explicitly specify how the first step is carried out. The method presented here differs in that the sample position with respect to the centre of rotation can be determined in two dimensions, along one of the axes normal to the beam as well as along the axis parallel to the beam, simultaneously. Furthermore, the method does not require a 180° sample rotation. This last point is particularly important as it is often either not feasible or not possible to rotate the sample in this manner owing to ancillary equipment such as a cryostat, furnace or pneumatic DAC membrane assembly, or owing to the close proximity of peripheral beam-conditioning equipment such as a collimator, 'clean-up' aperture or radiation shielding. One final point worth iterating is that the method works equally well for powder and single-crystal samples inasmuch as the characteristic profile used to define the sample position is due to the gasket rather than the sample.

After considering some preliminary details, a simplified version of the centring technique, suitable for most DAC applications, is presented. This version is then generalized for use in a wider range of applications. An example of the centring technique, together with an extended record of its use, over several days of experiments employing several beamline configurations, is presented to emphasize some practical considerations as well as possible limitations.

3.2. Coordinates and nomenclature

Fig. 1 shows a schematic diagram of the experimental configuration, together with a definition of the coordinate system. The positive y-axis runs parallel to the beam, the positive z- and x-axes make up the vertical and horizontal axes, respectively, of the plane normal to the beam, with the former pointing upward and the latter completing the right-handed coordinate system. The rotation axis ω is collinear with the z-axis, with positive rotation in the counter-clockwise direction when viewed from above. Starting at the base of the assembly, the *Scan z* and *Scan x* stages are employed for scanning the sample in the plane normal to the X-ray beam, *Centre ω* allows for the sample rotation necessary to carry out the centring process, and *Centre x* and *Centre y* are used to place the sample at the centre of rotation. All stages are motorized, with optical encoder resolution equal to or better than 0.1 µm, and with a unidirectional repeatability of just over 1 µm. It should be mentioned that, for the purposes of centring as described in the present work, it is compulsory to have x motion below the rotation stage for scanning the sample in the fixed reference frame of the hutch, and it is necessary to have x–y motion above the rotation stage to position samples at the centre of rotation. The particular location of z motion is a matter of choice in the current context.

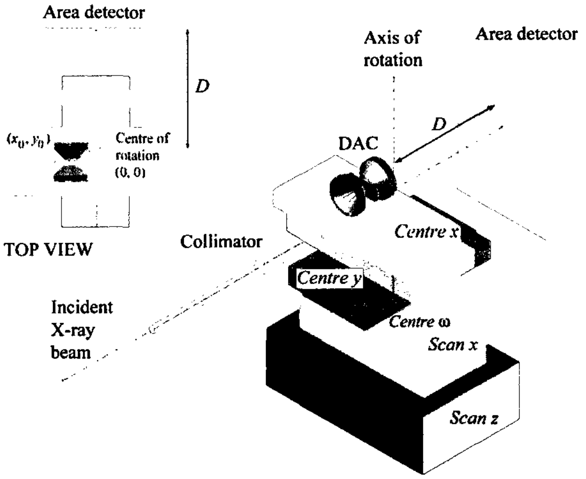

Figure 1
Schematic diagram of the experimental configuration and coordinate system. Motorized stage names are in italics. The top view is shown for the case of *Centre ω* at ω_0 (translation of the sample along y results in zero displacement along x) and illustrates an initial sample displacement (x_0, y_0) with respect to the centre of rotation.

3.3. Transmission profile and sample position

Fig. 2 shows a typical example of the transmission profile obtained by scanning the sample across the X-ray beam. The monochromatic focused X-ray beam was collimated using a square 30 µm aperture. (Note that for the purposes of this work it is assumed that the maximum beam dimensions do not exceed the minimum diameter of the sample chamber; in practice this is almost always the case as diffraction from the gasket material surrounding the sample introduces difficulty during data analysis.) The DAC had diamond anvils with 300 µm culets. The indented stainless steel gasket (T301, full-hard) was approximately 50 µm thick, with a sample chamber 100 µm in diameter. A schematic diagram of the anvils–gasket–sample region is shown in Fig. 2 above the plot. If one imagines the X-ray beam (shown to proper scale in the diagram) moving across the sample, with transmission intensity being recorded at discrete 10 µm intervals, the characteristic features of the transmission profile, two shoulder plateaus and one peak plateau, are readily obtained.

Placing the sample in the path of the X-ray beam is straightforward with such a transmission profile. However, for the purposes of centring it is important to define a unique sample position with the greatest possible accuracy. Furthermore, this unique position must still be identifiable in scans taken with the DAC at some angle with respect to the beam. Because of the plateau nature of the profile shown in Fig. 2, the position of maximum intensity can be ambiguous and is therefore rarely reliable for such purposes, so instead the position coordinate of the centroid (commonly referred to as the centre of mass) is used to define the sample position. This

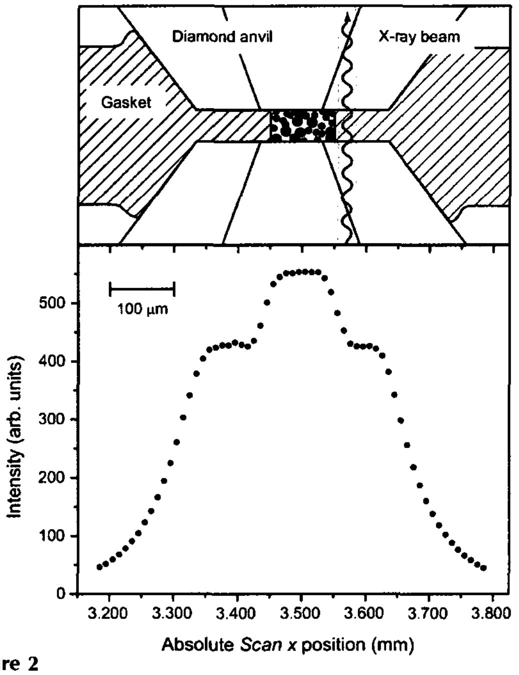

Figure 2
Typical example of the X-ray transmission profile intensity as a function of the scanning stage position. Above the plot is a schematic diagram (to scale) detailing the diamond anvils, gasket and sample configuration giving rise to such a characteristic profile. Note that the shaded region about the X-ray beam is scaled to correspond to 30 µm, the collimated width of the incident X-ray beam.

does not entirely solve the problem of defining an unambiguous sample position, as factors such as gasket material, gasket deformation at high pressure, sample chamber displacement from the centre of the gasket indentation, and choice of scan parameters can all contribute to deviations from the ideal shape and/or symmetry (or similarly, a consistent shape and/or symmetry) of the characteristic profile. These practical difficulties will be briefly addressed in the analysis and discussion.

3.3.1. Mathematical description. Prior to carrying out the centring routine, *Scan z* and *Scan x* are used to scan the sample in the plane normal to the beam and subsequently position the sample in the path of the beam. The centring routine requires the sample position, in *Scan x* space, to be determined at three unique angles. First, the position is determined at $\omega_0 = 0°$. (This angle is defined as the angle at which the sample can be translated along the beam and undergo no translation in the x direction.) The position of the sample is then determined for $\Delta\omega = \omega_+$ and ω_- (with an approximate range of 5°–35° for possible $\Delta\omega$ values). It is important to note that, for the description of the method as applied to DACs, $|\omega_-| = \omega_+$ is a requirement inasmuch as the method takes advantage of the even and odd properties of the cosine and sine functions, respectively (this requirement will be subsequently lifted for the generalized method). The sample displacement in *Scan x* space brought about by rotation is then used to calculate the sample position with respect to the centre of rotation.

Turning to a more complete mathematical description, when the sample is first placed on the positioning assembly, its position with respect to the centre of rotation (see Fig. 1, top view) can be expressed by a vector,

$$\mathbf{P}_0 = x_0\hat{\mathbf{i}} + y_0\hat{\mathbf{j}}. \tag{1}$$

Upon rotating the sample assembly through an angle ω, the new position of the vector in the fixed coordinate system of the experimental hutch is found by applying a coordinate transformation for pure rotation,

$$\begin{matrix} x_\omega \\ y_\omega \end{matrix} = \begin{bmatrix} \cos\omega & -\sin\omega \\ \sin\omega & \cos\omega \end{bmatrix} \begin{matrix} x_0 \\ y_0 \end{matrix}, \tag{2}$$

such that

$$\mathbf{P}_+ = (x_0\cos\omega_+ - y_0\sin\omega_+)\hat{\mathbf{i}} + (x_0\sin\omega_+ + y_0\cos\omega_+)\hat{\mathbf{j}} \tag{3}$$

and

$$\mathbf{P}_- = (x_0\cos\omega_+ + y_0\sin\omega_+)\hat{\mathbf{i}} + (-x_0\sin\omega_+ + y_0\cos\omega_+)\hat{\mathbf{j}}. \tag{4}$$

It is important to note that in (4) the even and odd properties of the cosine and sine functions, respectively, have been exploited such that $\mathbf{P}_-$ is written in terms of ω_+ (all subsequent equations will be written in terms of the positive angle, allowing the subscript on ω to be dropped). The experimentalist is privy only to the projection of the sample displacement onto *Scan x* space, which depends on the initial displacement (x_0, y_0) as well as the choice of ω,

$$(\mathbf{P}_+ - \mathbf{P}_0)\cdot\hat{\mathbf{i}} \rightarrow \delta Sx_+ = x_0(\cos\omega - 1) - y_0\sin\omega \tag{5}$$

and

$$(\mathbf{P}_- - \mathbf{P}_0)\cdot\hat{\mathbf{i}} \rightarrow \delta Sx_- = x_0(\cos\omega - 1) + y_0\sin\omega. \tag{6}$$

At this point it is necessary to introduce a small correction to the description. Because the beam remains stationary, each time the sample is displaced it is actually the entire coordinate system that must be translated to bring the sample back into line with the beam. To account for this, one simply needs to distribute a negative sign through (5) and (6), $-\delta Sx \rightarrow \Delta Sx$ yielding,

$$\Delta Sx_+ = x_0(1 - \cos\omega) + y_0\sin\omega \tag{7}$$

and

$$\Delta Sx_- = x_0(1 - \cos\omega) - y_0\sin\omega. \tag{8}$$

Solving this simple system yields the final result,

$$x_0 = \frac{\Delta Sx_+ + \Delta Sx_-}{2(1 - \cos\omega)} \tag{9}$$

and

$$y_0 = \frac{\Delta Sx_+ - \Delta Sx_-}{2\sin\omega}. \tag{10}$$

Relative motions of *Centre x* and *Centre y* by $-x_0$ and $-y_0$, respectively, will place the sample at the centre of rotation. Subsequent relative motion of *Scan x* by x_0 is then required to bring the sample back into the beam's path.

3.3.2. Generalized method. In the majority of X-ray scattering applications associated with DACs, the X-ray beam passes straight through the load axis. The accessible angular range about this load axis is typically symmetric and, furthermore, it is often quite limited owing to the diamond anvil supports. With this in mind, the specific method of centring presented above is well suited for DACs. However, there is no *a priori* reason for requiring that ω_0 be used, or for requiring the other two angles to be symmetric about ω_0, and therefore the method can be generalized to any three angles. Notably, the general method is not limited to atypical DAC applications; it could be employed in any experimental configuration for which the experimentalist can monitor the transverse displacement of a unique transmission feature upon rotation. In the general case, the sample position is measured at three angles α, ω and γ. Here no restrictions are made regarding the signs or values of the angles, except that they are known with respect to ω_0. Following the same procedure described above, one obtains the general form for the corrections,

$$x_0 = \frac{(\sin\gamma - \sin\alpha)\Delta Sx_\omega - (\sin\omega - \sin\alpha)\Delta Sx_\gamma}{(\cos\alpha - \cos\omega)(\sin\gamma - \sin\alpha) - (\sin\omega - \sin\alpha)(\cos\alpha - \cos\gamma)} \tag{11}$$

and

$$y_0 = \frac{(\cos\alpha - \cos\omega)\Delta Sx_\gamma - (\cos\alpha - \cos\gamma)\Delta Sx_\omega}{(\cos\alpha - \cos\omega)(\sin\gamma - \sin\alpha) - (\sin\omega - \sin\alpha)(\cos\alpha - \cos\gamma)}. \tag{12}$$

If $\alpha \to \omega_0 = 0°$, one obtains

$$x_0 = \frac{(\sin\gamma)\Delta Sx_\omega - (\sin\omega)\Delta Sx_\gamma}{(1 - \cos\omega)(\sin\gamma) - (\sin\omega)(1 - \cos\gamma)} \tag{13}$$

and

$$y_0 = \frac{(1 - \cos\omega)\Delta Sx_\gamma - (1 - \cos\gamma)\Delta Sx_\omega}{(1 - \cos\omega)(\sin\gamma) - (\sin\omega)(1 - \cos\gamma)}. \tag{14}$$

Finally, if $\gamma \to -\omega$, and the even/odd properties of the cosine/sine functions are used to write everything in terms of ω, one obtains equations (9) and (10).

3.4. Example

For the example presented here, as well as for the extended record of use of the centring method presented thereafter, the simplified centring method, with ω_0 and symmetric angles about ω_0, was used. A simple macro was employed, for which the user is required to input three parameters: the scan width (more specifically, the initial and final positions of the scan relative to the current *Scan x* position), the discrete step size and $\Delta\omega$. The same scan width and step size are used for each of the three ω angles. After the three scans are completed, the macro calculates the position coordinate of the centroid for each scan, and subsequently calculates the sample position with respect to the centre of rotation.

To facilitate the establishment of an accurate unique sample-to-detector distance D for all samples, calibration samples are mounted in DAC gaskets so as to mimic the centring process as it is carried out on regular research samples. The calibration samples are prepared by first indenting and drilling a stainless steel gasket with roughly the same dimensions as described for Fig. 2. After replacing the gasket in the DAC, the calibration sample is loaded into the sample chamber and gently packed using the opposing anvils. The gasket is removed from the DAC, covered with thin polyimide tape for protection, and permanently fixed in a custom mount. The calibration and DAC mounts are designed such that when a calibration sample is placed atop the sample goniometer it rests at approximately the same position as the mounted DAC samples. This is done to minimize long travel with any of the stages when switching between samples, thus minimizing errors introduced by slight deviations from orthogonality among stages in the sample assembly.

Fig. 3 shows an example of iterative use of the centring method. For each trio of scans, the relative scan endpoints were −300 to 300 µm, with a step size of 10 µm. $\Delta\omega$, the measured ΔSx displacements, and the calculated sample positions with respect to the centre of rotation (*i.e.* the x- and y-components of P_0) are presented in Table 1. The first iteration is represented by the top trio of scans. Despite the modest value of ω, the sample displacement owing to rotation, approximately ±14 µm for ω_+ and ω_-, respectively, is clearly noticeable. After making the calculated corrections, the centring process was repeated, only now $\Delta\omega$ was increased to ±10°. The resulting trio of scans in the middle of Fig. 3 shows a marked improvement; however, it is clear that the sample is still displaced slightly upon rotation. Again the calculated corrections were applied and the routine was executed a third and final time, with the resulting trio of scans shown at the bottom of Fig. 3.

Considering the iterative progression of the calculated corrections in Table 1, it is reasonable to estimate that, after applying the calculated corrections from the third iteration, a small positioning error of the sample centre with respect to the centre of rotation still persists, perhaps a little more than 10 µm along x and a little less than 10 µm along y. However, given the dimensions of the sample, this estimate puts the centre of rotation well within the sample volume. Considering the iterative progression of the sample displacement brought about by rotation, it is reasonable to conclude that rotation of the sample by ±10° (*i.e.* rocking the sample) during image capture would result in a sample displacement of not more than ±2.5 µm normal to the beam. Based on the estimated positioning error, the sample displacement along the beam would be slightly larger (*e.g.* less than ±5 µm for a 25 µm positioning error along x).

The final result presented in the description of the method, equations (9) and (10), is exact provided a unique feature can be identified and used to define the sample position for all pertinent values of ω. Unfortunately this is rarely the case, as demonstrated by the iterations required in this example. It is worth exploring some of the related factors that cause uncertainty in defining a unique sample position. This will not only provide some insight into the practical limitations of the

Table 1

Choice of $\Delta\omega$, the resulting projections onto *Scan x* space of the sample position owing to rotation, and the calculated correction from equations (9) and (10), for each iteration of the centring process for the example shown in Fig. 3.

Iteration	$\Delta\omega$ (°)	ΔSx_+ (μm)	ΔSx_- (μm)	x_0 (μm)	y_0 (μm)
First	5	14.1	−14.3	−24	163
Second	10	3.5	−7.6	−135	32
Third	10	2.7	−1.2	50	11

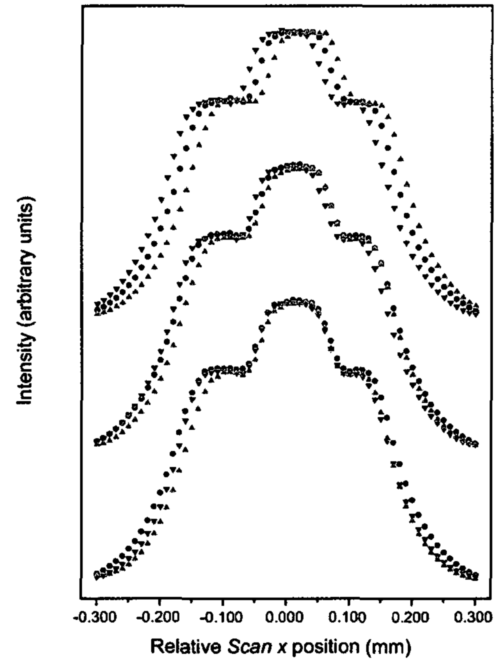

Figure 3

Three iterations, in order from top to bottom, of the centring process. In each trio of scans the circles, triangles and inverted triangles correspond to $\omega = \omega_0$, ω_+ and ω_-, respectively. With each iteration the displacement of the sample chamber portion of the profile is progressively minimized.

method, but will also lead to suggestions for utilizing the method to obtain the best possible result.

3.5. Discussion

The problem of identifying unique profile features for an arbitrary rotation angle is due primarily to a lack of uniformity in the characteristic transmission profile. Upon rotating the sample, the width of the features in the transmission profile are compressed by a factor of $\cos(\omega)$. For small ω, the corresponding effect is small, but for larger values of ω the difference can be substantial. Atypical features, caused for example by a deformed or unstable gasket at high pressure, or asymmetric features, for example a sample chamber not well centred in the gasket indentation, can exacerbate this problem. However, a careful choice of scan parameters can greatly mitigate these difficulties. In the example presented above, *the entire profile was included in the scan width* (the narrower transmission profiles for $\Delta\omega = \pm 10°$ are clearly visible in the tails of the bottom trio of Fig. 3). This generous scan width yielded satisfactory results; however, for the most demanding applications, the scan width can be chosen to include only the sample chamber and a few data points of each shoulder plateau to minimize uncertainty caused by asymmetric or atypical transmission profiles.

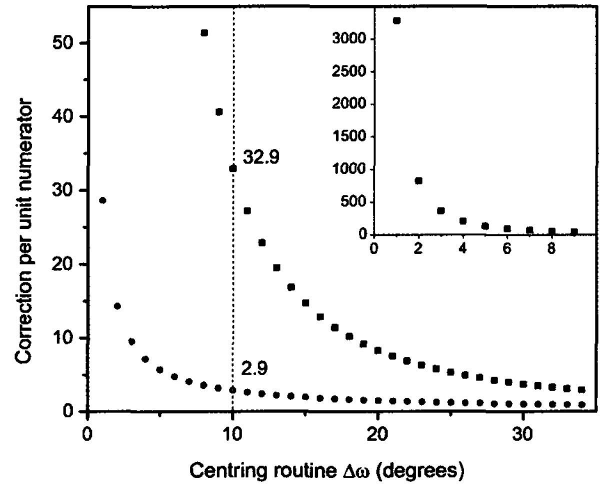

Figure 4

Calculated correction per unit numerator value of equation (9) along x (squares) and equation (10) along y (circles), as a function of $\Delta\omega$. The inset details the extreme correction along x for small angles. The dotted line at 10° is to draw attention to the angle used in the second and third iterations of the example.

The choice of ω is particularly crucial. To appreciate this more fully, Fig. 4 shows the calculated correction obtained from equations (9) and (10), per unit numerator value, as a function of $\Delta\omega$. For example, if one executes the centring routine with $\Delta\omega = \pm 10°$ and finds the sum $\Delta Sx_+ + \Delta Sx_- = 1$ μm, the magnitude of the calculated sample displacement x_0 *would be* 32.9 *μm. Conversely, if one finds the difference* $\Delta Sx_+ - \Delta Sx_- = 1$ μm, the magnitude of the calculated sample displacement y_0 would be just 2.9 μm. To reiterate, errors in positioning are the result of not accurately identifying the same unique feature for all ω. For small ω the distortion of the profile owing to rotation, and therefore the detrimental effect on the consistency and symmetry of the profile, is minimized, but at the same time small errors in positioning are magnified by the relatively large calculated correction, particularly for x_0. For large ω the magnitudes of the calculated corrections are much smaller, but at the same time the detrimental effect of rotation on the profile consistency can be substantial. For all values (and particularly small values) of ω, the method is more precise parallel to the beam than it is normal to the beam. One notable exception is the case of a 180° rotation. The method presented in this work does not require such a rotation, but it is important to note that the method nevertheless works for such a rotation and, when possible, this is still the ideal choice to position the sample along the axes normal to the beam. *However, this gives no information about the displacement* y_0,

Table 2
A record of several calibration images taken over several days of X-ray diffraction experiments.

An asterisk (*) indicates that there is no relation to the centre stage positions above owing to a change in the calibration mounts. A dagger (†) indicates that the sample was not disturbed between images. Notably, a change in beamline configuration and/or calibration sample brings about the most abrupt changes in *D*.

Standard	Day	Time	Configuration	*Centre y* (mm)	*D* (mm)
LaB_6	1	00:45	1	3.913	271.756
LaB_6	1	13:30	1	3.920	271.794
LaB_6	2	04:00	2	3.925	271.837
LaB_6	2	13:30	2	3.927	271.853
LaB_6	2	16:00	2	3.927	271.847
LaB_6	2	17:30	2	3.929	271.840
LaB_6	2	23:30	2	3.933	271.859
Si	3	0:00	2	4.015*	271.721
Si	3	14:00	2	4.020	271.715
LaB_6	4	5:30	3	3.855*	271.992
LaB_6	4	5:40	3	3.855†	272.001
LaB_6	6	4:00	4	3.889	271.854
LaB_6	6	4:30	4	3.889†	271.875

Table 3
Parameters detailing the four beamline configurations employed during the record of use.

Configuration	Energy (keV)	Mono (*hkl*)	Focusing optics?	Beam size (μm)
1	24.030	(111)	Yes	15 × 15
2	24.030	(111)	Yes	45 × 45
3	37.441	(220)	No	45 × 45
4	50.000	(220)	No	45 × 45

and therefore additional scans at moderate ω values are required to centre the sample along the beam.

In an effort to evaluate the effectiveness of the method over an extended period of repeated use, Table 2 shows a record of *Centre y* positions, together with *D* as determined from the fit of the calibration images. The calibration images were taken over a period of six days, during which the beamline configuration (detailed in Table 3) and/or calibration sample were periodically changed. This is an appropriate practical measure of the method as the refined sample-to-detector distances obtained from calibration images are often the only reliable measure of *D* available to the user during a typical experimental run. While the data in Table 2 are not extensive, a number of interesting features are observed. Starting with the first seven entries, the *Centre y* values have a range of 20 μm, whereas *D* has a range of over 100 μm. The ranges for *Centre y* and *D* drop to 8 μm and 20 μm, respectively, if one considers the LaB_6 data from configuration 2 only. The *Centre x* values (not shown) have a range of almost 150 μm. Similarly, this range decreases to 84 μm if one considers the LaB_6 data from configuration 2 only. The large range of *Centre x* values, approximately one order of magnitude greater than that observed for *Centre y*, is consistent with the order-of-magnitude difference between the calculated corrections of *Centre x* and *Centre y* for $\Delta\omega = \pm 10°$, as shown in Fig. 4.

Turning now to the last four rows of Table 2, each pair of images was recorded without disturbing the sample position between images. Therefore the refined *D* values should ideally be the same for each respective pair. While the values are not the same, the differences of 9 μm and 21 μm for the first and second pair, respectively, are relatively small.

Finally, considering all of the entries together, it appears that the primary obstacle to establishing an accurate and consistent *D* is the number of counts recorded by the detector. For example, by switching to a larger collimator (configuration 1 → configuration 2), the flux at the sample was increased by almost an order of magnitude. This had little effect (5 μm) on the calculated *Centre y* stage position, but had a significant effect (43 μm) on *D*. *D* was quite stable (a total range of 21 μm) in configuration 2 until the standard was changed to silicon. The higher symmetry and lower *Z*-value of Si as compared with LaB_6 result in fewer peaks and relatively fewer counts (for a given range of 2θ) used to refine the sample-to-detector distance. The discrepancy of over 100 μm for images taken with Si as compared with LaB_6 in configuration 2 is quite significant (note that a comparison of the *Centre x* and *Centre y* is not applicable, as the LaB_6 and Si calibration samples have separate mounts). Dera & Katrusiak (1999) report similar challenges, namely that source size and characteristics, as well as sample type, can have a significant influence on the results of the centring procedure described for single-crystal samples.

3.6. Centring summary

The centring method presented allows DAC samples to be positioned at an absolute unique position in space. The primary goal of the centring routine is to establish a consistent repeatable sample-to-detector distance *D*, and for LaB_6 data from beamline configuration 2, for which the most data were available, the refined values for *D* had a range of just over 20 μm, consistent with the variation observed when the sample was not disturbed between images. The method is valuable because it does not require a 180° rotation of the sample, which is often not feasible owing to the location of ancillary equipment present in high-pressure experimental configurations. Positioning the sample at the centre of rotation is a prerequisite for single-crystal studies, and it allows powder samples to be rocked during exposure. Because the characteristic transmission profile is due to the transmission contrast of the gasket and sample rather than the sample type itself, the method works equally well for powder and single-crystal samples. It is clear that the ultimate accuracy of the method depends on the ability to consistently identify a unique sample feature for all pertinent DAC rotation angles. This depends on a number of related factors including the anvils–gasket–sample region, as well as the actual scan parameters, all of which must be carefully considered in order to obtain the best possible result. However, it has been shown that, ultimately, the problem of defining a unique sample-to-detector distance is likely limited by the variance introduced by different calibration materials and/or beamline configurations.

4. Rocking

4.1. Overview

As discussed in the *Introduction*, the limited sample volume necessary to reach high-pressure conditions in the DAC, together with the near-parallel beam characteristic of typical synchrotron radiation sources, puts severe limits on the number of crystallographic planes satisfying the Bragg condition in polycrystalline samples. Consequently, poor counting statistics make it quite difficult to obtain reliable reproducible relative intensities. This difficulty is alleviated in part by the use of a flat two-dimensional detector such as those incorporating an imaging plate (IP) or charge-coupled device (CCD). By capturing entire Debye rings, the total intensity along a given ring can be summed, yielding a much more reliable intensity per unit length (of a given Debye ring) as compared with detection methods that record intensity from only a small portion of a given ring (as is often the case in conventional experimental configurations).

Area detectors, however, offer the added benefit of imaging, and, for the typical case when the DAC remains stationary during exposure, the images obtained frequently reveal spotty Debye rings as evidence of poor powder averaging. Qualitative accounts in the literature make it clear that rocking the DAC over a small angular range during image capture can significantly improve the homogeneity of intensity distribution along Debye rings (see, for example, Sakata *et al.*, 2004). However, the quantitative study presented here reveals that the benefits obtained by rocking are more substantial and varied than previously suggested. Interestingly, the results can be characterized by two distinct yet complimentary perspectives: improving intensity distribution and reducing detector saturation. Rocking the sample significantly increases the number of distinct crystallite orientations contributing to the total diffracted intensity, so, as one might expect, it improves the homogeneity of intensity distribution around Debye rings. But rocking also reduces the amount of time any particular group of crystallite orientations contributes to the total diffracted intensity, bringing about the less obvious result that it significantly reduces instances of detector saturation due to diffraction from large grains.

The latter perspective is of particular importance. IPs (and to a lesser extent CCDs) have a high dynamic range but, nevertheless, at the majority of second- and third-generation sources, exposure time is limited by detector saturation. Saturation results in lost information, such that an image with even a modest number of saturated pixels can no longer be relied upon for correct relative intensities. The obvious solution is to limit the exposure time, but this constitutes a compromise in achieving the best counting statistics. Sample rocking decreases the number of saturated pixels, thereby increasing the maximum exposure time; one makes the most of the detector's dynamic range for each image. Following some preliminary considerations associated with rocking, data are presented for various rocking scenarios, at both ambient and high-pressure conditions. The results are accompanied by a detailed discussion in the contexts of the two distinct yet complimentary perspectives of improving intensity distribution and reducing detector saturation.

4.2. Rocking *versus* spinning

At the outset it is worth briefly clarifying what is meant by sample rocking, and distinguishing it from similar strategies such as sample spinning, a technique often employed in conventional θ–2θ diffraction geometries. Fig. 5 offers a schematic view of the situation. In the case of a conventional θ–2θ reflection geometry (Fig. 5, left), only grains with sets of planes $\{hkl\}$ parallel to the sample holder contribute to the diffracted intensity as recorded by the detector. By spinning the sample holder about its normal axis, these planes remain essentially parallel to the sample holder. In short, spinning does little to change the orientation of these planes with respect to the beam; instead it may bring new grains into the path of the beam, increasing the number of grains which contribute to the observed intensity at a particular angle 2θ.

The situation is quite different in the case of transmission geometry using an area detector (Fig. 5, right). Data are collected simultaneously over the entire relevant 2θ range, such that all crystallites with planes satisfying the Bragg condition for the relevant 2θ range contribute to the observed intensity. Sample rocking involves rotating the DAC over a modest angular range about an axis normal to the incident beam. The result is that all of the grains contained in the irradiated sample volume will have a new orientation with respect to the incident beam. In short, rocking is far more effective than spinning in the context of changing the orientation of pertinent grains. This is imperative as the limited sample volume of the DAC does not afford the luxury of bringing a significant number of new grains into the path of the incident beam.

The rocking method employed in this work does not involve a continuous sweeping motion of the sample through the specified angular range, but rather the sample is rotated by

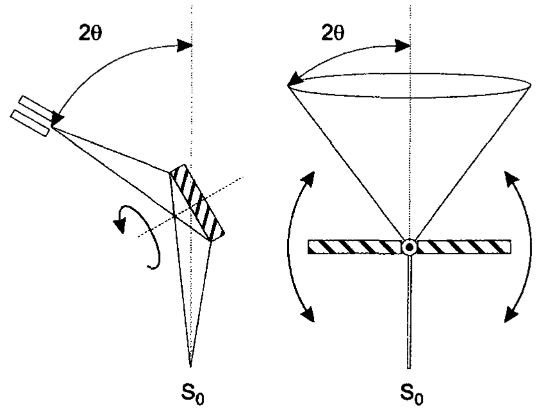

Figure 5
Schematic diagrams comparing the practice of sample spinning (left), often employed in conventional laboratory diffractometers, with the practice of sample rocking (right), employed in the present work. S_0 indicates the location of the X-ray source.

discrete intervals dictated by the user. Specifically, rocking is carried out by a simple macro which requires the user to input the end points of the rocking range, the discrete step size and the total exposure time. This information is used, together with the dynamic parameters of the rotation stage, to rock the sample over the entire range once during the specified exposure time, with the appropriate discrete step size. Note that rocking ranges as discussed in this work are complete and symmetric; a rocking range of 8° corresponds to rocking the DAC ±4° about the rotation axis origin.

4.3. Image series

The majority of the data were taken using a powder sample of LaB_6 (National Institute of Standards and Technology, Standard Reference Material 660a) under ambient conditions. To mimic the sample volume typically encountered in a DAC, the calibration standard was loaded into an indented gasket, as described above in the centring portion of this work. Depending on a number of factors including the type and/or quality of sample and type (or lack) of pressure-transmitting medium, application of pressure can introduce a number of complications including, for example, anisotropic strain broadening and/or preferred orientation. This makes a comprehensive quantitative evaluation of sample rocking at high pressure difficult. Therefore an almost ideal powder was chosen for the greater part of the study, with images taken at ambient pressure. However, an example of rocking at high pressure will also be presented below. Regarding the use of an IP area detector, despite the widespread use of CCDs at synchrotron radiation facilities, the combination of high dynamic range, exceptionally large area and tolerable readout time has resulted in IPs continuing to be the workhorses for most high-pressure powder X-ray diffraction studies. However, the characteristics of current CCDs are such that the issues of saturation and pixel bleeding are of key importance. The results presented here should be generally applicable to CCDs as well.

Three image series, each consisting of six powder X-ray diffraction images, were collected. For each of the first two series, a reference image was taken without rocking and with intentional overexposure to ensure a modest number of saturated pixels would be observed. Subsequent images were then taken with sample rocking, starting with a nominal rocking range and then doubling it for each subsequent image, all with a constant step size of 0.1°. For the third image series, a constant rocking range of 8° was used while the initial step size of 0.8° was halved for each subsequent image. Table 4 summarizes these key parameters for each series. In each series, care was taken to expose each image to the same incident photon intensity as determined by the number of total ion chamber counts.

4.4. Results and analysis

4.4.1. Improving intensity distribution. To appreciate the difference rocking can make in the context of improving intensity distribution, it is most instructive to examine the Debye rings observed at the highest 2θ values. There are several reasons why this is the case, but let it suffice to point out that these Debye rings are the least intense, and this weak intensity is distributed along the rings of greatest circumference. Fig. 6 shows a small region of the detector for three separate images from series 1. The salient feature of series 1 is the small incident beam size, resulting in a minute irradiated sample volume ($\sim 10^{-8}$ cm^3), making it particularly difficult to obtain an even azimuthal intensity distribution. This is particularly noticeable in the case of the stationary DAC (Fig. 6, left), where the rings can be described, for the most part, as intermittent spots superimposed on extremely faint rings. At the maximum rocking range of the series (Fig. 6, right), the rings appear much more homogeneous; the spotting is less prevalent and the continuous rings appear more intense.

To explore this improvement quantitatively, the observed intensity of the (331) reflection was rebinned as a function of azimuthal angle (*i.e.* along the Debye ring) for images in all three series. The (331) reflection was chosen because it was the largest Debye ring, at approximately 31.4° 2θ, captured in its

Table 4
Beam dimensions, rocking range and discrete step size for each of the three image series.

Series	Beam size (μm)	Rocking range (°)		Step size (°)	
1	15 × 15	Variable	0–16	Fixed	0.1
2	45 × 45	Variable	0–32	Fixed	0.1
3	45 × 45	Fixed	8	Variable	0.8–0.025

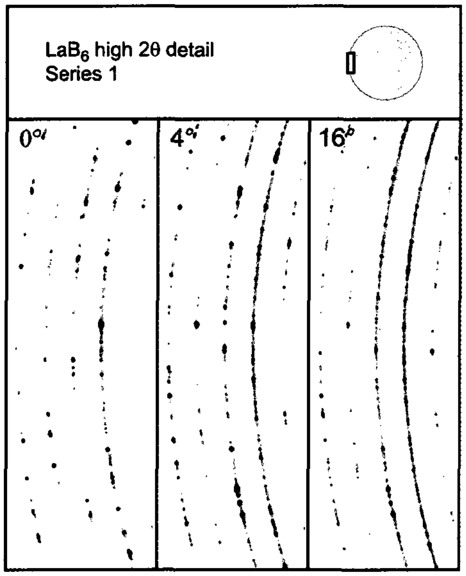

Figure 6
High 2θ detail of the detector (indicated by the small rectangle, with respect to the full image area, in the figure heading) for selected images from series 1. Note that as the rocking range (indicated in the upper left corner of each image) increases from the stationary sample (left) to the maximum rocking range of the series (right), the Debye rings exhibit a marked improvement in homogeneity of intensity distribution.

Table 5
Basic statistical information for the (331) reflection collected from 1400 azimuthal bins (from 5° to 355° by 0.25°) of fixed width ($2\theta \simeq 0.5°$).

In general, the mean intensity increases only slightly with rocking, suggesting that area detectors are quite effective in yielding reliable relative intensities, even for stationary samples. In general, the standard deviation about the mean and the total intensity range decreases significantly with rocking, suggesting that rocking is crucial to obtaining a more homogeneous distribution of intensities, with fewer occurrences of extreme (saturated) intensity.

Series	Range (°)	Step size (°)	Mean (counts)	Standard deviation (counts)	Intensity range (counts)
1	0	0.1	187	124	2869
	1		192	113	2501
	2		195	86	1332
	4		197	116	3037
	8		196	71	1567
	16		195	51	814
2	0	0.1	663	407	7656
	2		709	288	3187
	4		729	317	4055
	8		714	217	2220
	16		711	162	1792
	32		729	135	1473
3	8	0.8	651	254	3601
		0.4	683	217	2483
		0.2	664	194	1839
		0.1	695	211	2031
		0.05	672	204	2013
		0.025	663	200	1945

entirety by the detector. Specifically, the intensity recorded in a 3 mm strip (spanning approximately 0.5° 2θ) straddling the Debye ring was rebinned every quarter of an azimuthal degree, resulting in a total of 1440 bins. Table 5 shows the results of a basic statistical analysis carried out on the rebinned data. (Note that only a total of 1400 data points were considered in the analysis inasmuch as a 10-azimuthal-degree region was omitted to ensure the portion of the detector shielded by the beam stop did not contribute to the statistics.)

Some general (although not exclusively monotonic) trends arise in all three series as the rocking range is increased or as the step size is decreased: the mean intensity increases, while at the same time the standard deviation about the mean and the total range of observed intensities decrease. The combination of these three factors clearly demonstrates that the distribution of intensities along the (331) Debye ring is more homogeneous with rocking. (Note that a statistical analysis was carried out for three other rings in each image, with corroborating results; however, the details have been omitted for the sake of brevity.)

Looking a little more closely at the mean intensities in the first two series, the difference between the stationary DAC and the smallest rocking range is perhaps appreciable, but a subsequent increase in the rocking range does not result in a significant increase in the mean intensity. This is not surprising inasmuch as care was taken to expose the sample to the same number of counts for each image. Conversely, the decrease (*i.e.* the improvement) in the standard deviation is substantial as the rocking range is increased. This can readily be explained by an increase in the number of distinct crystallite orientations during exposure. The combination of these two factors leads to the conclusion that, although rocking improves the distribution of the intensities, it does not significantly affect the total observed intensity. In short, area detectors are quite effective in yielding reliable relative intensities, even in the absence of rocking (at least in the case of a good powder under ambient conditions).

To appreciate the difference in the total range of observed intensities, Fig. 7 provides a comparison of the intensity *versus* azimuthal angle for the (331) reflection in the case of the stationary DAC (top) as well as rocking over 32° (bottom) for images from series 2. The difference between the two is immediately apparent, further demonstrating that the intensity along the rings is more evenly distributed when the DAC is rocked. It should be reiterated that, despite the intense spikes observed in the case of the stationary DAC, the mean intensity is less than that observed for any of the rocking ranges. The significant reduction in the total range of observed intensities can be looked at not only from the perspective of improving intensity distribution but also from the perspective of reducing detector saturation. This latter perspective is further developed in the following section.

4.4.2. Reducing detector saturation. To appreciate the difference rocking can make in the context of reducing detector saturation, it is most instructive to look at the Debye rings at low 2θ values. Not only are these the most intense rings, but this strong intensity is packed into rings with the shortest circumference. It is these rings which will saturate first in the event of overexposure. The importance of this point cannot be overstressed; when it comes to data analysis (*e.g.* structural refinement), strong reflections can carry significant weight in a number of respects, including line shape and lattice

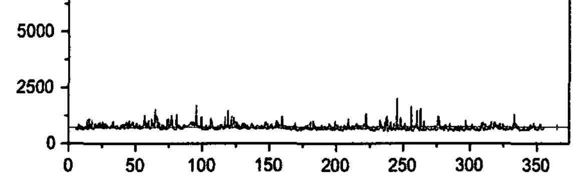

Figure 7
Intensity *versus* azimuthal angle for the (331) reflection for the stationary sample (top) and for the maximum rocking range of 32° (bottom) from series 2. Note that both are plotted on the same intensity scale to contrast the marked influence that sample rocking has on intensity distribution. The horizontal lines indicate the mean intensity and the vertical bars at the right indicate the standard deviation of the respective plots.

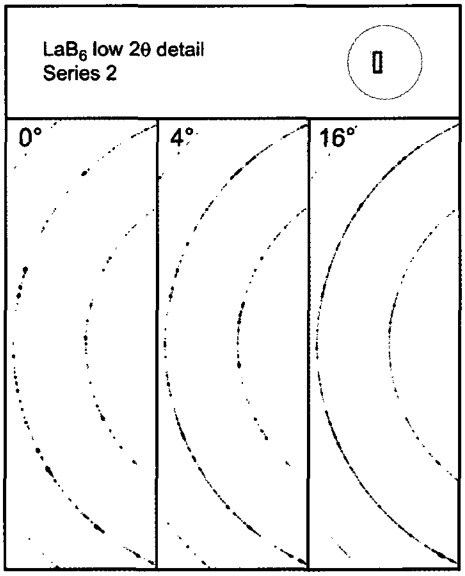

Figure 8
Low 2θ detail of the detector for selected images from series 2. Note that as the rocking range increases from the stationary sample (left) to a rocking range of 16° (right), the Debye rings exhibit a marked decrease in the occurrence of intense Bragg spots superimposed on the Debye rings.

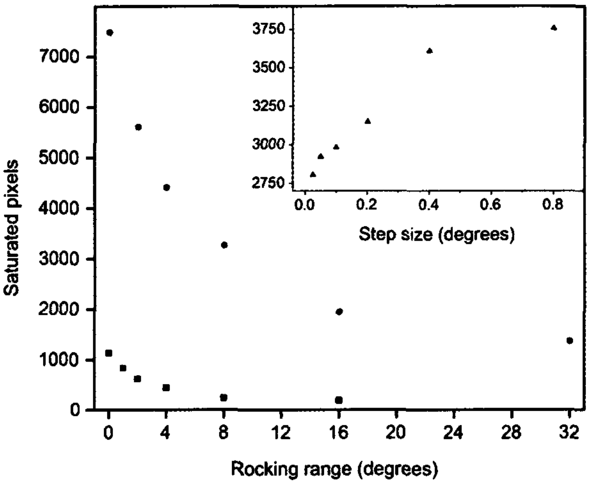

Figure 9
Number of saturated pixels *versus* rocking range for series 1 (squares) and series 2 (circles). At the maximum rocking range, for both series the number decreases by more than 80% as compared with the stationary sample. The inset is a plot of the number of saturated pixels *versus* step size for series 3 (triangles), showing a more modest decrease of approximately 25%.

constants. Also, relative intensities are often defined in terms of the most intense peak. Unfortunately, it is the most intense peaks which are most susceptible to intensity inaccuracies owing to pixel saturation.

Fig. 8 shows a portion of three images from series 2. In the case of the stationary DAC (Fig. 8, left), the reflections are marked by intense Bragg spots superimposed on Debye rings. As the DAC is rocked (Fig. 8, centre) and as the rocking range is subsequently increased (Fig. 8, right), the occurrence of the intense Bragg spots is significantly reduced, resulting in a more consistent line width along the rings. Also, the expected improvement in intensity distribution is noticeable.

Turning to a quantitative evaluation of the benefits, Fig. 9 shows the number of saturated pixels ($I_{\rm pixel} > 65535$ counts for the mar345 detector at 100 μm pixel resolution) as a function of the rocking range for series 1 and 2. In each series the number of saturated pixels fell by over 80% at the maximum rocking range (16° and 32° for series 1 and series 2, respectively) as compared with the stationary DAC. The inset of Fig. 9 shows the number of saturated pixels as a function of step size for the constant rocking range of 8°. Interestingly, for the smallest step size, the decrease in saturated pixels is only 25% as compared with the largest step size. In this particular case it is clear that both increasing the rocking range and decreasing the step size are effective in minimizing detector saturation; however, the maximum potential is primarily dependent on the overall rocking range, as this ultimately determines the maximum number of unique crystallite orientations that contribute to the intensity observed in the diffraction image.

4.4.3. Rietveld analysis.

Full-pattern structural refinements were carried out on all of the diffraction patterns from the three image series. One cannot overstate the importance of starting out with the highest quality data possible when carrying out such refinements. In the present work, however, poor data were intentionally collected in an effort to accentuate the effect that rocking has on reducing detector saturation; the reader should bear this in mind when considering the absolute results of the refinements. Notwithstanding this, some interesting results emerge from the analyses, which further demonstrate some of the benefits obtained by rocking polycrystalline samples.

The intense Bragg spots result in small bulges of intensity around the Debye rings. As these are progressively removed through rocking, the line width of the rings should progressively decrease. Fig. 10 (top) shows the line width *versus* 2θ for series 2. The most striking difference is observed between the stationary DAC and the 2° rocking range. In the case of the stationary DAC, the intense Bragg spots significantly affect the line width and, as the scattering angle is increased, this impact is exacerbated as the projections of intense Bragg spots onto the flat area detector increase by a factor of $\sim 1/\cos(2\theta)$, resulting in a maximum line width observed at $2\theta \simeq 18°$. At still higher 2θ, saturation effects are less prominent and the line width decreases accordingly. With even the most modest rocking range of 2°, the effects of pixel saturation are mitigated such that the line width remains roughly constant up to $2\theta \simeq 18°$, after which it decreases in a manner similar to that observed with the stationary DAC. Subsequent increases in rocking range show a systematic (although less pronounced) decrease in line width. Furthermore, the change in the overall shape of the curves is minimal, suggesting that rocking over

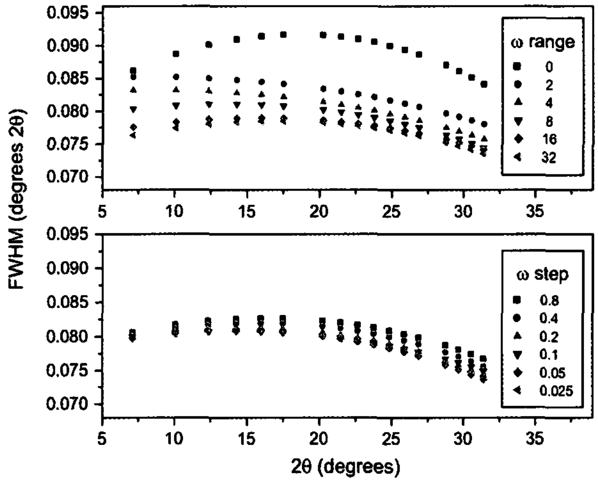

Figure 10
Line width *versus* 2θ for series 2 (top) and series 3 (bottom). Sample rocking decreases line width by minimizing the occurrence of intense Bragg spots, pixel saturation and pixel bleeding.

even a small range results in a more appropriate line shape. Notably, at the highest 2θ values, the line width remains roughly constant for ranges greater than 8°, suggesting that the effects of pixel saturation are essentially eliminated for these reflections. Fig. 10 (bottom) shows the line width for series 3. Note that the observed line width is almost exactly that observed for the 8° range from series 2, as expected. The decrease in line width is measurable, yet minimal as compared with series 1 and 2 (much like the decrease in saturated pixels). Again, it is clear that both range and step size play a role in minimizing line width, but range appears to play the dominant role.

Mixed results were obtained for the quality of the fits. Table 6 shows the R-factors for the images of each series. Series 1 exhibited a general trend of decreasing R values with increased rocking range; however, this was not the case for series 2. The refined parameters included an overall isotropic displacement (sometimes referred to as a temperature) factor. The refined values for B, shown in the final column in Table 6, reveal an important benefit of rocking (or more appropriately, minimizing saturated pixels). To clarify, the B parameter accounts for the mean-square displacement of the atoms from their equilibrium position, and if the magnitude of this displacement is appreciable with respect to the distance between a particular set of planes $\{hkl\}$ an appreciable decrease in observed diffraction intensity will result. By definition, B is positive. However, in the least-squares refinement procedure employed by *FullProf* there is no restriction on the sign of B (except that it is explicitly constrained by the user prior to refinement), and a physically meaningless negative B value can be obtained if the observed intensity for high 2θ reflections is too large relative to the intensity for low 2θ reflections. As stated earlier, saturated pixels were masked prior to data analysis, such that they did not contribute to the measured intensities of the resulting diffraction patterns.

Table 6
Quality of fit and overall displacement factors from Rietveld refinements of diffraction patterns from series 1 and 2.

Note that by reducing the number of saturated pixels recorded for low 2θ peaks the displacement parameter B goes from negative to positive.

Series	Rocking range (°)	$R_{\rm wp}$ (%)	$R_{\rm Bragg}$ (%)	$B_{\rm overall}$ (Å^2)
1	0	4.20	2.60	−0.13 (3)
	1	4.01	2.35	−0.17 (2)
	2	3.73	2.23	−0.12 (2)
	4	4.24	2.59	−0.12 (2)
	8	3.73	2.19	0.05 (2)
	16	3.69	1.70	0.19 (2)
2	0	4.64	2.53	−0.42 (2)
	2	4.86	3.14	−0.37 (2)
	4	4.55	2.82	−0.30 (1)
	8	4.70	2.57	0.94 (2)
	16	4.58	2.51	1.12 (2)
	32	4.46	2.13	0.99 (2)

Therefore the intensities of low 2θ reflections (where the majority of saturated pixels occurred) are too low relative to the higher 2θ reflections, resulting in a negative B value. As the rocking range was increased, the intensity information lost to masked pixels decreased, and eventually the detector saturation was reduced to the point that positive B values were obtained. For brevity, the detailed results for series 3 have been omitted from the table as there was less variation with the constant rocking range; however, the average value of the results were $R_{\rm wp}$ = 4.68%, $R_{\rm Bragg}$ = 2.34% and B = 0.72 Å^2, similar to the results obtained from the series 2 image rocked over 8°.

4.5. Application of pressure

Applying pressure to a sample introduces additional challenges which make it difficult to immediately appreciate the benefits of rocking. However, rocking is essential to improving the quality of data recorded from less-than-ideal samples. Depending on the particular sample, as well as the type (or lack) of pressure-transmitting medium used, X-ray diffraction images exhibit a number of features that may not be apparent at atmospheric pressure. Line width can be significantly broadened not only by intense Bragg spots but also by small crystallite size or by anisotropic strain in crystallites. The intensity distribution along Debye rings can vary significantly not only because of limited sample volume but also because of preferred orientation of crystallites owing to crystal growth habit and/or non-hydrostatic conditions.

Fig. 11 shows portions of two images from a sample containing a mixture of barium compounds (Smith *et al.*, 2007) at approximately 5.8 GPa (no pressure-transmitting medium was used as BaH_2 is extremely hygroscopic). At a glance, it is not apparent that the intensity distribution has been significantly improved by rocking, nor is it apparent that there are fewer intense regions. In fact, the striking feature is that the two images are almost identical in appearance. However, even in this severe case of crystallite strain and texture, rocking still

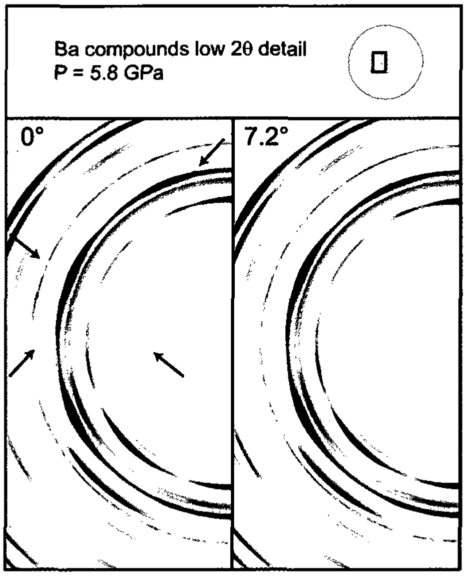

Figure 11
Low 2θ detail of the detector for selected images from experiments on barium compounds at high pressure. A visual comparison of the two images shows few differences; however, there is a respectable decrease, approximately 20%, in the number of saturated pixels in the case of the rocked DAC. Additionally, Kossel lines arising from the diamond anvils in the stationary DAC image (indicated by the arrows) are no longer present when the DAC is rocked.

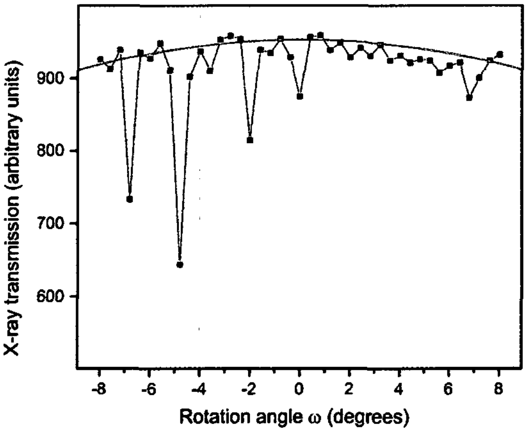

Figure 12
X-ray transmission through the DAC as a function of rotation angle ω. The measured values (squares) are connected with lines to emphasize dramatic dips in intensity owing to diffraction from the diamond anvils. The solid arc near the top of the plot indicates the approximate intensity fall-off expected owing to the increase in path length through the diamonds as the DAC is rotated. The shaded portions detail the rocking range for Fig. 7: the shaded portions on the far left and right indicate the limits of the rocking range, whereas the two narrow shaded portions indicate regions omitted from the total rocking range.

has a measurable effect. Rocking the DAC resulted in a decrease in the number of saturated pixels by 20% as compared with that observed for the stationary DAC. This is not as significant as the over 50% decrease observed for LaB_6 when rocked by 8°, but it is important to note that in the case of the standard the saturated pixels are due to discrete intense Bragg spots, whereas in the case of the barium compounds saturation is caused by preferred orientation resulting in significant portions (at periodic azimuthal angles) of the low 2θ rings reaching saturation level.

An additional, albeit minor, benefit brought about by rocking the DAC is that the Kossel lines (faintly visible in the reproduction of Fig. 11, left, but clearly visible in the original image) recorded with the stationary DAC disappear with rocking. Kossel lines arise from the edges of the diamond anvil facets. While these lines rarely cause any difficulty, they can occasionally influence observed intensities if by chance they coincide with a significant portion of a Debye ring (see, for example, Moriwaki *et al.*, 2006). Rocking the sample in turn rocks the diamond anvils, which removes any visible Kossel lines.

Interestingly, in the case of rocking, approximately 10% of the saturated pixels are due to diamond Bragg spots which were not observed in the case of the stationary DAC. Adding the anvils constitutes adding two very large single crystals to the experimental configuration, and as the sample is rocked the diamonds will invariably satisfy the Bragg condition at certain rocking angles. Consequently, the diffracted intensity recorded by the detector can be significant.

Fig. 12 shows a plot of the X-ray transmission through the DAC as a function of ω. The arc across the top of the plot is an estimate of the expected transmission owing to the effective change in thickness of the diamond as a function of ω. There are several moderate and a few severe intensity dips below this line owing to diffraction from the diamonds, which removes a number of photons from the transmitted beam *via* primary extinction. Of course, it is not necessarily the case that all of the Bragg spots indicated by the dips will fall on the detector, but invariably some of them do, and the intense spots reach saturation extremely quickly as compared with instances of saturation coming from the sample. One strategy is to avoid the angular ranges coinciding with the most intense diamond diffraction. In the macro used in the experimental control software, an option was incorporated to omit discrete angular ranges within the overall rocking limits. The shaded regions in Fig. 12 denote angular ranges omitted when rocking the DAC. In fact, Fig. 12 was obtained from the sample containing the barium compounds, so if the reader notes that the high-pressure sample in Fig. 11 was rocked over a range of 7.2°, it was actually rocked over 8° (−4° to 4°), omitting two regions totalling 0.8°. It should be noted that the rotation velocity of the stage is such that an omitted region is skipped in less than a second. This is sufficient to avoid significant diffraction at moderate X-ray sources. For intense sources where images are captured in a few seconds as opposed to a few minutes (see, for example, Mezouar *et al.*, 2005), it might prove necessary to use a high-speed shutter to block the beam during rotation through omitted ranges.

4.6. Rocking summary

From the preceding data it is clear that rocking significantly improves the quality of high-pressure powder diffraction images in two complimentary ways. First, it promotes a more homogeneous intensity distribution along Debye rings, and second, it reduces the occurrence of detector saturation. Regarding intensity distribution, for good powders which do not suffer too severely from strain or texture, the improvement is obvious. In the case of difficult samples, it is not clear that rocking will significantly improve the intensity distribution. An interesting result is that the data reinforce the idea that the use of an area detector to capture complete Debye rings is quite effective in yielding good intensities, even in the case of the stationary DAC.

The area detectors most commonly employed in high-pressure powder X-ray diffraction studies have a high, but nevertheless limited, dynamic range. The reduction of detector saturation was substantial for both the Standard Reference Material as well as the high-pressure sample, the latter suffering from a number of complicating factors. It is this aspect of sample rocking that is arguably most crucial. In practice, the number of saturated pixels should be minimal, and typically, exposure time is reduced to achieve this. However, rocking will allow exposure time to be increased slightly, in the end allowing one to make better use of the detector's full dynamic range. Furthermore, by reducing intense Bragg spots, other benefits such as decreased line width were observed. DAC samples should be rocked over the largest possible range with the smallest possible step size to maximize the number of unique crystallite orientations with respect to the beam and minimize the amount of time that any particular orientation contributes to the diffracted intensity.

5. Conclusion

The selected techniques described above can play a crucial role in optimizing the quality of data obtained when carrying out diamond anvil cell crystallography. Accurate reproducible positioning of samples at a unique position in the experimental configuration is critical as it allows the sample-to-detector distance obtained from images of calibration standards to be correctly applied to data analysis of research samples. The centring technique described above provides excellent results, while at the same time offering the flexibility often required to accommodate various (and often crowded) experimental configurations commonly encountered at synchrotron radiation facilities. Properly locating the sample at the centre of rotation affords the possibility of rocking polycrystalline samples during X-ray exposure. This practice is of particular importance to high-pressure diamond anvil cell crystallography, as the sample volume is severely limited. Rocking clearly yields the expected effect of improving the distribution of intensity along Debye rings. More importantly, it limits detector saturation by limiting the amount of time large grains assume a particular orientation with respect to the incident X-ray beam. These techniques are conceptually quite simple, and with a modicum of care exercised by the user they can be used to great effect; they should be incorporated as routine practices when carrying out diamond anvil cell crystallography.

SD wishes to acknowledge the Natural Science and Engineering Research Council of Canada for financial support. The research described in this paper was performed at the Canadian Light Source, which is supported by NSERC, NRC, CIHR and the University of Saskatchewan. The authors also gratefully acknowledge the work of Dr Ning Chen, Dr Chang-Yong Kim and Dr De-Tong Jiang in facilitating experiments carried out at the HXMA beamline of the Canadian Light Source.

References

Budzianowski, A. & Katrusiak, A. (2004). *High-Pressure Crystallography*, edited by A. Katrusiak and P. McMillan, pp. 101–112. The Netherlands: Kluwer.

Dera, P. & Katrusiak, A. (1999). *J. Appl. Cryst.* **32**, 510–515.

Hamilton, W. C. (1974). *International Tables for X-ray Crystallography*, Vol. IV, pp. 273–284. Birmangham: Kynoch Press. (Present distributor Kluwer Academic Publishers, Dordrecht.)

Hammersley, A. P., Svensson, S. O., Hanfland, M., Fitch, A. N. & Häusermann, D. (1996). *High Pres. Res.* **14**, 235–248.

King, H. E. & Finger, L. W. (1979). *J. Appl. Cryst.* **12**, 374–378.

Kunz, M., MacDowell, A. A., Caldwell, W. A., Cambie, D., Celestre, R. S., Domning, E. E., Duarte, R. M., Gleason, A. E., Glossinger, J. M., Kelez, N., Plate, D. W., Yu, T., Zaug, J. M., Padmore, H. A., Jeanloz, R., Alivisatos, A. P. & Clark, S. M. (2005). *J. Synchrotron Rad.* **12**, 650–658.

Mezouar, M., Crichton, W. A., Bauchau, S., Thurel, F., Witsch, H., Torrecillas, F., Blattmann, G., Marion, P., Dabin, Y., Chavanne, J., Hignette, O., Morawe, C. & Borel, C. (2005). *J. Synchrotron Rad.* **12**, 659–664.

Moriwaki, T., Akahama, Y., Kawamura, H., Nakano, S. & Takemura, K. (2006). *J. Phys. Soc. Jpn*, **75**, 074603.

Rodriguez-Carvajal, J. (2006). *FULLPROF*, version 3.70, July 2006. ILL, Grenoble, France.

Ruoff, A. L., Luo, H., Vanderborgh, C., Xia, H., Brister, K. & Arnold, V. (1993). *Rev. Sci. Instrum.* **64**, 3462–3466.

Sakata, M., Itsubo, T., Nishibori, E., Moritomo, Y., Kojima, N., Ohishi, Y. & Takata, M. (2004). *J. Phys. Chem. Solids*, **65**, 1973–1976.

Smith, J. S., Desgreniers, S., Tse, J. S. & Klug, D. D. (2007). *J. Appl. Phys.* **102**, 043520.

Chapter 7 Conclusion

This chapter constitutes a brief summary and related discussion of some common results obtained for the heavy alkaline earth hydrides and barium fluoride, together with suggestions for possible future avenues of high-pressure research with respect to these compounds. It also includes a short discussion regarding the selected experimental techniques presented in Chapter 6. Table 1 summarizes the compounds, together with the maximum experimental and theoretical pressures of the respective studies, presented in the preceding chapters.

Compound	P_{max} (GPa)	
	Experimental	Theoretical
CaH_2	22.9	35
SrH_2	113	200+
BaH_2	22.1	20
BaF_2	77	200+

Table 1: Summary of the compounds presented in the preceding chapters, together with the maximum experimental and theoretical pressures of the respective studies. Note that in some cases my collaborators and I have since extended the maximum experimental and/or theoretical pressure. Some of these more recent results will be discussed below.

1. Substitution and the Ni_2In transition

Cation and anion substitution in ionic compounds constitutes an important technique for modifying particular properties of a given material while still possibly maintaining some of the basic properties common to a related group of materials. As discussed in Chapter 3, this could be particularly relevant in commercial applications related to hydrogen storage where substitution could, for example, lower the pressure (or similarly, temperature) required to obtain a high-density phase for efficient hydrogen storage, or improve reaction kinetics to facilitate hydrogen exchange. While the HAEHs may not constitute a solution to the hydrogen storage/exchange problem, they nevertheless provide an instructive example of the benefits that may be gained by substitution.

All of the HAEHs, as well as barium fluoride, undergo a pressure-induced, first-order structural phase transition from the cotunnite-type structure to the Ni_2In-type structure. Furthermore, this transition is reversible; upon decreasing pressure the cotunnite-type structure is recovered (however, there is some hysteresis in the recovery pressure). Table 2 summarizes the transition pressures and stable pressure regimes of the two structures for each of the respective compounds.

Compound	Structure	$P_{transition}$ (GPa)	Stability Range (GPa)
CaH_2	Cotunnite	16	0 - 16
	Ni_2In		16 – 138
SrH_2	Cotunnite	8.3	0 - 8.3
	Ni_2In		8.3 – 115
BaH_2	Cotunnite	1.6	0 - 1.6
	Ni_2In		1.6 – 48
BaF_2	Cotunnite	14.3	3 - 14.3
	Ni_2In		14.3 - 77+

Table 2: Cotunnite→Ni_2In transition pressure and stability range of the respective phases for each of the compounds in this study.

Looking at Table 2, for the HAEHs, the pressure required to obtain the higher-density Ni_2In phase decreases with increasing cation mass. The same is true regarding the maximum stable pressure of the Ni_2In phase; it decreases with increasing cation mass. A similar trend is observed for the fluorides. Both CaF_2[1] and BaF_2 adopt the cubic fluorite structure at ambient conditions, and subsequently transform to the cotunnite type structure at 9.5 GPa,[2] and 3.0 GPa, respectively. For fluorides and hydrides, an increase in cation mass leads to a decrease in transition pressure.

Interestingly, the substitution of a heavier anion has the opposite effect. BaF_2 does not transform to the Ni_2In structure until 14.3 GPa (as compared to 1.6 GPa for BaH_2), and there are no reports of high-density phases beyond the cotunnite structure for CaF_2. Furthermore, while the AlB_2 phase has been observed for BaH_2, and has been predicted by first-principles calculations for CaH_2 and SrH_2 at experimentally attainable pressures, the AlB_2 phase is not expected to occur in BaF_2 (at least not for several hundred GPa). For these compounds, an increase in anion mass leads to an increase in transition pressure

Of course, substitution frequently involves a compromise of some sort, and in some cases the pros can be (quite literally) outweighed by the cons. For the current study, substitution proved very successful from a fundamental point of view. The cotunnite phase of MgH_2 remained stable up to 57 GPa, whereas a post-cotunnite phase was observed for all of the HAEHs at pressures well below 57 GPa, and furthermore, a post-Ni_2In phase has been observed for BaH_2 at approximately 50 GPa.

Considering a possible subsequent pressure-induced phase transition in MgH_2, the answer is unclear. With regard to the progression of the cation coordination number in ionic AX_2 compounds, there are several examples of 9→10→11, yet all of the HAEHs and barium fluoride skip a coordination number of 10, as the cotunnite→Ni_2In transition is characterized by an increase in the cation coordination number from 9 to 11. A straightforward approach for future studies on MgH_2 would be to carry out calculations and experiments up to 100 GPa or more. Perhaps a more valuable approach, however, would be a systematic study of the compounds that both adopt and skip a 10-coordinated cation structure, looking for a general mechanism or structural characteristic that would allow one to reliably predict which structural progression a particular AX_2 compound will follow.

As far as future research prospects for the fluorides, from a fundamental point of view it might be interesting to explore CaF_2 at high pressure in the search for a post-cotunnite phase. However, BaF_2 constitutes a particularly interesting opportunity for further study. I further discuss this in the following section.

2. The AlB_2 structure

I hope the reader will forgive a personal aside: with regard to the observed Ni_2In→AlB_2 phase transition in BaH_2, I was beaten to the punch. I suppose this is not unusual in the case where several different research groups are studying the same compounds. However, it turns out that there is still some work to be done on the AlB_2 phase of BaH_2. As discussed in previous chapters, the transition from the Ni_2In to the AlB_2 structure is characterized by a change from ionic to covalent bonding. However, recent first-principles calculations by my collaborators, Dr. Klug and Professor Tse, have revealed some interesting results.

Klug has carried out first-principles calculations of the pressure-dependent frequencies of the two Raman modes observed in the Ni_2In phase of BaH_2. Interestingly, the calculations predict a softening (i.e., a decrease in frequency with pressure) of the low-wavenumber mode associated with barium just prior to the phase transition (Figure 1).

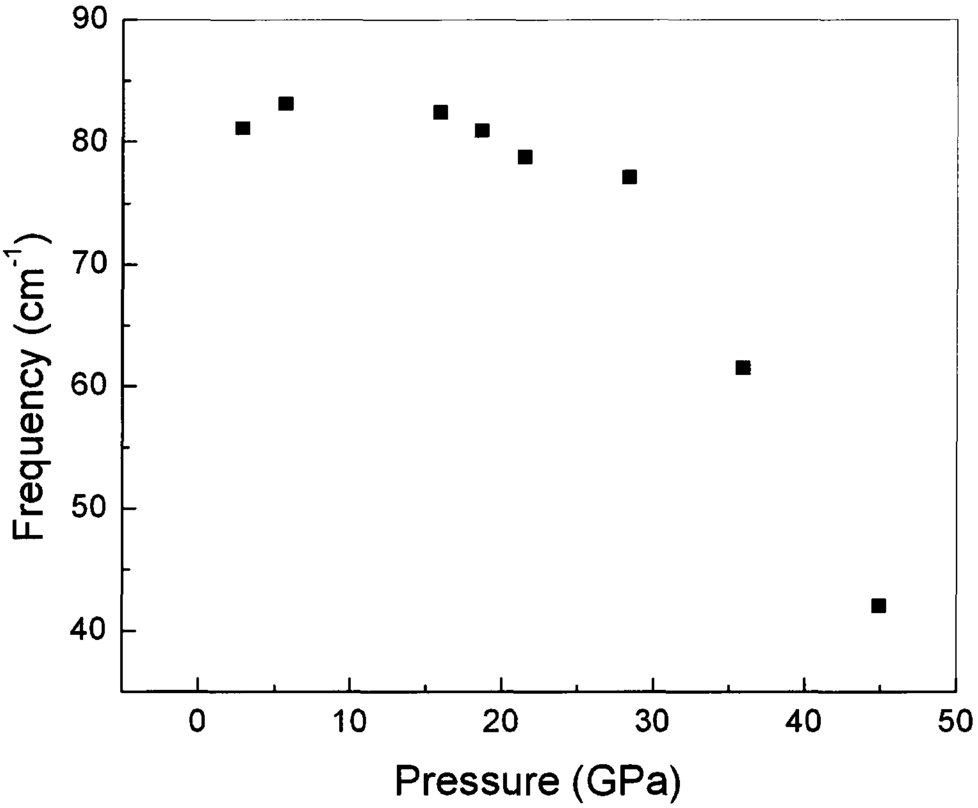

Figure 1: Calculated pressure dependence of the low-wavenumber mode of BaH_2 in the Ni_2In structure. The predicted mode softening is unusual. However, it has not yet been observed experimentally. These results are unpublished.

This is an unusual phenomenon. As discussed in Chapter 1, as the pressure (and correspondingly the density) of a crystalline solid increases, the energy of the system increases, such that the frequencies of the lattice vibrations giving rise to the optical phonon spectrum increase. This predicted mode softening before the transition would serve as an important precursor characterizing the phase transition, and further study of the lattice dynamics which give rise to this mode softening is certainly of interest. I have since carried out Raman experiments on BaH_2 in an attempt to observe this mode softening experimentally. Unfortunately, I have not yet been able to observe it. However, it should be noted that because this mode is observed at low wavenumbers (and is supposed to decrease to even lower wavenumbers before the transition), it is extremely difficult to observe this weak mode, as it is so close to the extremely strong Rayleigh scattering of the laser (i.e., the mode is too close to the laser line to be detected with the current Raman spectroscopy apparatus). Furthermore, upon transforming to the AlB_2 structure, the sample is no longer transparent to visible light. The result is that the scattering volume is significantly decreased (it becomes more of a scattering surface than a scattering volume, as the laser light can no longer penetrate into the sample). Another difficulty encountered with the change in opacity is the corresponding increase in the intensity of the background. The combination of these various factors has proved challenging, however I am still hopeful that this softening can be observed in future experimental attempts.

Tse has carried out first-principles calculations of the band structure, and has reported (personal communication) that the AlB_2 phase of BaH_2 is metallic. Furthermore, while it is not part of the research presented in this thesis, I have recently obtained high-pressure powder x-ray diffraction data of BaH_2 in the AlB_2 phase. My collaborators and I are currently in the process of preparing these combined experimental and theoretical results for the publication of a more complete description of this high-pressure structure.

As mentioned several times throughout the previous chapters, a cation coordination number of 11 marks the highest observed for ionic AX_2 compounds. While it is true that in the AlB_2 structure Ba is 12-coordinated, the material is no longer an ionic solid (the bonding is either covalent or metallic). As BaF_2 is not predicted to undergo this same transition, it constitutes perhaps the best opportunity to search for a cation coordination number of 12 in an ionic AX_2 compound for which the bonding remains ionic. Unfortunately, it is not clear at what pressure a proposed structural phase transition may occur. At this point the best way forward would either be to carry out *ab initio* first-principles calculations to search for possible structures or to put it in a DAC and increase the maximum experimental pressure well over 100 GPa to look for a possible phase transition.

3. Ionic AX_2 compounds as a function of pressure

In the preceding chapters I have discussed in several places the observed relationship among the molar volume, the mean cation-anion distance, and coordination number in ionic AX_2 compounds. Specifically:

$$V_{molar} = kd_0^{\,3}/N ; k = 14.4(6) \tag{1}$$

I first came across this relationship when reading the work of Leger *et al.* on BaF_2, which includes a figure showing this relationship for a number of oxides, fluorides, bromides, etc., for both ambient- and high-pressure phases. This relationship is shown in Figure 2.

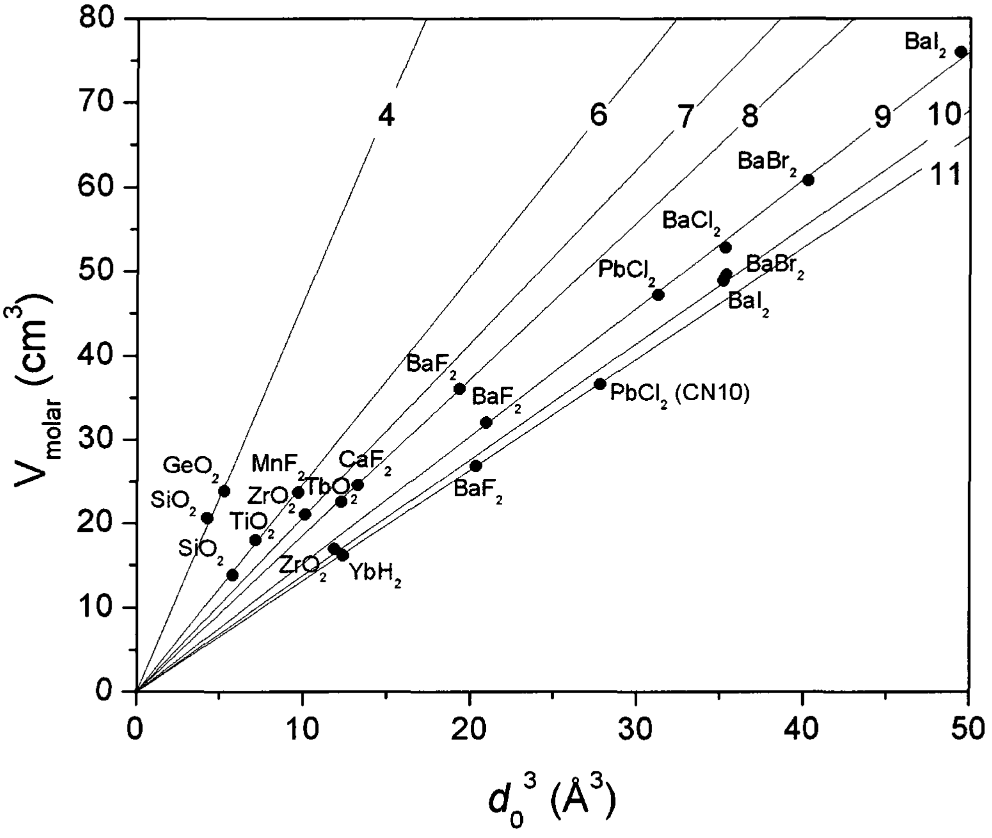

Figure 2: Molar volume as a function of the cube of the mean cation-anion distance for several ionic AX_2 compounds, including both ambient- (black) and high-pressure (blue) structures. The solid lines have a slope of 14.4(6)/*N*, where *N* is the cation coordination number (indicated on the plot).

Figure 9 of Chapter 3 demonstrates that this relationship holds for CaH_2 and BaH_2 not only at ambient pressure and immediately following a pressure-induced phase transition, but also as a function of pressure throughout the stable pressure range of a given phase. In the subsequent work on BaF_2, this pressure dependence turned out to be an important corroborating factor for arguing that BaF_2 remains an insulator up to at least 77 GPa (the maximum pressure of the experimental study). Figure 3 includes all of the data from the preceding chapters. Again, this relationship holds for all of the HAEHs and BaF_2 at ambient pressure, immediately following a pressure-induced structural phase transition, and throughout the entire stable pressure regime of the respective phases.

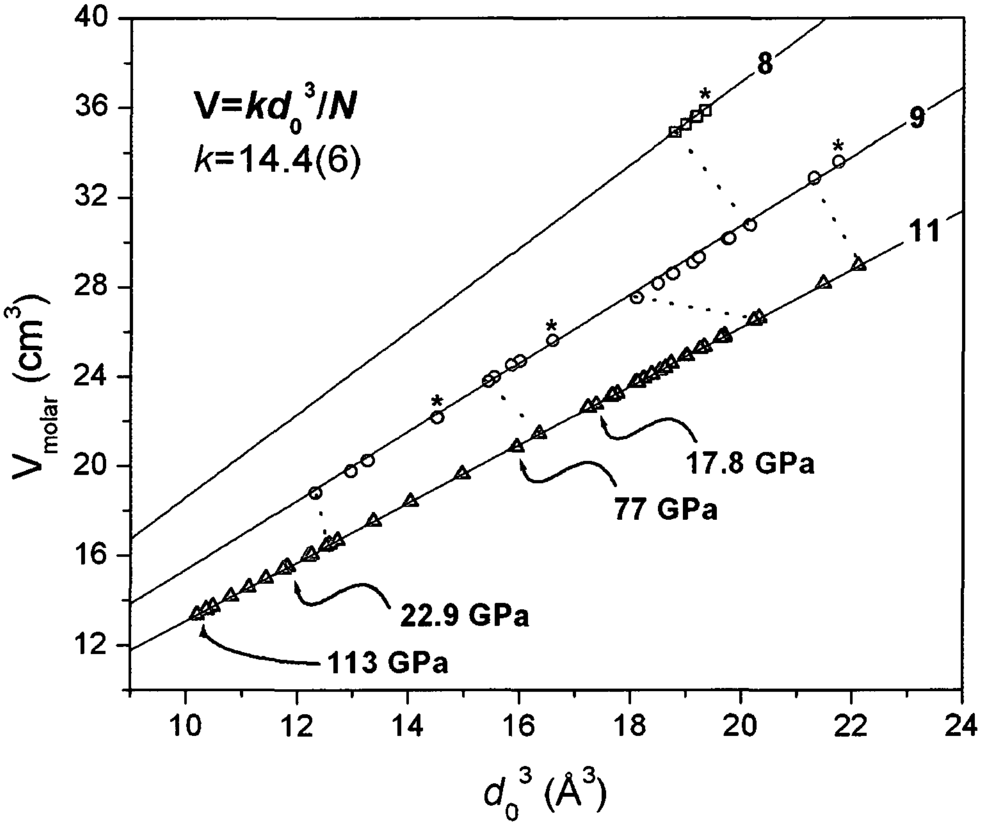

Figure 3: Molar volume *vs.* the cube of the mean cation-anion distance for CaH_2 (black), SrH_2 (red), BaH_2 (magenta), and BaF_2 (blue). Ambient pressure data points are indicated by asterisks (*). As the pressure is increased, data tend toward the origin along the coordination number line, or increase in coordination number across a phase transition (dotted lines). The relationship holds up to the maximum pressure of the respective experimental studies (indicated on the plot) for all of these compounds.

It should also be noted that this could serve as an excellent method for measuring the ionic radii of ions as a function of pressure. Specifically, the mean cation-anion distance is very close to the sum of the individual ionic radii of the atoms (in a particular valence state and for a particular coordination). It is certainly worth further investigating the degree to which the pressure dependence of the ionic radii could be determined using this relationship.

4. Development of experimental techniques

While Chapter 6 may seem a little out of place to the reader, it has been included in this work in light of my recent experience and informal discussions with peers at conferences. For example, at a recent high-pressure workshop, I was asked by a peer to explain my method for centering samples. Naturally, after going through some of the basic details of my method, I asked about his particular method for achieving the same goal, and was surprised to hear that "[our group] doesn't worry too much about that." However, it should be clear from Chapter 6 that the proper use of a few conceptually simple experimental techniques can significantly improve the quality of the experimental data, and hence the accuracy of the structural information obtained from the data. The development of high-pressure experimental techniques, including advances in diamond anvil cell methods and the use of synchrotron radiation, has been fast and furious. There has been a push to go to ever increasing pressure and temperature extremes, and develop rapid data collection methods. In short, the goal to reach the highest-possible pressure has often come at the expense of obtaining the highest-quality data. There has been a recent movement in the field of high-pressure research to develop and perfect methods to obtain data of the very highest quality (even at extreme pressure conditions). The selected experimental techniques presented in Chapter 6 will, I believe, be universally adopted (and perhaps improved upon) by the high-pressure community. Another recent innovation has been the introduction of high-pressure gas loaders.

Gas loading at high pressure presents an opportunity to carry out ultra-high pressure experiments under the best-possible hydrostatic conditions. They allow the best-possible pressure transmitting media, namely hydrogen and helium, to be loaded with a sample. With the exception of one sample of barium fluoride, all of the experimental results presented in this work were obtained under non-hydrostatic pressure conditions. Unfortunately, there just aren't that many gas loading systems currently available (perhaps less than a dozen in the world), and furthermore, the existing apparatus are not well-suited to loading samples which are sensitive to the atmosphere (e.g., the HAEHs). As soon as gas loading becomes more accessible (and gas loaders are built with more sophisticated designs) there should be an opportunity to revisit the HAEHs to study their compression and phase transitions under the best-possible hydrostatic conditions.

5. Summary

I am hopeful that the work presented above has been of some interest to the reader. As it stands, the basic pressure-dependent structural progression and compression of the HAEHs has been well-established. However, there are some results in the preceding chapters that I believe will have a broader impact in my field, going beyond the context of the HAEHs. I close with a brief discussion of some of these results.

It is frequently difficult to narrowly define the transition pressure between two phases—phase lines appear to give way to metastable phase areas. This can be true in the context of an individual study (where the onset and completion pressures of a phase transition differ) as well as in the context of multiple studies (where different groups report different transition pressures). There are many factors which can lead to this, for example, pressure gradients within samples, the particular calibration used for pressure measurements, or even inaccurate pressure measurements. In Chapter 3 on barium hydride, the proposed transition pressure was based on Raman spectroscopy measurements. Specifically, I was able to identify a pressure at which the persistent peaks for the low-pressure phase no longer increased in frequency with an increase in pressure. I think, in some case, this can serve as a valuable tool in the future for more narrowly determining transition pressures.

It is well known that the compression obtained under non-hydrostatic pressure conditions will differ from that obtained under hydrostatic pressure conditions. However, I am not aware of a previous report of such a marked difference as that demonstrated for barium fluoride in Chapter 4. In this particular case, the gross disparity between non-hydrostatic and hydrostatic pressure conditions was shown to be due to the particular tendency of the hexagonal crystallites to become oriented in the process of uniaxial compression. I believe this marked difference will serve as one example which calls for the development of techniques which facilitate the best hydrostatic pressure conditions at ultra-high pressures. Furthermore, as BaF_2 has served as an archetype for the cotunnite→Ni_2In transition, I think the results are particularly important as they clear up difficulties associated with the original high-pressure work on BaF_2. Furthermore, I think it also provides strong motivation for developing computational methods which can model non-hydrostatic pressure conditions.

Spinning, rocking, and oscillating a sample are common techniques (employed in almost every type of diffraction geometry) used to improve the scattering statistics in powder x-ray diffraction. In the context of diamond anvil cell crystallography, however, it yields the additional (and in my opinion, more important) benefit of significantly reducing instances of detector pixel saturation. As a personal aside, in my original manuscript I described the two-fold benefit as “improving the good, removing the bad.” I doubt it will surprise the reader to learn that this phrase was not appreciated; one referee was particularly critical. I appealed to the editor by pointing out that this was a simple literary device, employing both rhyme and meter, and using polar opposites to emphasize the contrasting nature of the respective benefits. As for the editor’s decision regarding my appeal, I invite the reader to return to Chapter 6 and count the number of instances this phrase appears (don’t search too long).

While the phrase now has little chance being picked up by the high-pressure community, I am confident the experimental technique will become commonplace, particularly because of reduced detector saturation.

In summary, I believe the results presented in this work will have a significant impact in my field. However, there remains much opportunity for future study of the heavy alkaline earth hydrides, related compounds, and experimental methods and techniques. With rapid advances in equipment, methods, and techniques, the study of materials subjected to extreme pressure conditions promises many exciting results in the near future.

---

[1] H. E. Swanson and E. Tatge, Nat. Bur. Standards **539**, 69 (1953).

[2] L. Gerward, J. Staun Olsen, S. Steenstrup, M. Malinowski, S. Åsbrink, and A. Waskowska, J. Appl. Cryst. **25**, 578 (1992).